HAL
open science

High frequency tunable delay by microwave-photonics techniques for antenna networks

Noor Hamdash

To cite this version:

Noor Hamdash. High frequency tunable delay by microwave-photonics techniques for antenna networks. Electronics. Université de Bretagne occidentale - Brest, 2021. English. NNT : 2021BRES0058 . tel-03652661

HAL Id: tel-03652661

https://theses.hal.science/tel-03652661

Submitted on 26 Apr 2022

HAL is a multi-disciplinary open access archive for the deposit and dissemination of scientific research documents, whether they are published or not. The documents may come from teaching and research institutions in France or abroad, or from public or private research centers.

L'archive ouverte pluridisciplinaire **HAL**, est destinée au dépôt et à la diffusion de documents scientifiques de niveau recherche, publiés ou non, émanant des établissements d'enseignement et de recherche français ou étrangers, des laboratoires publics ou privés.

THESE DE DOCTORAT DE

L'UNIVERSITE
DE BRETAGNE OCCIDENTALE

ECOLE DOCTORALE N° 601
Mathématiques et Sciences et Technologies
de l'Information et de la Communication
Spécialité : *Électronique*

Par
Noor HAMDASH

High Frequency Tunable Delay by Microwave-Photonics Techniques for Antenna Networks

Thèse présentée et soutenue à Brest, le 12 Juillet 2021
Unité de recherche : Laboratoire des Sciences et Techniques de l'Information, de la Communication et de la Connaissance (Lab-STICC / UMR CNRS 6285)

Rapporteurs avant soutenance :

Christelle AUPETIT-BERTHELEMOT	Professeur des universités, Université de Limoges, XLIM / *Rapporteur*
Philippe FERRARI	Professeur des universités, Université de Grenoble, RFIC-Lab / *Rapporteur*

Composition du Jury :

Président :	Jean-Pierre VILCOT	Directeur de Recherche, CNRS, IEMN / Examinateur
Examinateurs :	Perrine BERGER	Ingénieur Docteur, Thales / Examinateur
	Philippe FERRARI	Professeur des universités, Université de Grenoble, RFIC-Lab
	Christelle AUPETIT-BERTHELEMOT	Professeur des universités, Université de Limoges, XLIM
Co-dir. de thèse :	Ammar SHARAIHA	Professeur des universités, Lab-STICC, ENIB
Co-encadrants de thèse :	Thierry RAMPONE	Maîtres de conférences, Lab-STICC, ENIB
	Noham MARTIN	Maîtres de conférences, Lab-STICC, UBO
	Denis LE BERRE	Maîtres de conférences, Lab-STICC, UBO
Invité(s)		
Cédric QUENDO	Professeur des universités, Lab-STICC, UBO / Directeur de thèse	

Acknowledgments

The completion of the work presented in this thesis would not have been possible without the help and support of many people along the way. First, I would like to thank my director Professor Cédric Quendo and co-director Professor Ammar Sharaiha for their guidance and support throughout the research work. Their professional knowledge and skills have been an invaluable asset in all the work discussed here, their positive impact cannot be overstated. My warmest gratitude also goes to my supervisor Dr. Thierry Rampone for his endless insights in photonics, and his active help on photonics devices and microwave photonics measurements in the lab. I would also like to thank my supervisors, Dr. Noham Martin and Dr. Denis Le Berre who were helpful and available whenever called upon, for providing their experience in Microwave. Working with the people mentioned previously has been a great learning experience for me both professionally and personally.

I would also like to thank the many members of the Microwave and Photonics labs from UBO and ENIB who were my friends, co-workers and confidants for the last 3+ years. Thanks to Dimitrios Kastritsis, Jacqueline Sime, Odette Sandrine Bakam, and Dr. Marwa Braiki for a cherished time spent together in the lab, always being available to listen, provide guidance and lend a hand, for always greeting me with a smile, and for the enjoyable environment.

This thesis could not have been completed without the moral support of friends and family. I would like to express my deepest appreciation and gratitude to my family for their infinite, unconditional love and inspiration, and their continuous support and encouragement to help me overcome all the obstacles during these years. Thanks to Yana Nehme; to my sisters, Jana, Hala, Mira and Lea; to my parents Maher and Sawsan. Endless love to my fiancé Hani Naanaa for inspiring me, taking care of me, and enduring this long journey and providing his unwavering support.

. . . Dedicated to my beloved parents

Table of Contents

General Introduction **7**

Bibliography **11**

Chapter 1
Implementation of phase shifting based on RF and optical approaches **13**

1.0 Introduction **15**

1.1 Phase shifter and true time delay for array antenna **16**

1.1.1 Definition of phase shifter and true time delay 16
1.1.2 Beam squint 18

1.2 RF and Photonic phase shifters/true time delay **20**

1.2.1 Phase shifter based on electrical approaches 20
1.2.1.1 Introduction to phase shift based on transmission lines 20
1.2.1.2 Topologies of phase shifters 22
1.2.1.3 Switched-line phase shifter 22
1.2.1.4 Loaded-line phase shifter 23
1.2.1.5 Reflection type phase shifter 25
1.2.1.6 Summary of RF phase shifter approaches 26
1.2.2 Microwave photonic phase shifter and true time delay based on optical approaches 27
1.2.2.1 Dispersion fiber delay lines 27
1.2.2.2 Stimulated Brillouin scattering based microwave photonic phase shifter 28
1.2.2.3 Fiber Bragg grating based microwave photonic phase shifter 30
1.2.2.4 CPO effects in SOA based microwave photonic phase shifter 31
1.2.2.5 Up converted CPO effects in SOA based microwave photonic phase shifter 33
1.2.2.6 True time delay based on FBG prism 34
1.2.2.7 Separate carrier tuning technique 35

1.2.2.8 True time delay based on SCT using SBS delay line with FBG.....37
1.2.2.9 True time delay based on SCT using dual-parallel MZM and SBS.....37
1.2.2.10 Summary of optical delay and true time delay techniques.....38

1.3 Conclusion.....40

Bibliography of chapter 1.....41

Chapter 2
Coherent population oscillations (CPO) and Up-converted CPO in different structures of semiconductor optical amplifiers.....46

2.0 Introduction.....48

2.1 Semiconductor optical amplifier.....49

2.1.1 SOA operating principle.....49
2.1.2 Basic structure of SOAs.....50
2.1.3 SOA gain.....50
2.1.4 Gain saturation.....51
2.1.5 SOA nonlinearities.....53
2.1.5.1 Self-Gain and Cross Gain Modulation.....53
2.1.5.2 Self-Phase and Cross Phase Modulation.....53
2.1.5.3 Four-Wave Mixing.....53
2.1.5.4 Self-induced Polarization Rotation and Cross-Polarization Modulation.....54
2.1.6 SOA modeling.....54

2.2 Characteristics of used SOAs in static regime.....57

2.3 CPO effects in different structures of SOAs.....59

2.3.1 CPO modeling by small signal analysis.....59
2.3.2 Asymptotic behavior of the CPO responses in amplitude and phase.....63
2.3.3 Experimental results and discussions.....65
2.3.3.1 Experimental setup.....65
2.3.3.2 Experimental results of the CPO frequency responses.....67
2.3.3.3 Case of $R\alpha < 0$ in SOA-XN.....71

2.4 Optically controlled of RF phase shift using Cross Gain Modulation.....73

2.4.1 Small-signal analysis of ASE and optical control of RF phase shift.....73
2.4.2 Numerical calculation of RF phase shift.....76
2.4.3 Experimental realization and results of the controllable RF phase shifts in SOA.....79

2.5 Up-converted CPO in different structures of SOAs.....83

2.5.1 Principle of Up-converted CPO.....84
2.5.2 Small-signal analysis of Up-converted CPO.....85

2.5.2.1 Up-converted CPO optical power response as a function of the SOA mean carrier density 85
2.5.2.2 Small-signal frequency response of the carrier density 86
2.5.2.2.1 Carrier density modulation in the first and second section 88
2.5.2.2.2 Probe output power 89
2.5.2.3 Evaluation of the dynamic carrier lifetime 91
2.5.2.4 Full Up-CPO frequency response 92
2.5.3 Calculation and measurement of frequency responses for pump-probe and Up-CPO setups 92
2.5.3.1 Pump-probe characterization 92
2.5.3.2 Calculation of the absolute Up-CPO frequency response 95
2.5.4 Validation of small-signal calculations by experimental results of Up-CPO responses 97
2.5.5 Experimental verification of the influence of the operating frequency (fc) .. 102
2.5.6 Delay calculation of Up-CPO 103

2.6 Conclusion 106

Bibliography of chapter 2 108

Chapter 3
Radio frequency phase shifter and true time delay hybrid structure 111

3.0 Introduction 113

3.1 Theory of microstrip lines 115

3.2 Theory of microwave filters 117

3.2.1 Transfer functions and general definition 119
3.2.2 Prototype lowpass Chebyshev filter 120
3.2.3 Chebyshev bandpass filter with lumped networks 121
3.2.4 Lowpass to bandpass transformation using immittance inverter 122
3.2.5 Richards transformation 124
3.2.6 Stub-type microstrip bandpass filters 125
3.2.7 Generalized coupling matrix 128
3.2.8 Cross coupling 130

3.3 Tunable radio frequency filter 131

3.3.1 Tunable filter design with ideal transmission lines 131
3.3.2 Synthesis of the tunable RF filter with distributed lines 135
3.3.3 Basic model of varactor diodes 138
3.3.4 Layout and EM simulation 140
3.3.4.1 Folded design 140
3.3.4.2 Curved design 142

3.4 Tunable radio frequency phase shifter 144

3.4.1 Analysis of the proposed structure 146

3.4.2 RF-PS design and simulation 148

3.5 Simulation of hybrid structure 152

3.5.1 Simulation results of delay correction 153
3.5.2 Simulation results of TTD hybrid structure 159

3.6 Conclusion 161

Bibliography of chapter 3 162

Chapter 4
Hybrid correction structure 164

4.0 Introduction 165

4.1 Manufacture and experimental results of the RF filter 166

4.1.1 Experimental results of RF-FF using VNA bias tee 166
4.1.2 Experimental results of RF-FF using an external bias tee 173

4.2 Characterization of SOA-XN 174

4.3 Complete hybrid correction structure 179

4.3.1 Measurement of the hybrid correction structure 179
4.3.2 Simulation of the hybrid correction structure based on experimental data of SOA-XN 182

4.4 Conclusion 193

Bibliography of chapter 4 194

Conclusion and outlook 195

Glossary of Acronyms 198

List of Figures 200

List of Tables 208

Publications 210

Appendix 212

A.1 Parameter values of the model implemented under ADS 212
A.2 SOA-NL-OEC-1550 datasheet 213
A.3 40G-2R-ORP datasheet 214
A.4 SOA-NL-OEC-1550 datasheet 215
A.5 SOA-XN-OEC-1550 datasheet 216

General Introduction

Microwave radio systems are frequently used in broadcasting and in telecommunications transmissions, providing over-the-air end-to-end delivery of thousands of individual information channels. In wireless communication, signal processing functionalities in micro or millimeter-wave are implemented using digital electronics. However, the speed and bandwidth of such methods are limited by the electronic sampling rate.

Microwave photonics (MWP) technology [1] was introduced to overcome the complexity and limitations of electronic devices. It has been defined as the study of high speed photonic devices operating at micro or millimeter-wave frequencies and their applications in microwave or photonic systems [2], MWP is a discipline which combines microwave engineering and optoelectronics [3]. The aim of this study is to leverage the features of photonic technologies to provide functions in microwave systems that are complex to carry out directly in the radiofrequency (RF) domain. Such features include high-speed transmission, broad operation bandwidth, low loss, constant attenuation over the entire microwave frequency range, small footprint, lightweight, and strong resistance to electromagnetic interferences.

The typical schematic of a microwave photonic system is depicted in Figure 1. It comprises two fundamental units, a transmitter and a receiver. In the transmission unit, the microwave signal is transported via the intensity-modulated envelope of a propagating optical wave. An optical signal is generated from an optical source, often a semiconductor laser diode. This optical wave is then externally modulated by an RF signal through an electro-optic modulator, the output of which is then fed into an optical signal processor. The optical processed signals are then captured by a photodetector (Pd) at the reception unit that performs an optical to electrical conversion (O/E) and retrieves the electrical information contained in the optical carrier. This conversion enables the microwave signal propagation and processing to be explicitly implemented in the optical domain.

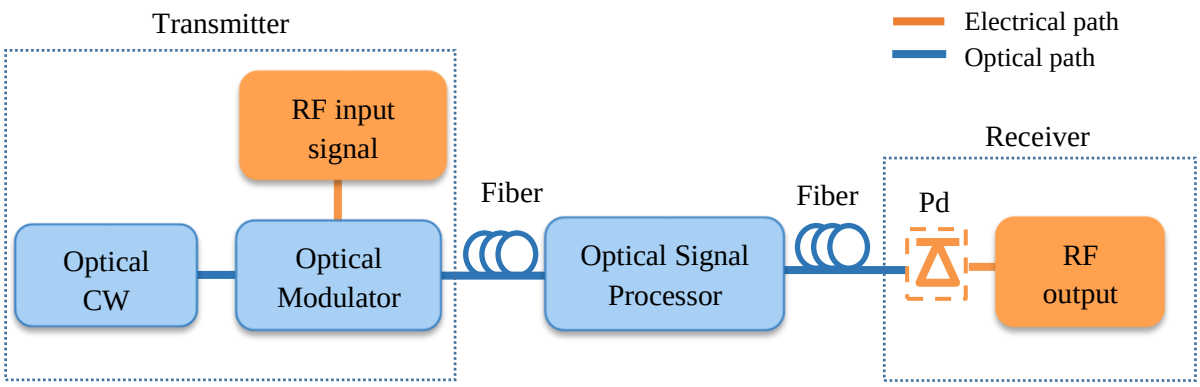

Figure 1 Microwave photonic system.

The capabilities of a microwave photonic system include the generation, distribution, control and processing of microwave signals [4]. MWP is key to achieve frequency conversion [5], reconfigurable filtering [6] [7], the ability to control both phase and amplitude independently [8], and the ability to realize phase shifting and true time delay (TTD) [9] [10] [11]. MWP applications are targeting higher operation at high frequencies and functionalities that demand small and light devices with a low power consumption. In this context, wideband tunable microwave phase shifters and TTD are key elements in MWP.

Achieving true time delay is extremely valuable for embedded systems, satellite communication and radars. TTD operation implies a perfectly proportional evolution of the phase shift of microwave signals with respect to their frequency. The main applications for TTD are phased-array antennas (PAAs) and microwave photonic filters [12]. In broadband phased-array antennas, if an array is supplied via wideband signals, and a constant phase shift is produced from element to element, the beam pointing will vary based on the frequency components. This gives credence to the notion that the far-field pattern of the antenna is affected when the microwave frequency is scanned over a wide range, this phenomenon is called beam squinting [13].

The implementation of wideband tunable microwave phase shifters and TTD, with application in optically fed phase array-antennas, is difficult in the microwave domain. The association of photonic and microwave technologies to achieve these delay lines increases the capabilities and design freedoms of photonic components over conventional electrical transmission systems, while benefiting from a high immunity to electromagnetic interferences and low losses of optical fibers. One of the most promising photonic approaches is the Coherent Population Oscillation (CPO) in a semiconductor optical amplifier (SOA), which allows the tunability of a phase shift/delay based on the SOA bias current or the input optical power, and suits the requirement in terms of high-speed reconfiguration, low power consumption and small footprint.

The main goal of this research is to achieve a TTD at a high frequency. This can be done through a two-stage approach; the first stage consists of a tunable optical phase shifter at high frequency, based on microwave photonics approaches, using Up-converted CPO in a SOA.

The second stage consists of using a tunable RF phase shifter, based on an RF filter, which will correct the non-linearity responses of the first stage. The idea of the association between an optical phase shifter and an RF phase shifter was originally introduced by Perrine Berger [14].

This thesis is a joint doctoral research effort at the Lab-STICC UMR CNRS 6285 which brings together the skills in photonics that is conducted at École Nationale d'Ingénieurs de Brest (ENIB), with the expertise in microwave of the Université de Bretagne Occidentale (UBO). In this work, we use semiconductor optical amplifier, using the up-converted coherent population oscillation (up-CPO) technique to produce a tunable phase shift as a function of the frequency of the signal, cascaded by a microwave phase shifter in order to linearize the SOA response over a wide RF bandwidth. This work is the first step to provide a proof of concept demonstrating that the "Up-CPO" technique associated with a microwave device could allow the generation of a tunable delay for microwave signals on the optical channel. The effort was undertaken in order to analyze, design and link the optical and the RF stages. This research was financially co-supported by Brittany Region (France) through an ARED "Allocations de Recherche Doctorale" project and the UBO.

The thesis is organized as follows: after the introduction, the chapter one describes the difference between phase shifts and true time delays. It provides an overview of the state of the art for the implementation of phase shifters in electrical and optical approaches. It represents different types of true time delays based on optical approaches. A brief summary of various approaches of phase shift and true time delay is also given.

Chapter two presents a tunable microwave photonics phase shifter that is based on CPO and Up-CPO effects in SOA. Theoretical responses of a tunable phase shifter based on CPO for linear and nonlinear SOAs are computed first by small-signal analysis, then experimental results are obtained for four different SOA structures. A new technique of optically controlled RF phase shifts using cross gain modulation (XGM) is presented. The generation of tunable phase shift or delay at high frequencies, based on Up-CPO technique in "linear" and "nonlinear" SOAs is modeled by a small-signal development and validated by experimental results.

Chapter three presents the proposed hybrid optical-microwave structure so-called "TTD hybrid structure" to correct the nonlinear response of the first optical stage (Up-CPO in a SOA) and to generate a TTD system. The second stage consists of two RF phase shifts. First, a tunable RF phase shifter is designed, based on an RF filter which correct the nonlinearity responses of Up-CPO in SOAs. This stage is known as "hybrid correction structure". Secondly, an analog tunable RF phase shifter (RF-PS) that employs an all-pass topology phase shifter is designed in order to induce a phase offset, based on transmission lines and varactors diode. RF-PS is placed after the tunable RF filter, so that the phase offset can be tuned. The theoretical analysis of the filter based on microstrip transmission line is presented. Simulation results of the tunable RF phase shift and tunable RF filter are given. We present the simulation results of the hybrid correction structure. By combining the first optical stage with the second RF stage (tunable RF filter and RF-PS), we show by simulation in this chapter that a TTD can be achieved.

Chapter four describes the building blocks of the proposed hybrid correction structure, which correspond to the association of the phase shift based on Up-CPO (explained in chapter 2) and the tunable RF folded filter (proposed in chapter 3). Measured results of the tunable RF filters are given. The measured results of the hybrid correction structure are presented. Finally, we present and discuss the simulation results based on experimental data of the proposed hybrid correction structure. This chapter is followed by a general conclusion and an outlook.

Bibliography

[1] A. J. Seeds, "Microwave photonics" in *IEEE Transactions on Microwave Theory and Techniques*, vol. 50 no. 3 pp. 877-887 Mar. 2002, doi: 10.1109/22.989971.

[2] D. Jager, A. Stohr, "Microwave photonics-from concepts to applications," *Proc. 2005 German Microwave Conference*, pp. 136-139, 2005.

[3] J. Capmany and D. Novak, "Microwave photonics combines two worlds," *Nat. Photonics*, vol. 1, no. 6, pp. 319–330, Jun. 2007, doi: 10.1038/nphoton.2007.89.

[4] D. Marpaung, C. Roeloffzen, R. Heideman, A. Leinse, S. Sales, J. Capmany, "Integrated microwave photonics," *Laser & Photonics Reviews*, 2013, vol. 7, no 4, p. 506-538, 2013, doi:10.1002/lpor.201200032.

[5] K. Xu *et al.*, "Microwave photonics: radio-over-fiber links, systems, and applications [Invited]," *Photonics Res.*, vol. 2, no. 4, p. B54, Aug. 2014, doi: 10.1364/PRJ.2.000B54.

[6] J. Capmany, B. Ortega, and D. Pastor, "A tutorial on microwave photonic filters," *J. Light. Technol.*, vol. 24, no. 1, pp. 201–229, Jan. 2006, doi: 10.1109/JLT.2005.860478.

[7] E. Hamidi, D. E. Leaird, and A. M. Weiner, "Tunable Programmable Microwave Photonic Filters Based on an Optical Frequency Comb," *IEEE Trans. Microw. Theory Tech.*, vol. 58, no. 11, pp. 3269–3278, Nov. 2010, doi: 10.1109/TMTT.2010.2076970.

[8] X. Yi, T. X. H. Huang, and R. A. Minasian, "Photonic Beamforming Based on Programmable Phase Shifters With Amplitude and Phase Control," *IEEE Photonics Technol. Lett.*, vol. 23, no. 18, pp. 1286–1288, Sep. 2011, doi: 10.1109/LPT.2011.2158815.

[9] Liwei Li, Xiaoke Yi, and T. X. H. Huang, "Microwave Photonic Hybrid Phase-Time Shifter and Widely Tunable Microwave Filter," *IEEE Photonics Technol. Lett.*, vol. 24, no. 24, pp. 2288–2291, Dec. 2012, doi: 10.1109/LPT.2012.2224652.

[10] Jianping Yao, Jianliang Yang, and Yunqi Liu, “Continuous true-time-delay beamforming employing a multiwavelength tunable fiber laser source,” *IEEE Photonics Technol. Lett.*, vol. 14, no. 5, pp. 687–689, May 2002, doi: 10.1109/68.998726.

[11] D.-H. Yang and W.-P. Lin, “Phased-array beam steering using optical true time delay technique,” *Opt. Commun.*, vol. 350, pp. 90–96, Sep. 2015, doi: 10.1016/j.optcom.2015.03.066.

[12] S. Pan, X. Ye, Y. Zhang and F. Zhang, “Microwave Photonic Array Radars,” in IEEE Journal of Microwaves, vol. 1, no. 1, pp. 176-190, Jan. 2021.

[13] M. Longbrake, “True time-delay beamsteering for radar,” in *2012 IEEE National Aerospace and Electronics Conference (NAECON)*, Dayton, OH, USA, Jul. 2012, pp. 246–249, doi: 10.1109/NAECON.2012.6531062.

[14] P. Berger, “Lumière lente et rapide dans les amplificateurs optiques à semi-conducteurs pour des applications en optique micro-onde et aux RADAR,” *Thèse de doctorat*, Université de Paris Sud, U.F.R. Scientifique d’Orsay, 2012.

CHAPTER 1

Implementation of phase shifting based on RF and optical approaches

1.0 Introduction 15

1.1 Phase shifter and true time delay for array antenna 16

1.1.1 Definition of phase shifter and true time delay 16
1.1.2 Beam squint 18

1.2 RF and Photonic phase shifters/true time delay 20

1.2.1 Phase shifter based on electrical approaches 20
1.2.1.1 Introduction to phase shift based on transmission lines 20
1.2.1.2 Topologies of phase shifters 22
1.2.1.3 Switched-line phase shifter 22
1.2.1.4 Loaded-line phase shifter 23
1.2.1.5 Reflection type phase shifter 25
1.2.1.6 Summary of RF phase shifter approaches 26
1.2.2 Microwave photonic phase shifter and true time delay based on optical approaches 27
1.2.2.1 Dispersion fiber delay lines 27

1.2.2.2 Stimulated Brillouin scattering based microwave photonic phase shifter 28
1.2.2.3 Fiber Bragg grating based microwave photonic phase shifter 30
1.2.2.4 CPO effects in SOA based microwave photonic phase shifter 31
1.2.2.5 Up converted CPO effects in SOA based microwave photonic phase shifter 33
1.2.2.6 True time delay based on FBG prism 34
1.2.2.7 Separate carrier tuning technique 35
1.2.2.8 True time delay based on SCT using SBS delay line with FBG 37
1.2.2.9 True time delay based on SCT using dual-parallel MZM and SBS 37
1.2.2.10 Summary of optical delay and true time delay techniques 38

1.3 Conclusion 40

Bibliography of chapter 1 41

1.0 Introduction

This chapter first presents the difference between phase shifter (PS) and true time delay (TTD). Secondly, it provides a review of state of the art for the implementation of phase shifts or delay lines by employing optical and electrical approaches. Section 1.2.1 presents the following electrical approaches: switched-line phase shifter, loaded-line phase shifter, and reflection type phase shifter. While the following microwave photonic phase shifters based on optical approaches are shown in section 1.2.2: dispersive fibers, fiber Bragg gratings (FBGs), stimulated Brillouin scattering (SBS), coherent population oscillation effects in SOA (CPO) and Up-converted CPO (Up-CPO). Finally, true time delay based on several optical approaches are presented: TTD based on FBG Prism, TTD relying on separate carrier tuning (SCT), such as, SCT using SBS delay line with fiber Bragg grating, SCT using two SBS system, and SCT using Dual-parallel Mach-Zehnder modulator.

1.1 Phase shifter and true time delay for array antenna

1.1.1 Definition of phase shifter and true time delay

In this section, we explain the main differences between phase shifter (PS) and true time delay (TTD), this concept was discussed in [1]. Phase shifter is used to change the transmission phase angle of an input signal, they ideally provide an output signal that is equal in amplitude to the input signal. The input signal is shifted in phase at the output based on the phase shifter's selected offset. Therefore, phase shifting can be described as adding a phase offset ϕ_{offset} to the input RF signal S_{in}. Spectrally, the output signal can be given as:

$$S_{out}(f) = e^{j\phi_{offset}} \sum_f S_{in}(f) \tag{1.1}$$

The frequency response of the phase shifter in Eq. (1.1) is:

$$H_{\phi}(f) = e^{j\phi_{offset}} \tag{1.2}$$

with magnitude equal to 1, and phase response equal to ϕ_{offset} for all frequencies. We notice from (1.2) that the phase response is constant with respect to the RF frequency. The amplitude and the phase responses of the phase shift are illustrated in Table 1.1.

Adversely, when applying a true time delay (τ) to the input RF signal S_{in}, the output signal, spectrally, is given by:

$$S_{out}(f) = \sum_f S_{in}(f)\, e^{-j2\pi f\tau} \tag{1.3}$$

The frequency response of the phase shifter in (1.3) is:

$$H_{TTD}(f) = e^{-j2\pi f\tau} = e^{-j\phi(f)} \tag{1.4}$$

With magnitude equal to 1, and phase response of $\phi(f) = -2\pi f\tau$, we can see that from (1.4), the phase response (ϕ) is proportional to the RF frequency. The amplitude and phase response of the TTD are illustrated in Table 1.1.

Table 1.1 shows that the amplitude is constant and flat over the whole frequency range for both phase shifter and true time delay. At a single frequency, both types have the same interpretation of the phase shift, thus the delay can be computed either by the time delay or by the phase shifter, they are related through $\phi = -2\pi f_n\tau$, where f_n is the signal frequency. When the

frequency is altered, phase shifting and time delaying lose their common interpretation, leading to different functions and resulting in a different dependence of the phase shift on the frequency.

In phased array antennas, it can be assumed for true time delay, that all frequency components of the microwave signal are pointed at the same fixed direction. It is important to note that the features of an ideal true time delay are a flat magnitude response, and a linear relation between the phase shift and the frequency. Consequently, a constant delay is then required over the frequency.

Table 1.1 Amplitude and phase response in frequency domain for phase shift and TTD.

	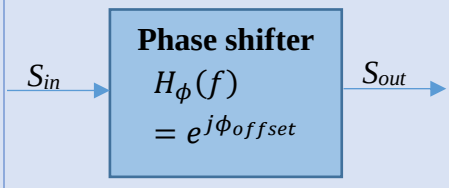	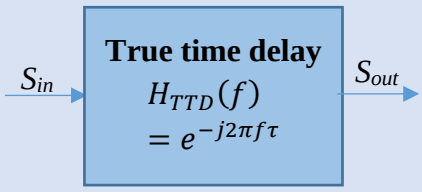
Amplitude response	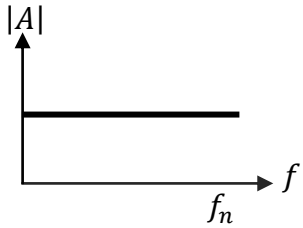	
Phase response	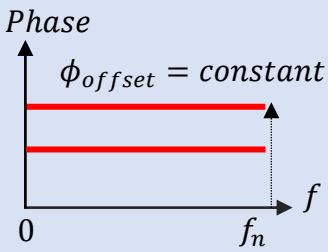 (a) Phase shifter	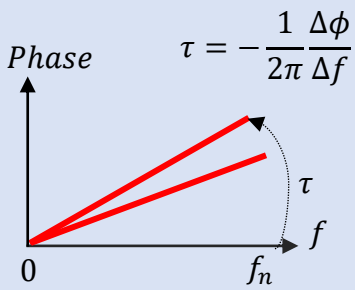 (b) TTD

A response comparison between the phase shifter and the TTD is performed in [1], through estimation of the error. The total phase error ε_{tot} is given by:

$$\varepsilon_{tot}(f) = \left|\phi_{offset}\right| F_B \tag{1.5}$$

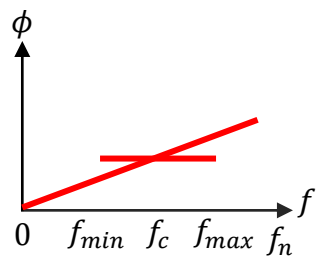

Figure 1.1 Illustration of error.

where fractional bandwidth signal is $F_B = \frac{|f_{max} - f_{min}|}{f_c}$, f_c is the carrier frequency, $f_{min} = f_c - \frac{B}{2}$, $f_{max} = f_c + \frac{B}{2}$, and the signal bandwidth $B = f_{max} - f_{min}$.

The assumption for TTD and PS to be similar is valid only for a small phase error (Figure 1.1), in case where $F_B << 1$. Therefore, for very narrowband applications, phase shift and TTD can perform the same function.

1.1.2 Beam squint

The squint phenomenon is described as the position of the array factor's main lobe being oriented at different angles for different microwave signal frequencies. This means that the energy associated with different frequencies is oriented in different directions [2]. In other words, beam squinting means that main antenna lobe points to $\theta_0 + \Delta\theta$ at frequency $f_0 + \Delta f$ instead of θ_0, which was the pointing direction at frequency f_0, as shown in Figure 1.2. As a result, a receiver would experience a decrease in the gain of the RF signal frequency spectrum, which distorts of the waveform in direction θ_0, limiting the bandwidth of the system, and the occurrence of reception errors.

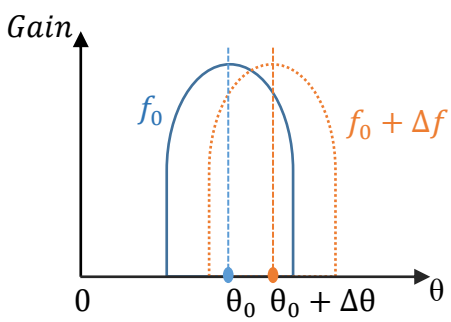

Figure 1.2 illustrated beam squint.

Figure 1.3 illustrates the schematic diagram of beam steering using a phase shifter, where a linear array of 2 elements A and B, is separated by distance d.

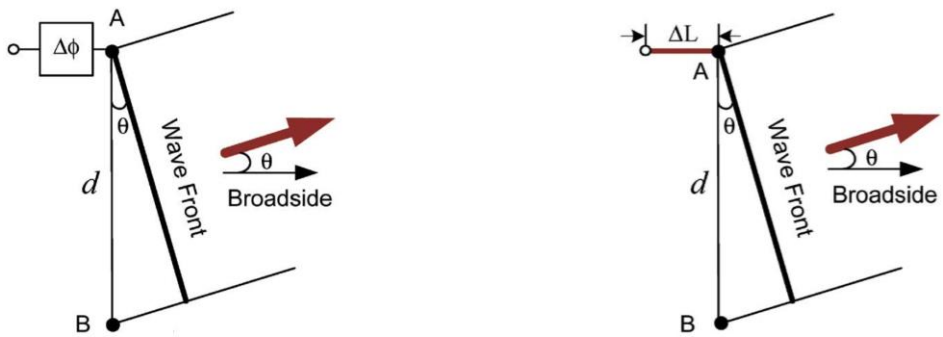

Figure 1.3 Beam steering (a) using a phase shifter, and (b) using a delay line. [2]

The phase shift difference $\Delta\phi$ between neighboring elements to form the steering angle θ is given by:

$$\Delta\phi = 2\pi \frac{d\ sin(\theta)}{\lambda} \tag{1.6}$$

where λ is the wavelength of the radiated microwave signal.

The beam steering direction is then given by:

$$\theta = sin^{-1}\left(\frac{\lambda\Delta\phi}{2\pi d}\right) \tag{1.7}$$

It can be seen from (1.7) that the beam steering direction (θ) is a function of the microwave wavelength (λ). Thus, phase shifter based beamformer systems can only operate for narrowband signals. From the far-field radiation pattern of the array factor in Figure 1.4(a), we can see that the orientation of the main-lobe varies with the feed signal frequency. This phenomenon significantly hampers the performance of the system. An advantage of a constant time delay is that beam steering is independent of the frequency; this can be achieved by replacing the phase shifter with a delay line with length $\Delta L = \frac{\lambda\Delta\phi}{d}$ as shown in Figure 1.3(b).

The beam steering direction is then given as in [2]:

$$\theta = sin^{-1}\left(\frac{\Delta L}{d}\right) \tag{1.8}$$

Equation (1.8) shows that the beam steering angle is independent of the microwave signal frequency and dependent on the true time delay. Figure 1.4(b) shows that the orientation of the main lobe using TTD does not vary with the feed signal frequency while the contrary is observed when using phase shifter.

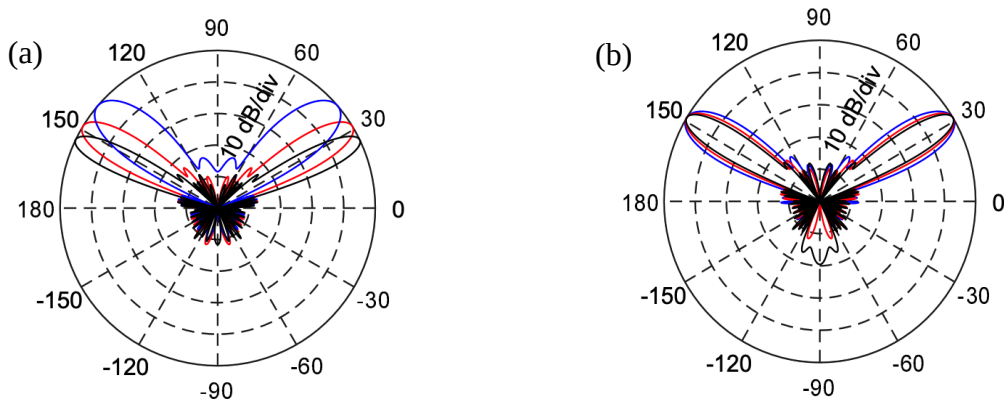

Figure 1.4 Beam patterns of 3 microwave frequencies with (a) phase shifter, (b) true-time delay, Blue: 12 GHz. Red: 15 GHz. Black: 18 GHz. [3]

1.2 RF and Photonic phase shifters/true time delay

True time delay refers to a system's ability to apply a delay or a linear phase shift on input RF signals, independently of the RF frequency. In this section, we analyze two principal methods for implementing delay lines for true time delay. The first and second methods employ an optical and an electrical approach, respectively. True time delay based on several optical approaches are presented.

1.2.1 Phase shifter based on electrical approaches

Phase shifters are essential components in a phased array for adjusting the phase of each antenna path and steering the beam. A Phase Shifter is simply a two-port device that changes the phase of any incoming RF signal. Ideally, it changes the phase of the transmission (phase of S_{21}) of a network while keeping the insertion losses (amplitude of S_{21}) constant. The requirements of phase shifters ideally includes a broad phase-control range (360º) and low insertion losses on a wide frequency range. The main types of RF phase shifters, such as switched-line, loaded-line, and reflection-type phase shifters, are analyzed in this section. These phase shifters are well described in the literature [4] [5] [6] [7].

1.2.1.1 Introduction to phase shift based on transmission lines

The origin of phase shift relies on a simple fact derived from the transmission line theory: a wave traveling along a transmission line has a phase shift between its output and input voltages that is dependent on the characteristic impedance and the length of the line [7].

An RF signal with frequency $f\,(=\omega/2\pi)$ which travels through a transmission line, of a distance Δl with propagation velocity V_p, will have a time delay:

$$Time\ delay\ (seconds)\ = \frac{\Delta l}{V_p} = \frac{\Delta l}{f\lambda_g} = \frac{\beta \Delta l}{\omega} \tag{1.9}$$

where β is the phase constant and is given by $\beta = \omega/V_p$, (ω) is the angular frequency, Δl is the distance travelling by the signal, and λ_g is the guide wavelength.

Time delay can be expressed in term of phase shift $\Delta\phi$ as:

$$Time\ delay\ (seconds) = \frac{\Delta\phi}{2\pi f} \tag{1.10}$$

Substituting (1.9) into (1.10), gives the corresponding phase shift:

$$\Delta\phi = 2\pi \frac{\Delta l}{\lambda_g} \tag{1.11}$$

Therefore, by switching the transmission lines of different lengths, different values of phase shift are obtained. Figure 1.5 shows the RF signal experiences with different time delays by switching several transmission lines of different lengths (Δl_0, Δl_1 and Δl_2).

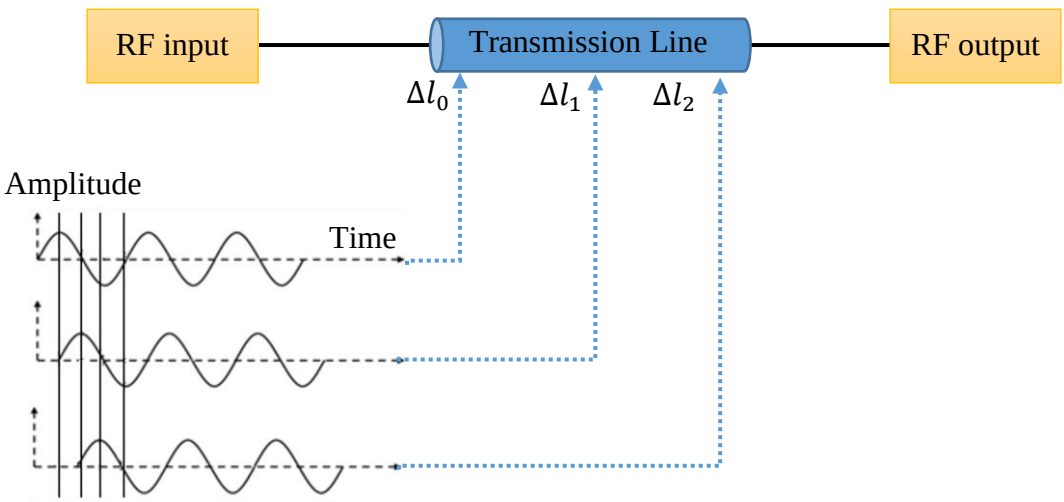

Figure 1.5 Delay/phase shift experienced by RF signal travelling through transmission line.

Group delay is defined as the average delay time that a specified narrow range of frequencies experiences when passing through a circuit. It is proportional to the rate of phase shift at each frequency of interest, and is expressed as:

$$Group\ delay\ (seconds) = -\frac{1}{360^{\circ}}\frac{\Delta\phi}{\Delta f} \tag{1.12}$$

1.2.1.2 Topologies of phase shifters

Depending on the control mechanism, phase shifters can be categorized into two types, analog and digital. Analog phase shifters are variable devices, offering continuous variable phase shift that varies between the prescribed ranges of a minimum to a maximum value. They are usually controlled by a voltage control to get the desired phase shift. Varactor diodes are used for achieving continuously variable phase shifts [8]. Generally, modifying the voltage affects the capacitance of the varactor diode to change the reactance of the circuit and achieve a variable phase shift of the RF signal. Digital phase shifters are realized by using PIN diodes [9] or micro-electro-mechanical [10] systems (MEMS). They are used as a variable impedance or high-frequency switches (on/off) to achieve the desired phase shift. Digital phase shifters can only target a specific set of discrete phase shift values and cannot supply an arbitrary phase shift.

1.2.1.3 Switched-line phase shifter

A switched-line phase shifter is a simple way to implement microwave phase shifters, as it uses a simple time delay difference between two direct paths to achieve the desired phase shift. The basic configuration for a 1-bit phase shifter is illustrated in Figure 1.6. As can be seen, two signal paths are possible, and single pole double throw switches (SPDT) are used to route the signal between one of the two transmission lines of different lengths. SPDT switches can be realized in a wide variety of ways, using FET, diode, or MEMS. One of the two transmission lines is considered a reference line (l_r) and the other a delay line (l_d). The differential path between the two lines determines the amount of phase shift.

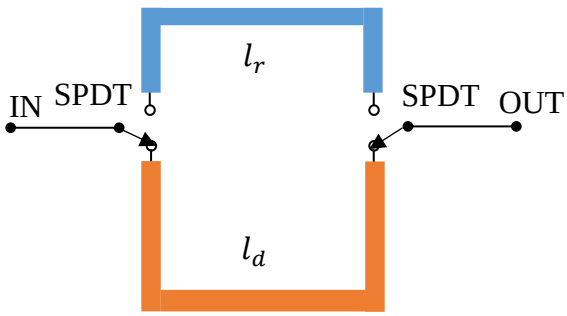

Figure 1.6 Basic schematic of switched-line phase shifter.

The phase shift $\Delta\phi$ is the phase difference between the two states, which is given by (1.11): $\Delta\phi = 2\pi\frac{\Delta l}{\lambda_g}$, with $\Delta l = l_d - l_r$. As an example, to obtain 180° phase shift, the required physical length difference should be $\Delta l = \lambda_g/2$. In this type of phase shifter, the insertion loss is mainly

due to the switches. An advantage of the switched-line phase shift is its linear relation between phase and frequency.

An N-bit phase shifter is made by cascading each 1-bit phase shifter with different delay line lengths. The main problem with multibit phase shifters is the significant variation of return loss across the phase states that can limit the accuracy of their phase. A 3-bit switched-line phase shifter using a MEMS series switch was demonstrated in [7], where each bit comprises a delay line generating the required amount of 45°, 90°, and 180° phase shift, respectively, and a reference line (refer to 0°), with switching elements in both directions delay and reference lines. In order to generate 270° phase shift, the second and third bits must be selected. However, to generate 180° phase shift only third section should be selected.

A flat wideband phase shift response was invented by Bernard Schiffman, published for the first time a phase shifter using a $\lambda_g/4$ wavelength coupler section [11]. Figure 1.7 shows the standard 90° Schiffman phase shifter. It consists of a switched line with two SPDT switches, one reference line of length 3L, and two other parallel coupled lines of equal length L = $\lambda_g/4$, directly connected to each other at one end. The phase shift is determined by the phase difference of signals transmitted through the coupled section of length L and the reference line of length 3L, provides a flat 90° phase difference over a fractional bandwidth as 5:1 in microwave range.

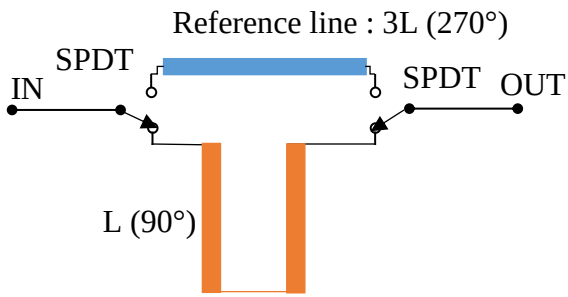

Figure 1.7 Schiffman phase shifter.

1.2.1.4 Loaded-line phase shifter

The second transmission line type is the loaded-line phase shift. Figure 1.8 illustrates the basic loaded-line phase shifter that comprises a transmission line having a characteristic impedance Z_{TL}, an electrical length θ_l, and two equal two-state susceptance (imaginary part of admittance) B_1 and B_2 connected in shunt with the main transmission line. The loading susceptance of these elements is controlled by switching diodes to shorten or lengthen the transmission line electrically. The required phase shift $\Delta\phi$ corresponds to the transition load elements B_1 to B_2, which causes the input signal to experience a particular phase shift. The lumped-elements loaded-line phase shifter is used for low frequencies, while for higher frequencies, the loaded-line phase shifter based on short-circuited stubs is used.

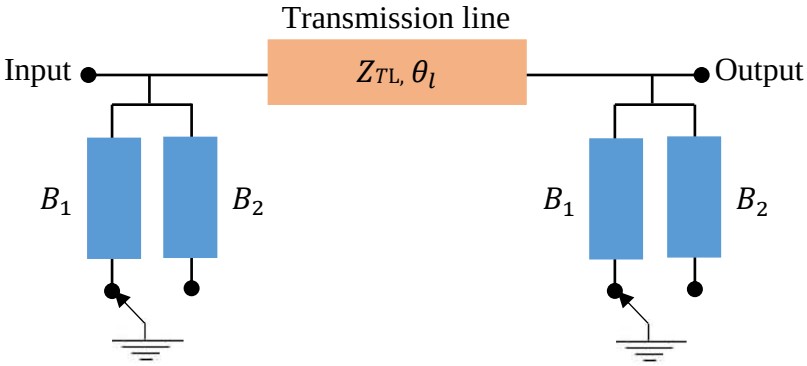

Figure 1.8 Loaded-line phase shifter, switch here is to choose between two lines of different length and impedance.

For B_i (i = 1, 2), the transmission phase can be given from [12] [13]:

$$\phi_i = \cos^{-1}(\cos\theta_l - B_i Z_{TL} \sin(\theta_l)), \qquad i=1, 2 \tag{1.13}$$

The required phase shift due to the switching between two states (the susceptance values B_1 and B_2) is:

$$\Delta\phi = \phi_1 - \phi_2 \tag{1.14}$$

When the length of the main transmission line is around $\lambda_g/4$, the drawback of reflection from the loaded-line producing the phase shift can be overcome, therefore the maximum bandwidth is achieved [14] [15] [16] [17]. This type of configuration is used for phase shift values up to 45° with a flat phase response from 1743 MHz to 1924 MHz [18]. For a higher phase shift, several phase shifters of the same type can be cascaded. In [19], two 45º phase shifters are cascaded to achieve the 90º phase shift over 10% frequency band within the L band. However, the circuit size is doubled because a $\lambda_g/4$ transmission line is required for each phase shifter.

Depending on the values of B_i, loaded-line phase shifters can be separated into three classes [12] [13]:

- Class I: $B_1 \neq B_2$ and $B_i \neq 0$, the corresponding phase is nonzero and unequal.
- Class II: B_1 or $B_2 = 0$, this mode is called a load–unload since the line load is conceptually applied to and removed from the line.
- Class III: $B_1 = -B_2$, the loading is switched between complex-conjugate values. The line length is necessarily θ_l = 90°, and the loading switches the phase by $\Delta\phi/2$.

1.2.1.5 Reflection type phase shifter

The third kind of phase shifter is the reflection type phase shifter (RTPS). RTPS are presented in [20] [21] [22], they are mostly based on 90° branch-line couplers, where the two ports (through and coupled) are loaded with reflective loads Z_r as shown in Figure 1.9.

The quadrature coupler is an hybrid coupler that provides a 3dB power split for the two output arms with a 90° phase difference in the outputs of the through and coupled arms. The hybrid 90° coupler is a microwave circuit that is typically implemented using microstrip lines. The input signal from port 1 is split into two equal parts between the through port 2 and coupled port 3 with a 90° phase difference. Each part of the signal is then reflected by a load with an input impedance (Z_r), which is different from the characteristic impedance of the coupler (Z_0), inducing an additional phase shift θ caused by the loads, which is equal to the phase of the load reflection coefficient (Γ), assuming that the two reflective loads and the 90° coupler are lossless. The two reflected signals from each load combine in-phase at the output, which is the isolation port. However, the two reflected signals reach the input port with 180° out of phase, canceling each other. The desired phase shift is obtained by varying the impedance values of loads, thus varying the transmission phase.

For lossless reflective loads, the final phase shift between the input and isolated (output) ports varies with the load impedance values of θ, which can be calculated as:

$$\Delta\phi = -90° - 2\tan^{-1}\left(\frac{Z_r}{Z0}\right) = -90° - \angle\Gamma \tag{1.15}$$

Γ is the reflection coefficient of Z_r normalized by Z_0.

If the load impedance varies from $Z_{r,max}$ to $Z_{r,min}$, the corresponding phase shift can be calculated as:

$$\Delta\phi = 2\left[arctan\left(\frac{Z_{r,max}}{Z0}\right) - arctan\left(\frac{Z_{r,min}}{Z0}\right)\right] \tag{1.16}$$

where $Z_{r,max}$ and $Z_{r,min}$ denote the maximum and minimum reflection impedances, respectively.

Instead of changing the load impedances, they are replaced by a variable reactance, such as a varactor diode. Therefore, a variable phase shifter is obtained, with minimum and maximum varactor capacitances C_{min} and C_{max}. The load impedance can be expressed by $Z_{r,min} = 1/j\omega C_{min}$ and $Z_{r,max} = 1/j\omega C_{max}$. By cascading two stages of RTPS, a full span 360° continuous phase shift from 11~13 GHz [21] and across 58~64 GHz [22] is achieved.

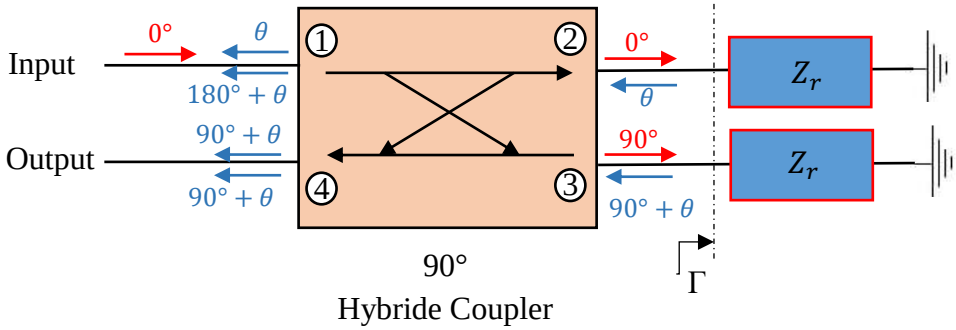

Figure 1.9 Schematic of the RTPS using 90° *hybrid coupler and loaded lines.*

1.2.1.6 Summary of RF phase shifter approaches

Table 1.2 presents the compared performance characteristics of the different types of the RF phase shift. It shows that different kinds of RF phase shifters do not have the same properties, reflection types have a simple architecture, and that switched-lines and loaded-lines tend to have a relatively large size. Switched lines and reflection types allow a large phase shift with a wide bandwidth, while loaded lines have a good behavior for smaller phase shifts. All comparisons between various type of phase shifter have been discussed in [23].

Table 1.2 Typical qualitative performance of integrated phase shifter approaches.

Type of PS	***1 stage Maximum phase***	***Bandwidth***	***Size***	***Power***	***Loss***	***Tunability***
Switched-lines	∞	Large	Large	Medium	Small	D.C
Loaded-lines	45°	Medium	Large	High	Small	D.C / Varactor
RTPS	180°	Large	Medium	High	Small	D.C / Varactor

D.C: Digital control, technology for these RF phase shifts is printed circuit.

1.2.2 Microwave photonic phase shifter and true time delay based on optical approaches

Optical approaches used for implementation of TTD rely on optical delay lines. In a MWP delay line, either an intensity or phase modulator is needed to implement electrical to optical conversion, and a photodetector (Pd) is needed to convert the optically time delayed signal to an electrical signal. Different techniques have been proposed to implement MWP delay lines or phase shifts, these techniques can be implemented based on fiber optics such as dispersive fibers, fiber Bragg gratings (FBGs) and stimulated Brillouin scattering (SBS). The following subsection provides a review of the state of the art of MWP phase shifters which is the essential element for implementing TTD. Slow and fast light effects in stimulated Brillouin scattering (SBS) offer compact solutions used in microwave phase shifting and in TTD lines. In this section, TTD based on FBG Prism is presented. Besides, the recent generation of TTD relying on separate carrier tuning (SCT), such as, SCT using SBS delay line with fiber Bragg grating, SCT using two SBS system, and SCT using Dual-parallel Mach-Zehnder modulator are presented.

1.2.2.1 Dispersion fiber delay lines

The phenomenon in which phase velocity of a wave depends on its frequency is known as dispersion, a medium that possesses such properties is known as a dispersive medium [24]. An optical fiber, such as a single-mode fiber (SMF) or a dispersion-compensating fiber (DCF) can be used as dispersive elements.

Figure 1.10 depicts the structure to implement a tunable delay line using a dispersive fiber (DF). An input optical signal with a tunable wavelength from a tunable laser source (TLS) is sent to a Mach-Zehnder modulator (MZM), which is modulated by an electrical radio frequency (RF) signal. At the output of the MZM, the modulated optical signal is launched across the length of the dispersive fiber. Different wavelengths would experience different time delays because of the chromatic dispersion. Finally, the delayed signal is detected using a photodetector.

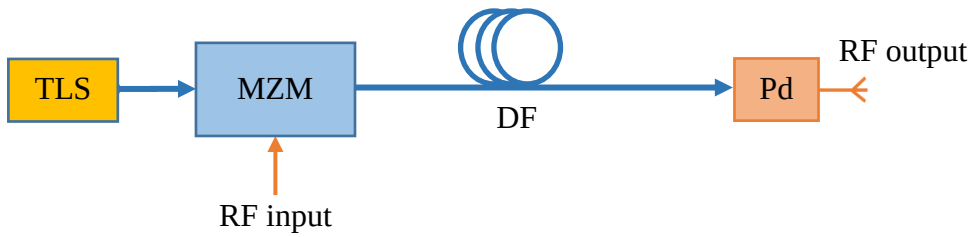

Figure 1.10 Tunable MWP delay line structure by using a length of DF.

The delay at different wavelengths with a wavelength $\lambda_0 + \Delta\lambda$ in a dispersive fiber can be expressed as in [24] [25] :

$$\tau = \tau_0 + LD\Delta\lambda \tag{1.17}$$

with the time delay (τ_0) at reference wavelength (λ_0), (L) the length of fiber, (D) the dispersion parameter of fiber, and $\Delta\lambda$ is the spectral width of the light source.

Tunability can be achieved by changing the optical carrier wavelength or the length of the dispersive fiber. Furthermore, tunable MWP delay lines based on dispersive fibers have been used to implement true time beamforming in a phased array antenna [26].

1.2.2.2 Stimulated Brillouin scattering based microwave photonic phase shifter

Stimulated Brillouin scattering (SBS) in fiber optics relies on nonlinear interactions between counter-propagating optical waves, single sideband modulated carrier with pump and Stokes waves in an optical single mode fiber. The application of SBS for phase shifting mechanisms was first introduced by Loayssa and Lahoz [27].

The illustration of the working principle of SBS is shown in Figure 1.11, where the frequencies of the two optical waves are symmetrically up and down shifted from that of the optical carrier by (Ω), which is approximately equal to the Brillouin frequency shift (v_b). Pump1 acting as an SBS pump wave (upper sideband) leads to a gain resonance in the vicinity of the optical carrier (Brillouin gain (b)), while Pump2 (lower sideband) acting as an SBS Stokes wave leads to a loss resonance in the vicinity of the optical carrier (Brillouin loss (a)).

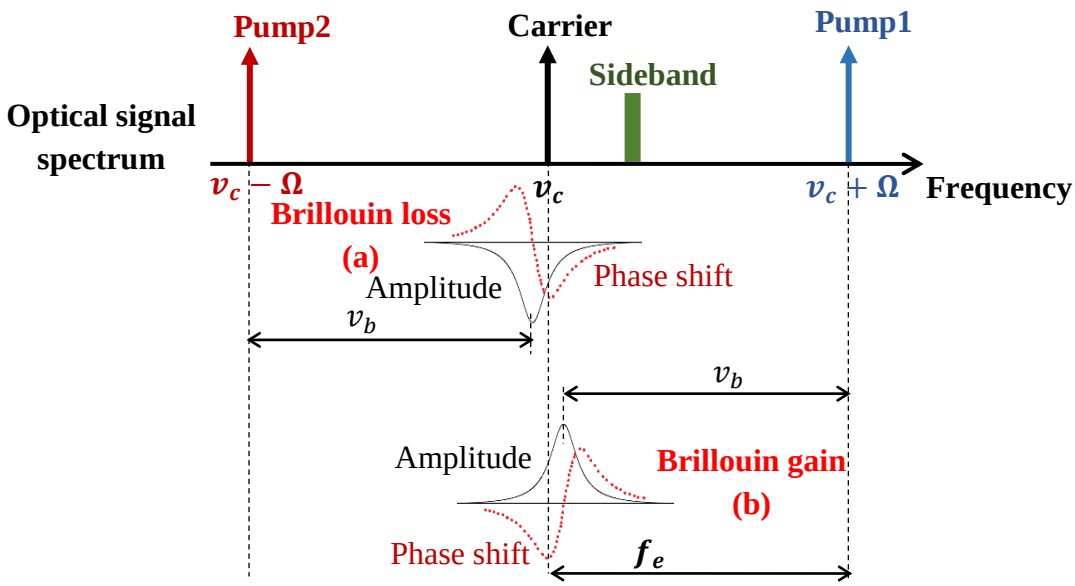

Figure 1.11 Spectral distribution of Brillouin gain and loss resonances and the associated optical phase shifts.

It can be noticed from Figure 1.11, on one hand, that the optical carrier is inside the narrowband spectral region (loss/gain spectral) providing a phase shift that can be tuned in a range greater than 2π [28]; on the other hand, RF sidebands are placed outside the SBS band, therefore no phase shift occurs on it.

Tunable phase shifting is obtained by changing the frequency differences (f_e) among the pump waves and the carrier signal. Besides, it can be varied through changing the pump power [29] [30]. Moreover, if the two pumps have identical power, the amplitude gain/loss will exactly compensate for any detuning of their central resonance frequency, and the phase change will sum up [30]. The phase shifting results from the phase response of the Brillouin gain that varies linearly around the peak gain frequency. The bandwidth of MWP phase shifter based on SBS is limited by the bandwidth of the optical transmitters/receivers installed [28] [29] [30].

An experimental configuration of tunable RF phase shift using SBS in optical fibers [27] [28] is presented in Figure 1.12. The input optical signal is launched through two paths, the first goes through an optical single-sideband (OSSB) modulator while the second goes through a Mach-Zehnder electrooptic modulator, which is driven by an RF frequency (f_e) in order to generate a double sideband suppressed carrier signal (DSB-SC) [31]. The two sidebands of DSB-SC act as two pump waves. A circulator is used to counter-propagate this DSB-SC signal with the OSSB modulated carrier in dispersion shifted single-mode fiber (DS-SMF). In DS-SMF, SBS interaction takes place between the optical carrier and the two sidebands. A photodiode (Pd) is used to convert the OSSB modified signal back to RF signal. The RF phase shift can be tuned by adapting the frequency detuning (f_e) of the SBS gain/loss from the carrier. The phase shifter based on SBS can be considered an essential building block of true time delay function.

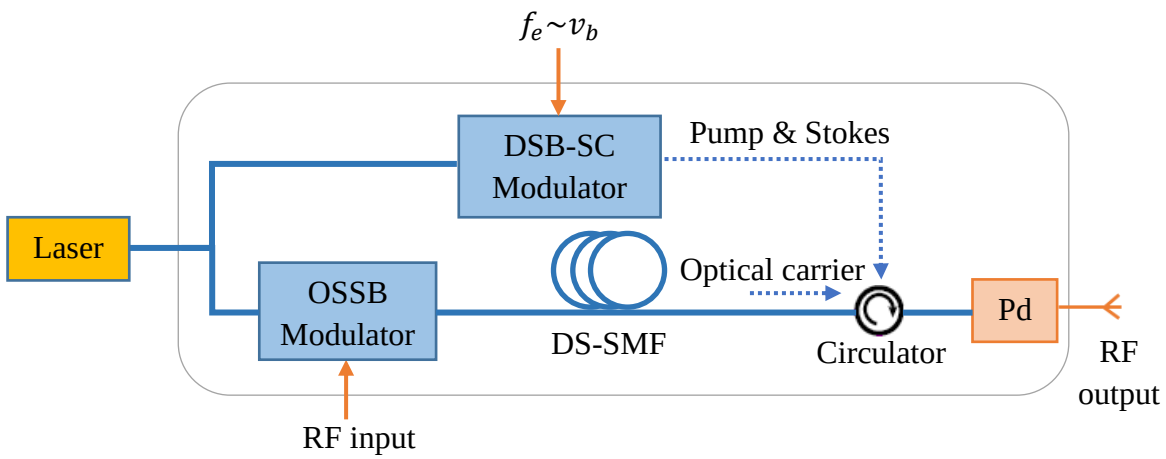

Figure 1.12 Experimental configuration of tunable RF phase shift using SBS in optical fibers.

1.2.2.3 Fiber Bragg grating based microwave photonic phase shifter

Fiber Bragg grating (FBG) is an optical reflector constructed in a short segment of optical fibers that reflects particular wavelengths of light while transmitting all others. The optical wavelength reflected along the FBG is decided by the refractive index. This is achieved by inducing permanent periodic changes in the refractive index of the core of an optical fiber. The formation of permanent gratings in an optical fiber was first demonstrated in [32]. The Schematic is shown in Figure 1.13.

The schematic diagram of the microwave photonic phase shifter based on tilted FBG (TFBG) is shown in Figure 1.14. TFBG have a periodic refractive index modulation along the fiber axis, but different from FBG. In TFBG, there is a tilt angle between the grating plane and fiber cross-section, leading to more complex mode coupling. The grating period along the fiber axis Λ is different from that perpendicular to grating plane Λg, and their relationship can be expressed as $\Lambda = \Lambda g/cos\theta_{ti}$, where θ_{ti} represents the tilted angle. Due to the existence of a tilt angle, two coupling modes are generated from this angle. One is between the forward direction and backward direction. The other is between the cladding and the counter-propagation direction. As a result, two wavelength resonances (Bragg resonance and cladding resonance) are created, which are given by [33] as:

$$\lambda_B = \frac{2n_{eff,core}\,\Lambda_g}{cos\theta_{ti}} \tag{1.18}$$

$$\lambda_{cl} = \frac{(n_{eff,cladding}+n_{eff,core})\,\Lambda_g}{cos\theta_{ti}} \tag{1.19}$$

where λ_B is Bragg resonance wavelength, λ_{cl} is the resonance wavelength of cladding, $(n_{eff,core})$ and $(n_{eff,cladding})$ are the effective refractive indices of the core and the cladding mode, respectively. Based on Kramers-Kronig relations, a change in the amplitude results in a change in the phase (φ), and consequently leads to a change in the group delay. A tunable phase shift/time delay can be achieved by slightly tuning the wavelength [33].

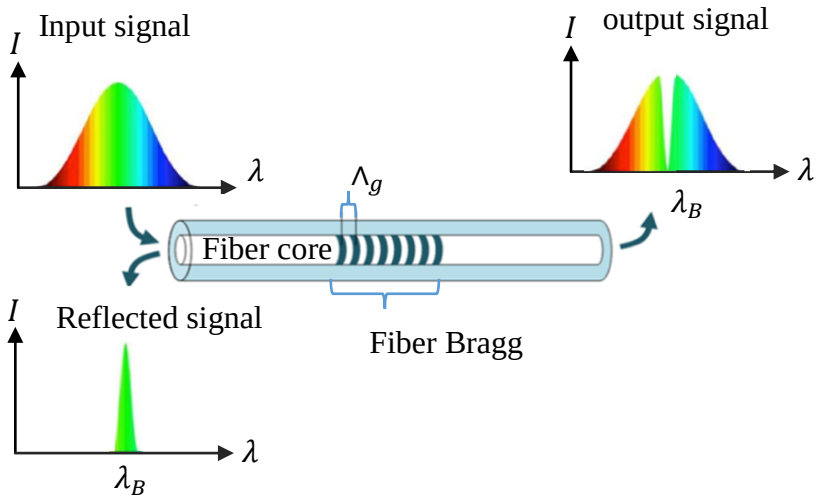

Figure 1.13 Fiber Bragg grating.

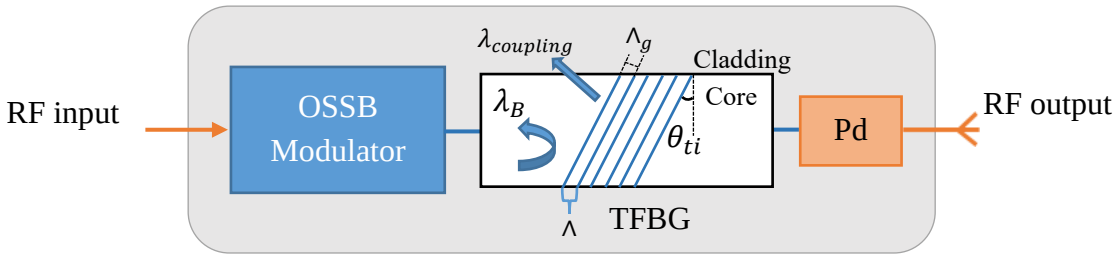

Figure 1.14 TFBG based microwave photonic phase shifter, OSSB: optical signal-sideband, Pd: photodetector.

1.2.2.4 CPO effects in SOA based microwave photonic phase shifter

Coherent population oscillations (CPO) is a phenomena that can give rise to resonances much narrower than the relaxation rate of optical coherences [34]. The former happens in a two-level system (TLS), by applying an optical pump at the angular frequency (ω_0) and a probe at ($\omega_0 + \Omega$), the total optical intensity is then modulated in amplitude at the detuning frequency (Ω). When (Ω) is set at low frequency, which is much less than the inverse of population lifetime (τ^{-1}), the population inversion is modulated in antiphase with respect to the incident optical intensity as illustrated in Figure 1.15(a). This implies that the gain is also modulated by antiphase. These leads to a dynamic variation of the optical gain, inducing in turn a phase shift. On the other hand, when (Ω) is set at a high frequency, which is much greater than (τ^{-1}), the population is too slow to perceive the fast modulation of the optical intensity. Thus, the population inversion and the gain are not modulated, as illustrated in Figure 1.15(b). The population oscillation is significant when the detuning frequency is smaller than the inverse carrier lifetime. Therefore, the bandwidth CPO is limited by the inverse of the carrier lifetime (τ^{-1}) to few hundreds of MHz.

Practically, it is not necessary to use two separate lasers as the pump and probe as they can be generated by using a single laser with temporal modulation [36].

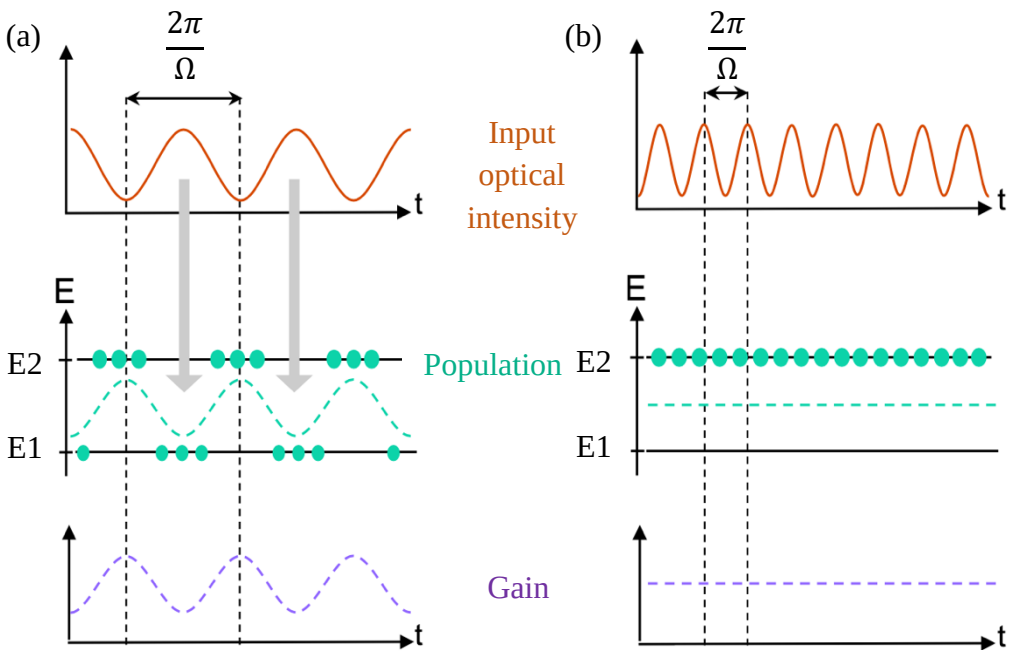

Figure 1.15 Principle of CPO illustrated in a gain medium of two levels (E1 and E2), (a) Ω at low frequency, (b) Ω at high frequency. [36]

The schematic structure of CPO based phase shifter is shown in Figure 1.16 where SOA is used as a gain medium. Phase shifters based on CPO effects in SOA can be achieved by injecting an intensity-modulated optical signal into an SOA at a modulation frequency at low frequency (below the carrier density cut-off frequency). Therefore, the carrier density oscillating at the frequency modulation leads to a dynamic variation of the optical gain, inducing a phase shift, after photodetection the output signal is phase-shifted relative to the input signal. CPO effects are controlled by the average optical gain. Both the optical input power and the electrical injection current can be used to tune the phase shift. CPO in SOA can support both true time delays and broadband microwave phase shifters at low frequencies.

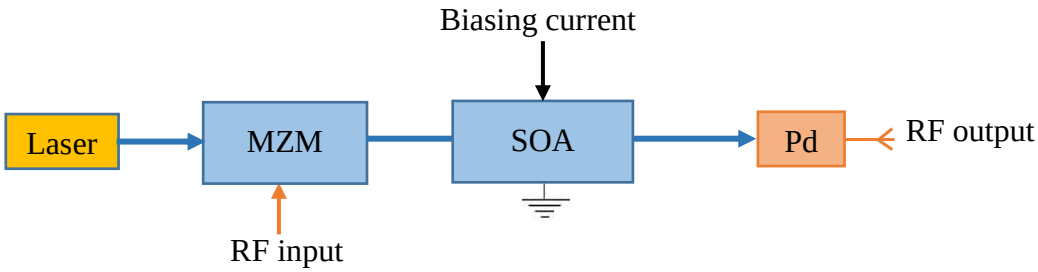

Figure 1.16 Schematic diagram of CPO based phase shifter.

Several works have been done on tunable phase-shifting based on CPO configurations in SOA [36] [37] [38] [39]. In experiments based on CPO in SOA, the gain dynamics limit the RF phase shift to a few tens of degrees and the available RF bandwidth to a few GHz. Besides, phase shifts up to 2π have been reached when cascading several stages based on SOAs [40] [41].

Instead of using cascaded SOAs, optical filtering of the red-shifted modulation sideband (low sideband) before detection is used, it enables a significant increase in phase shifts up to 180° [36] [42] [43]. The large phase shift obtained by red sideband filtering is accompanied by a significant RF signal reduction. Moreover, the enhancement of phase shift in an SOA by forced coherent population oscillations (forced CPOs) has been experimentally demonstrated by modulating SOA's current, so-called forced SOA, and without the need of sharp optical filter [44].

The operating frequency provided by CPO is limited by the inverse of the carrier lifetime to a few hundreds of MHz [45]. To overcome this limitation, up-converted CPO in an SOA noted by Up-CPO is used, leading to the generation of time delays on signals of up to THz [46].

1.2.2.5 Up converted CPO effects in SOA based microwave photonic phase shifter

The generation of true time delays at a high frequency, that is a linear relationship between the RF phase shift and the RF frequency with an adjustable slope is done by Up-CPO.

A schematic description of Up-CPO principle is shown in Figure 1.17. The principle of Up-converted CPO [46] is to combine CPO and cross gain modulation (XGM) that it is achieved by injecting two optical modulated signals into the SOA. A first optical signal P_{in1} at wavelength λ_1 is modulated at a high frequency (f_1), with $f_1 >> 1/(2\pi\tau_d)$ where τ_d is the dynamic carrier lifetime. Thus, the carrier density in the active region and the SOA optical gain is not affected by this modulation. On the other hand, the second optical signal P_{in2} at wavelength λ_2 is modulated at a low frequency f_2 with $f_2 << 1/(2\pi\tau_d)$. Therefore, the carrier density oscillating at f_2 leads to a dynamic variation of the optical gain. Thus, through XGM, the high frequency modulated signal P_{in1} is modulated by P_{in2}, and intermodulation products at high frequency $f = f_1 \pm f_2$ are generated.

After photodetection by Pd, the output RF signal at $f = f_1 \pm f_2$ provides information on the phase shift, which can be tuned through the operating condition of the SOA (the injected current or the input optical power).

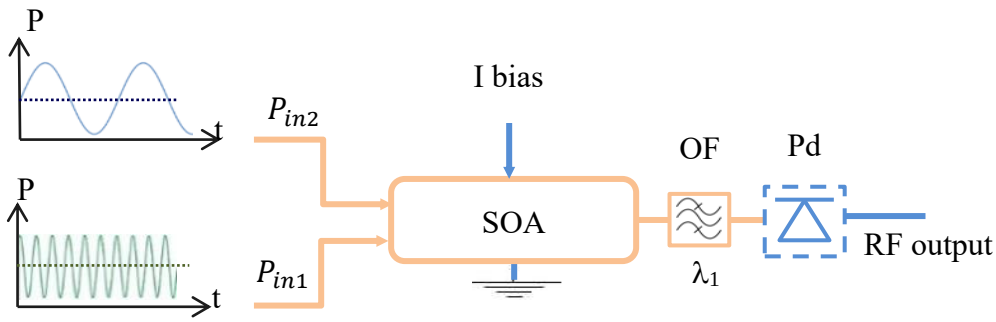

Figure 1.17 Principle of Up-CPO, OF: Optical filter, Pd: Photodiode.

1.2.2.6 True time delay based on FBG prism

The realization of tunable true time delays based on fiber optic prism consisting of an array of dispersive delay lines was demonstrated in [47]. To reduce the size of the fiber optic prism, the dispersive delay lines can be replaced by FBG delay lines. The FBG prism consists of different channels of FBG (presented in section 1.2.2.3) delay lines created in a prism format as shown in Figure 1.18.

The architecture consists of four discrete time delay lines, with each delay line having five FBGs to achieve five discrete beam pointing directions for beam steering. The optical signal emitting from the tunable laser source (TLS) is externally modulated with a MZM, then is fed into the four delay lines via an optical splitter. The signal is then reflected by the FBGs in the delay lines. Different reflection positions can be obtained depending directly on the TLS wavelength. The recovered RF signal after the Pd has a particular phase corresponding to the time delay induced by the grating position.

For a given light wavelength λ_i, with i=1,..,5, the time delay difference caused by adjacent FBG fiber is given in [48] [49] as:

$$\Delta\tau_{FBG,i} = 2\, n_{eff} \frac{\Delta d_i}{c} \tag{1.20}$$

where n_{eff} is the effective refractive index of the fiber core, Δd_i is the position difference between FBGs with same Bragg wavelength λ_i at adjacent FBG fiber, and c is the speed of light. The beam steering direction can be set by tuning the wavelength of the optical carrier. A fully tunable phase shift cannot be achieved, as the number of steered directions is limited by the number of FBGs. The disadvantage of this system is the prism which consists of several discrete FBGs rendering the system to be too bulky, complicated and unstable.

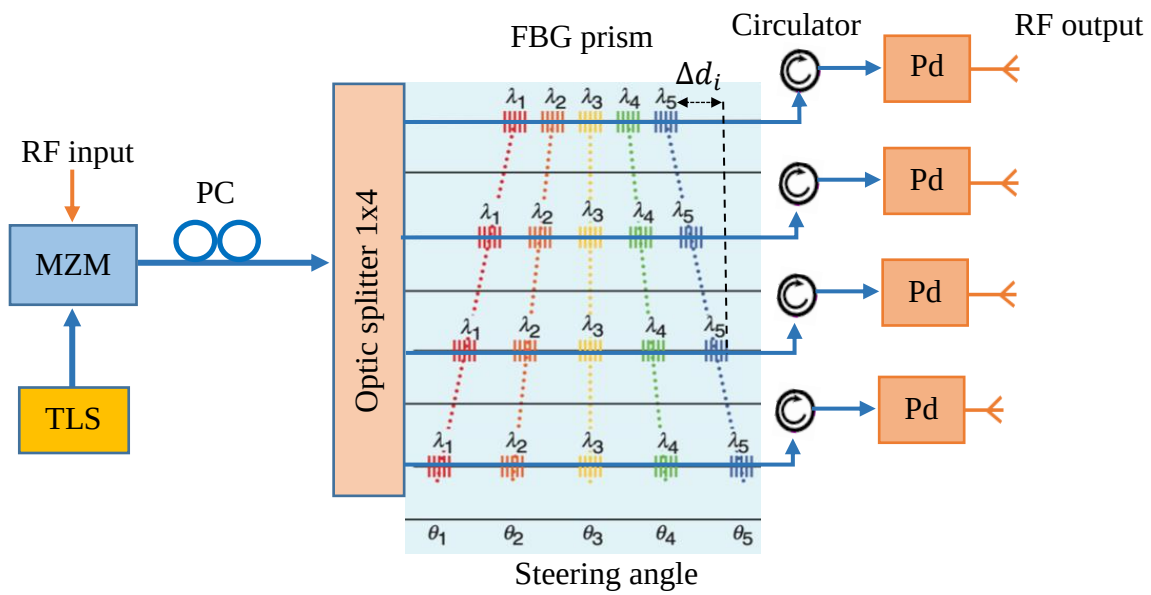

Figure 1.18 TTD beamforming system based on an FBG prism. TLS, Tunable laser source; PC, Polarization controller; Pd, photodetector; MZM, Mach-Zender modulator. [50]

A solution is to use a single wideband Chirped Bragg Grating [2] [50]. To achieve tunable time delays, the wavelength spacing should be tunable. Therefore, a multi-wavelength laser source with tunable wavelength spacing is required.

1.2.2.7 Separate carrier tuning technique

Tunable delay lines suffer from a trade-off between the achievable time delay and the bandwidth. To get rid of this limitation, a smart approach that consists of the use of separate carrier tuning (SCT) is proposed in [51] [52] [53].

In general, to implement a delay line, a linear phase response should be applied to the modulated signal spectrum. By using a single-sideband modulation, a larger bandwidth can be achieved than by using a double-sideband modulation. Therefore, considering the case of an SSB modulated optical signal having an optical carrier (OC) at (v_c) and a modulated single sideband, where only the upper sideband is kept $(v_c + v_{RF})$, as in Figure 1.19.

TTD requires a constant delay over the whole frequency range. This case refers to Figure 1.19(a), where a time delay is introduced by an ideal delay line with a linear phase slope over the whole frequency range (red dashed line).

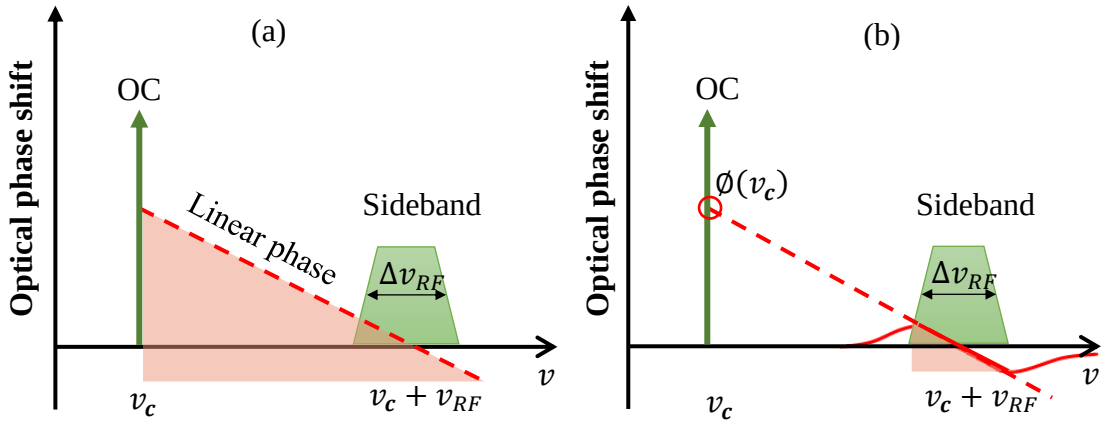

Figure 1.19 Principle of TTD (a) covering the full bandwidth and (b) using the separate carrier tuning technique. [53]

RF group delay is given by [51] [52] [53] as:

$$T_{RF} = \frac{\phi(v_c + v_{RF}) - \phi(v_c)}{2\pi v_{RF}} \tag{1.21}$$

In a broadband frequency, no data is occupied between OC and modulation sideband, as in Figure 1.19. Therefore, it is not necessary to have a linear phase response in the unoccupied region. For optical TTD to be more effective, SCT is used. It provides the generation of TTD (linear phase shift) over the RF sideband, yield to constant group delay over the frequency range Δv_{RF}, and then separately tuning the RF phase delay at the optical carrier. This allows us to extrapolate the linear phase shift applied over the whole optical sideband as shown in Figure 1.19(b) which depicts TTD using SCT technique. The phase response introduced by a dispersive component, here SBS single sideband, is used to induce Brillouin gain at $v_c + v_{RF}$. As presented in the previous part, it implies a linear slope at the upper sideband (red solid line). Thus, the signal group delay T_{sig} introduced to the signal at the frequency $v_c + v_{RF}$ is given by:

$$T_{sig} = \frac{1}{2\pi}\frac{d\phi}{dv}\bigg|_{v_c+v_{RF}} \tag{1.22}$$

At the resonance center the phase $\phi(v_c + v_{RF})$ is null. To perform TTD by only phase tuning of OC, two delays are required to be equal $T_{sig} = T_{RF}$. It is done by choosing a proper phase shift to OC in order to match signal and RF delays. The calculated phase shift is given from the expression [51] [52] [53] as:

$$T_{sig} = T_{RF} = \frac{-\phi(v_c)}{2\pi v_{RF}} \tag{1.23}$$

1.2.2.8 True time delay based on SCT using SBS delay line with FBG

The generation of true time delay using SBS (explained in section 1.2.2.2) in optical fibers and separate phase shift of the optical carrier has been experimentally demonstrated in [54]. The experimental set-up of TTD is illustrated in Figure 1.20.

The SCT technique consists of two parts. First, the implementation of a constant group delay over the frequency range of interest, while the second implements an optical carrier phase shifting by means of an FBG. The first part is performed by using the principle described in the previous section SBS process by only using one pump wave in the DSF (Dispersion shifted fiber), and SBS generated Brillouin gain. The central frequency of Brillouin gain is down shifted from the pump frequency in such a way that the optical carrier signal falls into the SBS Brillouin gain. The spectral slope of phase shift experienced by the RF sideband can be tuned by simply changing the power of the pump wave.

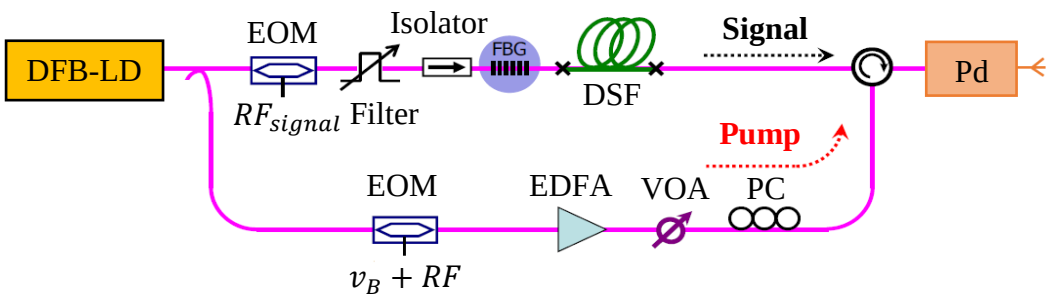

Figure 1.20 Experimental set-up, DFB-LD; Distributed Feedback Laser Diodes DFB, EOM; electro-optic modulator, DSF; dispersion shifted fiber, PC; polarization controller, EDFA; erbium doped fiber amplifier, VOA; variable optical attenuator, Pd; photodetector.[54]

The second part is described in section 1.2.2.7 and corresponds to the extrapolated value of that achieved in the RF spectral region [54]. Since, optical delays and RF sidebands experience the same delay, 0.5 to 50 ns of TTD tunability is achieved, across 10 MHz of bandwidth, limited by the SBS bandwidth.

Another approach is based on the same technique without using FBG, but by using a second Brillouin pump signal to generate a narrowband resonance in the vicinity of the carrier frequency [51] [52]. The phase of the optical carrier is then adjusted to ensure $T_{RF} = T_{sig}$ by detuning the central frequency of the resonance with respect to the carrier frequency.

1.2.2.9 True time delay based on SCT using dual-parallel MZM and SBS

Figure 1.21 represents the schematic of a true time delay system in [53]. Three MZMs structured as two MZMs set in parallel and forming a third MZM3, so-called dual-parallel MZM (DPMZM). They were combined together to achieve a double sideband carrier

suppressed with optical carrier modulated signal (DSB-SC+ OC) the details in [53]. DPMZM is used to achieve optical carrier phase tuning.

Optical carrier is amplified by an EDFA1 and is fed into a MZM driven by RF signal of frequency (v_p) to generate DSB-SC modulated signal. The signal is pre-amplified by EDFA2 and acts as pump signal. The pump power is adjusted by using a variable optical attenuator (VOA). An optical circulator is used to counter propagate the pump and the DSB-SC modulated signals. In the DSF, SBS generates both Brillouin gain and loss. By properly setting the driven frequency of MZM, a single sideband of the DSB-SC+OC modulated signal located at the Brillouin gain/loss are achieved as depicted in Figure 1.22 for the case of $v_{RF} < v_P$ and $v_P = v_{RF} + v_B$, so a linear phase shift is achieved.

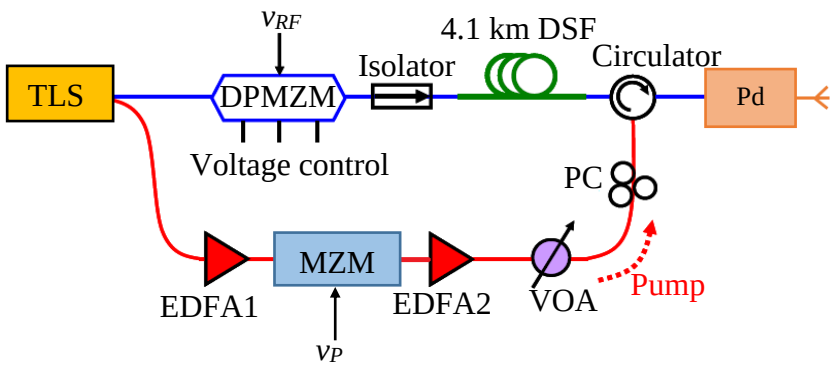

Figure 1.21 Schematic configuration of the TTD system, TLS: tunable laser source; DPMZM: dual-parallel Mach-Zehnder modulator; DSF: dispersion shifted fiber; EDFA1 and EDFA2: erbium-doped fiber amplifier; VOA: variable optical attenuator; PC: polarization controller; Pd: photodetector. [53]

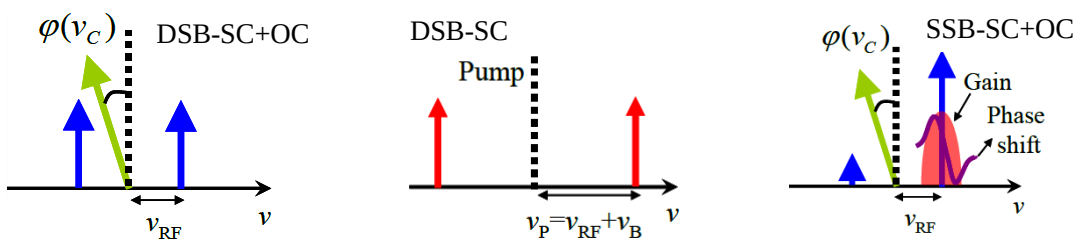

Figure 1.22 SSB-SC + OC modulation are realized by counter propagating a DSB-SC + OC signal at a frequency of v_{RF} and a DSB-SC pump signal at a frequency of v_P in a length of DSF. [53]

1.2.2.10 Summary of optical delay and true time delay techniques

A comparison between different types of microwave phase shifts based on fiber optical delay lines and TTD is presented in Table 1.3 and Table 1.4. The comparison is done in terms of time delay, loss, bandwidth and tunable functions.

Table 1.3 Summary of fiber optic delay line [35].

Type of delay line	***Time delay***	***Bandwidth***	***Loss***	***Tunability***
Dispersive Fiber [24] [25]	Tens of ps	Tens of GHz	Small	Changing: -Carrier frequency
SBS [27]-[30]	Tens of ns	Hundreds of MHz	Quite large	Changing: -Pump power -Pump frequency -Carrier frequency
FBG [32] [33]	Hundreds of ps	Tens of GHz	Quite large	Changing: -Carrier frequency
CPO [34]-[39]	Tens of ps	Few GHz	Small	Changing: -Input optical power -Biasing current -Frequency detuning

Table 1.4 Summary of true time delay.

Type of TTD	***Time delay***	***Bandwidth***	***Tunability***
FBG Prism [50]	Hundreds of ps	Few GHz	Changing: -Optical carrier wavelength
SCT based on SBS-FBG [54]	Tens of ns	Few MHz	Changing: -Pump power
SCT based on Two SBS [52]	Tens of ns	Hundreds of MHz	Changing: -Carrier frequency
SCT based on DPMZM-SBS [53]	Tens of ns	Hundreds of MHz	Changing: -Pump power -Dc bias of DPMZM

1.3 Conclusion

In this chapter, we have pointed out first the principle of MWP systems, we discussed the difference between phase shift and true time delay, we have provided an overall review of the main realization of phase shift, based on optical and electrical approaches, and the realization of true time delay relied on optical approaches. The key features of the reviewed techniques of RF phase shift, microwave phase shifter based on optical approaches, and true time delay using several optical approaches, have been reviewed and summarized in Table 1.2, Table 1.3, and Table 1.4, respectively.

- TTD relies on FBG prism: the system is bulky, complicated, and unstable since the sensitivity of FBG to environmental temperature.
- TTD relies on two SBS and SCT: required an additional optical sideband filter and a separate carrier phase shifter, adding complexity to system.
- TTD relies on DPMZM and SCT: optical sideband filter is not required, but high pump power is required for a larger phase shift.

Electrical approaches operating at high frequency (or mm-wave) tend to be bulky, lossy, and susceptible to electromagnetic interference. The most promising technique among the presented optical approaches is CPO in a semiconductor optical amplifier, which suits the requirement in terms of bandwidth (fewer GHz), low power, small device, and simple tunability of phase shift/delay based on SOA current or input optical power. The generation of phase shift/delay at any high frequency in a single SOA can be done using Up-converted CPO (Up-CPO), which will be presented in chapter 2.

Bibliography of chapter 1

[1] R. Bonjour, S. A. Gebrewold, D. Hillerkuss, C. Hafner, and J. Leuthold, “Continuously tunable true-time delays with ultra-low settling time,” *Opt. Express*, vol. 23, no. 5, p. 6952, Mar. 2015, doi: 10.1364/OE.23.006952.

[2] J. Yao, “Microwave Photonics,” *J. Lightwave Technol.*, vol. 27, no. 3, pp. 314–335, Feb. 2009, doi: 10.1109/JLT.2008.2009551.

[3] X. Xue *et al.*, "Microcomb-Based True-Time-Delay Network for Microwave Beamforming With Arbitrary Beam Pattern Control," in *Journal of Lightwave Technology*, vol. 36, no. 12, pp. 2312-2321, 15 June15, 2018.

[4] Ellinger, F. (2008). *Radio frequency integrated circuits and technologies*. Springer Science & Business Media.

[5] L. G. Maloratsky, “Passive RF & Microwave Integrated Circuits,” *Passive RF & Microwave Integrated Circuits*, pp. 1–368, Nov. 2003.

[6] A. Grebennikov, *RF and Microwave Transmitter Design: Grebennikov/Transmitter Design*. Hoboken, NJ, USA: John Wiley & Sons, Inc., 2011.

[7] Uttamchandani, D. (Ed.). (2013). *Handbook of MEMS for wireless and mobile applications*. Elsevier.

[8] A. Vilenskiy and M. Makurin, "Analog varactor phase shifter," *2017 Progress In Electromagnetics Research Symposium - Spring (PIERS)*, St. Petersburg, 2017, pp. 3820-3825. doi: 10.1109/PIERS.2017.8262425.

[9] Shi Xiao-Ming and Bai Li-Dong, "Digital phase-shifter controlled by PIN diode," *ICMMT'98. 1998 International Conference on Microwave and Millimeter Wave Technology. Proceedings (Cat. No.98EX106)*, Beijing, China, 1998, pp. 901-904.doi: 10.1109/ICMMT.1998.768435.

[10] G. M. Rebeiz, Guan-Leng Tan and J. S. Hayden, "RF MEMS phase shifters: design and applications," in *IEEE Microwave Magazine*, vol. 3, no. 2, pp. 72-81, June 2002.doi: 10.1109/MMW.2002.1004054.

[11] B. M. Schiffman, “A New Class of Broad-Band Microwave 90-Degree Phase Shifters,” *IEEE Trans. Microwave Theory Techn.*, vol. 6, no. 2, pp. 232–237, Apr. 1958, doi: 10.1109/TMTT.1958.1124543.

[12] F. L. Opp and W. F. Hoffman, “Design of Digital Loaded-Line Phase-Shift Networks for Microwave Thin-Film Applications,” *IEEE J. Solid-State Circuits*, vol. 3, no. 2, pp. 124–130, Jun. 1968, doi: 10.1109/JSSC.1968.1049855.

[13] J. F. White, “High Power, p-i-n Diode Controlled, Microwave Transmission Phase Shifters,” *IEEE Trans. Microwave Theory Techn.*, vol. 13, no. 2, pp. 233–242, Mar. 1965, doi: 10.1109/TMTT.1965.1125968.

[14] I. J. Bahl and K. C. Gupta, “Design of Loaded-Line p-i-n Diode Phase Shifter Circuits,” *IEEE Trans. Microwave Theory Techn.*, vol. 28, no. 3, pp. 219–224, Mar. 1980, doi: 10.1109/TMTT.1980.1130044.

[15] X. Tang and K. Mouthaan, “Dual-band Class III loaded-line phase shifters,” *2010 Asia-Pacific Microwave Conference*, Yokohama, 2010, pp. 1731-1734.

[16] H. A. Atwater, “Circuit Design of the Loaded-Line Phase Shifter,” *IEEE Trans. Microwave Theory Techn.*, vol. 33, no. 7, pp. 626–634, Jul. 1985, doi: 10.1109/TMTT.1985.1133038.

[17] B. Vasudev Anand, E. S. Shajahan, and M. S. Bhat, “Stub mounted loaded line phase shifter using novel RF MEMS switch,” in *2012 IEEE International Conference on Electron Devices and Solid State Circuit (EDSSC)*, Bangkok, Thailand, Dec. 2012, pp. 1–4, doi: 10.1109/EDSSC.2012.6482859.

[18] X. Tang and K. Mouthaan, "Dual-band Class III loaded-line phase shifters," *2010 Asia-Pacific Microwave Conference*, Yokohama, 2010, pp. 1731-1734.

[19] J. Komisarezuk, “Four bit phase shifter for the L band,” in *12th International Conference on Microwaves and Radar. MIKON-98. Conference Proceedings (IEEE Cat. No.98EX195)*, Krakow, Poland, 1998, vol. 2, pp. 590–594, doi: 10.1109/MIKON.1998.740927.

[20] W.-T. Li, Y.-H. Kuo, Y.-M. Wu, J.-H. Cheng, T.-W. Huang, and J.-H. Tsai, “An X-band full-360° reflection type phase shifter with low insertion loss,” in *2012 42nd European Microwave Conference*, Amsterdam, Oct. 2012, pp. 1134–1137, doi: 10.23919/EuMC.2012.6459298.

[21] H. R. Fang, Xinyi Tang, K. Mouthaan, and R. Guinvarc’h, “180° and 90° Reflection-Type Phase Shifters Using Over-Coupled Lange Couplers,” *IEEE Trans. Microwave Theory Techn.*, vol. 60, no. 11, pp. 3440–3448, Nov. 2012, doi: 10.1109/TMTT.2012.2216892.

[22] T.-W. Li and H. Wang, “A Millimeter-Wave Fully Integrated Passive Reflection-Type Phase Shifter With Transformer-Based Multi-Resonance Loads for 360° Phase Shifting,” *IEEE Trans. Circuits Syst. I*, vol. 65, no. 4, pp. 1406–1419, Apr. 2018, doi: 10.1109/TCSI.2017.2748078.

[23] A. Chakraborty and B. Gupta, "Paradigm Phase Shift: RF MEMS Phase Shifters: An Overview," *IEEE Microwave*, vol. 18, no. 1, pp. 22–41, Jan. 2017, doi: 10.1109/MMM.2016.2616155.

[24] G. Keiser, "Optical Fiber Communications, 3rd ed.," McGraw- Hill: Columbus, OH, 2000.

[25] H. Shahoei and J. Yao, "Delay Lines," in *Wiley Encyclopedia of Electrical and Electronics Engineering*, Hoboken, NJ, USA: John Wiley & Sons, Inc., 2014, pp. 1–15.

[26] R. D. Esman *et al.*, "Fiber-optic prism true time-delay antenna feed," *IEEE Photon. Technol. Lett.*, vol. 5, no. 11, pp. 1347–1349, Nov. 1993, doi: 10.1109/68.250065.

[27] A. Loayssa and F. J. Lahoz, "Broad-band RF photonic phase shifter based on stimulated Brillouin scattering and single-sideband modulation," *IEEE Photon. Technol. Lett.*, vol. 18, no. 1, pp. 208–210, Jan. 2006, doi: 10.1109/LPT.2005.861307.

[28] A. Loayssa, D. Benito, and M. José Garde, "Applications of Optical Carrier Brillouin Processing to Microwave Photonics," *Optical Fiber Technology*, vol. 8, no. 1, pp. 24–42, Jan. 2002, doi: 10.1006/ofte.2002.0364.

[29] Shaowen Peng, Zhiyao Zhang, Qihao Yang, Di Peng, Yali Zhang, and Yong Liu, "Gain fluctuation in microwave photonic phase shifters based on stimulated Brillouin scattering," in *2016 25th Wireless and Optical Communication Conference (WOCC)*, Chengdu, China, May 2016, pp. 1–4, doi: 10.1109/WOCC.2016.7506587.

[30] M. Pagani, D. Marpaung, D.-Y. Choi, S. J. Madden, B. Luther-Davies, and B. J. Eggleton, "Tunable wideband microwave photonic phase shifter using on-chip stimulated Brillouin scattering," *Opt. Express*, vol. 22, no. 23, p. 28810, Nov. 2014, doi: 10.1364/OE.22.028810.

[31] R. Montgomery and R. DeSalvo, "A novel technique for double sideband suppressed carrier modulation of optical fields," *IEEE Photon. Technol. Lett.*, vol. 7, no. 4, pp. 434–436, Apr. 1995, doi: 10.1109/68.376826.

[32] K. O. Hill, "Photosensitivity in optical fiber waveguides: from discovery to commercialization," *IEEE J. Select. Topics Quantum Electron.*, vol. 6, no. 6, pp. 1186–1189, Nov. 2000, doi: 10.1109/2944.902166.

[33] H. Shahoei and J. Yao, "Tunable microwave photonic phase shifter based on slow and fast light effects in a tilted fiber Bragg grating," *Opt. Express*, vol. 20, no. 13, p. 14009, Jun. 2012, doi: 10.1364/OE.20.014009.

[34] T. Lauprêtre *et al.*, "Ultranarrow coherent population oscillation resonance in a Λ-type system," *2012 International Conference on Fiber Optics and Photonics*, pp. 1-3, Chennai, 2012.

[35] H. Shahoei and J. Yao, "Delay Lines," in *Wiley Encyclopedia of Electrical and Electronics Engineering*, Hoboken, NJ, USA: John Wiley & Sons, Inc., 2014, pp. 1–15.

[36] P. Berger, "Lumière lente et rapide dans les amplificateurs optiques à semi-conducteurspour des applications en optique micro-onde et aux RADAR," *Thèse de doctorat*, Université de Paris Sud, U.F.R. Scientifique d'Orsay, 2012.

[37] A. Meehan and M. Connelly, "Slow light based microwave photonic phase shifter using coherent population oscillations in a bulk tensile-strained semiconductor optical amplifier, " *25th IET Irish Signals & Systems Conference 2014 and 2014 China-Ireland International Conference on Information and Communications Technologies (ISSC 2014/CIICT 2014)*, Limerick, 2014, pp. 328-330.

[38] J. Mørk, R. Kjær, M. van der Poel, and K. Yvind, "Slow light in a semiconductor waveguide at gigahertz frequencies, " *Optics Express*, 2005, vol. 13, no 20, p. 8136-8145.

[39] C. J. Chang-Hasnain and S. L. Chuang, "Slow and Fast Light in Semiconductor Quantum-Well and Quantum-Dot Devices, " in *Journal of Lightwave Technology*, vol. 24, no. 12, pp. 4642-4654, Dec. 2006.

[40] Jianjun Yu and P. Jeppesen, "Improvement of cascaded semiconductor optical amplifier gates by using holding light injection, " in *Journal of Lightwave Technology*, vol. 19, no. 5, pp. 614-623, May 2001.

[41] S. Sales, W. Xue, J. Mork, and I. Gasulla, "Slow and Fast Light Effects and Their Applications to Microwave Photonics Using Semiconductor Optical Amplifiers," *IEEE Trans. Microwave Theory Techn.*, vol. 58, no. 11, pp. 3022–3038, Nov. 2010, doi: 10.1109/TMTT.2010.2075510.

[42] P. Berger, J. Bourderionnet, F. Bretenaker, D. Dolfi, *et al*., "Influence of optical filtering on nonlinearities in SOA-based slow and fast light microwave phase shifter," *2010 IEEE International Topical Meeting on Microwave Photonics*, IEEE, 2010. p. 185-188.

[43] W.-T. Li, Y.-H. Kuo, Y.-M. Wu, J.-H. Cheng, T.-W. Huang, and J.-H. Tsai, "An X-band full-360° reflection type phase shifter with low insertion loss," in *2012 42nd European Microwave Conference*, Amsterdam, Oct. 2012, pp. 1134–1137, doi: 10.23919/EuMC.2012.6459298.

[44] P. Berger *et al.*, "Experimental demonstration of enhanced slow and fast light by forced coherent population oscillations in a SOA," *2nd IEEE International Semiconductor Laser Conference*, 2010, pp. 105-106, doi: 10.1109/ISLC.2010.5642729.

[45] P. Berger, M. Alouini, J. Bourderionnet, *et al*., "Dynamic saturation in semiconductor optical amplifiers: accurate model, role of carrier density, and slow light," *Optics express*, 2010, vol. 18, no 2, p. 685-693.

[46] P. Berger, J. Bourderionnet, F. Bretenaker, D. Dolfi, and M. Alouini, "Time delay generation at high frequency using SOA based slow and fast light," *Opt. Express,* 2011, vol. 19, no 22, p. 21180-21188, dio: 10.1364/OE.19.021180.

[47] R. D. Esman *et al.*, "Fiber-optic prism true time-delay antenna feed," *IEEE Photon. Technol. Lett.*, vol. 5, no. 11, pp. 1347–1349, Nov. 1993, doi: 10.1109/68.250065.

[48] H. Zmuda, R. A. Soref, P. Payson, S. Johns, and E. N. Toughlian, "Photonic beamformer for phased array antennas using a fiber grating prism," *IEEE Photon. Technol. Lett.*, vol. 9, no. 2, pp. 241–243, Feb. 1997, doi: 10.1109/68.553105.

[49] X. Gao *et al.*, "A high-resolution compact optical true-time delay beamformer using fiber Bragg grating and highly dispersive fiber," *Optical Fiber Technology*, vol. 20, no. 5, pp. 478–482, Oct. 2014, doi: 10.1016/j.yofte.2014.05.015.

[50] Yunqi Liu, Jianliang Yang, and Jianping Yao, "Wideband true-time-delay unit using discrete-chirped fiber Bragg grating prism," in *Technical Digest. CLEO/Pacific Rim 2001. 4th Pacific Rim Conference on Lasers and Electro-Optics (Cat. No.01TH8557)*, Chiba, Japan, 2001, vol. 2, pp. II-28-II–29, doi: 10.1109/CLEOPR.2001.970793.

[51] P. A. Morton and J. B. Khurgin, "Microwave Photonic Delay Line With Separate Tuning of the Optical Carrier," *IEEE Photon. Technol. Lett.*, vol. 21, no. 22, pp. 1686–1688, Nov. 2009, doi: 10.1109/LPT.2009.2031500.

[52] S. Chin *et al.*, "Broadband true time delay for microwave signal processing, using slow light based on stimulated Brillouin scattering in optical fibers," *Opt. Express*, vol. 18, no. 21, p. 22599, Oct. 2010, doi: 10.1364/OE.18.022599.

[53] W. Li *et al.*, "True-time delay line with separate carrier tuning using dual-parallel MZM and stimulated Brillouin scattering-induced slow light," *Opt. Express*, vol. 19, no. 13, p. 12312, Jun. 2011, doi: 10.1364/OE.19.012312.

[54] I. Gasulla, J. Capmany, J. Sancho, J. Lloret, and S. Sales, "Application of slow and fast light effects to microwave photonics," *Optica Pura y Aplicada*, vol. 44, no. 3, pp. 405-412, 2011.

CHAPTER 2

Coherent population oscillations (CPO) and Up-converted CPO in different structures of semiconductor optical amplifiers

2.0 Introduction 48

2.1 Semiconductor optical amplifier 49

2.1.1 SOA operating principle 49
2.1.2 Basic structure of SOAs 50
2.1.3 SOA gain 50
2.1.4 Gain saturation 51
2.1.5 SOA nonlinearities 53
2.1.5.1 Self-Gain and Cross Gain Modulation 53
2.1.5.2 Self-Phase and Cross Phase Modulation 53
2.1.5.3 Four-Wave Mixing 53
2.1.5.4 Self-induced Polarization Rotation and Cross-Polarization Modulation 54
2.1.6 SOA modeling 54

2.2 Characteristics of used SOAs in static regime 57

2.3 CPO effects in different structures of SOAs 59

2.3.1 CPO modeling by small signal analysis 59

2.3.2 Asymptotic behavior of the CPO responses in amplitude and phase..... 63
2.3.3 Experimental results and discussions..... 65
2.3.3.1 Experimental setup 65
2.3.3.2 Experimental results of the CPO frequency responses..... 67
2.3.3.3 Case of $R\alpha < 0$ in SOA-XN 71

2.4 Optically controlled of RF phase shift using Cross Gain Modulation..... 73

2.4.1 Small-signal analysis of ASE and optical control of RF phase shift 73
2.4.2 Numerical calculation of RF phase shift..... 76
2.4.3 Experimental realization and results of the controllable RF phase shifts in SOA..... 79

2.5 Up-converted CPO in different structures of SOAs..... 83

2.5.1 Principle of Up-converted CPO 84
2.5.2 Small-signal analysis of Up-converted CPO..... 85
2.5.2.1 Up-converted CPO optical power response as a function of the SOA mean carrier density..... 85
2.5.2.2 Small-signal frequency response of the carrier density..... 86
2.5.2.2.1 Carrier density modulation in the first and second section 88
2.5.2.2.2 Probe output power 89
2.5.2.3 Evaluation of the dynamic carrier lifetime 91
2.5.2.4 Full Up-CPO frequency response..... 92
2.5.3 Calculation and measurement of frequency responses for pump-probe and Up-CPO setups..... 92
2.5.3.1 Pump-probe characterization..... 92
2.5.3.2 Calculation of the absolute Up-CPO frequency response 95
2.5.4 Validation of small-signal calculations by experimental results of Up-CPO responses 97
2.5.5 Experimental verification of the influence of the operating frequency (fc) .. 102
2.5.6 Delay calculation of Up-CPO 103

2.6 Conclusion 106

Bibliography of chapter 2 108

2.0 Introduction

The study of photonics-induced tunable microwave phase shifts and delay lines has gained increasing interest over the past decades. One of the most successful approaches to generate tunable microwave phase shifts is based on CPO effects in SOAs [1] [2].

This chapter focuses on the experimental and theoretical analysis of tunable microwave phase shifts based on CPO and Up-converted CPOs effects in SOAs. In the first section (2.1), we review the SOA applications and nonlinearities. We explore the CPO effects in different SOA structures using small-signal analysis in section (2.2). Then, we investigate the difference in performance achieved by using four different SOAs as microwave phase shifters (section 2.3) and propose the addition of the cross-gain modulation response (XGM) (section 2.4) to achieve the desired optical control of the RF phase shift in SOAs. Based on the understandings of CPO, we study the Up-converted CPO in different SOA structures (section 2.5), a method shown to produce a tunable microwave phase shift at high frequencies.

2.1 Semiconductor optical amplifier

A semiconductor optical amplifier (SOA) is an optoelectronic device, similar to a semiconductor laser, specifically designed to amplify optical signals under suitable operating conditions. Unlike semiconductor lasers, a SOA can amplify optical signals in a single pass, so there is no optical cavity. The nonlinear behavior of semiconductor materials with respect to optical power is commonly used in all-optical and optoelectronic applications such as wavelength conversion and switching functions [3] [4]. SOAs are the most promising candidates for the realization of all-optical processing devices due to their small size, fast and strong nonlinearity characteristics, and high integration potential with other electronic and optical devices.

2.1.1 SOA operating principle

SOAs are optical amplifiers whose gain medium is a semiconductor element that amplifies an optical signal. When the SOA is pumped, carriers (electrons from the conduction band and holes from the valence band) are injected into the active zone, where they can recombine in a radiative or a non-radiative manner. During radiative recombination, the energy (Ep) released by the electron-hole pair appears in the form of a photon whose angular frequency (ω) satisfies the following relationship: Ep = $\hbar\omega$, with $\hbar = \frac{h}{2\pi}$ where h is the Planck's constant. This phenomenon occurs through either a spontaneous or a stimulated emission. These two mechanisms are illustrated in Figure 2.1.

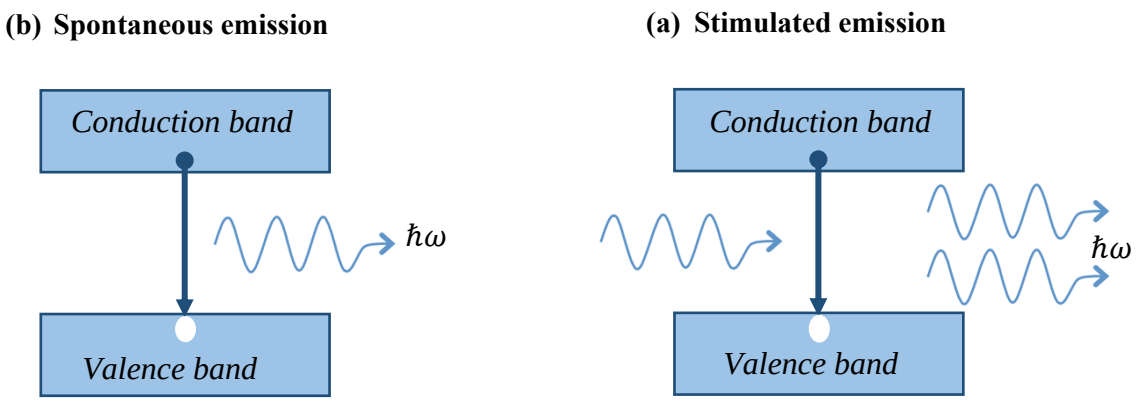

Figure 2.1 Schematic of: Spontaneous emission (a), and (b) Stimulated emission.

In the case of a spontaneous emission, the created photon is emitted in a random direction, with a random phase. For a stimulated emission, the radiative recombination is induced by an incident photon; the generated photon is then emitted having the same direction, phase and energy as the incident photon. This latter mechanism allows optical amplification if the carrier

density (electrons and holes) is high enough. Thus, it is necessary to confine both the carriers and the photons in the active zone in order to produce an efficient amplifier. Next, we will briefly describe the typical structure of SOAs.

2.1.2 Basic structure of SOAs

A schematic of an SOA is given in Figure 2.2. It has an antireflection treatment on its input and output facets in order to minimize parasitic reflectivity. The p-type and the n-type semiconductors are put together to create the p-n junction, which contains the recombination of electrons and holes. The active region is a thin layer between the "p" and "n" semiconductor layer that has a smaller bandgap than those of the layers surrounding it. Optical gain can be realized by electrically injecting an external current into the device's active region, realizing the population inversion necessary for the amplification by stimulated emission process. An input optical power experiences a single pass gain after traveling through the SOA active region of length L, always accompanied by the amplified spontaneous emission (ASE) which is generated from the spontaneous emission light and then amplified during the propagation inside the SOA. The ASE is considered as a noise source for the transmitted signal [3].

The type of material used in the SOA's active region determines its gain spectrum and operating characteristics. SOA can cover all the various optical communication bands (O-, E-, S-, C- and L-bands) in addition to 0.8µm band. It is made out of the same III-V material as the material used to manufacture the laser sources in these regions. These materials are III-V semiconductors, including InP, InGaAs, InGaAsP, AlGaAs and InAlGaAs.

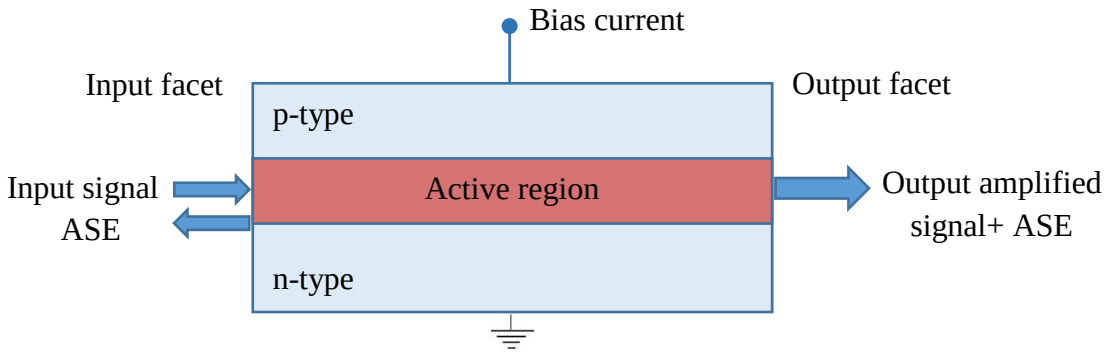

Figure 2.2 Schematic diagram of an SOA.

2.1.3 SOA gain

We have seen that the semiconductor material forming the SOA's active area exhibits optical amplification under certain conditions. The gain presented by this material at the wavelength (λ) is called material gain (g_m), [m^{-1}]. Analysis done in [5] shows the dependence of this gain

on the carrier density (N) $[m^{-3}]$ as well as the wavelength of the signal (λ). The material gain is asymmetrical as a function of the wavelength of the incident optical signal.

During its propagation along the cavity, the optical signal will benefit from net gain (g_n), $[m^{-1}]$, which considers the total loss (α) $[m^{-1}]$, in the cavity. The net gain is defined as the difference between the modal gain and total loss and is given by the following equation:

$$g_n = \Gamma g_m(N, \lambda) - \alpha \tag{2.1}$$

where Γ is the optical confinement factor.

The optical gain seen by an optical signal which passes through an SOA of length (L) is defined by the ratio of the output and input powers (P_{out}) and (P_{in}) , and is equal to:

$$G = \frac{P_{out}}{P_{in}} \tag{2.2}$$

Assuming that the carrier density is constant in the SOA, the signal propagating along the active region takes advantage of what is referred to as the single-pass gain (G). This term is measurable and can also be determined by:

$$G = e^{g_n L} \tag{2.3}$$

2.1.4 Gain saturation

In Figure 2.3(a), the gain saturation for high currents is caused by two phenomena. One is that the amplified spontaneous emission consuming carriers become preponderant. The other is that at high currents, the density of carriers becomes significant, which increases the rate of non-radiative recombination.

In Figure 2.3(b), the increase in the injected optical power induces a depletion of the carriers along the active region, thus causing gain saturation in the device. In fact, the gain remains quasi-constant for low powers of the incident signal because they do not significantly modify the density of carriers leading the amplifier to operate in linear mode, this is referred to as unsaturated gain. When the power of the injected signal becomes strong, the stimulated emission considerably reduces the carrier density, which decreases the gain of the SOA. Saturation not only results in a drop in gain, but also in a shift from the top of the gain curve towards long wavelengths as shown in Figure 2.3(c). The saturated and unsaturated gain curves merge for long wavelengths.

The SOA gain saturation can be characterized by the optical output saturation power. This power represents the output power of the amplifier for which the gain decreases to half of its

maximum value, in other words, the gain decreases by 3 dB compared to the unsaturated gain (Figure 2.3(b)). $P_{out,-3dB}$ is written in a first approximation in [3]:

$$P_{out,-3dB} = \frac{wd}{\Gamma}\frac{G\ ln(2)}{(G-2)}\ I_{sat} \tag{2.4}$$

$$I_{sat} = \frac{\Gamma P_{sat}}{wd} = \frac{h\nu}{a_0\tau} \tag{2.5}$$

where I_{sat} is the saturation intensity of the amplifying material of the active medium, P_{sat} is the saturation power of the semiconductor material, w is the optical active zone width of height d, ν denotes the optical frequency of the incident signal, a_0 is the differential gain and τ represents the carriers lifetime in the active region due to the different rates of radiative and non-radiative recombinations. The presence of high input power will lead to reduce the carrier lifetime, which leads to better dynamic performances [6].

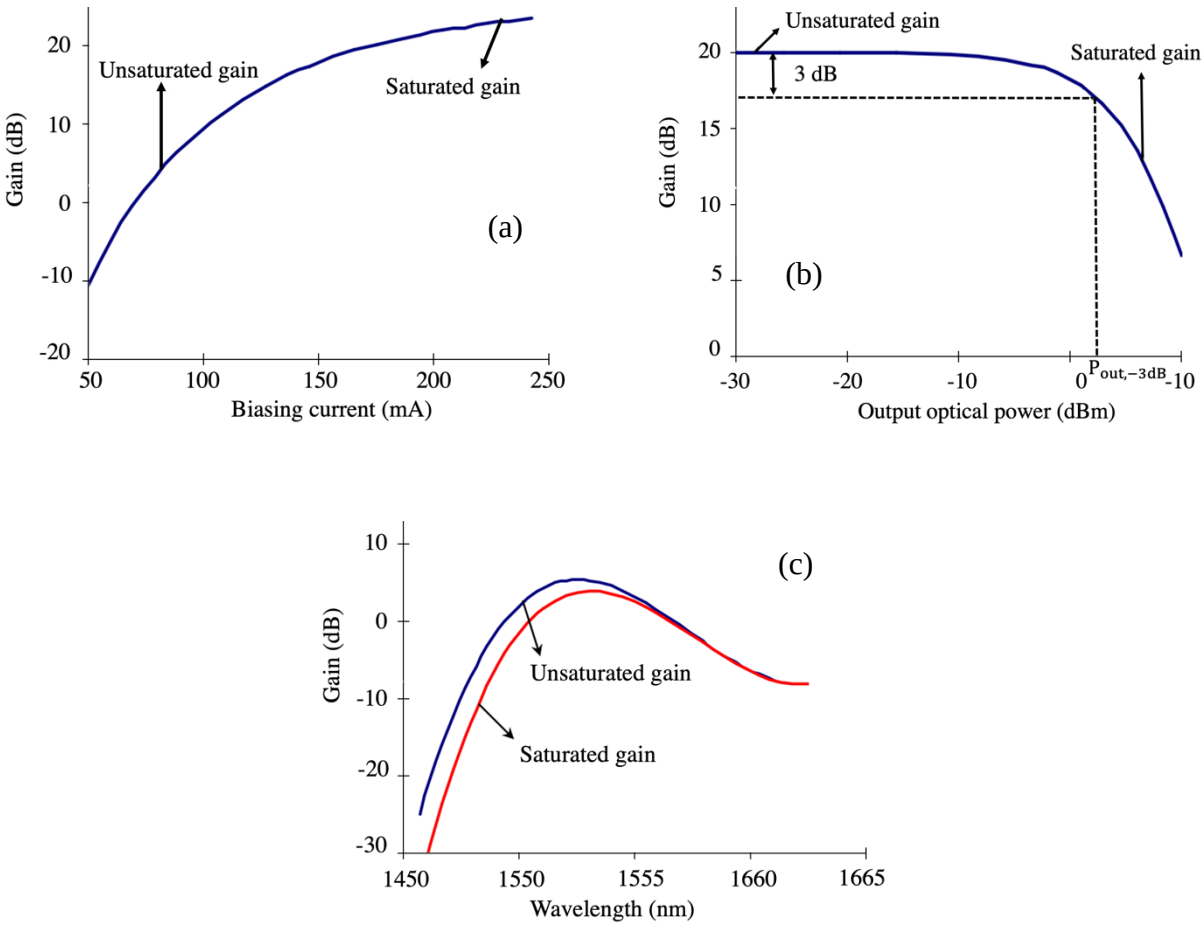

Figure 2.3 Evolution of the SOA gain as a function of bias current of SOA at low input signal power (a), output optical power (b), and wavelength (c).

2.1.5 SOA nonlinearities

Nonlinearities in SOAs are principally caused by variation of the carrier density induced by the amplifier gain that reacts to changes in the input signal power, producing variations both in power and phase. The main types of nonlinearity are self-gain modulation (SGM), cross gain modulation (XGM), self-phase modulation (SPM), cross phase modulation (XPM), four-wave mixing (FWM), self-induced polarization rotation (SPR), and cross-polarization modulation (XPolM) [3] [7].

2.1.5.1 Self-Gain and Cross Gain Modulation

Self-gain modulation (SGM) occurs when an input optical signal is injected into the SOA, a change on its optical power leads to a variation of the optical gain, due to the SOA saturation.

Cross gain modulation (XGM) is a nonlinear effect which is related to the SOA gain modulation as the SGM. It implies the modulation of the gain induced by an optical signal (known as pump signal), which affects the gain of a second injected optical signal (known as probe signal) propagating simultaneously into the SOA. XGM is a technique that allows the wavelength conversion of an optical signal.

2.1.5.2 Self-Phase and Cross Phase Modulation

An optical input signal, when injected into the SOA, causes modulation of the carrier density in the active region of SOA, which in turn can alter the refractive index of the medium. As a result, the input signal modifies its own phase at the SOA output. This process is known as self-phase modulation (SPM) [8].

In cross-phase modulation (XPM), an optical control signal is used to modulate the phase of another input signal. An intensity-modulated optical control signal propagating into the SOA modulates the carrier density in the SOA's active region, leading to a change in its refractive index (SPM). As a consequence, the phase of a second signal will be modulated by this index modulation, that depends upon the intensity modulation of the control signal. A number of applications based on XPM, such as wavelength conversion or RF mixing by using two SOAs in an interferometric structure (SOA-MZI), have been developed [9] [10].

2.1.5.3 Four-Wave Mixing

Four-wave mixing (FWM) mechanism is obtained in presence of two input optical (CW) signals, each having different wavelengths, that are coupled into a SOA. Inside the active region of the SOA, the beatings of the two signals modulate the carrier density, and therefore the intermodulation terms will generate gain modulation and a refractive index modulation. This produces new optical signals at its output, having different frequency components from

the two optical input signals. FWM generated in SOAs can be used in many applications such as all-optical wavelength converters [11].

2.1.5.4 Self-induced Polarization Rotation and Cross-Polarization Modulation

The SPR and XPolM effects describe the nonlinear rotation of the polarization state of a signal at the output of the SOA with respect to its input polarization. SPR and XPolM are due to the modification of the structural birefringence of the SOA and the difference between the gain of transverse electric (TE) and transverse magnetic (TM) (the gain saturation of the TE and TM modes is different) induced respectively by the variation of the optical signal power itself (SPR) and by that of another signal injected simultaneously with the first one in the SOA (XPolM). The SOA bias current and the input power are among the parameters that determine the amplitude of the polarization rotation.

2.1.6 SOA modeling

The modeling of a SOA can be done by considering, in a first approximation, the SOA cavity as a single section where the carrier and photon density are constant. To better consider gain saturation effects and the evolution of the carrier density along the SOA in the propagation direction z, the active region (cavity) of SOA is divided into several calculation sections. Since the carrier density is not constant along the length of the device, we divide the SOA into M-sections along its length. The modeling used in this thesis utilizes the model proposed in the thesis of P. Morel [5] and [12], which was implemented using the simulation software ADS (Advanced Design System). The parameter values of the model implemented under ADS are presented in Table A1 [Appendix]. The aim of using this model is to obtain the operating points that we used in the theoretical part of our study.

Figure 2.4 shows the SOA of length L, divided into M-sections. L is the total length of the active area, and L_i is the length of a single section. N_i represents the carrier density in the "i" calculation section. The total I_{bias} is equally divided into I_i where I_i is the electrical bias current applied on the ith calculation section.

The $\pm$ signs denote propagation in +z and –z directions, where z is the position along the device. In each section, the input signal and the ASE are expressed respectively by the propagation of the envelop of the optical filed $\mathcal{F}_i^{\pm}$, due to the injected optical input powers $P_{in}^{\pm}$, and optical intensity $I_{ASE,i}^{\pm}$.

The determination of the optical output power $P_{out}^{\pm}$ and the SOA characteristics are obtained from the coupled equations in each section i of the optical signal fields propagation and the rate equation of the carrier densities.

The propagation equation of the optical field signal E of z length can be given as:

$$E^{\pm}(z) = e^{\mp ik(N,\lambda)L_i}\, E^{\pm}(0) \tag{2.6}$$

where $n_{eq}(N_i,\lambda)$ is the refractive index, $k(N_i,\lambda)$ refers to the wavevector it is expressed as:

$$k(N_i,\lambda) = n_{eq}(N_i,\lambda) + \frac{i}{2} g_n(N_i,\lambda) \tag{2.7}$$

where $k(N_i,\lambda)$ describes the action of the medium in section i on the optical field, in terms of propagation-linked dephasing and gain.

The optical field (of dimension $\sqrt{W/m^2}$) can be expressed in function of the envelop as:

$$E^{\pm}(z) = \mathcal{F}_{in}^{\pm}(z) e^{i\Omega t} \tag{2.8}$$

where Ω is the angular frequency of the optical field at wavelength λ and the expression of the envelop is given by:

$$\mathcal{F}^{\pm}(z) = e^{\mp ikz}\, \mathcal{F}^{\pm}(0) \tag{2.9}$$

For an input power P_{in}, the input optical envelop field can be written in function of the optical power by:

$$\mathcal{F}_{in}^{\pm} = \sqrt{\frac{\Gamma}{wd}|P_{in}|} e^{i\phi(P_{in})} \tag{2.10}$$

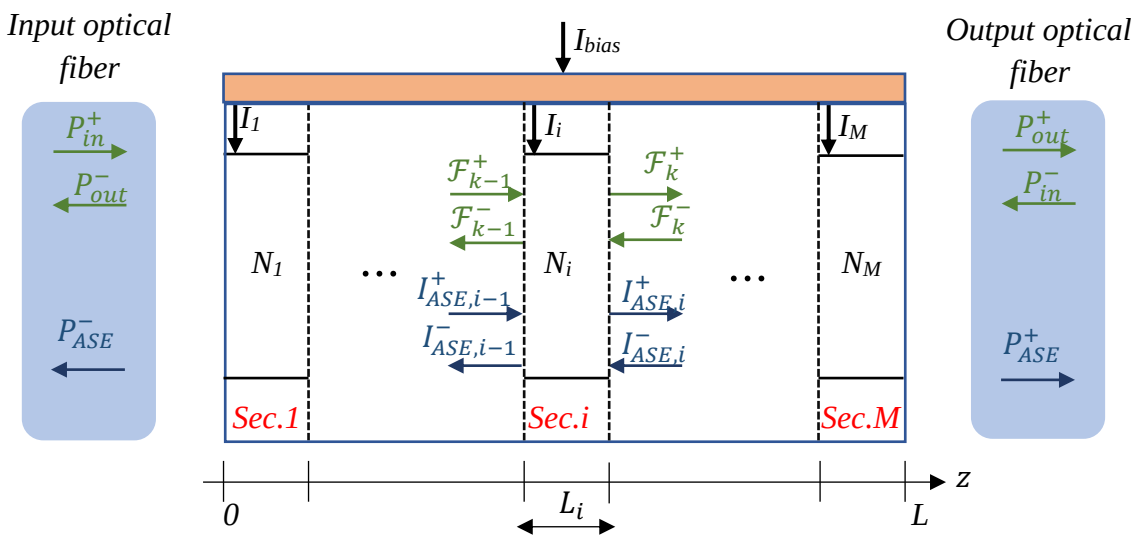

Figure 2.4 Schematic of dividing the cavity of the SOA into M-sections.

The general form of the rate equation for section *i* is given by

$$\frac{dN_i}{dt} = \frac{I_i}{q_e V_i} - R_{nst,i} - R_{st,i} - R_{ASE,i} \tag{2.11}$$

where index *i* refers to the section number, I_i is the SOA bias current for section *i*, V_i is the optical active zone volume of length L_i.

The first term on the right-hand side represents the addition of carriers in the active region from the bias current. These injected carriers are then depleted by various mechanisms within the amplifier. The second term is due to nonradiative and radiative recombination mechanisms. The third and fourth terms represent the radiative recombination of carriers due to the amplified signal and amplified spontaneous emission (ASE) respectively.
Nonradiative and radiative recombination can be defined by:

$$R_{nst,i} = \frac{N_i}{\tau_i} \tag{2.12}$$

where τ_i and N_i are the carrier lifetime and carrier density in section *i*, respectively. The carrier lifetime is N_i dependent and is obtained by:

$$\frac{1}{\tau_i} = A + BN_i + C{N_i}^2 \tag{2.13}$$

where *A* is the nonradiative coefficient due to recombination, *B* is the spontaneous radiative recombination coefficient, and *C* is the Auger coefficient.

The recombination rate due to the amplified spontaneous emission is determined by taking into account the ASE spectral dependence. This is achieved by defining M_{ASE} pseudo-modes. The pseudo-modes take into account the entire spectrum of the amplified spontaneous emission. $R_{ASE,i}$ due to pseudo-modes M_{ASE} in each section is calculated as follows:

$$R_{ASE,i} = \sum_{k=1}^{M_{ASE}} R_{ASE,i}^k \tag{2.14}$$

where the recombination rate due to a single pseudo-mode, at wavelength λ_k, it is given by the following equation:

$$R_{ASE,i}^k = \frac{2}{wdL_i}\left(\frac{G_{ASE,i}^k - 1}{g_{n,ASE,i}^k} - 1\right) r_{sp,ASE,i}^k \tag{2.15}$$

where $G_{ASE,i}^{k}$ is the ASE gain in section i, $g_{n,ASE,i}^{k}$ is the net gain of ASE in section i, and $r_{sp,ASE,i}^{k}$ is the spontaneous rate in section i at wavelength λ_k. w is the width and d the height of the active zone.

The stimulated recombination due to photons of M_{sig} signals propagating in section i is given by:

$$R_{st,i} = \sum_{j=1}^{M_{sig}} R_{st,i}^{j} \tag{2.16}$$

with $R_{st,i}^{j}$ is the stimulated recombination rate produced by the signal (sig), at wavelength λ_i in section i. It can be expressed as:

$$R_{st,i}^{j} = \frac{g_{m,sig,i}^{j}}{g_{n,sig,i}^{j}} \frac{P_{sig,i}^{j}(G_{sig,i}^{j} - 1)}{\Gamma L_i \tau_i \, a_i \, P_{sat,sig,i}^{j}} \tag{2.17}$$

where $G_{sig,i}^{j}$ is the signal gain in section i at λ_j, $g_{n,sig,i}^{j}$ is the net gain of the signal in section i at λ_j, a_i is the peak-gain coefficient of section i. $P_{sig,i}^{j}$ is the signal input optical power in section i at λ_j, and $P_{sat,sig,i}^{j}$ is the material saturation power at λ_j.

2.2 Characteristics of used SOAs in static regime

In this work, we have used four different SOAs available in our laboratory: SOA-L, a device from InPhenix, which is identified as linear SOA reference INPHENIX-IPSAD 1501 (see appendix [A.2]), as well as two nonlinear and one extra nonlinear SOAs by CIP photonics; SOA-NL1 reference 40G-2R-ORP [A.3], SOA-NL reference SOA-NL-OEC-1550 [A.4], and SOA-XN reference SOA-XN-OEC-1550 [A.5].

Each SOA device being different, performance comparison is made with respect to the static optical gain. We have firstly reviewed the static characteristic for the four SOAs used. We classified the SOAs in static regime in terms of their output power over a wide range of wavelengths, input powers and bias currents. A continuous optical signal is injected into the SOA input, we then measure the optical gain as the input optical power, bias current and wavelength are varied.

Figure 2.5(a) shows the evolution of the optical gain as a function of injected input optical power, for a fixed maximum biasing current I_{max}, with I_{max} = 300 mA for SOA-L at wavelength 1527 nm and SOA-NL at wavelength 1550 nm, I_{max} = 380 mA for SOA-NL1 at wavelength 1550 nm, and I_{max} = 400 mA for SOA-XN at wavelength 1550 nm. The increase in the input optical power after saturation leads to a decrease in the SOA's optical gain. The optical gain of

SOA-L, SOA-NL1, SOA-NL and SOA-XN is respectively 20.6 dB, 23 dB, 29 dB and 29.5 dB. Figure 2.5(b) shows the evolution of the optical gain as a function of the output optical power, for a fixed maximum biasing current I_{max}.

Figure 2.5(c) shows the evolution of the optical gain as a function of injected bias currents, for a fixed input optical power at -20 dBm, at wavelength 1527 nm for SOA-NL, at wavelength 1550 nm for SOA-NL1, SOA-NL and SOA-XN. Figure 2.5(d) shows the evolution of the optical gain as a function of wavelength, for a fixed maximum biasing current I_{max} and input optical power at −20 dBm for each SOA.

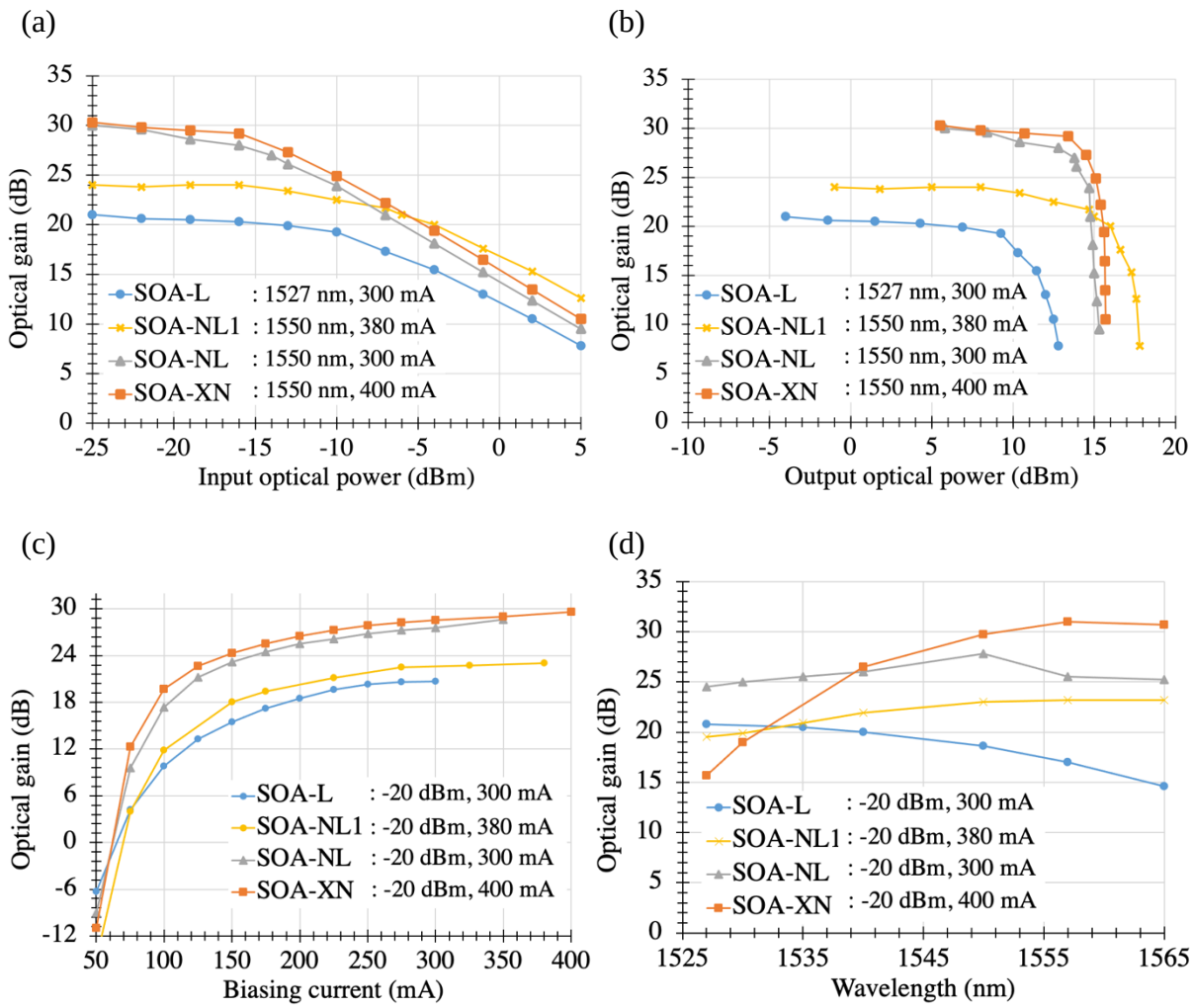

Figure 2.5 Experimental results of optical gain of the four SOAs as function of: the input optical powers applied at their input at bias current I_{max} (a), the output optical powers (b), the bias currents with input optical power at -20 dBm (c), and wavelength by fixing input optical power at -20 dBm and Imax (d).

Table 2.1 represents the static characteristics of SOAs measured at the maximum biasing current and at −25 dBm input optical power, and the output saturation power at the maximum bias current of each SOA. The wavelength is fixed at 1550 nm for all SOAs.

Table 2.1 Static characteristics of four commercial SOAs at wavelength 1550 nm.

	SOA-L	***SOA-NL1***	***SOA-NL***	***SOA-XN***
Unsaturated gain (dB)	18.8	24	30.2	30.5
$P_{out,-3dB}$ (dBm)	12.6	15	13.7	14.5
I_{max}	at 300 mA	at 380 mA	at 300 mA	at 400 mA

2.3 CPO effects in different structures of SOAs

In this part, we derive the small-signal variation of SOA carrier density and its optical output power due to the variation of the input signal. This allows us to evaluate the effects of self-gain modulations on amplitude and phase at the SOA's output. The modeling is done by considering one calculation section (i = 1) equal to the length of the SOA for a simple approach, where the carrier density N is constant all along the SOA.

2.3.1 CPO modeling by small signal analysis

The model used for small-signal analysis is based on a carrier density rate equation (2.11) and a set of travelling-wave equations describing the amplified signal fields (2.6) [12] [13] [14] [15]. In order to perform a small-signal analysis, an intensity-modulated optical signal is injected into the SOA. The signal has a power of P_{in}^{x} at wavelength λ_x, and is modulated at a low frequency (f) with $f \ll 1/(2\pi\tau_d)$ where τ_d is the dynamic carrier lifetime.

The time varying input signal can be written:

$$P_{in}^{x} = \overline{P_{in}^{x}} + \delta p_{in}^{x} = \overline{P_{in}^{x}} + \frac{p_{in}^{x}}{2} e^{\,j\omega_x t} + \frac{p_{in}^{*x}}{2} e^{-j\omega_x t} \tag{2.18}$$

$\overline{P_{in}^{x}}$ is the mean input power at λ_x, the sinusoidal variation is denoted by δp_{in}^{x} is the amplitude of the RF modulation at an angular frequency ω, $\omega = 2\pi f$ of the optical signal at the wavelength λ_x and (*) stands for the complex conjugate value.

By using a first-order Taylor expansion, the input electrical field E_{in}^{x} corresponding to P_{in}^{x} can be written [16], expressed in square root of Watt:

$$E_{in}^{x} = \sqrt{P_{in}^{x}}\, e^{j\Omega\, t} \approx \overline{E^{x}}\left(1 + \frac{p_{in}^{x}}{4\overline{P_{in}^{x}}} e^{j\omega t} + \frac{p_{in}^{*x}}{4\overline{P_{in}^{x}}} e^{-j\omega t}\right) \tag{2.19}$$

where $\overline{E^{x}} = \sqrt{\overline{P_{in}^{x}}} e^{j\Omega\, t}$ and Ω the angular frequency of the optical field at λ_x.

The amplification of the time varying optical signal P_{in}^{x} induces a modulation of carrier density N_i in the active region of the SOA, leading to a dynamic variation of the optical gain G_i^x at λ_x. Limited to a first-order expansion N_i and G_i^x, the expression of the carrier density N_i and G_i^x in section i can be written as:

$$N_i = \overline{N_i} + \delta n_{i,\omega} = \overline{N_i} + \frac{n_{i,\omega}}{2} e^{j\omega t} + \frac{n_{i,\omega}^{*}}{2} e^{-j\omega t} \tag{2.20}$$

$$G_i^x = \overline{G_i^x} + \delta n_{i,\omega} \frac{\partial G_i^x}{\partial N_i} = \overline{G_i^x} + \frac{n_{i,\omega}}{2} \frac{\partial G_i^x}{\partial N_i} e^{j\omega t} + \frac{n_{i,\omega}^{*}}{2} \frac{\partial G_i^x}{\partial N_i} e^{-j\omega t} \tag{2.21}$$

$\overline{N_i}$ and $\overline{G_i^x}$ represent the static operating points in each section i, δn_i is the carrier density variation, $n_{i,\omega}$ is the complex amplitude of the carrier density modulation in section i at ω, and $n_{i,\omega}^{*}$ is the complex conjugate of $n_{i,\omega}$.

The gain of SOA (2.3) as well as the partial derivative of the gain with respect to the carrier density are given by the following equations:

$$G_i^x(N_i) = e^{\Gamma g_{m,i}^{x} L_i - \alpha L_i} \tag{2.22}$$

$$\frac{\partial G_i^x}{\partial N_i} = \Gamma a_i^x L_i\, \overline{G_i^x} \tag{2.23}$$

where $g_{m,i}^{x} = a_i^x (N_i - N_0)$ and N_0 is the carrier density at transparency.

The recombination rate induced by the amplification of the optical carrier at wavelength is given by the following equation from (2.16) as:

$$R_{st,i} = \frac{g_{m,i}^{x}}{g_{n,i}^{x} \Gamma a_i^x L_i\, \tau_i}\left(\frac{P_{in,i}^{x}\,(G_i^x - 1)}{P_{sat,i}^{x}}\right) \tag{2.24}$$

$P_{sat,i}^{x} = wdW_p^x / \Gamma a_i^x \tau_i$ is the material saturation power, where W_p^x is the photon energy at the signal wavelength λ_x, Γ is the optical confinement factor in the active zone and a_i^x is the peak-gain coefficient in section i at the signal wavelength λ_x.

The $R_{nr,i}$ and $R_{ASE,i}$ can be taken into account from (2.12)-(2.13) by:

$$\frac{N_i}{\tau_{e,i}} \tag{2.25}$$

with $\tau_{e,i}$ is the effective carrier lifetime calculated from the carrier lifetimes τ_i, due to $R_{nr,i}$, and $\tau_{ase,i}$, due to $R_{ASE,i}$, with $\frac{1}{\tau_{e,i}} = \frac{1}{\tau_i} + \frac{1}{\tau_{ase,i}}$ [17] [18].

By substituting (2.17) and (2.25) into (2.11), the rate equation for section *i* is given as:

$$\frac{dN_i}{dt} = \frac{I_i}{q_e V_i} - \frac{N_i}{\tau_{e,i}} - \frac{g_{m,i}^x}{g_{n,i}^x} \frac{P_{in,i}^x (G_i^x - 1)}{\Gamma a_i^x L_i \, \tau_{e,i} P_{sat,i}^x} \tag{2.26}$$

Considering exclusively first-order modulation terms, the rate equation (2.26) can be derived for the SOA modeled by one section device ***i* = 1** as:

$$j\omega n_\omega + \frac{n_\omega}{\tau_e} + \frac{\overline{g_m^x}}{\overline{g_n^x}} \frac{\left(n_\omega \, \overline{P_{in}^x} \frac{\partial G}{\partial N}\right)}{\Gamma a^x L \tau_e P_{sat}^x} = -\frac{\overline{g_m^x}}{\overline{g_n^x}} \frac{(\overline{G^x} - 1)}{\Gamma a^x L \tau_e P_{sat}^x} p_{in}^x \tag{2.27}$$

By substituting the derivative of gain with respect to N_i (2.23) into (2.27), the small-signal modulation component n_ω of the carrier density at the angular frequency ω relative to the optical modulation power p_{in}^x can be given as:

$$n_\omega = -\frac{\overline{g_m^x}}{\overline{g_n^x}} \frac{\frac{\tau_d}{\tau_e}}{\Gamma a^x L \tau_e P_{sat}^x} \left(\frac{\overline{G^x} - 1}{1 + j\omega\tau_d} \right) p_{in}^x \tag{2.28}$$

where $\overline{G^x}, \overline{g_m^x}$ and $\overline{g_n^x}$ are considered in the static regime. The dynamic carrier lifetime τ_d is developed from the small signal analysis by:

$$\frac{1}{\tau_d} = \frac{1}{\tau_e} \left(1 + \frac{\overline{g_m^x}}{\overline{g_n^x}} \left(K\overline{G^x} - \alpha \frac{(\overline{G^x} - 1)K}{\Gamma L \overline{g_m^x} \, \overline{g_n^x}} \right) \right) \tag{2.29}$$

with

$$K = \frac{\overline{P_{in}^x}}{P_{sat}^x} \tag{2.30}$$

At the SOA's output, $P_{out}^{x} = P_{in}^{x} G^{x}$ presents a modulation component at the angular frequency ω due to the modulation of the carrier density N. The output power at the angular frequency ω is given by:

$$p_{out}^{x} = p_{in}^{x} \overline{G^{x}} + p_{SGM} \tag{2.31}$$

where the self-gain modulation (SGM) term p_{SGM} is related to the modulation of N given as the following:

$$p_{SGM} = n_{\omega} \overline{P_{in}^{x}} \frac{\partial G^{x}}{\partial N} = n_{\omega} \Gamma L a^{x} \overline{P_{in}^{x}} G^{x} \tag{2.32}$$

By substituting (2.28) and (2.29) into (2.31), we obtain the RF small-signal modulation component at the output of the SOA:

$$p_{out}^{x} = p_{in}^{x} \overline{G^{x}} \frac{\tau_d}{\tau_e} R_{\alpha} \frac{1 + sgn(R_{\alpha}) j\omega\tau_n}{1 + j\omega\tau_d} \tag{2.33}$$

where $sgn(R_{\alpha})$ refers to a positive or a negative sign of R_{α}, and

$$R_{\alpha} = 1 - \frac{\overline{g_m^{x}}}{\overline{g_n^{x}}} K \left(\alpha \frac{(\overline{G^{x}} - 1)}{\Gamma L \overline{g_m^{x}}\, \overline{g_n^{x}}} - 1 \right) \tag{2.34}$$

$$\begin{aligned} \tau_n = \frac{\tau_e}{|R_{\alpha}|} &= \frac{\left(1 + \frac{\overline{g_m^{x}}}{\overline{g_n^{x}}} \left(K\overline{G^{x}} - \alpha \frac{(\overline{G^{x}} - 1)K}{\Gamma L \overline{g_m^{x}}\, \overline{g_n^{x}}} \right)\right)}{|R_{\alpha}|} \tau_d \\ &= \frac{\left(|R_{\alpha}| + \frac{\overline{g_m^{x}}}{\overline{g_n^{x}}} K(\overline{G^{x}} - 1) \right)}{|R_{\alpha}|} \tau_d \end{aligned} \tag{2.35}$$

It should be noted that, for positive R_{α}, $\alpha = 0$ and $\frac{\overline{g_m^{x}}}{\overline{g_n^{x}}} = 1$, we obtained the CPO response as [1] [19], and it can be written from (2.33) as :

$$\begin{aligned} p_{out}^{x} &= p_{in}^{x} \overline{G^{x}} - \frac{K\overline{G^{x}}}{(1 + K\overline{G^{x}})} \frac{(\overline{G^{x}} - 1)}{1 + j\omega\tau_d} p_{in}^{x} \\ &= p_{in}^{x} \overline{G^{x}} \left(\frac{1 + K}{1 + KG^{x}} \right) \frac{\left(1 + j\omega \frac{\tau_e}{1 + K}\right)}{\left(1 + j\omega \frac{\tau_e}{1 + KG^{x}}\right)} \end{aligned} \tag{2.36}$$

2.3.2 Asymptotic behavior of the CPO responses in amplitude and phase

In this section we portray the asymptotic CPO frequency responses in amplitude and phase to highlight the theoretical limits of the CPO frequency responses. In (2.33) the phase evolution is depending on the sign of R_α.

The evolution of R_α as a function of K for several SOA gains after resolving the rate is given in Figure 2.6. It is obtained by resolving the rate equation (2.26) in function of P_{in}^x for different SOA bias currents, by using one calculation section for the SOA presented in [5] [12] (see Table A1 [Appendix]). Figure 2.6 shows that R_α becomes negative for K range and for high SOA gain.

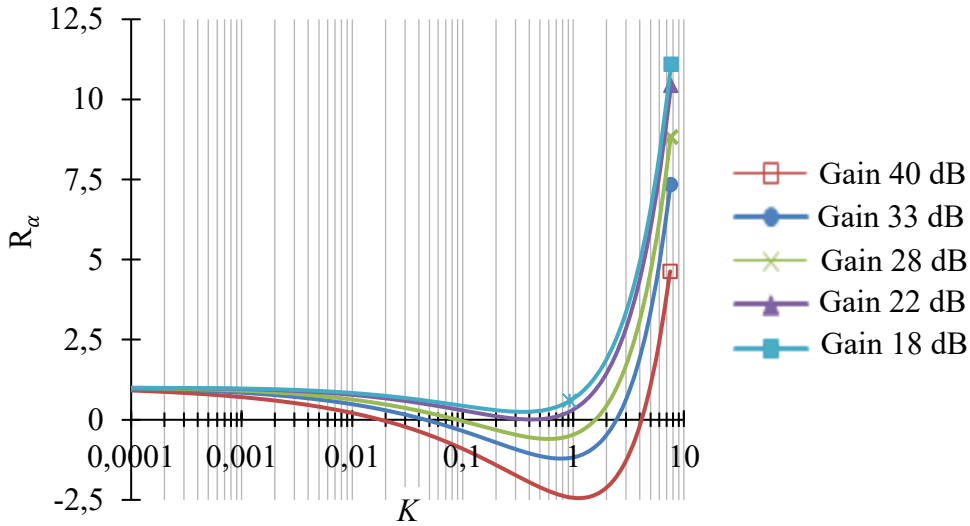

Figure 2.6 Evolution of R_α as function of K for several SOA gains.

From (2.35), we have $\tau_n > \tau_d$ for $\overline{G^x} > 1$. For $R_\alpha > 0$, Figure 2.7(a) shows that the asymptotic amplitude of the CPO's frequency response presents a change from $p_{in}^x \overline{G^x} \frac{\tau_d}{\tau_e} R_\alpha$ at low frequency ($\omega \to 0$) to $p_{in}^x \overline{G^x} \frac{\tau_n}{\tau_e} R_\alpha$ at high frequency ($\omega \to \infty$). Thus, the ratio between the CPO's amplitude response variation at low and high frequency is dependent on $\frac{\tau_n}{\tau_d} = \frac{\left(|R_\alpha| + \frac{\overline{g_m^x}}{\overline{g_n^x}} K(\overline{G^x} - 1)\right)}{|R_\alpha|}$ which increases by increasing the SOA gain or the SOA optical input power. Besides, the phase tends to have a maximum value of $\frac{\pi}{2}$ in the angular frequency range $\frac{1}{\tau_n} < \omega < \frac{1}{\tau_d}$, as seen in Figure 2.7(b).

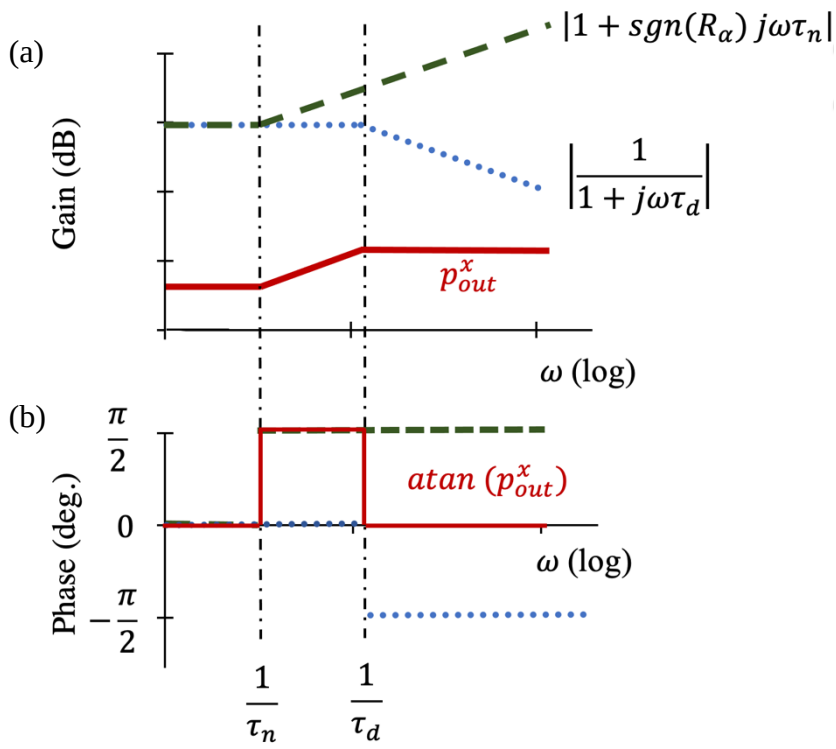

Figure 2.7 Asymptotic responses of p_{out}^x in frequency domain of: (a) amplitude response, and (b) phase response, for the case of positive R_α.

For the case where $sgn(R_\alpha)$ is negative (Figure 2.8), the amplitude response of p_{out} will have the same response as $sgn(R_\alpha)$ is positive. However for the phase, we can see that it can be started form π at $\omega < \frac{1}{\tau_n}$. At $\omega > \frac{1}{\tau_n}$ the phase response will have the same behavior as in Figure 2.7(b), where the maximum phase shift is about $\frac{\pi}{2}$ in frequency range $\frac{1}{\tau_n} < \omega < \frac{1}{\tau_d}$, as seen in Figure 2.8(b).

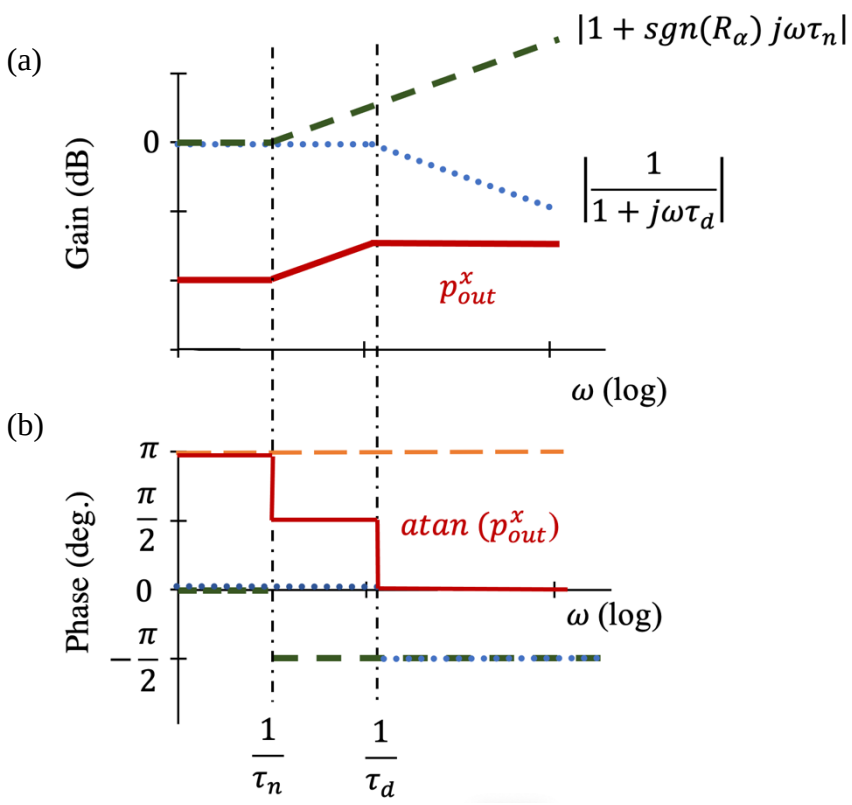

Figure 2.8 Asymptotic responses of p_{out}^x in frequency domain of: (a) amplitude response, and (b) phase response, for the case of negative R_α.

In the next section we will demonstrate the phase response of both cases of the sgn(R_α) by means of measurement.

2.3.3 Experimental results and discussions

In this section, we present the experimental comparison between four different SOAs for tunable RF phase shifts. It is based on CPO effects in a SOA, which were introduced in 1.2.2.4. The comparison between SOAs is done in terms of maximum phase shift, RF penalty on gain and CPO_{3dB} bandwidth. An evidence of a specific CPO response is indicated, where the response of the phase shift is different from the known CPO. This regime is explained by small-signal equations and presented in section 2.3.3.3.

2.3.3.1 Experimental setup

The static characteristics of the four different commercial SOAs used in this work are presented in section 2.2. The experimental setup of the microwave photonic phase shifter based on CPO in a semiconductor optical amplifier is shown in Figure 2.9. A continuous-wave (CW) $\overline{P_{in}^x}$ is

generated from a laser source emitting at λ_x = 1550 nm, and then modulated via an external Mach-Zehnder Modulator (MZM), which has a measured electrical bandwidth of 6 GHz. It is driven by a continuously variable RF signal at frequency f_{VNA}, swept from 100 MHz to 20 GHz, from a Vector Network Analyzer (VNA). By incorporating an Erbium Doped Fiber Amplifier (EDFA) having an optical gain of 17 dB, and a variable optical attenuator (VOA), the input optical power $\overline{P_{in}^{x}}$ can be adjusted between -30 dBm to 11.6 dBm at the SOA's input. An amplified photodetector (Pd) converts the optical output of the SOA into an RF signal that is received by the VNA. The detected RF signal is compared with the RF reference signal to determine the microwave phase shifts or time delays, which are caused by the SOA. The RF modulation power is fixed at 0 dBm.

In the experiment, we measure the phase of this RF signal while f_{VNA} is swept. To ensure a good comparison between all SOAs, the measurements are all made with respect to their static optical gains.

The measurements of RF power and phase shift are made by measured the S-parameters using VNA. The RF power of the output RF signal is measured relatively to a back-to-back measurement, without the SOA in the optical path. Therefore, the measured RF power is obtained by $20\log(|S_{21,z}|) - 20\log(|S_{21,y}|)$, where *z* refers to SOAs static optical Gain (0, 5, 10, 13, 15 dB) and *y* is the back-to-back measurement without SOA.

A phase measurement is a relative (ratio) measurement and not an absolute one. Therefore, RF phase shift is measured relative to a reference. This is done by measuring the relative S_{21} phase responses of the RF output signal with respect to a reference: $\phi_{relative} = arg(S_{21,z}) - arg(S_{21,reference})$, where reference is fixed at a lower gain at -5 dB.

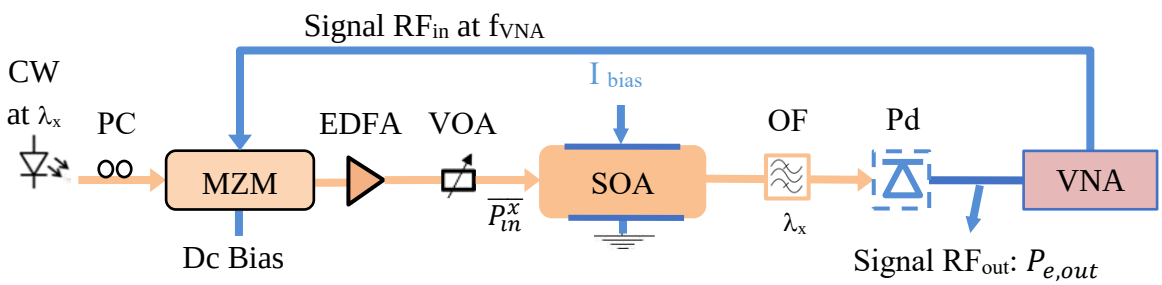

Figure 2.9 Experimental setup to measure microwave phase shifts induced by CPO effects in a SOA. PC: Polarization controller.

2.3.3.2 Experimental results of the CPO frequency responses

Figure 2.10 and Figure 2.11 detail the CPO frequency response in terms of amplitude and phase. For the amplitude response, we define the RF penalty as the difference between the minimum and maximum RF power, at low and high frequencies of the output of the corresponding RF signal, respectively, to a saturated and an unsaturated dynamic optical gain. The CPO_{3dB} bandwidth corresponds to the frequency for which the minimum value of the output RF signal increases by 3 dB.

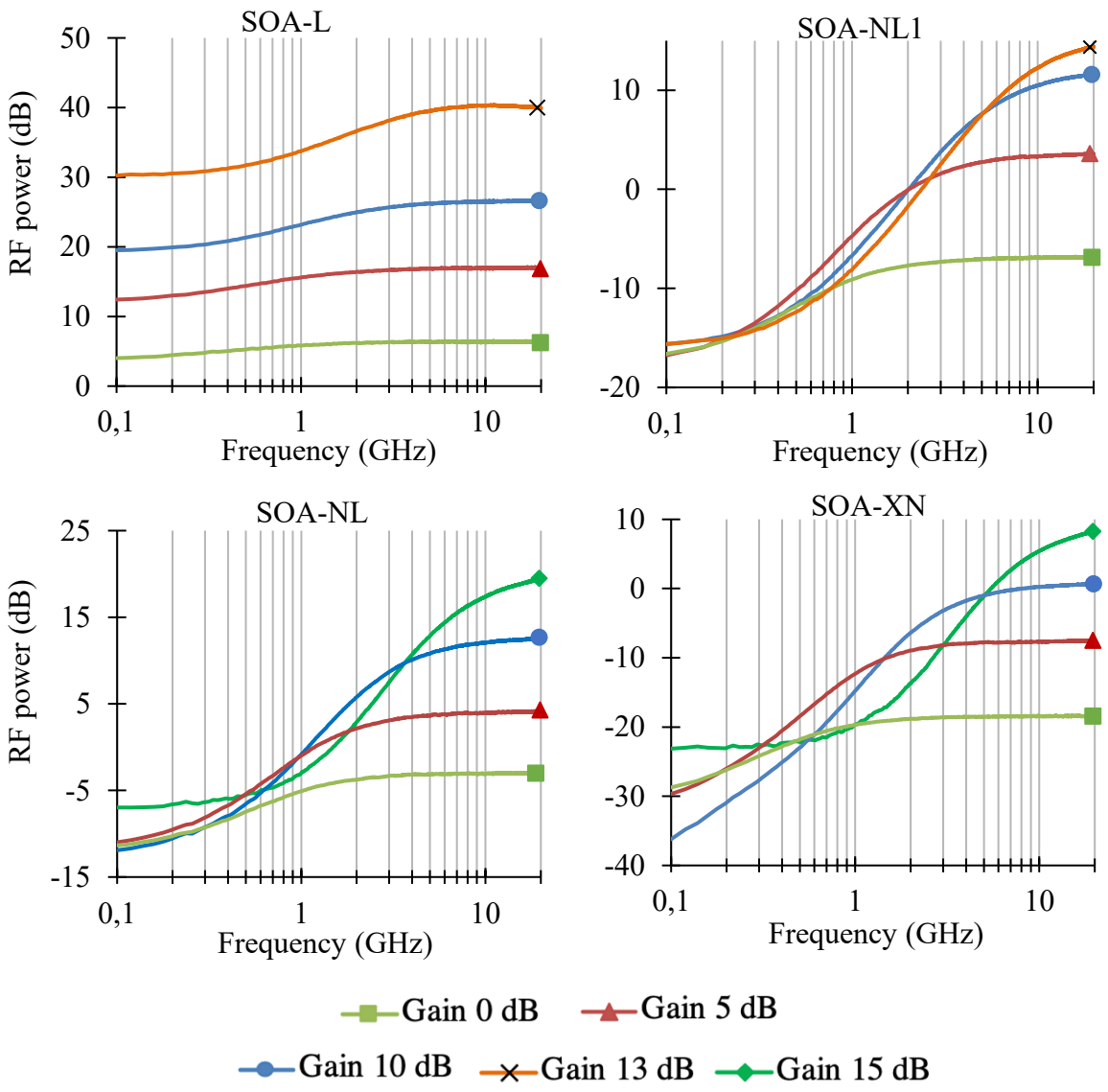

Figure 2.10 Measured RF power as function of the frequency for different optical gains.

The measured RF power has high pass filter characteristics resulting from the presence of CPOs, as explained via asymptotic behavior of the CPO responses in section 2.3.2.
At low microwave frequencies, the oscillations of the carrier density (CPO) are modulated by saturation due to the modulated optical intensity. This in turn induces gain variation that typically occurs at frequency lower than the inverse of carrier lifetime $\left(\frac{1}{2\pi\tau_d}\right)$, which is associated with a maximum microwave phase shift. Besides, at high microwave frequencies, the limited response time of the SOAs leads to smaller microwave phase shifts due to the finite carrier lifetime, as shown in Figure 2.11.

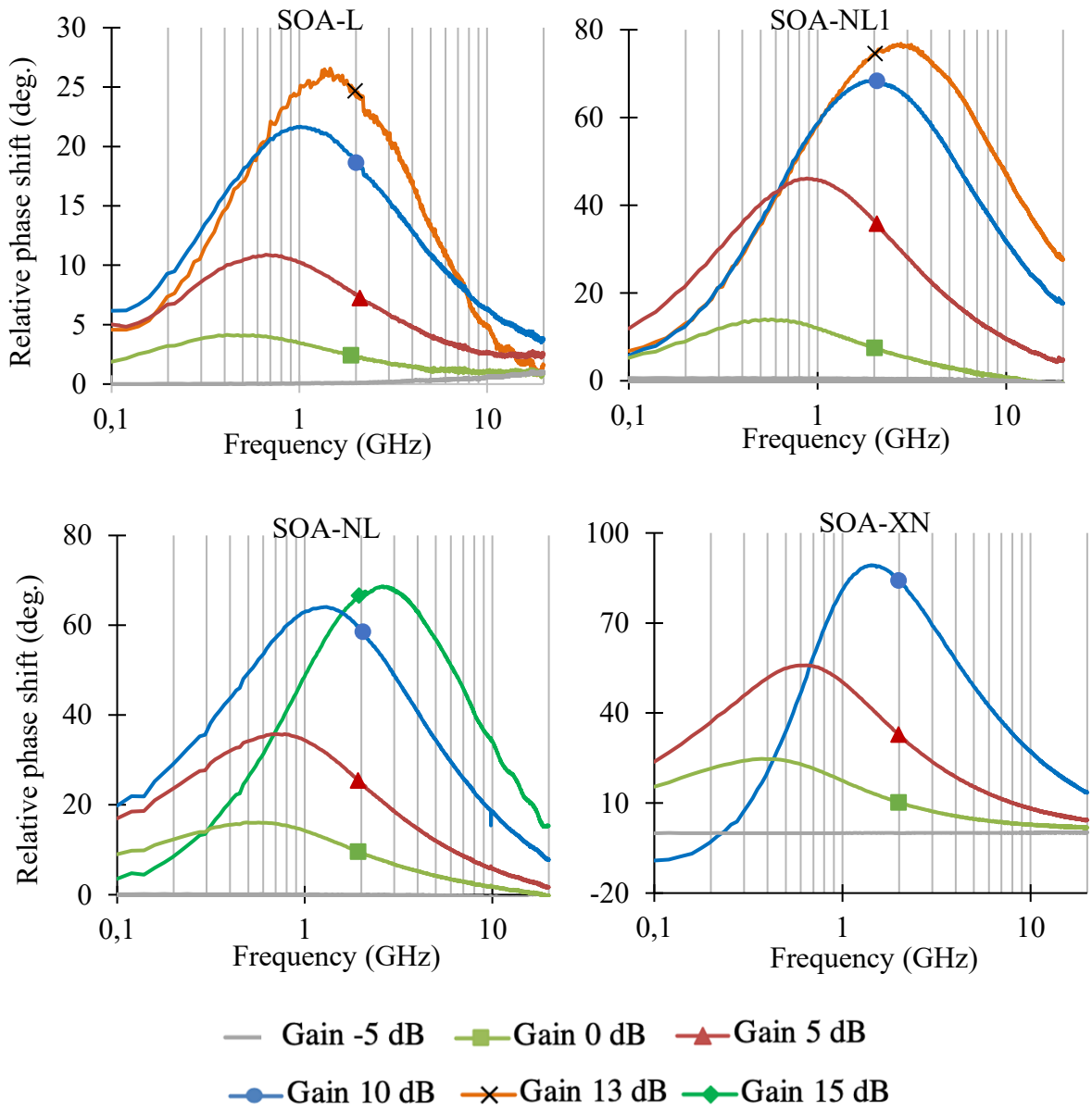

Figure 2.11 Measured relative phase shift as function of the frequency for different optical gains.

The maximum phase shift typically increases with, and can be controlled by, adjusting the optical gain (bias current and input optical power). SOA-L has a similar behavior to [13] [20] [21], where the maximum phase shift of 26° is obtained. Moreover, a tunable microwave relative phase shift as high as 89°, which is the maximum obtained phase shift to the best of our knowledge, is measured at an operating frequency of 1.5 GHz at the optical gain of 10 dB for SOA-XN.

Table 2.2 summarizes the comparison between the four SOAs for achieving maximum phase shift. It is obtained at the same static gain of 10 dB. SOA-L has the lower RF penalty of 7.1 dB and higher CPO bandwidth is about 780 MHz, but it has a lower maximum relative phase shift, compared to other SOAs. The maximum relative phase shift attains 89,3 (close to the maximum theoretical value) for the SOA-XN but is accompanied with an RF penalty of about 36,2 dB and a limited CPO bandwidth of 160 MHz. The larger the phase shift is, the larger the penalty over RF gain becomes.

Table 2.2 Maximum relative phase shifts, RF penalty and CPO bandwidth for the 4 SOAs at the gain 10 dB.

	Maximum relative phase shift	***Penalty (dB)***	***CPO_{3dB} (GHz)***
SOA-L	21.4°	7.1	0.78
SOA-NL1	68°	28.2	0.41
SOA-NL	63.7°	24	0.32
SOA-XN	89.3°	36.2	0.16

For the use of the CPO as a tunable delay line, we focus on the relative phase response and RF power for 4 SOAs at low frequencies. Figure 2.12 and Figure 2.13 present the measured RF power and relative phase shift over 0.5 GHz. We can see that a linear response of the phase shift over a small bandwidth occurs for 4 SOAs in Figure 2.12 and Figure 2.13 (a) and (c). Besides, at Gain 5 dB, SOA-L has an interesting RF power (Figure 2.12 (b)), which only deviates by 1.5 dB over 0.5 GHz, while for SOA-NL1, SOA-NL and SOA-XN RF power deviates by 6.5 dB, 6 dB and 11.5 dB, respectively. Thus, at low frequency, only the SOA-L can realize a tunable delay line, which satisfies both condition of constant RF power and linear phase shift over frequency lower than 0.4 GHz.

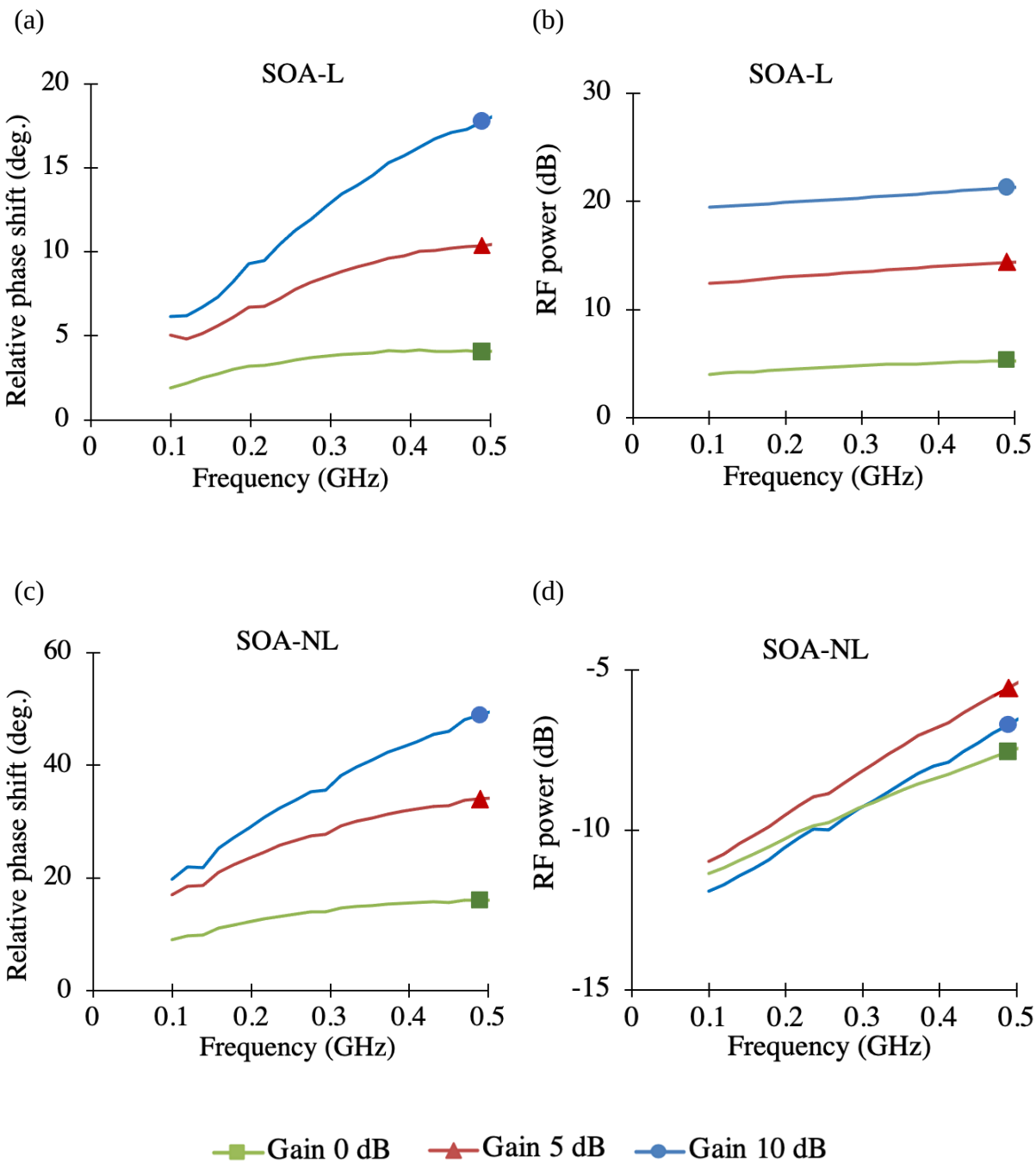

Figure 2.12 Measured relative phase shift as function of the frequency over 0.5 GHz for different optical gains, SOA-L (a), SOA-NL1 (c). Measured RF power as function of the frequency for different optical gains over 0.5 GHz, SOA-L (b), SOA-NL1 (d).

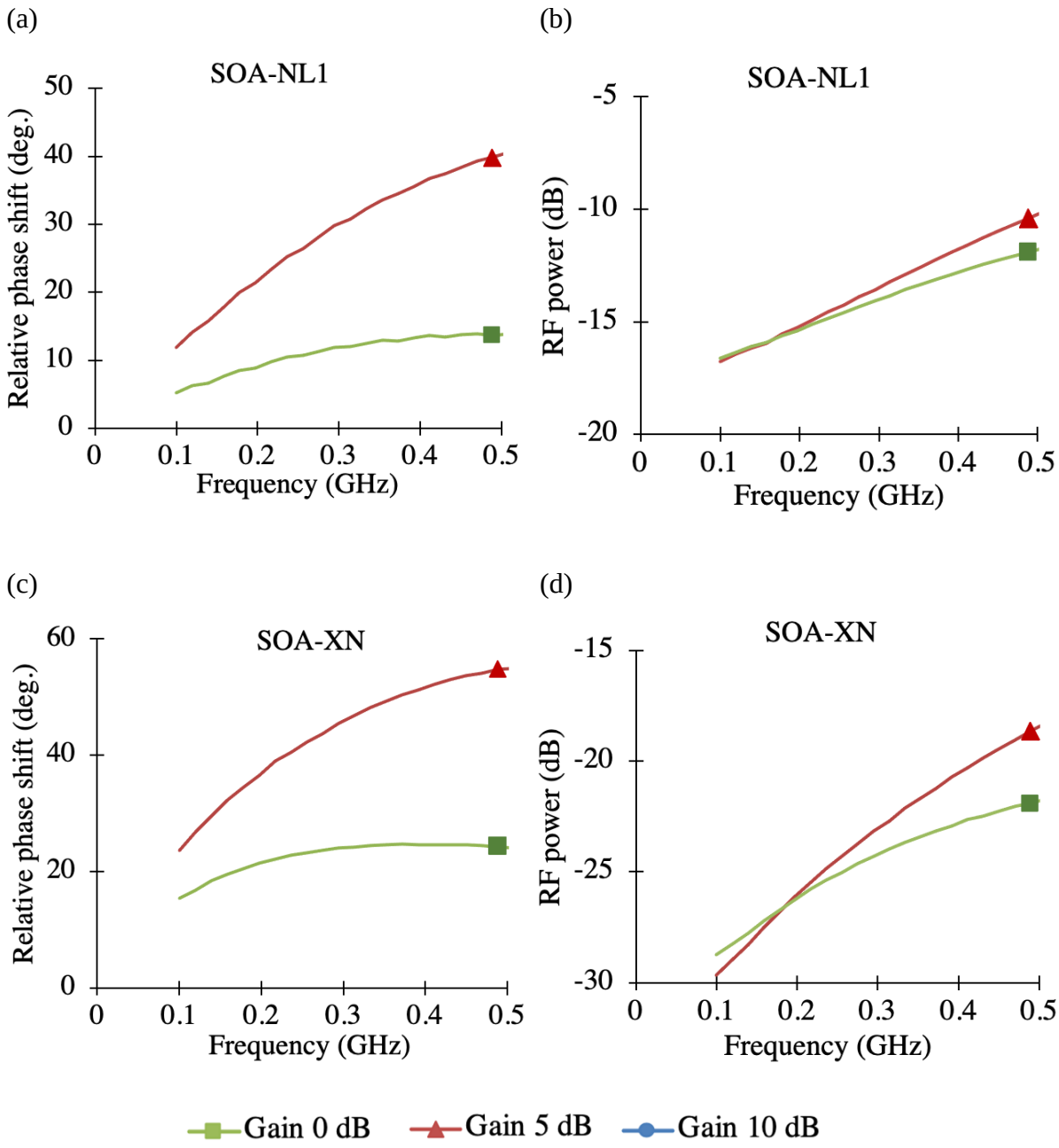

Figure 2.13 Measured relative phase shift as function of the frequency over 0.5 GHz for different optical gains, SOA-NL (a), and SOA-XN (c). Measured RF power as function of the frequency for different optical gains over 0.5 GHz, SOA-NL (b), SOA-XN (d).

2.3.3.3 Case of $R_\alpha < 0$ in SOA-XN

In Figure 2.14(a), we see that under certain conditions, the SOA-XN present a specific evolution of the phase shift below 1 GHz. It exhibits different behaviors, leading to a large range of phase values at 100 MHz, from 12° up to more than 150°.

A specific regime of phase variation is established for biasing currents of 180, 220, 325 and 350 mA. In addition, if the bias current is kept constant at 325 mA, this particular response occurs for optical input powers ranging from -5 to 3 dBm (Figure 2.14(b)). However, for input powers higher than 5 dBm and lower than -10 dBm, this specific response is not present. It should be noted that this phenomenon has been observed experimentally only with a SOA-XN.

(a)

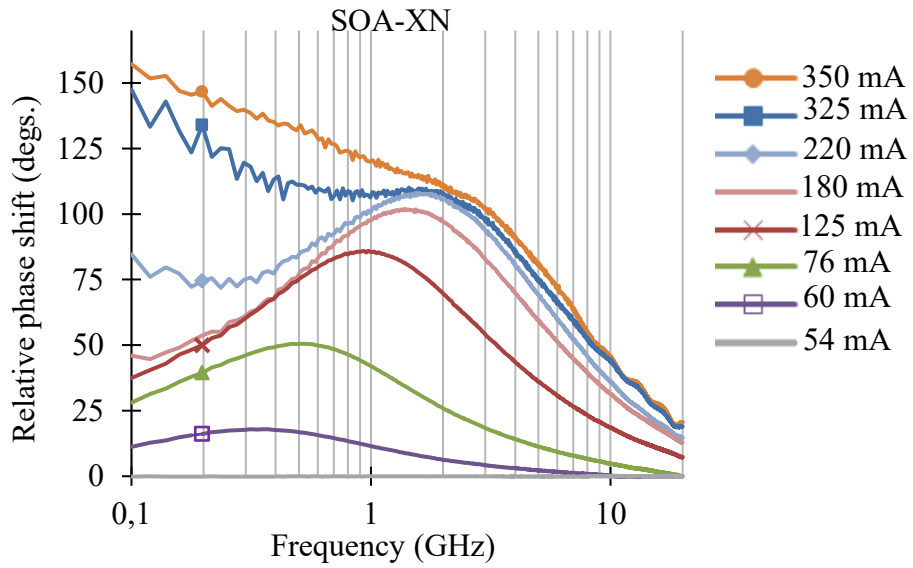

(b)

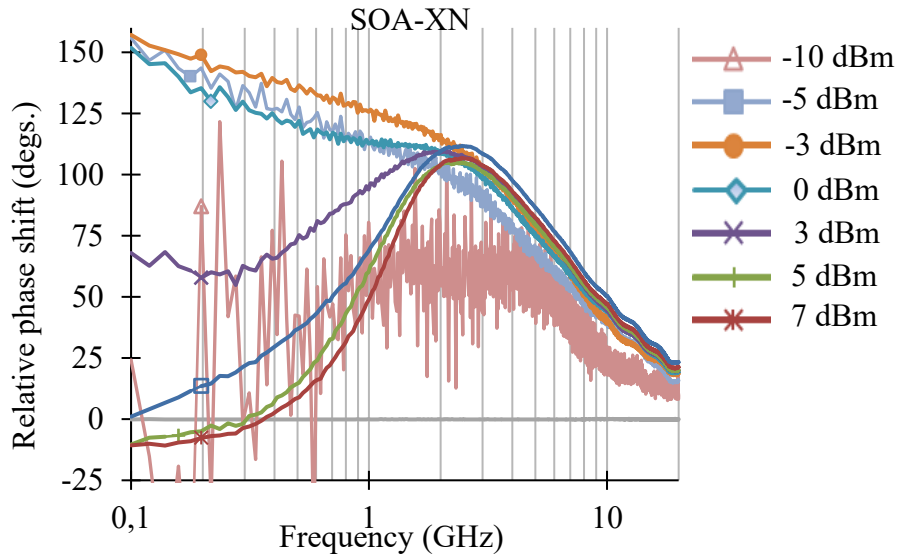

Figure 2.14 Measured phase shift as a function of both SOA-XN bias currents and frequency (f_{VNA}) with (a) fixed optical input power (0 dBm). (b) fixed bias current (325 mA).

This specific phase shift response, for the case $R_\alpha < 0$ compared to a usual CPO response ($R_\alpha > 0$) [20] [21] is possible as we show using small-signal analysis (2.33) for a range of optical input powers through K and the amplification parameters of the SOA through $\overline{G^x}$, $\overline{g_m^x}$ and $\overline{g_n^x}$. Thereby, the theoretical response of p_{out}^x through the reversal sign of R_α and the asymptotic responses of p_{out}^x for the case of negative R_α (Figure 2.8) allows us to explain the evolution of the phase shift of the experimental results.

2.4 Optically controlled of RF phase shift using Cross Gain Modulation

In the previous sections, we have established a set of equations associated with optical signals, all based on the knowledge of the carrier density in the calculus section. In this section, we focus on the possibility of achieving optical control of RF phase shifts in a SOA, based on the addition of the XGM of a CW signal at a SOA output. Moreover, the impact of the XGM response of the amplified spontaneous emission (ASE) on the relative phase shift is also presented. A small-signal analysis of ASE and optical CW control power is developed. A numerical calculation is used to analyze the controllable RF phase shift. The measurement results are presented for several control signal powers using SOA-L, which can perform at low frequency both tunable phase shifter and tunable delay line. For a simple approach, the SOA is also modeled from [10-14] and [19] [20] by considering one calculation section.

2.4.1 Small-signal analysis of ASE and optical control of RF phase shift

In order to investigate the role of CW and ASE signals at the output of the SOA, the setup presented in Figure 2.15 is employed. An intensity-modulated optical signal P_{in}^{sig} at the wavelength λ_{sig} is injected in addition to a CW optical control power $\overline{P_{in}^{CW}}$ at λ_{CW}, at the SOA input. In the proposed configuration, we detect P_{out} the sum of the powers of the output modulated signal P_{out}^{sig}, the control signal P_{out}^{CW} and the SOA ASE output P_{out}^{ASE}.

Figure 2.15 Scheme of the operating principle.

For a simplified approach, the SOA is modeled from [12] and [22] by considering one calculation section and one pseudo-mode at λ_{ASE} for the ASE output power P_{ASE}. We consider that $\overline{g_n^x} = \overline{g_m^x}$, and the losses are null.

The stimulated recombination rate due to photons of signal **sig** and **CW** can be given as:

$$R_{st} = \frac{1}{\Gamma L \tau}\left(\frac{P_{in}^{sig}\left(G^{sig}-1\right)}{a^{sig}P_{sat}^{sig}} + \frac{P_{in}^{CW}(G^{CW}-1)}{a^{CW}P_{sat}^{CW}}\right) \tag{2.37}$$

where G^x is the SOA gain at λ_x, and a^x is the peak-gain coefficient at the signal wavelength λ_x. Here ***x*** refers to **sig**, **CW** or **ASE** signal at the wavelength λ_x**.**

The signal amplification also depends on the amount of ASE generated by the amplifier. This is because ASE consumes the available carrier density and helps to saturate the gain. By considering the previous simplification, the stimulated recombination rate due to ASE (R_{ASE}) and the ASE power can be expressed from [12] as:

$$R_{ASE} = \frac{2}{wdL}\left(\frac{G^{ASE}-1}{g_n^{ASE}L} - 1\right) r_{sp}^{ASE} \tag{2.38}$$

$$P_{out}^{ASE} = 2W_p^{ASE}\frac{G^{ASE}-1}{g_n^{ASE}} r_{sp}^{ASE} \tag{2.39}$$

$$r_{sp}^{ASE} = \frac{2\Gamma c_0 \Delta\lambda}{{\lambda_{ASE}}^2} g_m'^{ASE} \tag{2.40}$$

where $\Delta\lambda$ is the optical bandwidth of the considered ASE pseudo-mode, $g_m'^{ASE}$ is the material gain coefficient leading to guided spontaneous emission, and W_p^{ASE} is the photo energy at λ_{ASE} and c_0 stands for the speed of the light. By considering $g_m'^{ASE} = a'^{ASE}(N - N_0)$ and by introducing (2.40) into (2.38) and (2.39), R_{ASE} and P_{out}^{ASE} can be written for $G^{ASE} \gg 1$ as:

$$R_{ASE} = \frac{P_{out}^{ASE}}{\Gamma a^{ASE} L \tau P_{sat}^{ASE}} \tag{2.41}$$

$$P_{out}^{ASE} = W_p^{ASE}\frac{4c_0\Delta\lambda}{\lambda_{ASE}^2}\frac{a'^{ASE}}{a^{ASE}} G^{ASE} \tag{2.42}$$

The amplitude of the carrier density modulation *n* as a function of the optical input power P_{in}^{sig} can be derived from the rate equation (2.11). It can be expressed by:

$$n = -\frac{1}{\Gamma a^{sig} L(1+K_T)P_{sat}^{sig}}\frac{G^{sig}-1}{1+j\omega\tau_d} p_{in}^{sig} \tag{2.43}$$

where

$$K_T = \frac{P_{out}^{ASE}}{P_{sat}^{ASE}} + \frac{\overline{P_{in}^{sig}}\,\overline{G^{sig}}}{P_{sat}^{sig}} + \frac{\overline{P_{in}^{CW}}\,\overline{G^{CW}}}{P_{sat}^{CW}} \tag{2.44}$$

τ_d is the dynamic carrier lifetime, can be expressed as:

$$\frac{1}{\tau_d} = \frac{1 + K_T}{\tau} \tag{2.45}$$

At the SOA's output, the three output signals, $P_{out}^{sig} = P_{in}^{sig} G^{sig}$, P_{out}^{ASE} and $P_{out}^{CW} = \overline{P_{in}^{CW}} G^{CW}$ contain a modulation term at the angular frequency ω due to the modulation of the carrier density N.

The signal power at the angular frequency (ω) p_{out}^{sig}, represent the usual CPO response. It is given by (2.31) as $p_{out}^{sig} = p_{in}^{sig}\overline{G^{sig}} + p_{in,SGM}$, where x is replaced by sig.

Moreover, P_{out}^{ASE} and P_{out}^{CW} are modulated due to the XGM mechanism leading to a modulated power at the angular frequency ω respectively given by:

$$p_{out}^{ASE} = n\Gamma L a^{ASE}\overline{P_{in}^{ASE}} G^{ASE} \tag{2.46}$$

$$p_{out}^{CW} = n\Gamma L a^{CW}\overline{P_{in}^{CW}} G^{CW} \tag{2.47}$$

The term of p_{out} at the angular frequency ω is given by:

$$p_{out} = p_{out}^{sig} + p_{out}^{\mathrm{ASE}} + p_{out}^{CW} \tag{2.48}$$

By using phasor diagram, we can illustrate that the RF signal phase shift is influenced by the ASE and can be controlled by $\overline{P_{in}^{CW}}$. In fact, Figure 2.16(a) shows that a phase shift ϕ_{sig} of p_{out}^{sig} exists due to the SGM term $p_{sig,SGM}$ (2.32) compared to the phase of the amplification term $p_{in}^{sig}\overline{G^{sig}}$.

After adding the ASE term p_{out}^{ASE} to p_{out}^{sig}. $p_{sig,SGM}$ (2.32) and p_{out}^{ASE} (2.46) are in phase, yields to an increase in the phase shift to $\phi_{\mathrm{sig+ASE}}$ as shown in Figure 2.16(b). Now, if an external control

power $\overline{P_{in}^{CW}}$ is injected, it contributes as the ASE power to increase the RF phase shift to $\phi_{\text{sig+ASE+CW}}$ as shown in Figure 2.16(c).

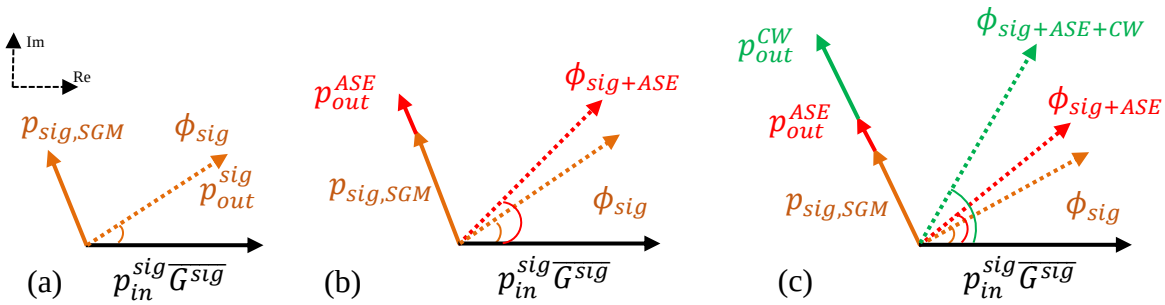

Figure 2.16 Phasor diagram illustration of the phase in polar form with: (a) p_{out}^{sig}, (b) $p_{out}^{sig}+p_{out}^{ASE}$, and (c) $p_{out}^{sig}+p_{out}^{ASE}+p_{out}^{CW}$. (Component signals: solid vectors, resultant: dotted vector).

2.4.2 Numerical calculation of RF phase shift

By substituting the carrier density modulation (2.43) into (2.31), (2.46), and (2.47), p_{out} become:

$$p_{out} = p_{in}^{sig}\overline{G^{sig}}\left(\frac{1+K_1(1+K_2)}{1+K_1(1+K_2)G^{sig}}\right)\frac{\left(1+j\omega\dfrac{\tau}{1+K_1(1+K_2)}\right)}{\left(1+j\omega\dfrac{\tau}{1+K_1(1+K_2)G^{sig}}\right)}$$

$$= \frac{p_{in}^{sig}\overline{G^{sig}}}{\rho}\frac{\left(1+j\dfrac{\omega}{\omega_1}\right)}{\left(1+j\dfrac{\omega}{\omega_2}\right)} \tag{2.49}$$

with:

$$\omega_1 = \frac{1+K_1(1+K_2)}{\tau} \tag{2.50}$$

$$\omega_2 = \frac{1+K_1\overline{G^{sig}}(1+K_2)}{\tau} \tag{2.51}$$

$$K_1 = \frac{\overline{P_{in}^{sig}}}{P_{sat}^{sig}} \tag{2.52}$$

$$K_2 = \frac{\frac{W_p^{ASE} P_{out}^{ASE}}{W_p^{sig} P_{sat}^{ASE}} + \frac{E_{CW}\,\overline{P_{in}^{CW}}\,\overline{G^{CW}}}{W_p^{sig} P_{sat}^{CW}}}{K_1 \overline{G^{sig}}} \tag{2.53}$$

$$\rho = \frac{\omega_2}{\omega_1} \tag{2.54}$$

The equation (2.49) shows that the frequency responses of the RF amplitude and the phase shift of p_{out} are related to ω_1 and ω_2 that are governed in turn by the carrier lifetime τ, P_{ASE}, the incident optical powers and their related gain and P_{sat}. We defined ρ (2.54) as the RF penalty on the amplitude p_{out} due to the optical gain saturation that occurs at low frequencies. From (2.49) $p_{out,\omega\to 0} = \frac{p_{in}^{sig}\overline{G^{sig}}}{\rho}$, this saturation disappears at high frequencies where $p_{out,\omega\to\infty} = p_{in}^{sig}\overline{G^{sig}}$ [2].

In the case that we consider that ASE is negligible and without the presence of $\overline{P_{in}^{CW}}$, K_2 is equal to zero in (2.49). We can then find that the RF small-signal modulation component at the output of the SOA is equal to (2.36), which refers to the usual CPO response. Moreover, the transfer function of (2.49) has the same transfer function of (2.33) for the case when R_α is positive, but the difference is the cut-off frequencies. From equation (2.49) and for $\omega_1 < \omega < \omega_2$, we can derive that we have a maximum phase shift ϕ_{max} at:

$$f_{max} = \frac{\omega_{max}}{2\pi} = \frac{\sqrt{\omega_1\,\omega_2}}{2\pi} \tag{2.55}$$

where the maximum achievable phase shift $\phi_{\max}$ of p_{out} can be given by:

$$\phi_{max} = 2atan\left(\sqrt{\frac{1 + K_{T12}\overline{G^{sig}}}{1 + K_{T12}}}\right) - \frac{\pi}{2} \tag{2.56}$$

with $K_{T12} = K_1(1 + K_2)$.

The equation (2.56) shows that for high enough $\overline{G^{sig}}$, the theoretical maximum phase shift of 90° can be asymptotically reached. Besides, the control of ϕ_{max} by $\overline{P_{in}^{CW}}$ is dependent on the ratio between $\overline{P_{in}^{sig}}$ and $\overline{P_{in}^{CW}}$ through the factor K_2, where the control of ϕ_{max} is effective if $\frac{W_p^{CW}\,\overline{P_{in}^{CW}}\,\overline{G^{CW}}}{W_p^{sig} P_{sat}^{CW}} > \frac{\overline{P_{in}^{sig}}\,\overline{G^{sig}}}{P_{sat}^{sig}}$. This condition will be the same for the penalty ρ.

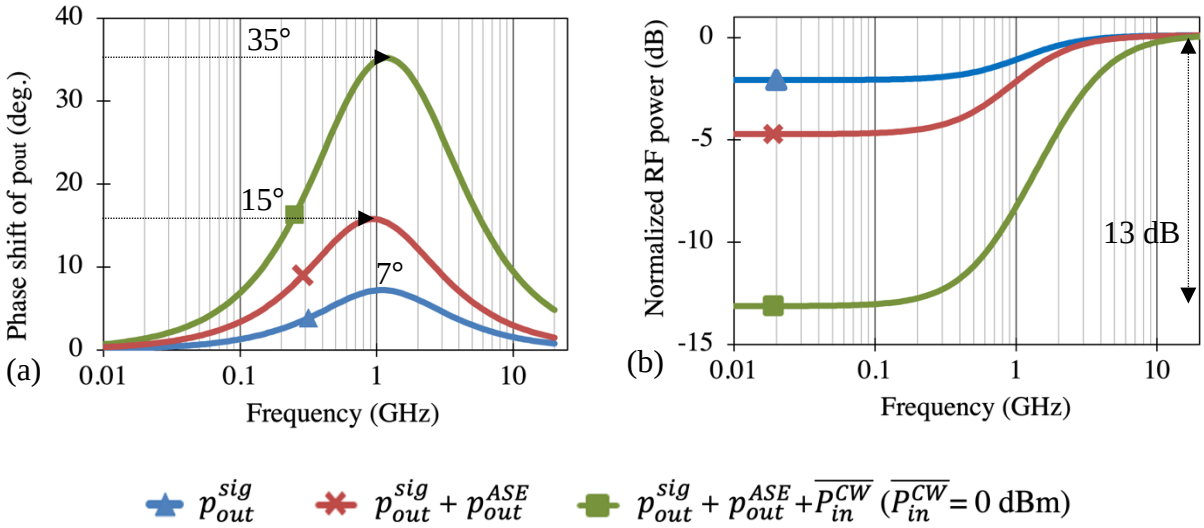

Figure 2.17 (a) Theoretical phase shift and (b) Normalized RF power of p_{out} as function of the frequency for $\overline{P_{in}^{sig}}$ = -15 dBm and $\overline{P_{in}^{CW}}$ = 0 dBm in presence of the ASE.

For a SOA with a gain of 20 dB, the calculation of the phase and the RF power of p_{out} (2.49) for $\overline{P_{in}^{sig}}$ = -15 dBm has been performed for three scenarios (Figure 2.17). The operating point has been obtained from the ADS model (presented in section 2.1.6). In each case the operating point has been obtained by solving the rate equation (2.11) in static regime, by using 1 calculation section for the SOA presented in [12]. In absence of $\overline{P_{in}^{ASE}}$ and $\overline{P_{in}^{CW}}$, case (i), the Figure 2.17(a) shows that the maximum phase shift is about 7° around the frequency f_{max} = 1.15 GHz. This phase shift is accompanied by a penalty ρ of 2.1 dB on the RF power (Figure 2.17(b)). By adding $\overline{P_{out}^{ASE}}$ to P_{out}^{sig} and in absence of $\overline{P_{in}^{CW}}$, case (ii), the phase shift at f_{max} clearly increases from 7° to 15° and is accompanied by an increase of 2.8 dB on ρ.

Finally, in presence of $\overline{P_{out}^{ASE}}$ and in presence of an external control power $\overline{P_{in}^{CW}}$ of about 0 dBm, the case (iii) shows a large improvement in the phase shift at f_{max} from 7° to 35° with a higher penalty of 13 dB, as shown in Figure 2.17(b). We can notice that the more variation we have between $p_{out,f_x \to 0}$ to $p_{out,f_x \to \infty}$ (Figure 2.17(a)), the more the phase shift is high.

The calculation of the maximum phase p_{out} (2.56) versus $\overline{P_{in}^{sig}}$ and for different $\overline{P_{in}^{CW}}$ (-20, -15, -10, -5 , and 0 dBm) has been performed (see Figure 2.18(b)), after resolving the rate equation in static state by using one calculation section for SOA presented in [12].

By increasing $\overline{P_{in}^{CW}}$, $\phi_{\max}$ increases before later decreasing at high values of $\overline{P_{in}^{CW}}$ due to gain saturation. When $\overline{G^{sig}} > 1$, the term ρ becomes equal to $\overline{G_{sig}}$ for high values of $\overline{P_{in}^{CW}}$, this refers to the case of $K_2 >> 1$.

Figure 2.18(b) shows clearly that $\phi_{\max}$ increases for $\overline{P_{in}^{CW}} > \overline{P_{in}^{sig}}$, but at high values of $\overline{P_{in}^{CW}}$ (= 0 dBm) the enhancement of ϕ_{max} will be reduced due to gain saturation. The increase of the power $\overline{P_{in}^{sig}}$ contributes to the reduction of K_2 (Figure 2.18(a)) then, at high saturation of $\overline{G^{sig}}$, ϕ_{max} decreases (Figure 2.18(b)).

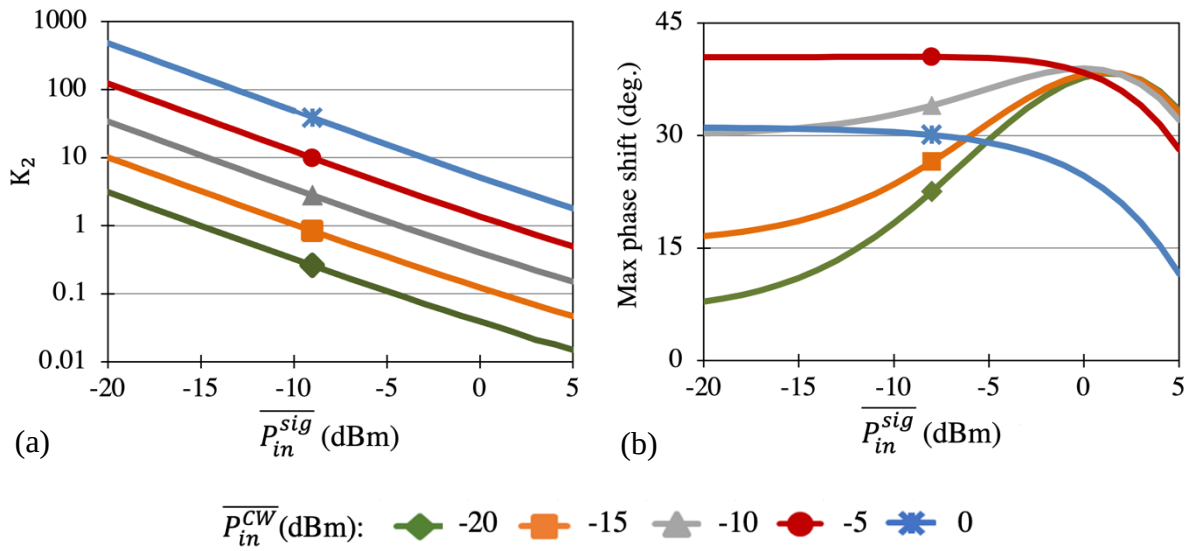

Figure 2.18 (a) Factor K_2. (b) ϕ_{max} of p_{out} as function of $\overline{P_{in}^{sig}}$ for several $\overline{P_{in}^{CW}}$ without ASE.

2.4.3 Experimental realization and results of the controllable RF phase shifts in SOA

The SOA used in this work is a commercially available device from InPhenix (IPSAD1502), referred to by SOA-L. It typically has an optical gain of 21 dB and an output saturation power of up to 11 dBm, the static characteristics are shown in Figure 2.5.

In order to experimentally investigate the role of CW signal injected into the SOA, the set-up shown in Figure 2.19 is utilized where SOA-L is used. Two optical signals are injected into the SOA. A first signal, $\overline{P_{in}^{sig}}$ is generated from a laser source emitting at λ_{sig} = 1527 nm close to the peak of the SOA optical gain and modulated by an external Mach-Zehnder modulator (MZM). The MZM is driven by a continuous variable RF signal, swept from f_{VNA} = 0.01 GHz to f_{VNA} = 20 GHz, from a Vector Network Analyzer (VNA). For the second signal, a laser source emitting at λ_{CW} = 1532 nm generates the optical control power $\overline{P_{in}^{CW}}$.

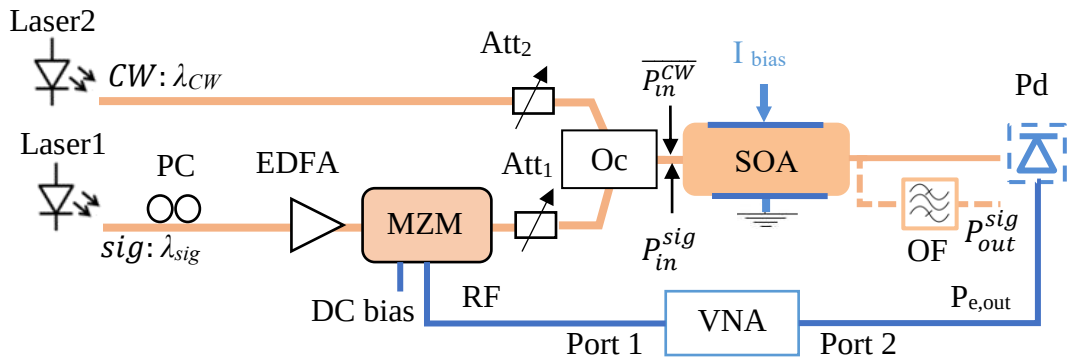

Figure 2.19 Experimental setup to measure the microwave phase shifts induced by CPO effects in a SOA and by adding XGM response of an optical signal. PC: Polarization controller, Att: attenuator, OF: optical filter at λsig, Pd: photodetector, I: Bias current, EDFA: Erbium-doped fiber amplifier. Oc: optical coupler.

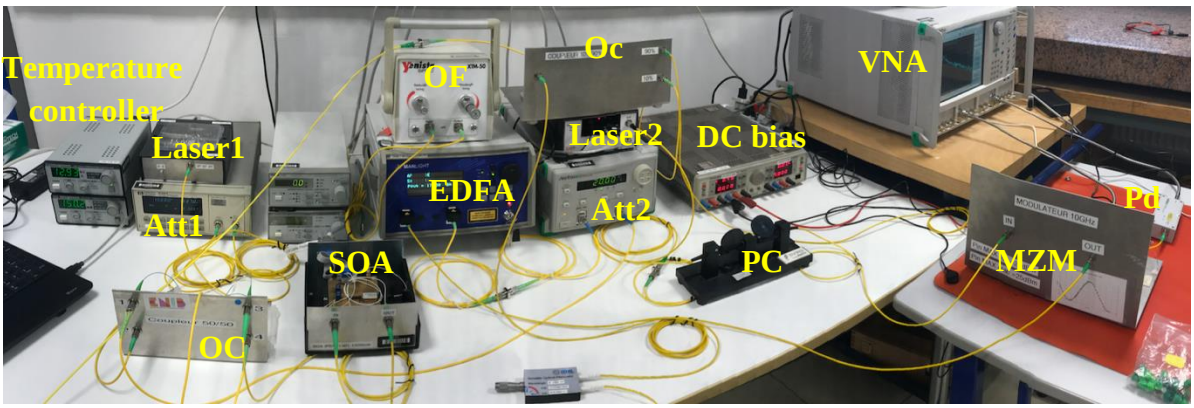

Figure 2.20 Experimental set-up.

The wavelength difference between λ_{CW} and λ_{sig} is sufficient to cancel the four-wave mixing effect due to mutual beating between the two laser sources. The optical power of $\overline{P_{in}^{sig}}$ and $\overline{P_{in}^{CW}}$ are respectively adjusted by the optical attenuators Att_1 and Att_2. It should be noted that the SOA's optical gain for $\overline{P_{in}^{sig}}$ and $\overline{P_{in}^{CW}}$ is close to 21 dB for low input powers and for the SOA's bias current of 250 mA. At the output of the SOA, the optical path in continuous line is used to detect the total power. To only measure the response of P_{out}^{sig}, an optical filter with an optical bandwidth of about 0.5 nm is set at λ_{sig} to block the ASE power. After detection by Pd, the phase shift of the microwave signal $P_{e,out}$ is measured by the VNA.

Actually, in measurement, phase shifts are evaluated relative to a reference signal corresponding to the SOA fed at the minimum current of 60 mA, referred to gain 0 dB, and the phases are then measured for the SOA fed at 250 mA, referred to gain 20 dB.

Figure 2.20 shows the devices used in the experimental set-up. Figure 2.21(a) shows that the experimentally measured relative phase shift at f_{max} of p_{out} is almost 8°, with a penalty of 1.8 dB (Figure 2.21(b)), corresponding to a weak power $\overline{P_{in}^{sig}}$ (−15 dBm). Now, by removing the optical filter and in absence of $\overline{P_{in}^{CW}}$, we measure the response of $p_{sig,out} + p_{ASE}$. This case which refers to Figure 2.16(b), shows that the presence of the ASE power increases the phase shift at f_{max} by 8°, with a penalty of 3.9 dB (Figure 2.21(b)).

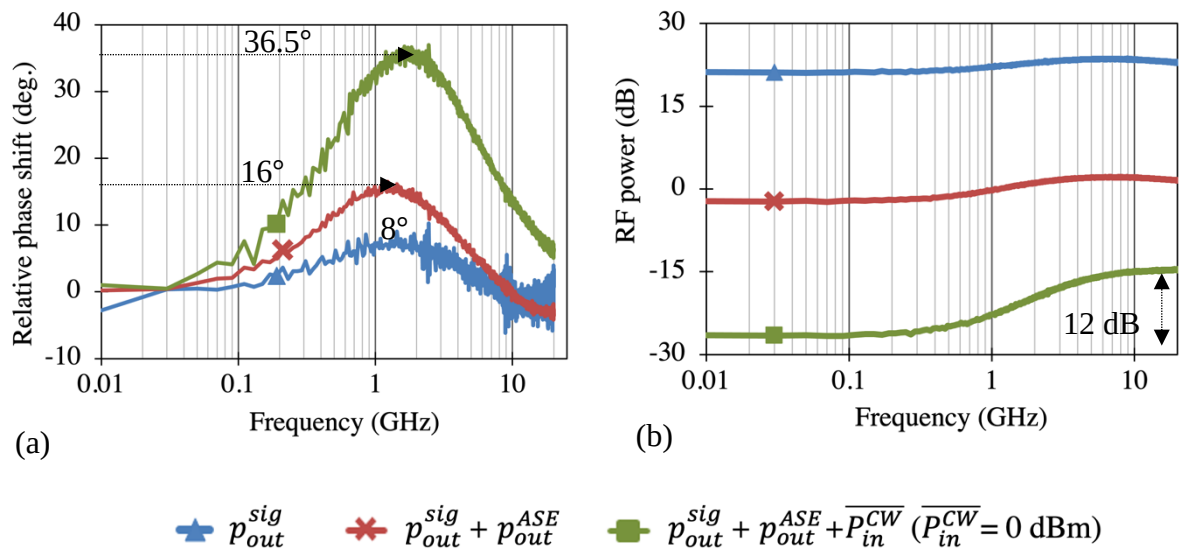

Figure 2.21 (a) Measured relative maximum phase shift, and (b) measured RF power of $P_{e,out}$ as a function of frequency. $\overline{P_{in}^{sig}}$ is fixed at -15 dBm.

After adding $\overline{P_{in}^{CW}}$ at the SOA input, we measure the responses of $p_{out} = p_{out}^{sig} + p_{out}^{ASE} + p_{out}^{CW}$, which refers to the phasor diagram in Figure 2.16(c). Due to a strong $\overline{P_{in}^{CW}}$ (0 dBm), an improvement in the phase shift at f_{max} by 28.5° is obtained compared to only 8° with $\overline{P_{in}^{sig}}$. It is accompanied by a penalty of 12 dB on the gain (Figure 2.21(b)). These results are in accordance with the small-signal calculation in Figure 2.17 and with equation (2.56).

The measured relative phase shift and RF power of SOA-L for different injection powers of $\overline{P_{in}^{CW}}$(−10, and 0 dBm) and with a fixed $\overline{P_{in}^{sig}}$ at low power −20 dBm and at high power 0 dBm are presented in Figure 2.22. We can clearly see the evolution of the relative phase shift by injecting different $\overline{P_{in}^{CW}}$ = −10, and 0 dBm for fixed $\overline{P_{in}^{sig}}$ = −20 dBm, compared to $\overline{P_{out}^{sig}}$ (see Figure 2.22(a)). The evaluation of the relative phase shift is accompanied by a depth in RF

power response at low frequency as seen in Figure 2.22(b). We can notice that at low frequency (up to 0.5 GHz), the injection of CW enables the control of CPO phase shift, leading to control of the delay lines. In contrary, at high fixed input optical power, $\overline{P_{in}^{sig}}$ = 0 dBm (Figure 2.22(c)), the evolution of phase shift is almost the same for $\overline{P_{in}^{CW}}$ = -10 and 0 dBm, due to gain saturation. The maximum phase shift of $p_{out} = p_{out}^{sig} + p_{out}^{ASE} + p_{out}^{CW}$ 0 dBm is 32°, compared to p_{out}^{sig} is 29°. We notice that it is less suitable to control the phase shift using CW for the case of high fixed input optical power.

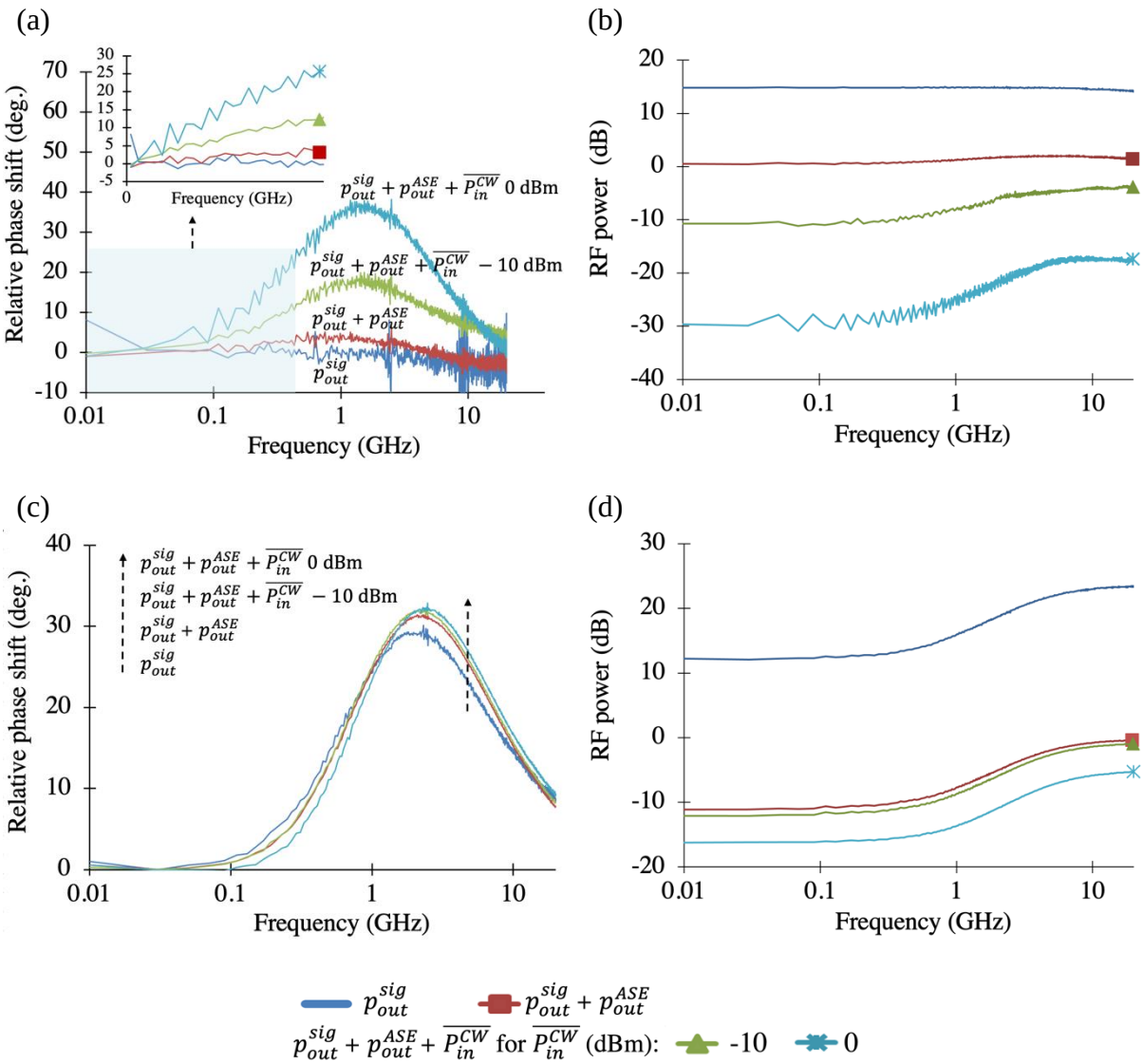

Figure 2.22 (a) Measured relative maximum phase shift, and (b) measured RF power of $P_{e,out}$ as a function of frequency for $\overline{P_{in}^{sig}}$ = -20 dBm. (c) Measured relative maximum phase shift, and (d) measured RF power of $P_{e,out}$ as a function of frequency for $\overline{P_{in}^{sig}}$ = 0 dBm.

The measured maximum relative phase shift and RF penalty for different scenario of injection powers of $\overline{P_{in}^{sig}}$ and $\overline{P_{in}^{CW}}$ are registered in Figure 2.23.At high injection powers of $\overline{P_{in}^{sig}}$(about 0 to 5 dBm) and without injection of a CW power, Figure 2.23(a) shows that the difference in relative maximum phase shift at f_{max} and the penalty remain quasi constant regardless of whether the ASE is filtered or not. This is due to the absence of ASE at high $\overline{P_{in}^{sig}}$, this case refers to $K_2 < 1$ in (2.53). Considering the case $\overline{P_{in}^{CW}} > \overline{P_{in}^{sig}}$ is injected, the relative maximum phase shift at f_{max} varies from 5° to up to 45°. The improvement in relative maximum phase shift is accompanied by a higher RF penalty as shown in Figure 2.23(b).By increasing $\overline{P_{in}^{sig}}$, K_2 is reduced, thus the relative phase shift and penalty becomes equivalent to the response of the signal $\overline{P_{in}^{sig}}$ (at 5 dBm) in presence of ASE (see Figure 2.23(a-b)).

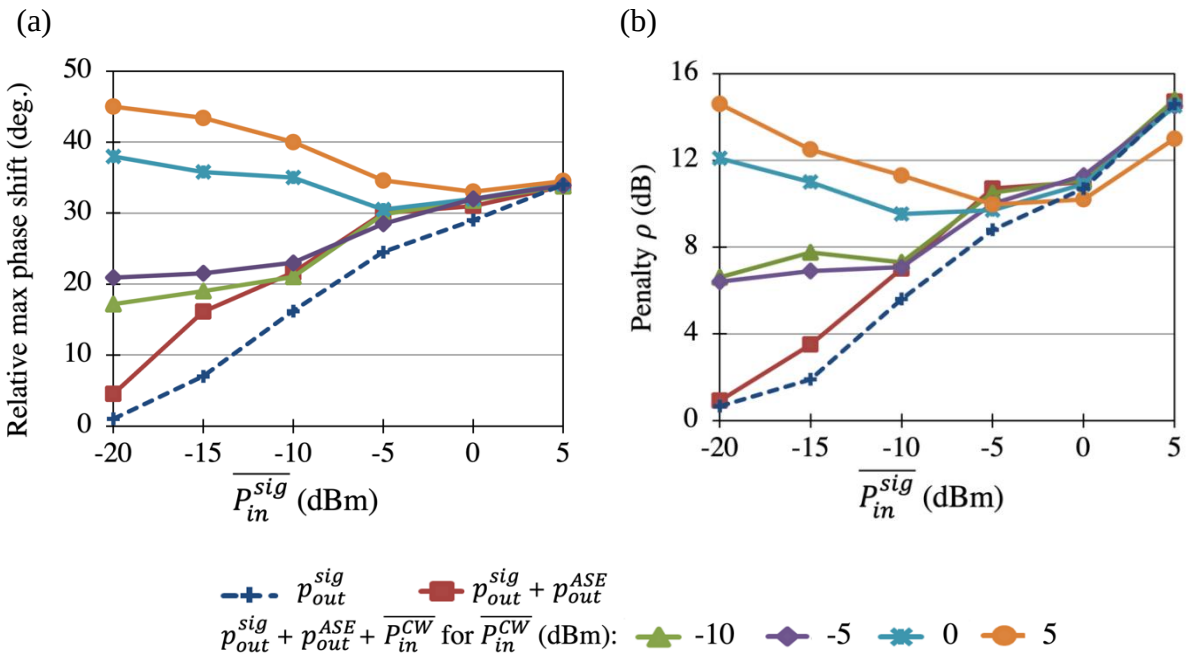

Figure 2.23 (a) Measured maximum relative phase shift at f_{max} of p_{out}, and (b) RF penalty ρ of p_{out}: p_{out}^{sig} only, p_{out}^{sig} with presence of ASE and with injection of several $\overline{P_{in}^{CW}}$(-10, -5, 0 and 5 dBm).

2.5 Up-converted CPO in different structures of SOAs

As we show previously, the CPO techniques is performed in baseband frequency domain up to 1 GHz due to the SOA carrier lifetime. However, it has been demonstrated that the integrated delay generator based on Up-converted CPO in a SOA, noted by Up-CPO, eliminates the issue of the intrinsic limitation of the carrier lifetime, leading to the generation of a time delay on signals of up to THz depending on the SOA optical bandwidth [13] [14]. In this section, we present theoretical and experimental results of Up-converted CPO, which is the first stage of a

TTD hybrid structure. We describe the principle of Up-CPO and we derive a small-signal analysis of Up-CPO optical power in function of the mean carrier density in SOA. We present the issue that has not been previously addressed in the literature regarding Up-CPO in nonlinear SOAs, namely the role of high-orders of carrier density modulation. We develop a small-signal analysis in a pump-probe configuration. The evaluation of the dynamic carrier lifetime is done by a static calculation as a function of the injected optical powers, using small-signal expressions. A comparison between theoretical and experimental data concerning the amplitude and phase shift of microwave signals is presented both in pump-probe and Up-CPO configurations, for three different types of SOAs (SOA-L, SOA-NL and SOA-XN), which is done for the first time.

2.5.1 Principle of Up-converted CPO

We recall the principles of Up-converted CPO (also noted Up-CPO), which has been described in section 1.2.2.5. A schematic describing the Up-CPO principle is shown in Figure 2.24. A first optical signal P_{in}^{c} at the wavelength λ_c is modulated at a high frequency f_c, with $f_c >> 1/(2\pi\tau_d)$ where τ_d is the dynamic carrier lifetime. Thus, the carrier density in the active region and the SOA optical gain are not affected by the modulation part at the high frequency f_c of this signal. Meanwhile, the second optical signal P_{in}^{d} at the wavelength λ_d is modulated at a low frequency f_d with $f_d << 1/(2\pi\tau_d)$. Therefore, the carrier density oscillations at f_d lead to a dynamic variation of the optical gain. Thus, through XGM, the high frequency modulated signal P_{in}^{c} is modulated by P_{in}^{d}, giving rise to signals at high frequencies $f = f_c \pm f_d$. In other words, the data signal at f_d is Up-converted around the high frequency of the carrier, at $f_c \pm f_d$. After photodetection, the RF output signal provides information on the phase shift that can be tuned through the operating condition of the SOA [14].

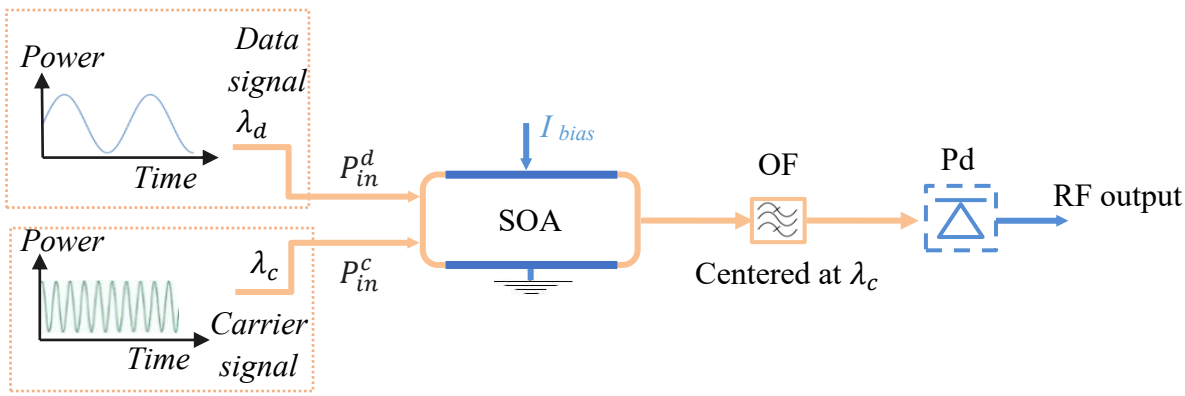

Figure 2.24 Principle of Up-CPO, OF: Optical filter, Pd: Photodiode.

2.5.2 Small-signal analysis of Up-converted CPO

The model used for small-signal analysis is based on a carrier density rate equation and a set of travelling-wave equations describing the amplified signal fields, which have been initiated in section 2.3.1. We develop first the Up-CPO optical power response as a function of the SOA carrier density variation. The calculation is performed by dividing the SOA into 2 sections to better consider the SOA gain saturation. Therefore, we develop the carrier density modulation in the first section followed by carrier density modulation in the second section Then, we show that the frequency responses of the carrier density can be extracted from the experimental results obtained in a pump-probe configuration in order to access to the Up-CPO frequency responses.

2.5.2.1 Up-converted CPO optical power response as a function of the SOA mean carrier density

We consider that the optical gains at λ_c and λ_d are equal to $\bar{G}$. At the SOA output, the optical field at the wavelength λ_c, can be obtained from (2.19) as:

$$E_{out}^{c} = E_{in}^{c}\sqrt{G}e^{j\Delta\varphi} \tag{2.57}$$

here **x** in (2.19) refers to carrier '**c**' or data '**d**' at wavelength λ_x. $\Delta\varphi$ is the difference of phase due to the propagation along the SOA.

Inside the SOA, the oscillation of the carrier density along the SOA length is induced by the two input signals P_{in}^{c} and P_{in}^{d} at the angular frequencies ω_c and ω_d respectively. By considering a first-order approximation, the beating terms at $\omega_{c\pm d} = \omega_c \pm \omega_d$ can be neglected.

By dividing the SOA in M sections along its length, we can define a mean carrier density N_e which is the mean value of the carrier densities in the M sections as

$$N_e = \sum_{i=1}^{M} \frac{N_i}{M} \tag{2.58}$$

where N_i is the carrier density in section i.

Therefore, the expression of the mean carrier density $N_e(t)$ in (2.20) is written as:

$$N_e = \overline{N_e} + \frac{n_{e,\omega_d}}{2}e^{j\omega_d t} + \frac{n_{e,\omega_d}^{*}}{2}e^{-j\omega_d t} + \frac{n_{e,\omega_c}}{2}e^{j\omega_c t} + \frac{n_{e,\omega_c}^{*}}{2}e^{-j\omega_c t} \tag{2.59}$$

$\overline{N_e}$ represents the static operating point and n_{e,ω_x} is the complex amplitude of the mean carrier density modulation at ω_x. Due to the cross-gain modulation, the SOA gain $G(t)$ at λ_c is

modulated at the same pulsations as the carrier density around the static operating point $\bar{G}$. $\sqrt{G}$ can be written, by using a first-order Taylor expansion, as:

$$\sqrt{G} \sim \sqrt{\bar{G}}\left(1+\frac{\frac{\partial G}{\partial N_e}}{2\bar{G}}\left(\frac{n_{e,\omega_d}}{2}e^{j\omega_d t}+\frac{n^*_{e,\omega_d}}{2}e^{-j\omega_d t}+\frac{n_{e,\omega_c}}{2}e^{j\omega_c t}+\frac{n^*_{e,\omega_c}}{2}e^{-j\omega_c t}\right)\right) \tag{2.60}$$

Therefore, at λ_c, the complex amplitude terms of the Up-CPO signal output power at the pulsations ω_{c+d} and ω_{c-d} can be obtained by the quadratic detection that were calculated in (2.19), (2.57) and (2.60) as:

$$p^c_{out,\omega_{c+d}} = \frac{p^c_{in}}{4} n_{e,\omega_d} \frac{\partial G}{\partial N}\left(1+\frac{\overline{P^c_{in}}}{p^c_{in}} n_{e,\omega_c}\frac{\partial G}{\partial N}\right) = \frac{p^c_{in}}{4} n_{e,\omega_d} \frac{\partial G}{\partial N}\left(1+\varepsilon_{c+d}(\omega_c)\right) \tag{2.61}$$

$$p^c_{out,\omega_{c-d}} = \frac{p^c_{in}}{4} n^*_{e,\omega_d} \frac{\partial G}{\partial N}\left(1+\frac{\overline{P^c_{in}}}{p^c_{in}} n^*_{e,\omega_c}\frac{\partial G}{\partial N}\right) = \frac{p^c_{in}}{4} n^*_{e,\omega_d} \frac{\partial G}{\partial N}\left(1+\varepsilon_{c-d}(\omega_c)\right) \tag{2.62}$$

with $\varepsilon_{c+d}(\omega_c) = \frac{\overline{P^c_{in}}}{p^c_{in}} n_{e,\omega_c}\frac{\partial G}{\partial N}$ and $\varepsilon_{c-d}(\omega_c) = \frac{\overline{P^c_{in}}}{p^c_{in}} n^*_{e,\omega_c}\frac{\partial G}{\partial N}$. These two terms must be taken into account if f_c is close or below the cutoff frequency of $n_e(\omega)$. In system application, $\omega_c = 2\pi f_c$ is the high up-mixing fixed angular frequency. Usually, f_c is significantly higher than the cutoff frequency of n_{e,ω_c}, thus the response in phase and amplitude of n_{e,ω_c} is negligible. It appears through (2.61) and (2.62) that the frequency response in amplitude and phase of the Up-CPO signals at ω_{c+d} and ω_{c-d} depends only on the frequency response of the mean carrier density oscillation due to the data signal through n_{e,ω_d} and n^*_{e,ω_d} respectively. Therefore, the Up-CPO frequency response in this case can be simplified as:

$$p^c_{out,\omega_{c+d}} \sim \frac{p^c_{in}}{4} n_{e,\omega_d} \frac{\partial G}{\partial N} \tag{2.63}$$

$$p^c_{out,\omega_{c-d}} \sim \frac{p^c_{in}}{4} n^*_{e,\omega_d} \frac{\partial G}{\partial N} \tag{2.64}$$

2.5.2.2 Small-signal frequency response of the carrier density

As shown in (2.61) and (2.62), the Up-CPO frequency responses at ω_{c+d} and ω_{c-d} are related to the frequency response of the carrier density of the data signal, n_{e,ω_d}. To access experimentally to the frequency response of n_{e,ω_d} due to XGM, without the oscillation of P^c_{in}, a pump-probe setup is used. In this case, P^c_{in} is set as a continuous-wave signal and used as a probe noted $\overline{P^{Pr}_{in}}$, and P^d_{in} is considered as the pump, a time varying signal noted P^{Pu}_{in}.

We assume that the SOA gains at λ_{Pu} and λ_{Pr} are the same: for the section i we have $\overline{G_i^{Pu}} = \overline{G_i^{Pr}} = \overline{G_i}$, and $a^{Pr} = a^{Pu} = a$. Generally, in small-signal analysis, the SOA is modeled by only one calculation section [11-14] and [19] [20]. In order to take into account the nonlinear effect due to the saturation regime, the model must include an extra number of sections, causing the analytical expression of $n_e(\omega_x)$ to become more complex. As we increase the number of sections, so does the complexity of the equations; thus, we divide the total SOA length into only two sections of equal lengths (L_1 = L_2 = L/2). Each section is biased by half of the total SOA bias current I (I_1 = I_2 = I/2) (see Figure 2.25).

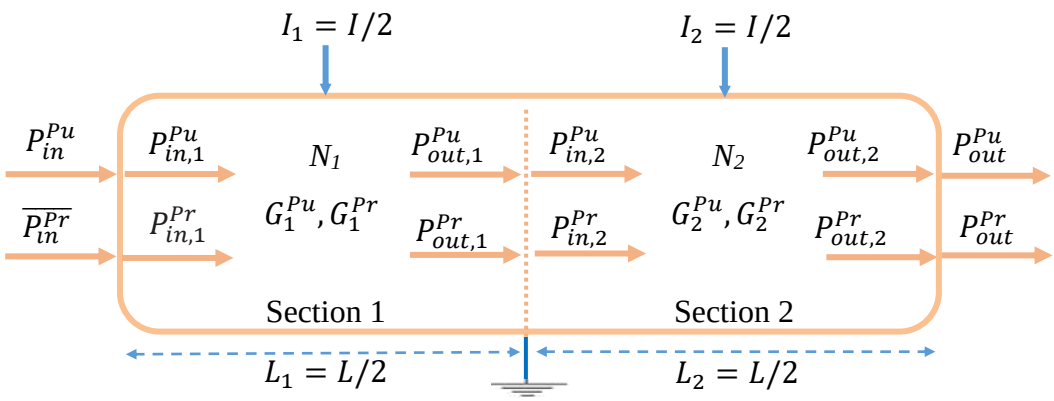

Figure 2.25 Principle of SOA modeling by two calculation sections in presence of an intensity-modulated pump signal P_{in}^{Pu} at λ_{Pu} and a continuous-wave probe signal $\overline{P_{in}^{Pr}}$ at λ_{Pr}.

Therefore, in the pump-probe configuration, an intensity-modulated optical power acting as a pump signal at λ_{Pu} is injected in the first SOA section at the SOA input (Figure 2.25), which is expressed at the SOA input as:

$$P_{in}^{Pu} = P_{in,1}^{Pu} = \overline{P_{in}^{Pu}} + \frac{p_{in}^{Pu}}{2} e^{j\omega_{Pu}t} + \frac{p_{in}^{*Pu}}{2} e^{-j\omega_{Pu}t} \tag{2.65}$$

where $\overline{P_{in}^{Pu}}$ is the average optical input power at λ_{Pu}, p_{in}^{Pu} is the modulation part at the angular frequency ω_{Pu} of the optical signal at wavelength λ_{Pu} and '*' stands for the complex conjugate value. A second signal, a continuous-wave power acting as a probe signal $P_{in1}^{Pr} = \overline{P_{in}^{Pr}}$ at λ_{Pr} is injected simultaneously at the SOA input.

From (2.16), the recombination rate $R_{st,i}$ due to the amplification of the optical pump and probe signals at wavelengths λ_{Pr} and λ_{Pu}, can be given in both sections by the following equation:

$$R_{st,i} = \frac{2}{\Gamma a L \tau_{e,i}} \left(\frac{P_{in,i}^{Pu}(G_i - 1)}{P_{sat,\mathrm{i}}^{Pu}} + \frac{\overline{P_{in,i}^{Pr}}(G_i - 1)}{P_{sat,\mathrm{i}}^{Pr}} \right) \tag{2.66}$$

where $P_{sat,\mathrm{i}}^{Pu} = \frac{wdW_p^{Pu}}{\Gamma a \tau_{e,i}}$ is the material saturation power at λ_{Pu}, $P_{sat,\mathrm{i}}^{Pr} = \frac{wdW_p^{Pr}}{\Gamma a \tau_{e,i}}$ is the material saturation power at λ_{Pr}, W_p^{Pu} and W_p^{Pr} are the photon energy at the signal wavelength λ_{Pu} and λ_{Pr}, respectively. Γ is the optical confinement factor in the active zone, a is the peak-gain coefficient.

The $R_{nst,i}$ and $R_{ASE,i}$ can be taken into account from (2.12)-(2.13) by:

$$\frac{N_i}{\tau_{e,i}} \tag{2.67}$$

with $\tau_{e,i}$ is the effective carrier lifetime calculated from the carrier lifetimes τ_i, due to $R_{nst,i}$, and $\tau_{ase,i}$, due to $R_{ASE,i}$, with $\frac{1}{\tau_{e,i}} = \frac{1}{\tau_i} + \frac{1}{\tau_{ase,i}}$ [17] [18].

2.5.2.2.1 Carrier density modulation in the first and second section

For the first section i = 1, we introduce (2.66) and (2.67) into the general form of the ate equation (2.11), the rate equation for the first section becomes:

$$\frac{dN_1}{dt} = \frac{I_1}{qV} - \frac{N_1}{\tau_{e,1}} - \frac{P_{in,1}^{Pu}(G_1 - 1)}{\Gamma a L_1 \tau_{e,1} P_{sat,1}^{Pu}} - \frac{\overline{P_{in,1}^{Pr}}(G_1 - 1)}{\Gamma a L_1 \tau_{e,1} P_{sat,1}^{Pr}} \tag{2.68}$$

The complex amplitude of the carrier density modulation $n_{1,\omega_{Pu}}$ (2.69) is given by small-signal modeling (section 2.3.1). By introducing the expression of the carrier density and the gain (2.20)-(2.21), for $\lambda_x = \lambda_{Pu}$, and (2.65) into (2.64). Then we derivative (2.68). We consider first order modulation terms, and substitute (2.23) into the derivative of (2.68).

$$n_{1,\omega_{Pu}} = -\frac{1}{\Gamma a\, L_1 (1 + K_1^{Pu}) P_{sat,1}^{Pu}} \left(\frac{\overline{G_1} - 1}{1 + j\omega\tau_{d,1}} \right) p_{in,1}^{Pu} \tag{2.69}$$

where $\tau_{d,1} = \frac{\tau_{e,1}}{1+K_1^{Pu}}$ is the dynamic carrier lifetime in the first section and $K_1^{Pu} = \frac{\overline{P_{in,1}^{Pu}}}{P_{sat,1}^{Pu}} \overline{G_1}$.

Now, for the second section i = 2, the input powers of the second section depends on the output powers of section 1, where $P_{out,1}^{Pu} = P_{in,2}^{Pu} = P_{in,1}^{Pu} G_1$ and $P_{out,1}^{Pr} = P_{in,2}^{Pr} = \overline{P_{in,1}^{Pr}} G_1$. Therefore, the rate equation for the second section is given as:

$$\frac{dN_2}{dt} = \frac{I_2}{qV} - \frac{N_2}{\tau_{e,2}} - \frac{P_{in,2}^{Pu}(G_2 - 1)}{\Gamma a L_2 \tau_{e,2} P_{sat,2}^{Pu}} - \frac{P_{in,2}^{Pr}(G_2 - 1)}{\Gamma a L_2 \tau_{e,2} P_{sat,2}^{Pr}} \tag{2.70}$$

The complex amplitude of the carrier density modulation $n_{2,\omega_{Pu}}$ in the second section can be calculated as in (2.71) by small-signal modeling using (2.20)-(2.21), and by applying the derivative of (2.70). We consider first order modulation terms, and substitute the partial derivative of the gain (2.23) into the derivative of (2.71).

$$n_{2,\omega_{Pu}} = -\frac{1}{\Gamma a L_2 (1 + K_2^{Pr} + K_2^{Pu}) P_{sat,2}^{Pu}} \left(\frac{\overline{G_2} - 1}{1 + j\omega\tau_{d,2}} \right) \left(p_{in,1}^{Pu} \overline{G_1} + \overline{P_{in,1}^{Pu}} n_{1,\omega_{Pu}} \frac{\partial G_1}{\partial N_1} + \overline{P_{in,1}^{Pr}} n_{1,\omega_{Pu}} \frac{\partial G_1}{\partial N_1} \right) \tag{2.71}$$

where $\tau_{d,2} = \frac{\tau_{e,2}}{1+K_2^{Pr}+K_2^{Pu}}$ is the dynamic carrier lifetime in the second section, $K_2^{Pu} = \frac{\overline{P_{in,1}^{Pu}}}{P_{sat,2}^{Pu}} \bar{G}$ and $\bar{G} = \overline{G_1}\,\overline{G_2}$.

The probe and pump optical powers at the input of the second section can be written respectively from the gain expression (2.21) where $\lambda_x = \lambda_{Pu}$, and (2.65) by considering first-order terms as:

$$P_{in,2}^{Pr}(t) = \overline{P_{in,1}^{Pr}}\,\overline{G_1} + \overline{P_{in,1}^{Pr}} \frac{n_{1,\omega_{Pu}}}{2} \frac{\partial G_1}{\partial N_1} e^{j\omega_{Pu}t} + \overline{P_{in,1}^{Pr}} \frac{n_{1,\omega_{Pu}}^*}{2} \frac{\partial G_1}{\partial N_1} e^{-j\omega_{Pu}t} \tag{2.72}$$

$$P_{in,2}^{Pu}(t) = \overline{P_{in,1}^{Pu}}\,\overline{G_1} + \left(\frac{p_{in,1}^{Pu}}{2} \overline{G_1} + \overline{P_{in,1}^{Pu}} \frac{n_{1,\omega_{Pu}}}{2} \frac{\partial G_1}{\partial N_1} \right) e^{j\omega_{Pu}t} + \left(\frac{p_{in,1}^{*Pu}}{2} \overline{G_1} + \overline{P_{in,1}^{Pu}} \frac{n_{1,\omega_{Pu}}^*}{2} \frac{\partial G_1}{\partial N_1} \right) e^{-j\omega_{Pu}t} \tag{2.73}$$

2.5.2.2.2 Probe output power

At the SOA output, the complex amplitude of the probe signal at $\pm\omega_{Pu}$ can be given from (2.21) and (2.65) by considering the first order terms to be:

$$p_{out,\omega_{Pu}}^{Pr} = \overline{P_{in,1}^{Pr}}\,\overline{G_2} \frac{n_{1,\omega_{Pu}}}{2} \frac{\partial G_1}{\partial N_1} + \overline{P_{in,1}^{Pr}}\,\overline{G_1} \frac{n_{2,\omega_{Pu}}}{2} \frac{\partial G_2}{\partial N_2} \tag{2.74}$$

$$p_{out,-\omega_{Pu}}^{Pr} = \overline{P_{in,1}^{Pr}}\,\overline{G_2} \frac{n_{1,\omega_{Pu}}^*}{2} \frac{\partial G_1}{\partial N_1} + \overline{P_{in,1}^{Pr}}\,\overline{G_1} \frac{n_{2,\omega_{Pu}}^*}{2} \frac{\partial G_2}{\partial N_2} \tag{2.75}$$

Then, by using (2.23) we express $p_{out,\pm\omega_{Pu}}^{Pr}$ in terms of the mean carrier density as:

$$p_{out,\omega_{Pu}}^{Pr} = \overline{P_{in,1}^{Pr}}\,\overline{G_1}\,\overline{G_2}\Gamma a\frac{L}{2}\frac{n_{1,\omega_{Pu}}}{2} + \overline{P_{in,1}^{Pr}}\,\overline{G_1}\,\overline{G_2}\Gamma a\frac{L}{2}\frac{n_{2,\omega_{Pu}}}{2} = \overline{P_{in,1}^{Pr}}\bar{G}\Gamma aL\frac{n_{e,\omega_{Pu}}}{2} \tag{2.76}$$

$$p_{out,-\omega_{Pu}}^{Pr} = \overline{P_{in,1}^{Pr}}\bar{G}\Gamma aL\frac{n_{e,\omega_{Pu}}^{*}}{2} \tag{2.77}$$

with $n_{e,\omega_{Pu}} = \frac{n_{1,\omega_{Pu}}+n_{2,\omega_{Pu}}}{2}$ and $n_{e,\omega_{Pu}}^{*} = \frac{n_{1,\omega_{Pu}}^{*}+n_{2,\omega_{Pu}}^{*}}{2}$ equivalent to the mean value of the complex amplitude of the carrier density.

Equations (2.76) and (2.77) show that a pump-probe setup can lead to access into the frequency response of the dynamic carrier density, which will be used to analyze the Up-CPO frequency response defined in (2.63) and (2.64). Substituting (2.69) and (2.71) into (2.76) and (2.77) yields an expression of the output probe power $p_{out,\pm\omega_{Pu}}^{Pr}$, $n_{e,\omega_{Pu}}$ and $n_{e,\omega_{Pu}}^{*}$ that can be written as:

$$p_{out,\pm\omega_{Pu}}^{Pr} = -\frac{K_{n1n2}\overline{P_{in,1}^{Pr}}\bar{G}}{2P_{sat,1}^{Pu}P_{sat,2}^{Pu}}\left(\frac{1\pm j\omega\tau_{d,12}}{(1\pm j\omega\tau_{d,1})(1\pm j\omega\tau_{d,2})}\right)p_{in,1}^{Pu} \tag{2.78}$$

$$n_{e,\omega_{Pu}} = -\frac{K_{n1n2}}{\Gamma aLP_{sat,1}^{Pu}P_{sat,2}^{Pu}}\left(\frac{1+j\omega\tau_{d,12}}{(1+j\omega\tau_{d,1})(1+j\omega\tau_{d,2})}\right)p_{in,1}^{Pu} \tag{2.79}$$

$$n_{e,\omega_{Pu}}^{*} = -\frac{K_{n1n2}}{\Gamma aLP_{sat,1}^{Pu}P_{sat,2}^{Pu}}\left(\frac{1-j\omega\tau_{d,12}}{(1-j\omega\tau_{d,1})(1-j\omega\tau_{d,2})}\right)p_{in,1}^{Pu} \tag{2.80}$$

with:

- $\tau_{d,12} = \frac{K_{n2}\overline{G_1}\tau_{d,1}P_{sat,1}^{Pu}+K_{n1}\tau_{d,2}P_{sat,2}^{Pu}}{K_{n1n2}}$ (2.81)
- $K_{n1n2} = P_{sat,2}^{Pu}K_{n1} + K_{n2}\overline{G_1}P_{sat,1}^{Pu}\left(1 - K_{n1}\left(\frac{\overline{P_{in,1}^{Pr}}+\overline{P_{in,1}^{Pu}}}{P_{sat,1}^{Pu}}\right)\right)$ (2.82)
- $K_{n1} = \frac{\overline{G_1}-1}{(1+K_1^{Pu})}$ (2.83)
- $K_{n2} = \frac{\overline{G_2}-1}{(1+K_2^{Pu}+K_2^{Pr})}$ (2.84)

2.5.2.3 Evaluation of the dynamic carrier lifetime

As the frequency response of $p_{out,\pm\omega_{Pu}}^{Pr}$ (2.78) depends on the dynamic carrier lifetimes $\tau_{d,12}$, $\tau_{d,1}$ and $\tau_{d,2}$, we analyze in this paragraph their evolution as a function of the injected powers $\overline{P_{in}^{Pr}}$ and $\overline{P_{in}^{Pu}}$. The calculation of $\tau_{d,12}$, $\tau_{d,1}$ and $\tau_{d,2}$ is done after resolving the rate equations (2.68) and (2.70) by using 2 calculation sections for the SOA presented in [5] [12]. We consider two cases where the probe input power $\overline{P_{in}^{Pr}}$ is set first at a low power (−30 dBm) and then at a high power to saturate the SOA (0 dBm). For each case, we vary the pump input power $\overline{P_{in}^{Pu}}$ from −30 to 10 dBm. Figure 2.26(a) and Figure 2.26(c) depict the gain evolution versus the pump input optical power for $\overline{P_{in}^{Pr}}$ = -30 dBm and 0 dBm, respectively. We deduce from these two figures $P_{sat,1}^{Pu}$ and $P_{sat,2}^{Pu}$, where $P_{sat,i}^{Pu} = \frac{\overline{P_{out,i}}|_{-3\,dB}}{ln(2)}$ [3], with $\overline{P_{out,i}}|_{-3\,dB}$ the optical output power in section i for the optical gain reduced by -3 dB.

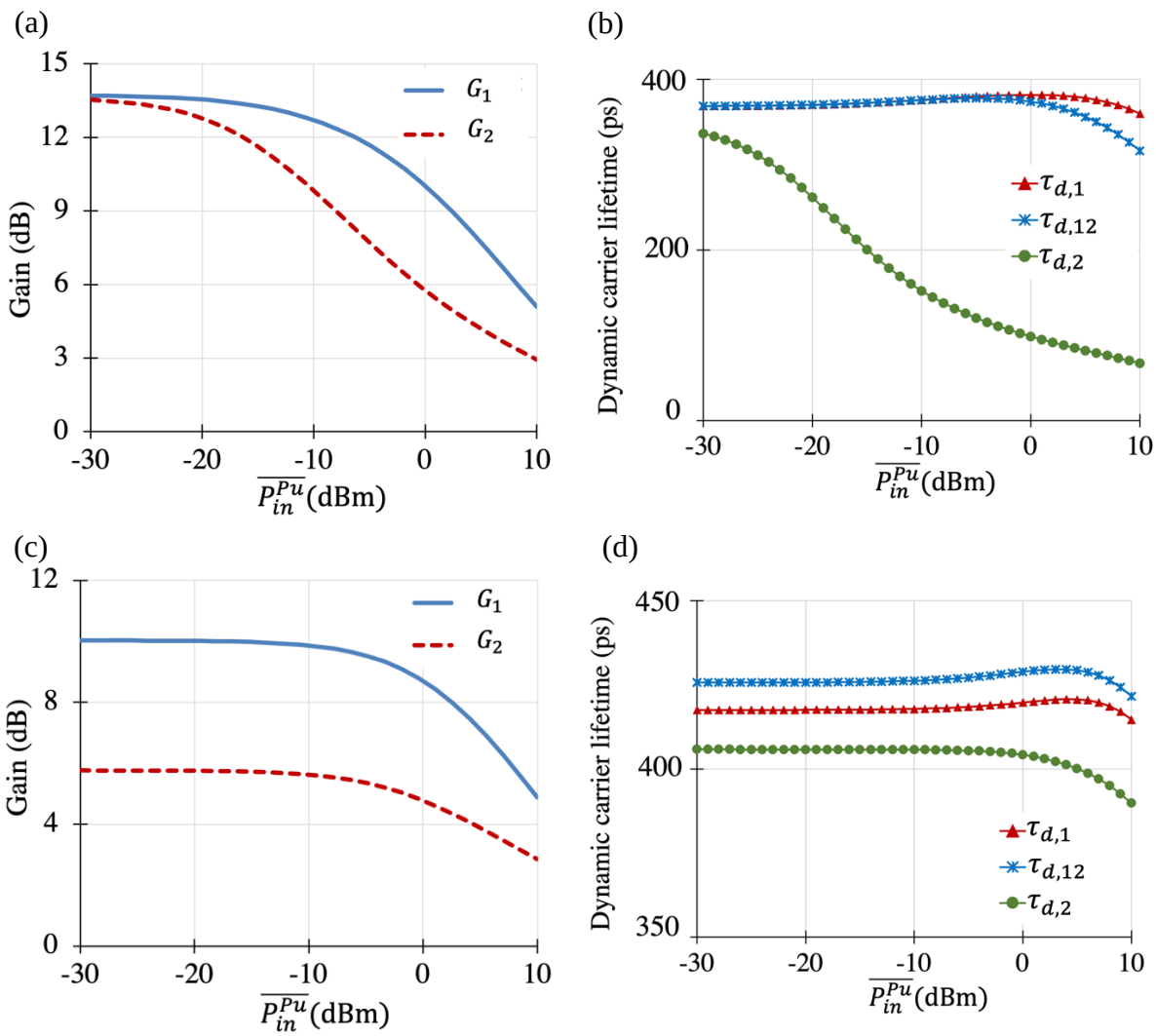

Figure 2.26 Gain for sections 1 and 2 for: $\overline{P_{in}^{Pr}}$ = -30 dBm (a), $\overline{P_{in}^{Pr}}$ = 0 dBm (c). Dynamic carrier lifetime for: $\overline{P_{in}^{Pr}}$ = -30 dBm (b), $\overline{P_{in}^{Pr}}$ = 0 dBm (d).

As seen in Figure 2.26(b) and Figure 2.26(d), $\tau_{d,1}$ is always greater than $\tau_{d,2}$. When the optical gain in each section is nearly unsaturated, corresponding to $\overline{P_{in}^{Pu}}$ lower than -10 dBm and $\overline{P_{in}^{Pr}}$ set at -30 dBm, Figure 2.26(b) shows that $\tau_{d,12}\sim\tau_{d,1}$. In this case, (2.78) tends to a first-order low-pass response. This indicates that modeling the SOA by only one section is sufficient.
For higher $\overline{P_{in}^{Pu}}$, G_2 is more saturated than G_1, this in turn leads to $\tau_{d,12} < \tau_{d,1}$ as shown in Figure 2.26(b). A deep saturation, for the case where $\overline{P_{in}^{Pr}}$ is set at 0 dBm, leads to always have $\tau_{d,12} > \tau_{d,1}$ (Figure 2.26(d)). Therefore, the frequency response of (2.78) no longer corresponds to a first order low-pass response.

2.5.2.4 Full Up-CPO frequency response

As we explained in section 2.5.2.2, the carrier density dynamics $n_{e,\omega_{Pu}}$ are obtained from the pump-probe configuration and then used to determine the full frequency response of the Up-CPO configuration. Thereby, the power of Up-CPO responses, $p_{out,\omega_{c\pm d}}^{c}$, can be calculated by substituting the carrier density expressions (2.79)-(2.80) into (2.61)-(2.62):

$$p_{out,\omega_{c\pm d}}^{c} = -\frac{p_{in,1}^{c}}{4}\left(\frac{K_{n1n2}\bar{G}}{P_{sat,1}^{d}P_{sat,2}^{d}}T_{\pm}(\omega)p_{in,1}^{d}\right)\left(1-\frac{K_{n1n2}\overline{P_{in,1}^{c}}\bar{G}}{P_{sat,1}^{d}P_{sat,2}^{d}}T_{\pm}(\omega_c)\right) \tag{2.85}$$

with

$$T_{\pm}(\omega) = \frac{1\pm j\omega\tau_{d,12}}{(1\pm j\omega\tau_{d,1})(1\pm j\omega\tau_{d,2})}, \text{ and } T_{\pm}(\omega_c) = \frac{1\pm j\omega_c\tau_{d,12}}{(1\pm j\omega_c\tau_{d,1})(1\pm j\omega_c\tau_{d,2})} \tag{2.86}$$

2.5.3 Calculation and measurement of frequency responses for pump-probe and Up-CPO setups

After presenting the principle and the small-signal analysis of the Up-CPO, in this section, we first give the experimental results of a pump-probe configuration in order to determine the values of $\tau_{d,12}$, $\tau_{d,1}$ and $\tau_{d,2}$ in equations (2.78) to (2.80). These parameters are then used in (2.85) to calculate and discuss the Up-CPO frequency response. Finally, we compare the theoretical and experimental Up-CPO frequency responses.

The experimental results were measured for three different SOAs. SOA-L, SOA-NL and SOA-XN, are identified respectively as linear, nonlinear and extra nonlinear SOAs. The static characteristics of SOAs measured at the maximum biasing current and at -25 dBm input optical power, are shown in Table 2.1.

2.5.3.1 Pump-probe characterization

The experimental setup of pump-probe is illustrated in Figure 2.27, an intensity-modulated optical pump of 5 dBm at λ_{Pu} = 1545 nm and a continuous wave (CW) optical probe of -5

dBm at λ_{Pr} = 1550 nm are simultaneously injected into the SOA. An optical filter is used at the SOA output to measure the signal converted at λ_{Pr} through XGM. After photodetection, the RF signal $p_{out,\omega_{Pu}}^{Pr}$ is measured with a vector network analyzer (VNA).

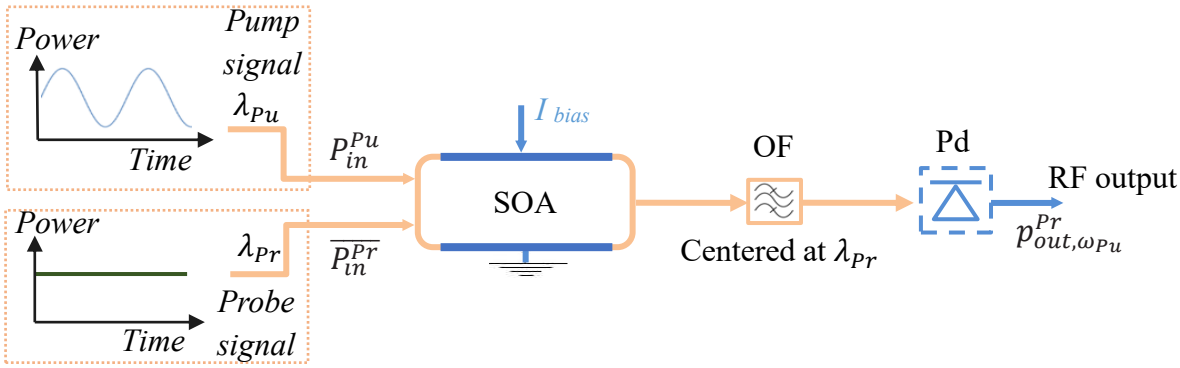

Figure 2.27 Pump-probe setup, OF: Optical filter, Pd: Photodiode.

As each SOA device is different, the measurements are made with respect to the static optical gains 0 dB, 5 dB and 10 dB in presence of the input pump power of 5 dBm and the input probe power of −5 dBm.

Figure 2.28(a), (b) and (c) show, in solid line, the normalized low-pass frequency response of the measured RF power $p_{out,\omega_{Pu}}^{Pr}$ for the three SOAs. The experimental results show that the SOAs NL and XN present, at −3 dB of the maximum RF power, a large bandwidth. SOA-XN can reach 18.45 GHz of bandwidth, while SOA-L has a 3.95 GHz bandwidth, obtained for gain 10 dB. We also notice that non-flat responses are obtained for SOAs NL and XN.

In order to determine the values of $\tau_{d,12}$, $\tau_{d,1}$ and $\tau_{d,2}$ we fit the experimental results of the pump-probe configuration by the normalized form of the measured RF power $p_{out,\omega_{Pu}}^{Pr}$ for SOA-L, SOA-NL and SOA-XN. The normalized function is obtained from (2.78) as:

$$T(f) = \frac{1 + j\omega\tau_{d,12}}{(1 + j\omega\tau_{d,1})(1 + j\omega\tau_{d,2})} = \frac{1 + j\frac{f}{f_{12}}}{\left(1 + j\frac{f}{f_1}\right)\left(1 + j\frac{f}{f_2}\right)} \tag{2.87}$$

where f_t is the cutoff frequency for each $1 + j\frac{f}{f_t}$ term with $f_t = \frac{1}{2\pi\tau_{d,t}}$ and t = 12, 1 and 2. The obtained value of $f_{d,12}$, $f_{d,1}$ and $f_{d,2}$ are shown in Table 2.3, Table 2.4, and Table 2.5, respectively.

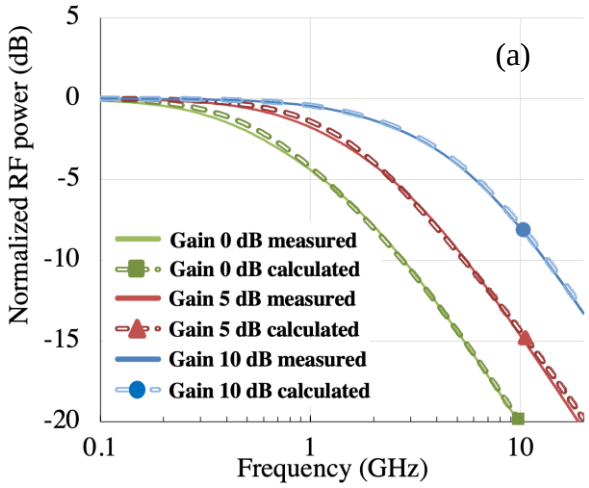

Table 2.3 Cutoff frequency of SOA-L (GHz)

	0 dB	*5 dB*	*10 dB*
f_{12}	0.81	1.46	2.17
f_1	0.5	1.03	1.82
f_2	1.62	2.7	5.33
f_{3dB}	0.76	1.63	3.95

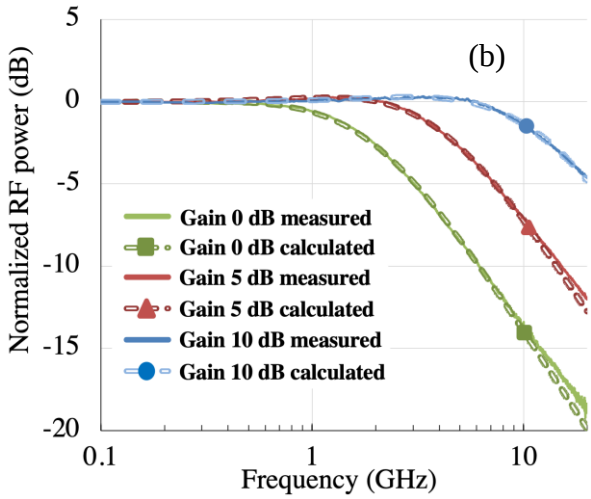

Table 2.4 Cut-off frequency of SOA-NL (GHz)

	0 dB	*5 dB*	*10 dB*
f_{12}	0.6	1.26	2.5
f_1	0.64	1.5	2.8
f_2	1.91	4	12
f_{3dB}	2.14	5.23	14.65

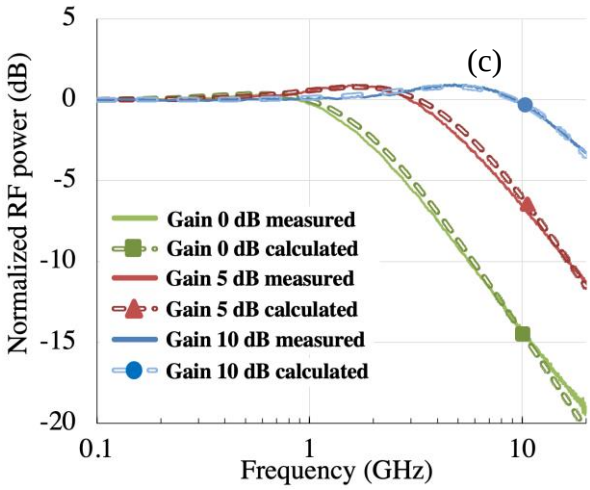

Table 2.5 Cut-off frequency of SOA-XN (GHz)

	0 dB	*5 dB*	*10 dB*
f_{12}	0.6	1.3	3.37
f_1	0.8	1.8	4.43
f_2	1.45	3.9	12
f_{3dB}	2.24	5.97	18.45

Figure 2.28 Normalized RF power for: SOA-L (a), SOA-NL (b) and SOA-XN (a). Calculated data are in dotted line and measured ones are in solid line.

The calculated data of the normalized RF power from $p^{Pr}_{out,\omega_{Pu}}$ show a good agreement with the measured ones (Figure 2.28) for the three different SOAs. These show that the SOA modeling by dividing its length into two sections allows us to reproduce their high-order frequency responses with a good accuracy.

Moreover, the fitting results show that a flat frequency response in the bandwidth at -3 dB is obtained when $f_{12} \geq f_1$, corresponding to $\tau_{d,12} \leq \tau_{d,1}$. Otherwise, a slight overshoot appears as for SOAs NL and XN at gains 5 dB and 10 dB, that corresponds to $\tau_{d,12} > \tau_{d,1}$, where (2.78) no longer has a first-order low-pass response (as stated in section 2.5.2.3).

2.5.3.2 Calculation of the absolute Up-CPO frequency response

For practical reasons, in experimental measurements, we only have an easy access to relative responses, i.e., the difference between two measurements, rather than the absolute ones. The absolute amplitude and phase responses of Up-CPO signals can be calculated by substituting the normalized function (2.87) of the calculated f_t in Table 2.3, Table 2.4, and Table 2.5, and into equations (2.85). $p^c_{out,\omega_{c\pm d}}$ can be written as:

$$p^c_{out,\omega_{c\pm d}} = -\frac{p^c_{in,1}}{4}\left(\frac{K_{n1n2}\bar{G}}{P^d_{sat,1}P^d_{sat,2}}T_{\pm}(f)p^d_{in,1}\right)\left(1-\frac{K_{n1n2}\overline{P^c_{in,1}}\bar{G}}{P^d_{sat,1}P^d_{sat,2}}\,T_{\pm}(f_c)\right) \tag{2.88}$$

The resulting $p^c_{out,\omega_{c\pm d}}$ can be rewritten as follows:

$$p^c_{out,\omega_{c\pm d}} = -\frac{A_G}{4m}p^d_{in,1}T_{\pm}(f)\left(1-A\,T_{\pm}(f_c)\right) \tag{2.89}$$

where $A_G = \frac{K_{n1n2}\overline{P^c_{in,1}}}{P^d_{sat,1}P^d_{sat,2}}\bar{G}$ is a constant for an operating point and $m = \frac{p^c_{in,1}}{\overline{P^c_{in,1}}}$ is the modulation index of the optical input signal at λ_c. We vary f in a range of 5 GHz around f_c with $f = f_c \pm f_d$.

The power, in dBm, and the phase of $p^c_{out,\omega_{c\pm d}}$ for an operating point corresponding to an optical gain G can be written form (2.89) as:

$$\left|p^c_{out,\omega_{c\pm d}}\right|_G(dBm) = B_G + 10log\left|T_{\pm}(f)\right| \tag{2.90}$$

$$arg\left(p^c_{out,\omega_{c\pm d}}\right)\Big|_G = \pi + C_G + arg\left(T_{\pm}(f)\right) + arg\left(p^d_{in,1}\right) - arg\left(p^c_{in,1}\right) \tag{2.91}$$

where B_G and C_G are constant terms with:

$$B_G = 10log\frac{A_G}{4m}\frac{p_{in,1}^{d}}{10^{-3}}\left|1 - A\,T_{\pm}(f_c)\right| \tag{2.92}$$

$$C_G = arg\left(1 - A\,T_{\pm}(f_c)\right) \tag{2.93}$$

We normalize the absolute power and the absolute phase shift of $p_{out,\omega_{c\pm d}}^{c}$ at f_c (Figure 2.29 and Figure 2.30). The Up-CPO technique operates as a frequency up-conversion function where the responses of the pump-probe configuration are shifted around f_c. The calculation is done in a bandwidth range of 5 GHz around f_c. For a SOA gain of 0 dB, all the three SOAs present a high phase shift and a high power variation (Figure 2.29) due to their limited frequency bandwidth ≤ 2.24 GHz (Table 2.3 to Table 2.5). By increasing the SOA gain to 5 and 10 dB, SOA-L shows a larger phase shift and power variation than for SOA-NL and XN (Figure 2.30) due to their higher cut-off frequencies (Table 2.3 to Table 2.5). In addition, the overshoot that exists for both SOA-NL and XN at gains 5 dB and 10 dB in Figure 2.28(b) and (c) also appears for the normalized absolute amplitude responses in Figure 2.29(b) and in Figure 2.30(b), (d), due to $f_1 \geq f_{21}$ it corresponding to $\tau_{d,12} \leq \tau_{d,1}$, as seen in section 2.5.2.3.

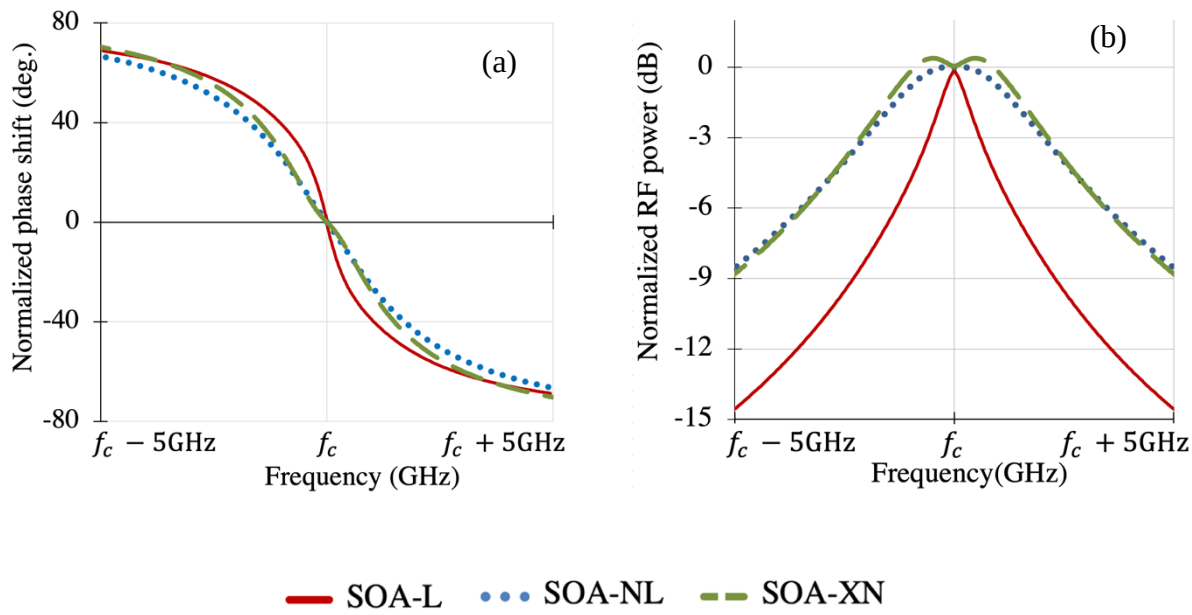

Figure 2.29 Up-CPO normalized phase shift for the three SOAs at gain 0dB (a). Normalized RF power for the three SOAs at gain 0 dB (b).

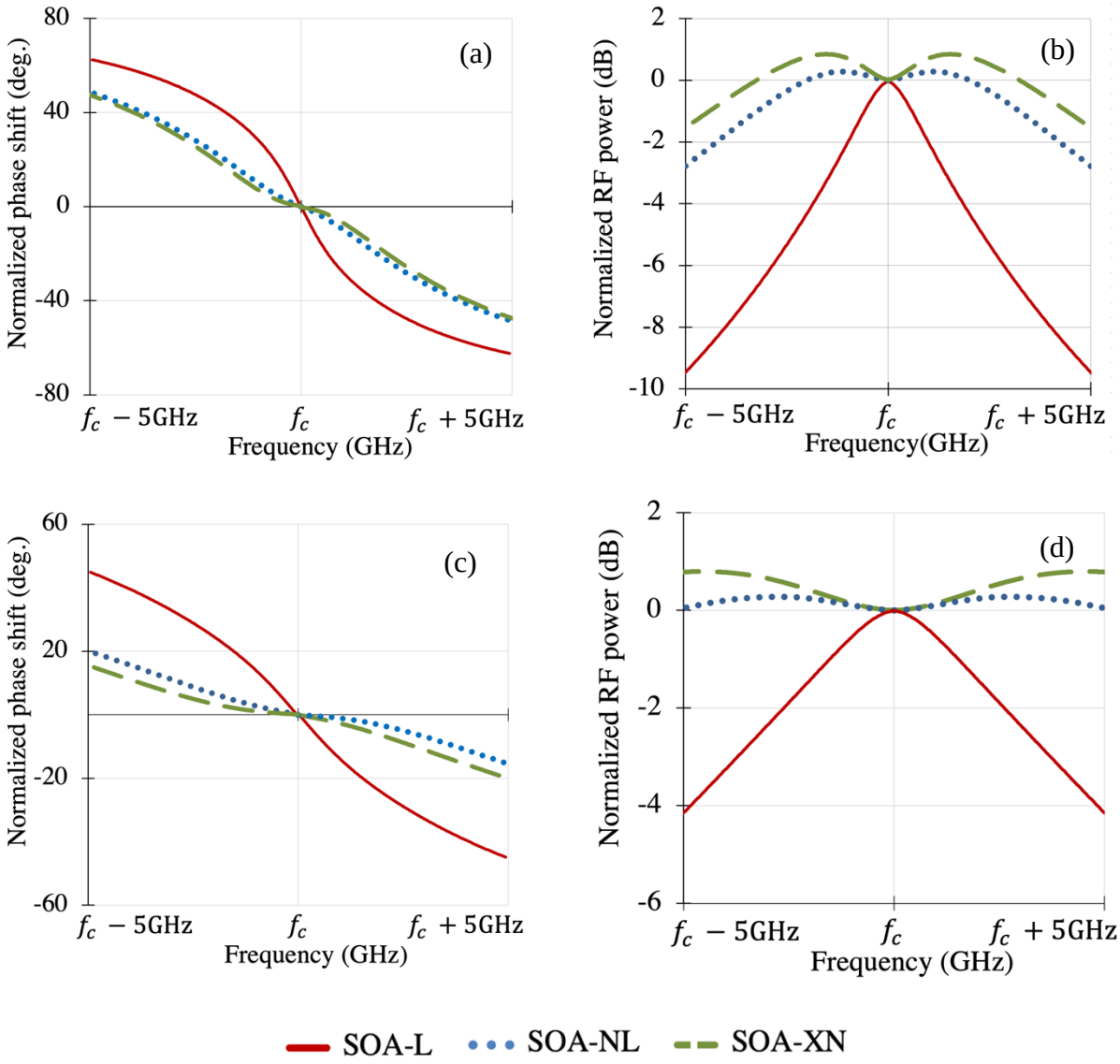

Figure 2.30 Up-CPO normalized phase shift for the three SOAs: at gain 5 dB (a), at gain 10 dB (c). Normalized RF power for the three SOAs: at gain 5 dB (b), and (d) at gain 10 dB.

2.5.4 Validation of small-signal calculations by experimental results of Up-CPO responses

The experimental setup is illustrated in Figure 2.31. A first optical signal emitted at λ_c= 1550 nm is intensity-modulated at a high radiofrequency f_c= 15 GHz via the Mach-Zehnder modulator MZM1. A second signal emitted at λ_d = 1545 nm is intensity-modulated via the Mach-Zehnder modulator MZM2 by a low RF frequency f_d varying from 0.1 to 5 GHz. It is generated by using a RF mixer, as the difference between f_c and f_{VNA} , a signal varying from 10 to 20 GHz generated by the VNA. The laser wavelengths are set to be close to the one for

which the gain of SOAs is maximum. An EDFA amplifies the modulated input data signal P_{in}^{d}. At the SOA output an optical filter (OF) with an optical bandwidth of about 0.5 nm is set at λ_c. The optical powers $\overline{P_{in}^{c}}$ and $\overline{P_{in}^{d}}$ are adjusted by the optical attenuators Att1 and Att2, respectively at 5 and −5 dBm. After the photodiode (Pd), the magnitude and phase shift of the RF signal $P_{e,out}$ are measured by a VNA at different static gains for each SOA device. The measurements of amplitude and the phase shift are evaluated relative to a reference that is the response at a gain of 10 dB, where the phase response supposed to be constant. The operating frequency is fixed at f_c = 15 GHz. It could be largely higher, but it was fixed at this value due to our experimental setup limitations. It should be noted that the used frequency f_c = 15 GHz for the SOA-NL and SOA-XN, is below their cutoff frequency for gain 10 dB (Table 2.4 and Table 2.5).

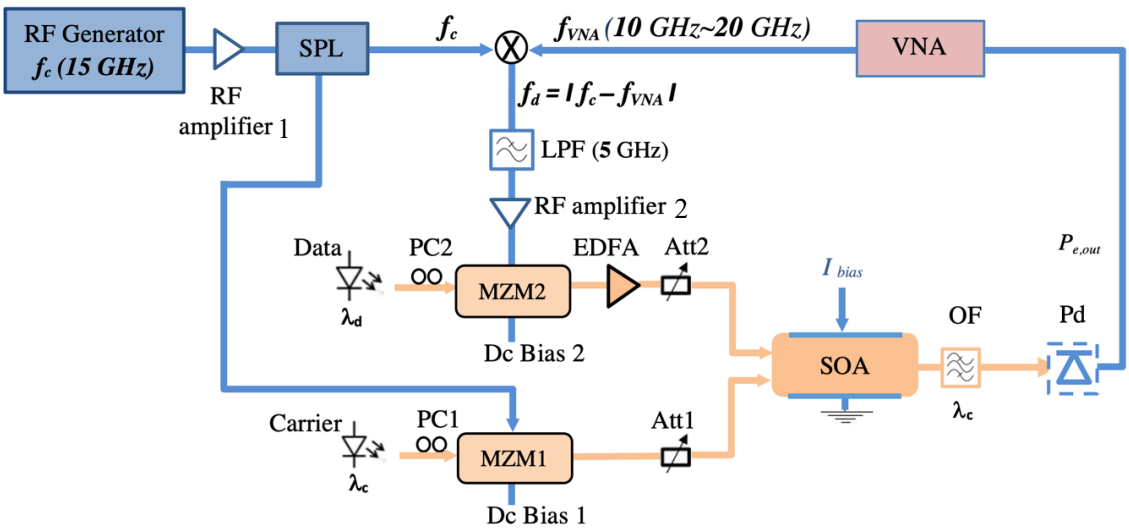

Figure 2.31 Experimental setup for Up-CPO measurements induced by slow and fast light effects and XGM in a SOA. PC1 and PC2: Polarization Controller, Pd: Photodetector, EDFA: Erbium-doped fiber amplifier, LPF: RF low-pass filter, SPL: RF Splitter.

The experimental results of the relative phase shift and normalized relative power of the Up-CPO signal are shown in Figure 2.33 and Figure 2.34 for gains 0 dB and 5 dB, respectively. We can see that the measured phase shift shows an offset at 15 GHz for both SOA-NL and SOA-XN. This offset is due to the large bandwidth of the reference response at gain 10 dB, where f_{3dB} =18.45 GHz for SOA-XN and 14.65 GHz for SOA-NL (see Table 2.4 and Table 2.5), which is close to or higher than f_c.

For the gain 5 dB, the cutoff frequency for SOA-XN (5.97 GHz) and for SOA-NL (5.23 GHz) are not significantly lower than f_c. In this case, the two terms $\varepsilon_{c+d}(\omega_c)$ and $\varepsilon_{c-d}(\omega_c)$ must be

taken into account if f_c is close or below the cutoff frequency of $n_e(\omega)$. Thus, the frequency response of Up-CPO at $\omega_{c\pm d}$ depends on both n_{e,ω_d} and n_{e,ω_c}, as described in 2.5.2.1.

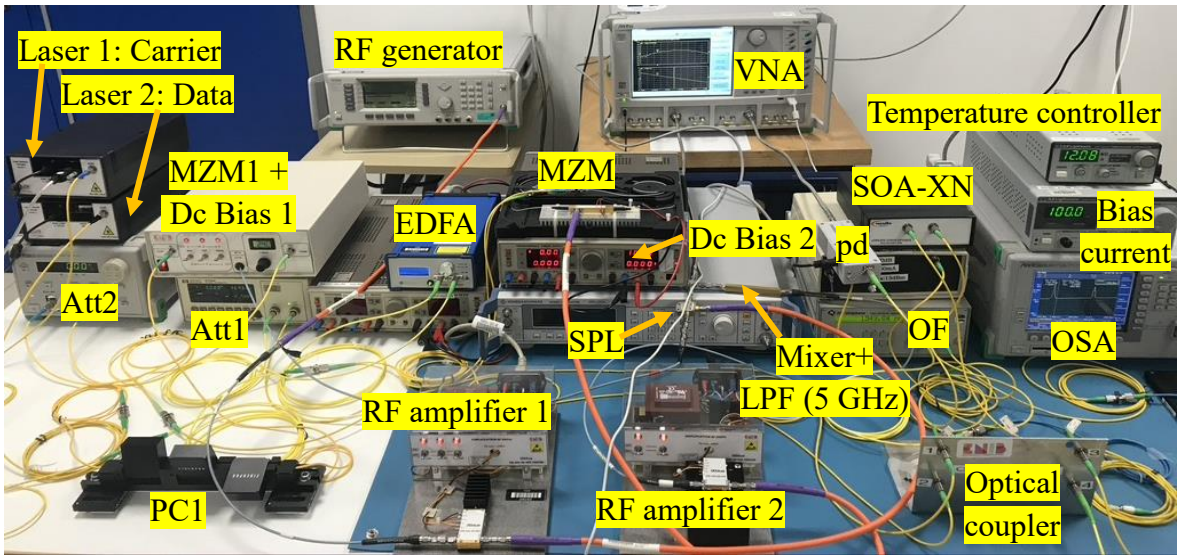

Figure 2.32 Photograph of Up-CPO experimental set-up using SOA-XN. OC: Optical Coupler, OSA: Optical Spectrum Analyzer.

The calculation of the relative amplitude and relative phase responses of Up-CPO are performed by using (2.90) and (2.91) and are then normalized at the frequency f_c. Figure 2.33 and Figure 2.34 shows a good agreement over all the 10 GHz measurement range around f_c for SOA-L between the theoretical (in dotted line) and experimental results (solid lines) for gains 0 dB and 5 dB of the relative amplitude and relative phase shift, where the SOA bandwidth is always lower than f_c.

For SOA-NL and SOA-XN, the frequency responses for the reference chosen at the gain 10 dB present a cutoff frequency close to f_c (for SOA-NL) or slightly above f_c (for SOA-XN). Although the approximations concerning the beating terms inside the SOA (that were made in section 2.5.2.1) are relatively rough in this case, the relative Up-CPO responses for gains of 0 and 5 dB are in agreement over the 10 GHz measurement range around f_c except for the SOA-XN responses for 5 dB gain (in Figure 2.33), where a difference appears between theoretical and experimental results.

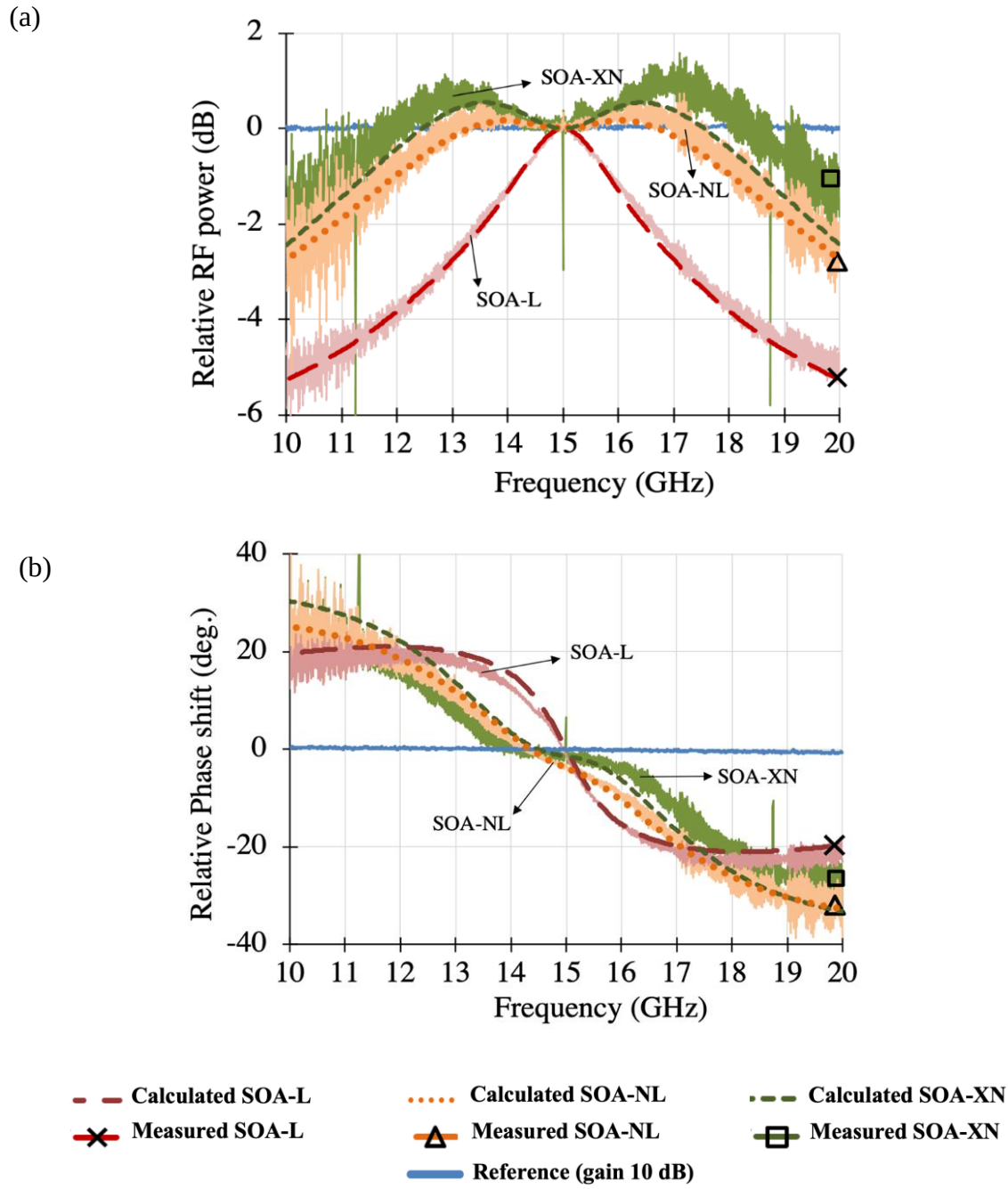

Figure 2.33 Measured and calculated results for a gain of 5 dB with a reference gain of 10 dB: (a) relative RF power for SOA-L, SOA-NL and SOA-XN, (b) relative phase shift for SOA-L, SOA-NL and SOA-XN. Calculated data are in dotted line and measured data are in solid line.

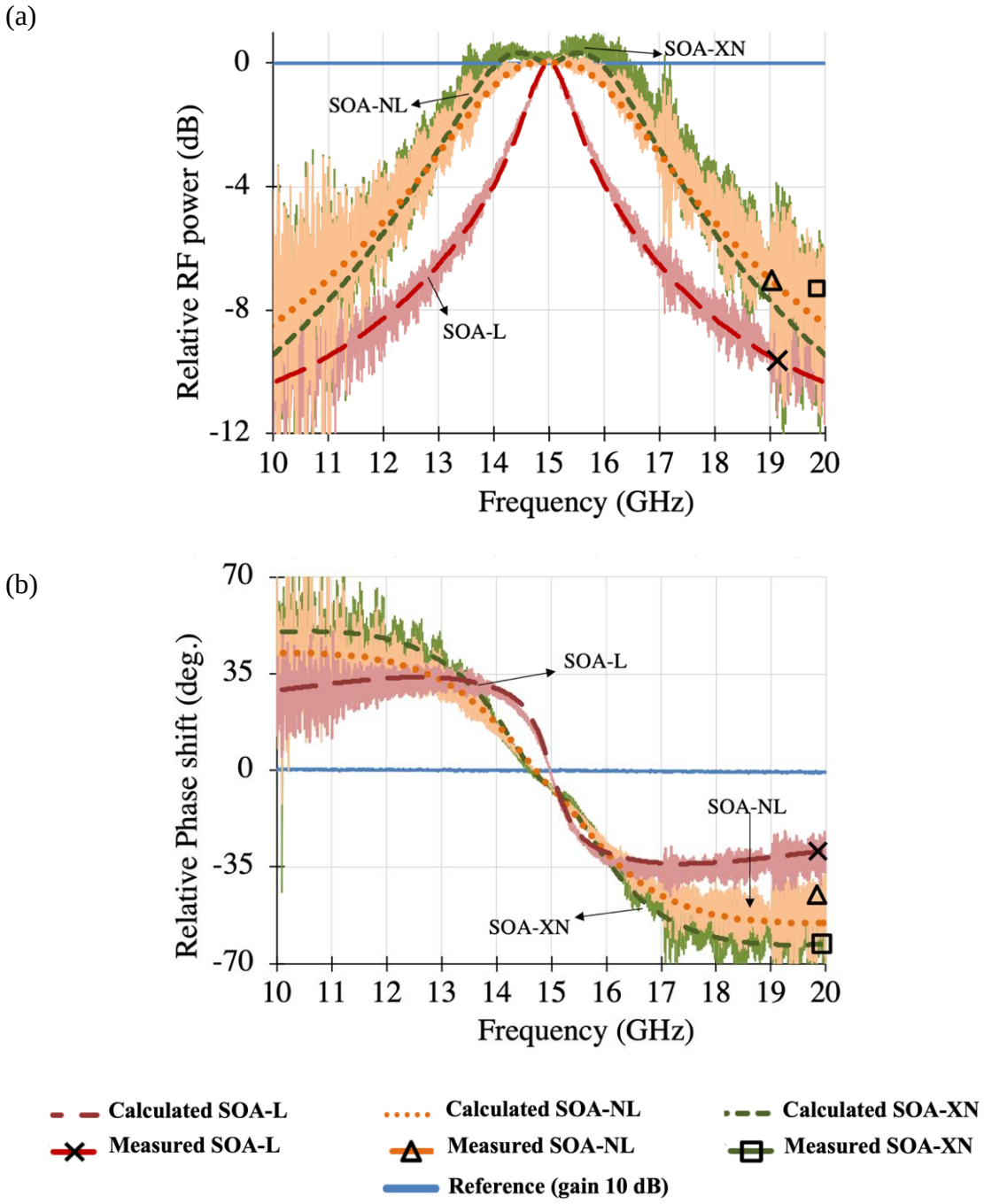

Figure 2.34 Measured and calculated results for a gain of 0 dB with a reference gain of 10 dB: (a) relative RF power for SOA-L, SOA-NL and SOA-XN, (b) relative phase shift for SOA-L, SOA-NL and SOA-XN. Calculated data are in dotted line and measured data are in solid line.

2.5.5 Experimental verification of the influence of the operating frequency (f_c)

As we saw in section 2.5.4, the measured phase shift shows an offset at 15 GHz for both SOA-NL and SOA-XN. It is due to the large bandwidth of the reference response at gain 10 dB, which is higher than f_c.

In order to verify the influence of f_c, on the Up-CPO response, a measurement of Up-CPO is done for two different operating frequencies f_c : at 10 GHz and 30 GHz. So, we recall the same experimental setup in Figure 2.31. We fix the bandwidth of the optical filter to 1 nm. The measurement of relative phase shift is done for different I_{bias}, where the reference is fixed at I_{bias} = 200 mA. The measured relative phase shift using SOA-XN is presented in Figure 2.35 (a) for f_c= 10 GHz, and f_c = 30 GHz in Figure 2.35(b).

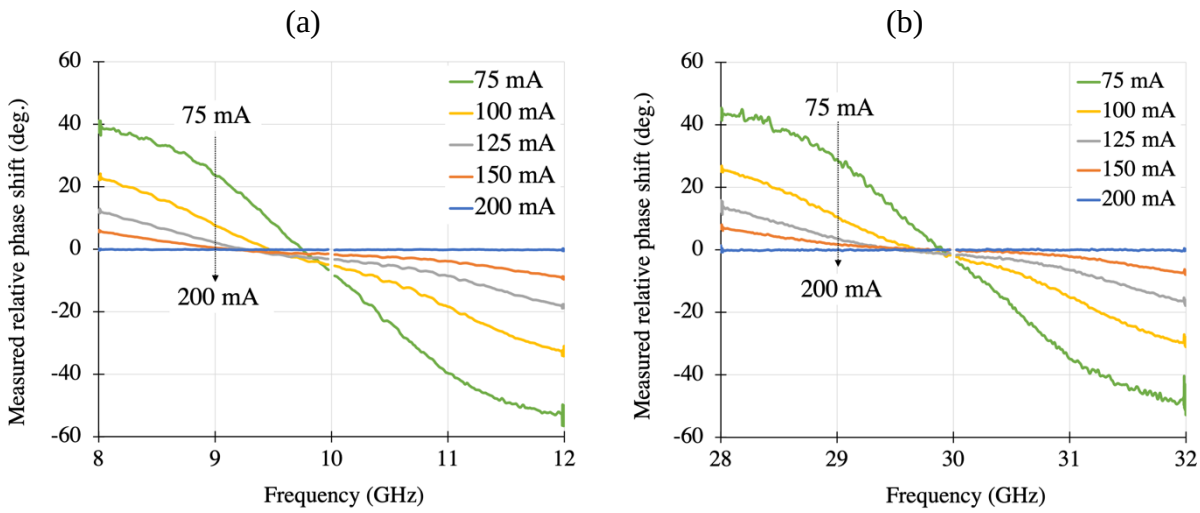

Figure 2.35 Measured relative phase shift using SOA-XN at different operating frequency: (a) at 10 GHz, and (b) at 30 GHz.

We can see that the measured relative phase shift for different bias currents at f_c = 10 GHz has the same phase variation as at f_c = 30 GHz. However, an offset on the relative phase shift response is obtained for f_c = 10 GHz, compared to f_c = 30 GHz.

The measured relative phase offset with respect to the reference for different I_{bias}, at f_c = 10 GHz and 30 GHz, is summarized in Table 2.6. We can note that the offset is lower for f_c = 30 GHz. Thus, the obtained experimental results validate the influence of f_c on the Up-CPO response that are given by the small signal analysis in equation (2.89).

Table 2.6 Phase offset for different bias current, at f_c = 10 and 30 GHz.

Bias current	***75 mA***	***100 mA***	***125 mA***	***150 mA***
f_c = 10 GHz	9.2°	5.5°	3.4°	1.8°
f_c = 30 GHz	2.5°	1.5°	0.4°	0°

2.5.6 Delay calculation of Up-CPO

After calculating the absolute Up-CPO phase responses in section 2.5.3.2, the corresponding delay can be calculated through the negative derivative of Up-CPO phase shift response versus frequency as in (1.12). The results are illustrated in Figure 2.36 and Figure 2.37. They show that the delay is not constant, a drop around $f_{c\pm10MHz}$ occurs. We notice that SOA-L responses present higher and sharper variations than SOA-NL and SOA-XN. We also see that the value of the drop decreases with the gain as seen in Figure 2.36 and Figure 2.37. We define the delay variation $\Delta_{delay\,p-p}$, as the variation between the top point at $f_{c\pm10MHz} \pm 0.5$ GHz and the bottom point at $f_{c\pm10MHz}$.

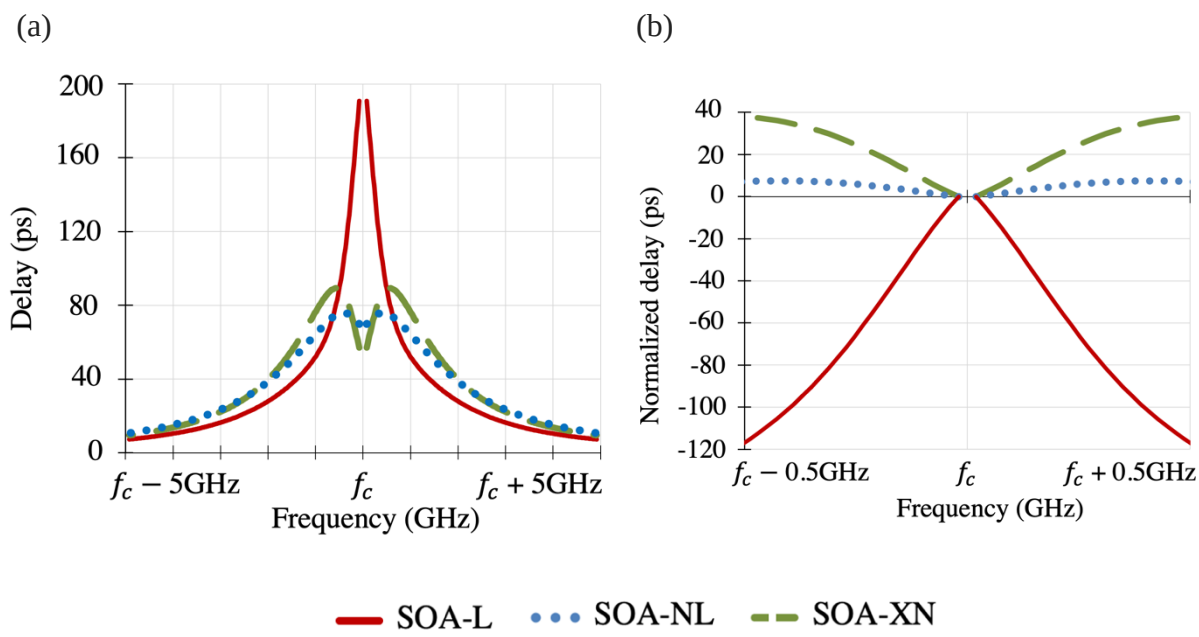

Figure 2.36 Calculated delay of SOA-L, SOA-NL and SOA-X for 10 GHz of frequency band at Gain 0 dB (a). Normalized delay of SOA-L, SOA-NL and SOA-XN for 1 GHz of frequency band (b).

As SOA-L presents a higher deviation, we only show the results of the delay variation for SOA-NL and SOA-XN in Table 2.7. We notice that at a gain 0 dB the variation for SOA-XN is about 41.1 ps, more significant than for the SOA-NL, about 8.1 ps. Besides, it shows that the higher the gain is, the smaller the variation in the delay response becomes.

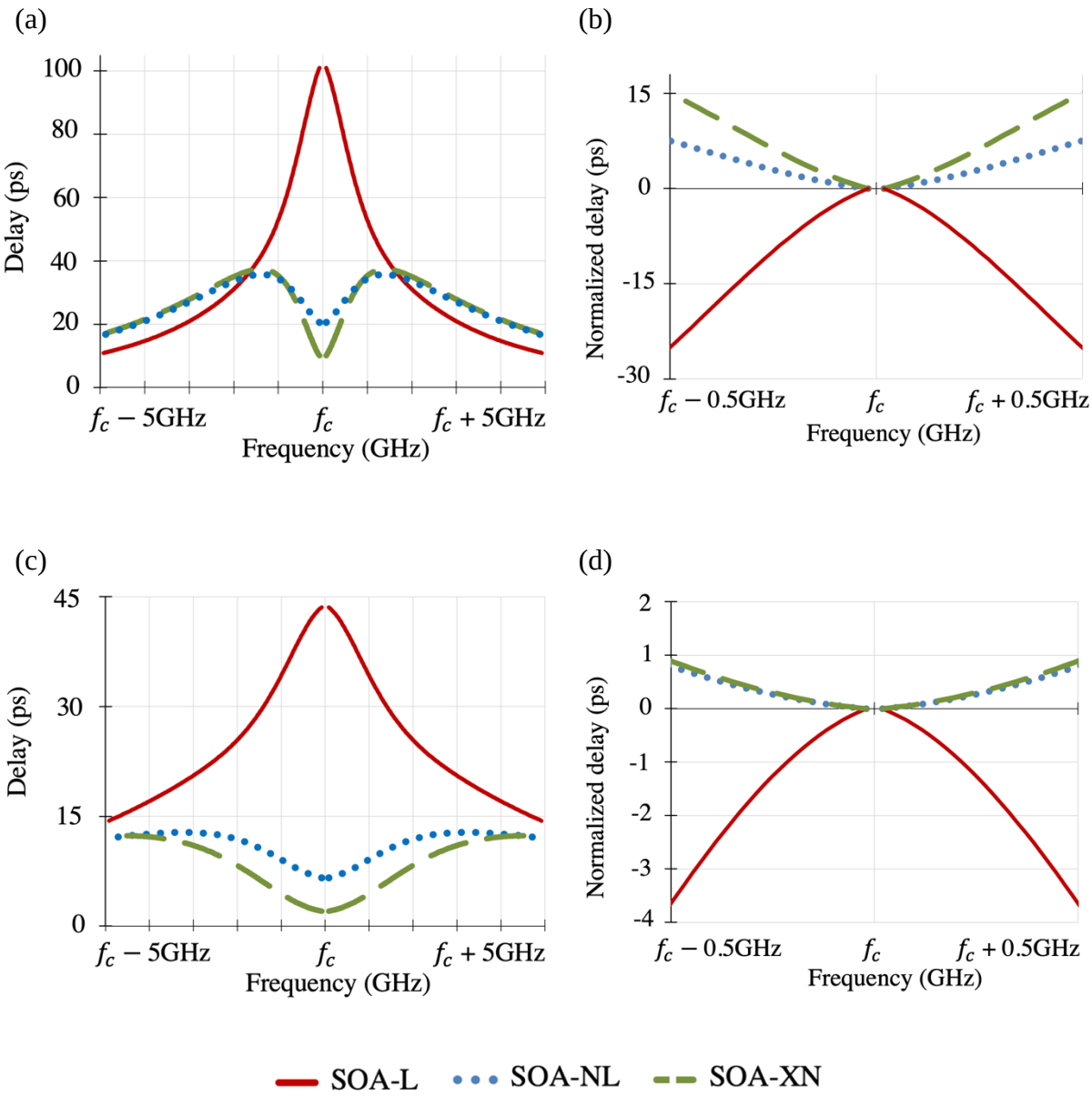

Figure 2.37 Calculated delay of SOA-L, SOA-NL and SOA-X for 10 GHz of frequency band: at Gain 5 dB (a), and at Gain 10 dB (c). Normalized delay of SOA-L, SOA-NL and SOA-XN for 1 GHz of frequency band at: Gain 5 dB (b), and Gain 10 dB (d).

Table 2.7 Delay variation ($\Delta_{delay\ p-p}$) over a frequency band of 1 GHz.

Delay depth (ps) at Gain	***0 dB***	***5 dB***	***10 dB***
SOA-NL	8.1	7.7	0.87
SOA-XN	41.1	11.2	0.91

$\Delta_{delay\ p-p}$ is measured for different frequency bands (0.15 GHz to 1.125 GHz) for SOA-NL and SOA-XN at gain 0 and 5 dB. The results are presented in Figure 2.38(a) and (c). We define the standard deviation of the delay σ_{delay} to measure the divergence from the mean value, Figure 2.38(b) and (d). A larger σ_{delay} indicates that the values tend to be far to the mean.

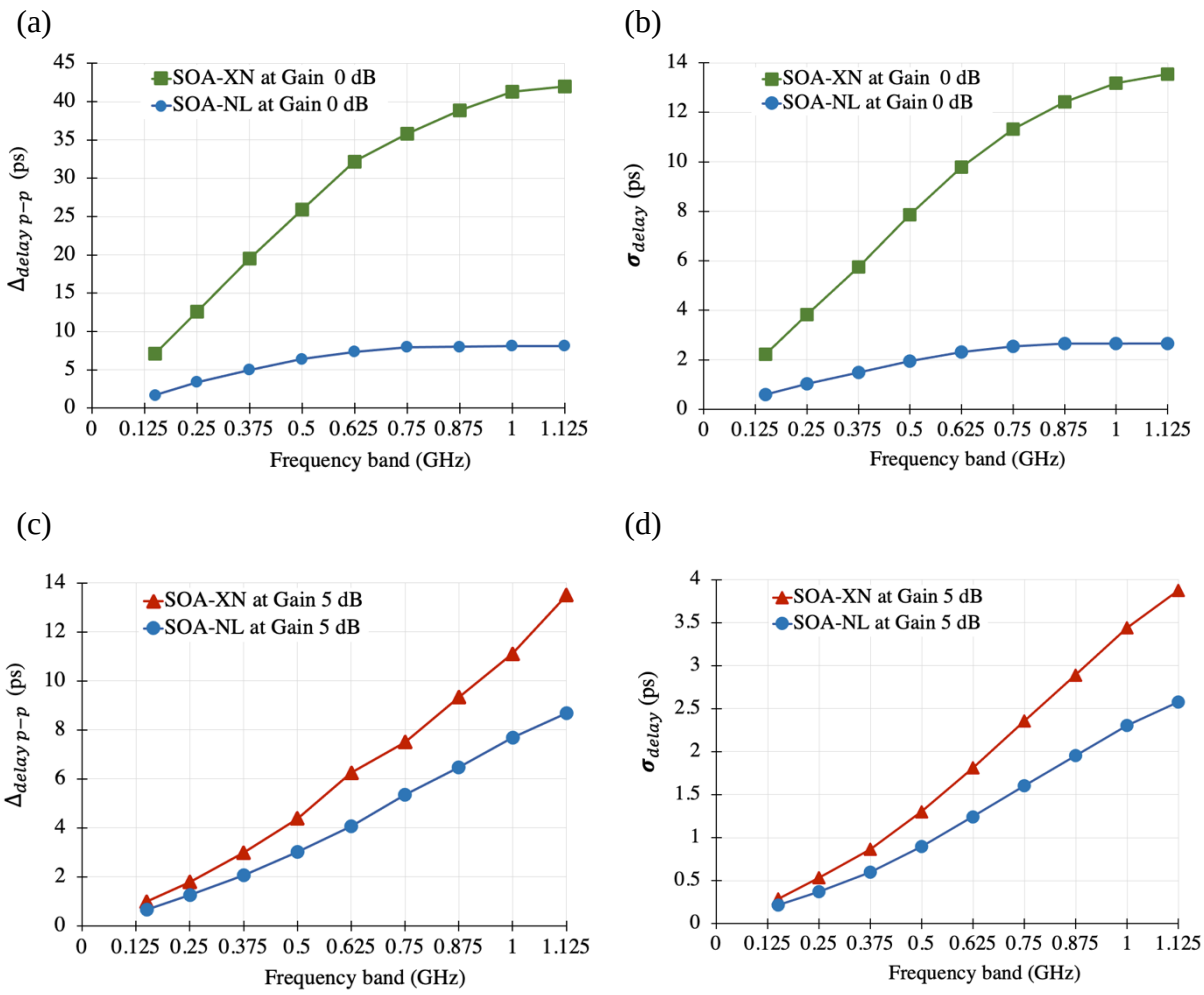

Figure 2.38 $\Delta_{delay\ p-p}$ and σ_{delay} for SOA-NL and SOA-XN versus frequency band at: Gain 0 (a)-(b), and 5 dB (c)-(d).

At gain 5 dB, the maximum $\Delta_{delay\,p-p}$ ~13.5 ps is registered for SOA-XN at 1.125 GHz accompanied with σ_{delay} of 3.8 ps, while for SOA-NL $\Delta_{delay\,p-p}$ is ~ 8.7 ps and σ_{delay} is 2.6 ps.

At gain 0 dB, $\Delta_{delay\,p-p}$ of SOA-XN varies from 7 ps to 42 ps in frequency bands ranging from 0.15 GHz to 1.125 GHz. This response is accompanied by a high σ_{delay} ~13 ps and is registered at gain 0 dB in the frequency band range of 1.125 GHz for SOA-XN.

For SOA-NL, $\Delta_{Delay\,p-p}$ varies from 1.7 to 8.2 ps. This response is accompanied by a σ_{delay} of 0.6 to 2.7 ps. We can conclude that both SOA-NL and SOA-XN have a non-constant delay response although SOA-XN has more nonlinearities compared to SOA-NL.

As we discussed in chapter one, to obtain TTD over a specific bandwidth, the delay must be constant over this frequency band. Our goal is to correct the delay variation of SOA-NL and SOA-XN over a bandwidth of 1 GHz. The focus is therefore to implement a second stage based on a RF approach, that will first correct first the Up-CPO nonlinear response of SOA (of the first stage), and second to obtain a TTD system.

2.6 Conclusion

In summary, an experimental comparison of phase shifts for four different SOA structures has been performed. We showed that nonlinear SOAs allow an adjustable relative phase shift higher than the linear ones. A relative phase shift of up to 89.3°, close to the theoretical maximum, is measured around 1 GHz for a SOA-XN at the cost of an increase in the RF gain penalty. With this latter SOA, we have also experimentally observed and theoretically investigated the particular response of the RF signal phase shift.

We have experimentally and theoretically analyzed the effects of XGM responses of a SOA on controlling the phase shift induced by CPO on an RF signal. We showed that, by using the XGM response of a control signal at the SOA output, the phase shifts on an RF signal can be adjusted independently of the optical power of the modulated input signal. The capabilities of the proposed setup can achieve tunable phase shifts in the range from 16° to 45°, for an input optical signal at −15 dBm and an external CW power of 5 dBm.

We have performed theoretical and experimental analysis of Up-CPO signal undergoing coherent population oscillations and pump-probe configuration in semiconductor optical amplifiers for different devices. We have calculated the amplitude, phase and delays of Up-CPO signal responses. We demonstrated that modeling SOAs by two sections is sufficient, both for linear and nonlinear SOAs, with a good agreement between theoretical and experimental results. Finally, we point to the delay variations of SOAs (SOA-NL and SOA-XN) and propose the use of a second stage to correct the delay response of SOA-NL and SOA-

XN in order to obtain a TTD system. This implementation is presented and described in chapter 3, based on high-frequency device which makes the originality of this study.

Bibliography of chapter 2

[1] S. Sales, W. Xue, J. Mork, and I. Gasulla, "Slow and Fast Light Effects and Their Applications to Microwave Photonics Using Semiconductor Optical Amplifiers," *IEEE Trans. Microwave Theory Techn.*, vol. 58, no. 11, pp. 3022–3038, Nov. 2010, doi: 10.1109/TMTT.2010.2075510.

[2] J. Mørk, R. Kjær, M. van der Poel, and K. Yvind, "Slow light in a semiconductor waveguide at gigahertz frequencies," *Opt. Express*, vol.13, no. 20, pp. 8136-8145, 2005, doi: 10.1364/opex.13.008136.

[3] M. J. Connelly, "Semiconductor optical amplifiers," Springer Science & Business Media, 2007, doi: 10.1007/b101817.

[4] M. J. Connelly, "Semiconductor Optical Amplifiers and their Applications," *3rd Spanish Meeting of Optoelectronics*, OPTOEL'03, 2003.

[5] P. Morel, "Modélisation des amplificateurs optiques à semi-conducteurs: du composant au système," *Thèse de doctorat, 2006.*

[6] R. Gutierrez-Castrejon, L. Schares, L. Occhi, and G. Guekos, "Modeling and measurement of longitudinal gain dynamics in saturated semiconductor optical amplifiers of different length," *IEEE J. Quantum Electron.*, vol. 36, no. 12, pp. 1476–1484, Dec. 2000, doi: 10.1109/3.892569.

[7] J. M. Senior and M. Y. Jamro, "Optical fiber communications: principles and practice," Pearson Education, 2009.

[8] G. P. Agrawal and N. A. Olsson, "Self-phase modulation and spectral broadening of optical pulses in semiconductor laser amplifiers," *IEEE J. Quantum Electron.*, vol. 25, no. 11, pp. 2297–2306, Nov. 1989, doi: 10.1109/3.42059.

[9] A. M. Clarke *et al.*, "FROG characterisation of SOA-based wavelength conversion using XPM in conjunction with shifted filtering up to line rates of 80 GHz," in *2006 IEEE LEOS*

Annual Meeting Conference Proceedings, Montreal, QC, Canada, Oct. 2006, pp. 152–153, doi: 10.1109/LEOS.2006.278919.

[10] D. Kastritsis, T. Rampone, K. E. Zoiros, and A. Sharaiha, "Modulation and Switching Architecture Performances for Frequency Up-Conversion of Complex-Modulated Data Signals Based on a SOA-MZI Photonic Sampling Mixer," *J. Light. Technol.*, vol. 38, no. 19, pp. 5375–5385, Oct. 2020, doi: 10.1109/JLT.2020.3011577.

[11] M. Matsuura and N. Kishi, "High-Speed Wavelength Conversion of RZ-DPSK Signal Using FWM in a Quantum-Dot SOA," *IEEE Photon. Technol. Lett*., vol. 23, no. 10, pp. 615–617, May 2011, doi: 10.1109/LPT.2011.2119396.

[12] P. Morel and A. Sharaiha, "Wideband Time-Domain Transfer Matrix Model Equivalent Circuit for Short Pulse Propagation in Semiconductor Optical Amplifiers," *IEEE J. Quantum Electron*., vol 45, no. 2, pp. 103-116, 2009, doi: 10.1109/JQE.2008.2001935.

[13] P. Berger, "Lumière lente et rapide dans les amplificateurs optiques à semi-conducteurs pour des applications en optique micro-onde et aux RADAR," *Thèse de doctorat*, Université de Paris Sud, U.F.R. Scientifique d'Orsay, 2012.

[14] P. Berger, J. Bourderionnet, F. Bretenaker, D. Dolfi, and M. Alouini, "Time delay generation at high frequency using SOA based slow and fast light," *Opt. Express,* 2011, vol. 19, no 22, p. 21180-21188, doi: 10.1364/OE.19.021180.

[15] C. Bohemond, T. Rampone, and A. Sharaiha, "Performances of a photonic microwave mixer based on cross-gain modulation in a semiconductor optical amplifier," *J. Lightw. Technol.*, vol. 29, no. 16, pp. 2402-2409, Aug. 2011, doi: 10.1109/JLT.2011.2158806.

[16] B. Cabon, J. Chazelas, and D. Dolfi, *Optoélectronique hyperfréquence: Modulation, liaisons et commutation*, vol. 4, E3331 vols. 2003.

[17] P. P. Baveja, D. N. Maywar and G. P. Agrawal, "Interband Four-Wave Mixing in Semiconductor Optical Amplifiers With ASE-Enhanced Gain Recovery," *IEEE J. Quantum Electron.,* vol. 18, no. 2, pp. 899-908, March-April 2012, doi: 10.1109/JSTQE.2011.2136372.

[18] P. P. Baveja, D. N. Maywar, A. M. Kaplan and G. P. Agrawal, "Self-Phase Modulation in Semiconductor Optical Amplifiers: Impact of Amplified Spontaneous Emission," *IEEE J. Quantum Electron.,* vol. 46, no. 9, pp. 1396-1403, Sept. 2010, doi: 10.1109/JQE.2010.2048743.

[19] D. A. O. Davies, "Small-signal analysis of wavelength conversion in semiconductor laser amplifiers via gain saturation," *IEEE Photon. Technol. Lett.*, vol. 7, no. 6, pp. 617–619, Jun. 1995, doi: 10.1109/68.388742.

[20] A. Meehan and M. Connelly, “Slow light based microwave photonic phase shifter using coherent population oscillations in a bulk tensile-strained semiconductor optical amplifier,” *25th IET Irish Signals & Systems Conference 2014 and 2014 China-Ireland International Conference on Information and Communications Technologies (ISSC 2014/CIICT 2014)*, Limerick, 2014, pp. 328-330, doi: 10.1049/cp.2014.0707.

[21] P. Berger, M. Alouini, J. Bourderionnet, F. Bretenaker, and D. Dolfi, “Dynamic saturation in semiconductor optical amplifiers: accurate model, role of carrier density, and slow light,” *Opt. Express*, vol. 18, no. 2, p. 685, Jan. 2010, doi: 10.1364/OE.18.000685.

[22] M. J. Connelly, “Wideband semiconductor optical amplifier steady- state numerical model,” *IEEE J. Quantum Electron.*, vol. 37, no. 3, pp. 439-447, 2001, doi: 10.1109/3.910455.

CHAPTER 3

Radio frequency phase shifter and true time delay hybrid structure

3.0 Introduction 113

3.1 Theory of microstrip lines 115

3.2 Theory of microwave filters 117

3.2.1 Transfer functions and general definition 119
3.2.2 Prototype lowpass Chebyshev filter 120
3.2.3 Chebyshev bandpass filter with lumped networks 121
3.2.4 Lowpass to bandpass transformation using immittance inverter 122
3.2.5 Richards transformation 124
3.2.6 Stub-type microstrip bandpass filters 125
3.2.7 Generalized coupling matrix 128
3.2.8 Cross coupling 130

3.3 Tunable radio frequency filter 131

3.3.1 Tunable filter design with ideal transmission lines 131
3.3.2 Synthesis of the tunable RF filter with distributed lines 135
3.3.3 Basic model of varactor diodes 138
3.3.4 Layout and EM simulation 140

3.3.4.1 Folded design 140
3.3.4.2 Curved design 142

3.4 Tunable radio frequency phase shifter 144

3.4.1 Analysis of the proposed structure 146
3.4.2 RF-PS design and simulation 148

3.5 Simulation of hybrid structure 152

3.5.1 Simulation results of delay correction 153
3.5.2 Simulation results of TTD hybrid structure 159

3.6 Conclusion 161

Bibliography of chapter 3 162

3.0 Introduction

As demonstrated in chapter 1, an ideal TTD must present a constant delay over the instantaneous bandwidth B_{ins} ((Figure 3.1(c)), with constant amplitude or RF power (Figure 3.1(a)) and the projections of the linear phase shift for each configuration of the tunable device at 0 Hz equal to ϕ_{offset} = 360° × k (k is an integer number) (Figure 3.1(b)). This chapter aims to realize constant tunable delay lines and TTD.

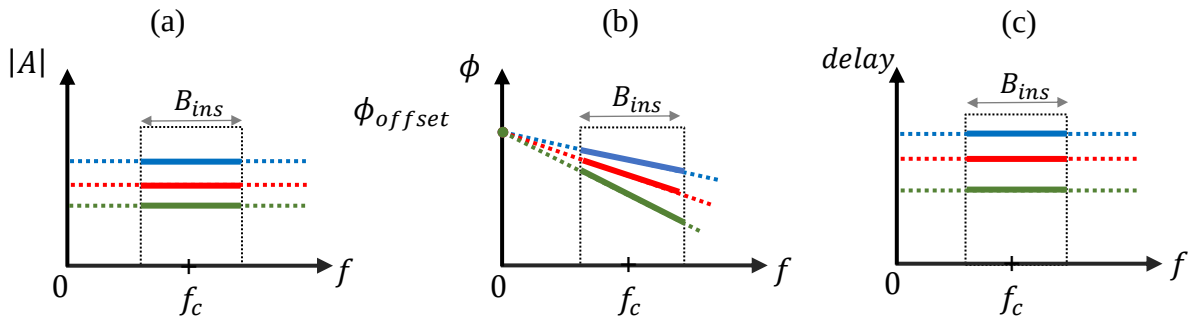

Figure 3.1 Characteristics of an ideal TTD over the instantaneous bandwidth (B_{ins}) near the carrier operating frequency (f_c), (a) amplitude frequency response, (b) phase frequency response, (c) delay frequency response.

As seen in chapter 2, SOA-NL and SOA-XN have nonlinear responses, where a depth occurs over the delay response (section 2.5.6). Therefore, to obtain a TTD, we first need to correct the nonlinearity responses of SOAs. In order to obtain a flat response of delay, a second stage should be added, having the shape of the inverse response of SOA delay. Figure 3.2(a) shows the delay response of SOA-NL/XN (solid line), and the delay response of RF filter, which has a ripple in delay, and it is equal to the inverse of the depth (dashed line). By combining the delay response of SOA-NL/XN and RF filter, a flat delay is obtained (see Figure 3.2(b)).

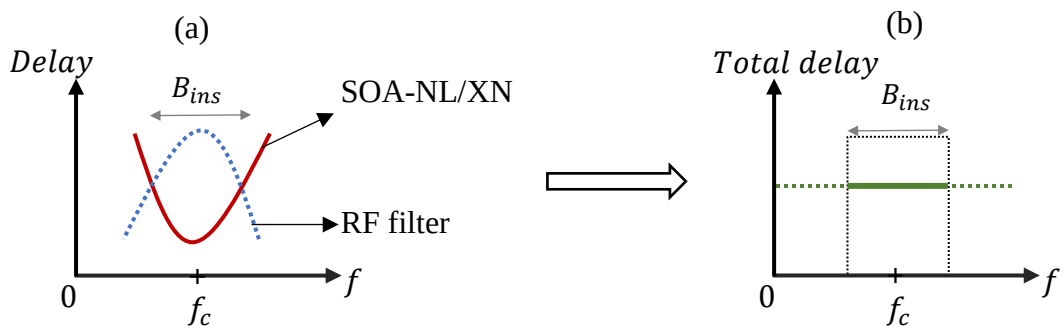

Figure 3.2 Illustration of hybrid delay correction.

In this chapter, we propose a hybrid optical-microwave structure to generate a TTD by implementing a photonic-RF hybrid structure as shown in Figure 3.3. The tunable RF phase shift/delay at high frequency function is performed by the photonic stage using an Up-converted CPO in SOAs (presented in Chapter 2), second is an RF stage needed to correct nonlinearity responses of SOAs, and for tuning the offset phase (ϕ_{offset}) of the corrected response to achieve a TTD system. The second stage consists of a tunable RF phase shift, based on a RF folded filter (RF-FF), which will correct the nonlinearity responses of SOAs. This stage is known as "hybrid correction structure". The corrected delay can be electrically manipulated by voltage control (V_{DC}) of variable capacitance (varactor) of RF folded filter with respect to the operating point of SOA (bias current). The RF phase shifter (RF-PS) will be placed after the tunable RF folded filter, so that the phase offset can be tuned by controlling the capacitance values. This stage is known as "TTD hybrid structure". Indeed, by combining the two stages, we will show in this chapter that a TTD can be achieved over a bandwidth of nearly 1 GHz by simulation.

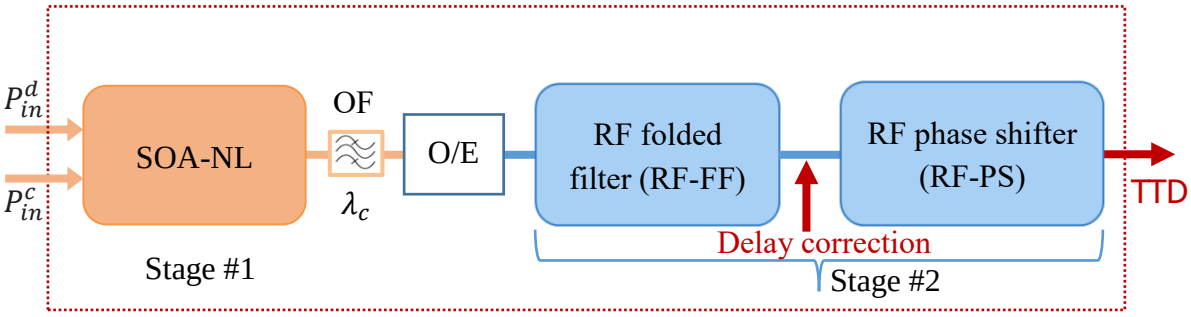

Figure 3.3 TTD hybrid structure.

In this chapter, we discuss the characteristics of a microstrip line, describe the theory behind a microstrip filter, and discuss the Chebyshev filter used in the design part where we introduce half-wavelength open-circuit stubs bandpass filters. First, we present tunable RF filters; folded filter (RF-FF) and curved filter (RF-CF), followed by a Radio Frequency Phase Shifter (RF-PS) with a tunable phase offset. We will discuss how cross coupling can be reconfigured to obtain a coupling that can be physically realized. We also present the layout and electromagnetic (EM) simulation of both tunable RF filters and RF-PS, followed by experimental results for the tunable RF filter's so-called folded and curved filters. Finally, RF-FF and RF-PS of the second stage are then merged with the first stage, in order to correct the nonlinearities and obtain a TTD. The simulation results of delay correction and TTD hybrid structure are presented.

3.1 Theory of microstrip lines

Printed circuit boards (PCBs) are the best common method for assembling electronic circuits. It offers a reduction size and weight of the overall electronic circuit, improving connection reliability, and low manufacturing cost. Planar transmission lines are widely used in printed circuits to ensure signal transport between various active and passive components. There are several reasons for the use of planar transmission lines, such as broadband, high reliability, and the realization of compact dimensions and light weight circuits. Due to the simplicity of the associated etching process, the microstrip line is the most widely used planar technology in the application of various microwave devices. It allows a simple assembly of elements in series. The transfer of lumped elements in parallel requires installing metallized holes between the conductor and the ground plane, leading to parasitic effects, which is a disadvantage of this technology. Microstrip has found applications frequencies ranging from 0.01 GHz up to 10 THz [1] [2].

A microstrip line consists of a flat metal strip acting as a conductor etched on the upper side of a dielectric substrate, and a ground plane placed on the opposite side as shown in Figure 3.4(a).

Due to the dielectric constant of the substrate being higher than that of air, the electromagnetic field lines are mainly concentrated in the substrate between the conductor and the ground plane. However, a small part of the electromagnetic field is located outside the dielectric (in air). In this case, the propagation mode is not pure transverse electric-magnetic (TEM), due to difference in velocities between the air and the substrate. Instead, the dominant mode of propagation is quasi-TEM mode with little dispersion. Figure 3.4(b) shows the distribution of the electric and magnetic fields in the cross-section of the microstrip line.

The quasi-TEM mode is the fundamental hybrid HE_0 mode with zero cut-off frequency [3]. As the frequency rises, higher order hybrid modes can propagate through the microstrip guide [3]. Their propagation is facilitated by the increase in substrate thickness. In order to avoid the appearance and propagation of these parasitic modes, it is therefore essential to have low substrate thicknesses at high frequencies. It should also be noted that for low permittivity values, microstrip structures are more likely to radiate at high frequencies. Similarly, radiation can be reduced by reducing the substrate thickness.

In the case of the microstrip line, the guided wavelength in the substrate for a frequency *f* is:

$$\lambda_g = \frac{\lambda_0}{\sqrt{\varepsilon_{eff}}} \tag{3.1}$$

where $\lambda_0 = \frac{c}{f}$ is the wavelength in free space, and ε_{eff} is the effective permittivity constant. The associated propagation constant and phase velocity are:

$$\beta = \frac{2\pi}{\lambda_g} \tag{3.2}$$

$$v_g = \frac{2\pi f}{\beta} \tag{3.3}$$

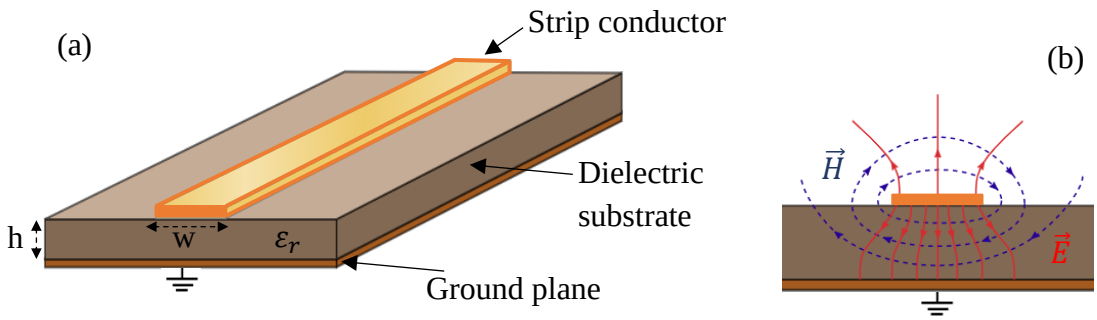

Figure 3.4 Schematic of (a) microstrip line, and (b) field distribution at the cross section of a microstrip line, $\vec{H}$: Magnetic field (doted lien), and $\vec{E}$: Electric field (solid line).

The effective dielectric constant of a microstrip line is given by [4] [5].

$$\varepsilon_{eff} = \begin{cases} \dfrac{(\varepsilon_r+1)}{2} + \dfrac{(\varepsilon_r-1)}{2}\left[\dfrac{1}{\sqrt{1+12\left(\frac{h}{w}\right)}} + 0.04\left(1-\left(\frac{w}{h}\right)\right)^2\right], & \dfrac{w}{h} \le 1 \\ \dfrac{(\varepsilon_r+1)}{2} + \left[\dfrac{(\varepsilon_r-1)}{2\sqrt{1+12\left(\frac{h}{w}\right)}}\right] & \dfrac{w}{h} \ge 1 \end{cases} \tag{3.4}$$

In equation (3.4), w represents the width of the microstrip line, h the thickness of the substrate, and ε_r the dielectric constant of the substrate.

Given the dimensions, the characteristic impedance of the microstrip line can be derived from the effective permittivity and the dimensions w and h, (see (3.5)).

$$Z_0 = \begin{cases} Z_0 = \dfrac{60}{\sqrt{\varepsilon_{eff}}} \ln\left(\dfrac{8h}{w} + \dfrac{w}{4h}\right), & \dfrac{w}{h} \leq 1 \\ \dfrac{120\pi}{\sqrt{\varepsilon_{eff}\left[\dfrac{w}{h} + 1.393 + 0.667\ln\left(1.444 + \dfrac{w}{h}\right)\right]}} & \dfrac{w}{h} \geq 1 \end{cases} \tag{3.5}$$

with the given value of Z_0 and the dielectric constant of ε_r, the ratio of *w/h* can be obtained by [4] [5]:

$$\frac{w}{h} = \begin{cases} \dfrac{8e^A}{e^{2A} - 2}, & \dfrac{w}{h} < 2 \\ \dfrac{2}{\pi}[B - 1 - \ln(2B - 1)] + \dfrac{\varepsilon_r - 1}{2\varepsilon_r}\left(\ln(B - 1) + 0.39 - \dfrac{0.61}{\varepsilon_r}\right) & \dfrac{w}{h} > 2 \end{cases} \tag{3.6}$$

where

$$A = \frac{Z_0}{60}\sqrt{\frac{\varepsilon_r+1}{2}} + \frac{\varepsilon_r-1}{\varepsilon_r+1}\left(0.23 + \frac{0.11}{\varepsilon_r}\right), \text{ and } B = \frac{377\pi}{2Z_0\sqrt{\varepsilon_{eff}}}.$$

The physical length of a microstrip line with electrical length of θ_l at frequency of *f* can thus be calculated by:

$$l = \frac{\theta_l}{\beta} = \frac{c\,\theta_l}{2\pi f\sqrt{\varepsilon_{eff}}} \tag{3.7}$$

3.2 Theory of microwave filters

In order to correct the nonlinear response of the SOA (presented in section 2.4.3.2 and section 2.4.4), we adopt the use of a microwave tunable filter to correct these nonlinearities. In the following parts, the theory of microwave filter is presented.

Microwave filters play an essential role in modern telecommunication systems. They enable many applications (audio, video, telecommunications, instrumentation, and radar) to share and maximize the use of limited spectrum resources, notably by limiting interference between systems. Filtering a signal is a delicate operation that consists of controlling the signal in a frequency band, selecting the useful components (bandwidths) and isolating the undesirable ones (attenuated bands).

A filter is defined, at a given frequency band, by the following specifications:

- The amplitude response (transmission and reflection).
- The group delay: it shows the linearity variation in the phase introduced by the filter. In some applications, it is necessary to have filters with a linear phase over the operating bandwidth. Such systems delay each frequency component by the same amount, thus avoiding time distortion.

Depending on the position of the bandwidth and attenuating bands in the frequency response, the filters can be classified into four categories: low-pass, high-pass, bandpass, and notch filters. As shown in Figure 3.5, the bandwidth of the low-pass filter is between 0 and ω_c, while high-pass filter has opposite specifications. The bandpass filter on the other hand only selects desired band frequencies between ω_{c1} and ω_{c2}. A complement to the bandpass filter is a Band reject or notch filter. It serves to eliminate undesired band frequencies between ω_{c1} and ω_{c2}.

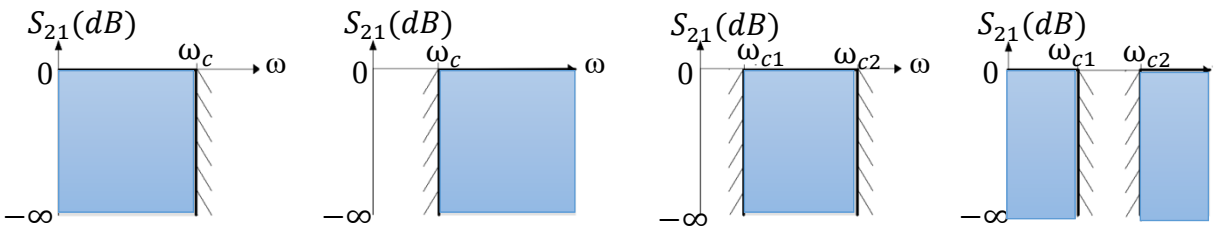

Figure 3.5 Idealized filter responses: (a) Low-pass, (b) High-pass, (c) Bandpass, and (d) notch.

Filter responses are mostly classified into four types: Butterworth, Bessel, Chebyshev, and Elliptic.

The Butterworth filter response refers to the maximally flat response, because the passband response offers the steepest roll-off (roll-off is the steepness of a transfer function with frequency) without inducing a ripple in the passband.

The Bessel filter has a flat response of the group delay (no ripple), with poor selectivity. The magnitude response decreases rapidly in the passband, and the stopband attenuation is reduced.

The Chebyshev filter is characterized by ripples that exist in the passband. The amplitude of these ripples is directly proportional to the steepness of the roll-off. For a steeper response, a more significant ripple response is required. The response of the phase and delay are nonlinear. Chebyshev filters have the smallest error between idealized and actual filter characteristics over the range of the filter, accompanied by ripples in the passband. Chebyshev filter has a steeper roll-off near the cutoff frequency when compared to Butterworth and Bessel filters. Chebyshev filters offer a better selectivity compared to Butterworth and Bessel filters.

Elliptic filters are known for their ripple response that is present in both passband and stopband. The passband ripple of the elliptic filter is similar to that of the Chebyshev filter. However, selectivity is greatly improved, which in turn requires more components (more complex filter).

In this work, only bandpass filter based on Chebyshev prototype filter is considered, which is characterized by the passband ripple and offers good selectivity. In addition, the ripple in passband can be adjusted.

3.2.1 Transfer functions and general definition

The transfer function of a two-port filter network is a mathematical description of network response characteristics, namely, a mathematical expression of S_{21} [6]. The Chebyshev response that exhibits the ripple in the passband and a maximally flat stopband is shown in Figure 3.6.

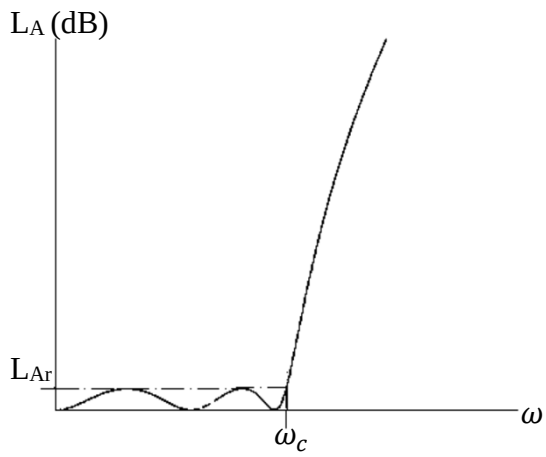

Figure 3.6 Chebyshev lowpass response, ω_c is the cutoff angular frequency [6].

The amplitude of the insertion loss of Chebyshev nth order can be expressed as:

$$|S_{21}(j\omega)|^2 = \frac{1}{1 + \varepsilon^2 {T_n}^2(\omega)} \tag{3.8}$$

In this expression, ω is an angular frequency variable, $T_n(\omega)$ is the nth order Chebyshev polynomial, and ε is related to the rate of ripple constant in the bandwidth. ε and $T_n(\omega)$ are defined as follows:

$$\varepsilon = \sqrt{10^{\frac{L_{Ar}}{10}} - 1} \tag{3.9}$$

where L_{Ar} is the passband ripple in dB and the nth order is determined from the attenuation requirement of the stopband.

$$T_n(\omega) \; == \begin{cases} \cos(n\, cos^{-1}), & |\omega| \leq 1 \\ \cosh(n\; cosh^{-1}) & |\omega| \geq 1 \end{cases} \tag{3.10}$$

The phase response and group delay of the filter can be found as:

$$\phi_{21}(\omega) = Arg\, S_{21}(j\omega) \tag{3.11}$$

$$\tau_{d,LPF}(\omega) = -\frac{d\phi_{21}(\omega)}{d\omega} \tag{3.12}$$

where $\phi_{21}(\omega)$ is in radians, ω is in rad/s and $\tau_{d,LPF}(\omega)$ is in seconds.

3.2.2 Prototype lowpass Chebyshev filter

A Chebyshev lowpass prototype filter is interpreted as the filter whose element values are normalized to make the source resistance or conductance equal to one, denoted by $g_0 = 1$, and the cutoff angular frequency $\omega_c = 1$ (rad/s).

A prototype lowpass filter comprises localized capacitive and inductive elements determined from the specifications. Design of the bandpass filter is based on this lowpass prototype, for which some necessary transformations will be rendered (impedance and frequency transformation). A schematic of the lowpass filter prototype is shown in Figure 3.7.
It's made by alternating shunt capacitances and series inductances. The g-elements represent impedances for the series elements and admittance for the shunt elements.

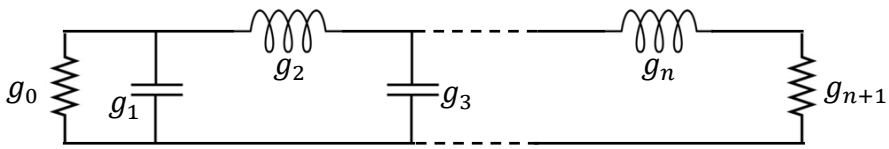

Figure 3.7 Lumped circuits for lowpass prototype Chebyshev filters with even n: first element is a shunt capacitor, and the last element is a series inductor.

The expressions for g-elements can be calculated using the following formulae [6]:

$$g_0 = 1$$

$$g_1 = \frac{2}{\gamma}\sin\left(\frac{\pi}{2n}\right)$$

$$g_i = \frac{1}{g_{i-1}} \frac{4sin\left[\frac{(2i-1)\pi}{2n}\right].sin\left[\frac{(2i-3)\pi}{2n}\right]}{\gamma^2 + sin^2\left[\frac{(i-1)\pi}{n}\right]} \qquad \text{for i = 2, 3, ...n}$$

$$g_{n+1} = \begin{cases} 1, & \text{for n even} \\ coth^2\left(\frac{\chi}{4}\right) & \text{for n odd} \end{cases} \tag{3.13}$$

where $\chi = \ln\left[coth\left(\frac{L_{Ar}}{17.37}\right)\right]$, and $\gamma = sinh\left(\frac{\chi}{2n}\right)$.

The passband ripples can be expressed as:

$$L_{Ar}(\omega) = -10\log_{10}(1 - 10^{0.1L_R}) \tag{3.14}$$

3.2.3 Chebyshev bandpass filter with lumped networks

Once the prototype filter is ready, it can be used for impedance and frequency transformation. A transformation to bandpass is needed for getting bandpass characteristics. In the transformation, the serial inductance *L* will be converted to serial combinations of L_{si} and C_{si}, whereas the shunt capacitance *C* becomes shunt combination of L_{pi} and C_{pi} as shows Figure 3.8.

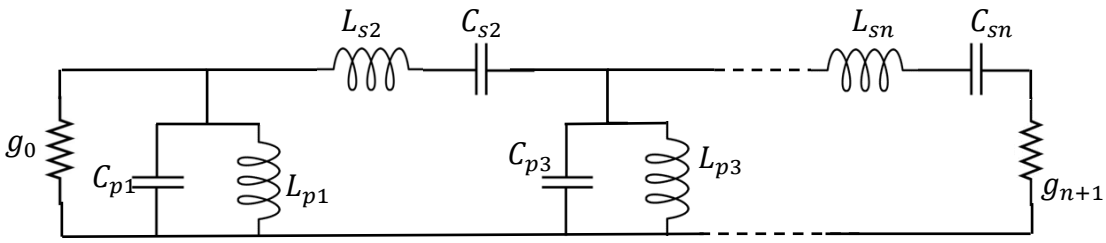

Figure 3.8 Lumped circuits for bandpass prototype Chebyshev filters with even n: first element is a shunt capacitor and a shunt inductor, and the last element is an inductor and capacitor in series.

The frequency response of a bandpass filter is given by the well-known conventional frequency transformation lowpass filter (LPF) to bandpass filter (BPF):

$$\omega_{new} = \frac{1}{FBW}\left(\frac{\omega}{\omega_0} - \frac{\omega_0}{\omega}\right) \tag{3.15}$$

where the center frequency is given by $\omega_0 = \sqrt{\omega_1 \omega_2}$, the fractional bandwidth is $FBW = \frac{\omega_2 - \omega_1}{\omega_0}$, and the cutoff frequencies ω_1 and ω_2 acting as lower and upper boundary.

The series inductors of the lowpass prototype are converted to series resonators as follows:

$$L_{si} = \left(\frac{1}{FBW\omega_0\omega_c}\right)\frac{Z_0}{g_0\, g_i} \qquad C_{si} = \left(\frac{FBW\omega_c}{\omega_0}\right)\frac{g_0\, g_i}{Z_0} \tag{3.16}$$

The shunt capacitors of the lowpass prototype are converted to shunt resonators as follows:

$$L_{pi} = \left(\frac{FBW\omega_c}{\omega_0}\right)\frac{Z_0\, g_i}{g_0} \qquad C_{pi} = \left(\frac{1}{FBW\omega_0\omega_c}\right)\frac{g_0}{Z_0\, g_i} \tag{3.17}$$

here Z_0 is the value of the load impedance, generally set to 50 Ω.

The group delay response of the bandpass filter is then computed with:

$$\tau_{d,BPF}(\omega) = \frac{\tau_{d,LPF}(\omega)}{FBW\omega_0}\left[1 + \left(\frac{\omega_0}{\omega}\right)^2\right] \tag{3.18}$$

3.2.4 Lowpass to bandpass transformation using immittance inverter

The term microwave applies to the frequency band ranging between 300 MHz and 300 GHz, which corresponds to wavelengths in the air between 1 meter and 1 millimeter. The dimensions used in this frequency range will therefore have to be considered in the device design. The distributed element is where the transmission lines-in which the resistance, capacitance and inductance are distributed throughout the line. Distributed networks are comprised of transmission line elements rather than resistors, inductors and capacitors. It used mostly at microwave frequencies, where lumped components are impossible to implement. Indeed, it is obviously no longer a question of using models with localized elements (resistor, inductor or capacitor) but distributed models. To do this, it is often interesting to use classical lumped schemes with impedance and admittance inverters [7]. Immittance inverters have the ability to shift impedance/or admittance depending on the choice of K or J parameters. Making use of these properties enables to convert a lumped filter circuit to an equivalent form that is more convenient for implementation with microwave structures.

Immittance inverters transform an impedance into an admittance (K-inverter) or, alternatively, an admittance into an impedance (J-inverter). The property of an idealized immittance inverter is frequency invariance. Referring to Figure 3.9(a), when the inverter is terminated with an immittance (Z_t *or* Y_t) at one end, the immittance seen at the other end (Z_1 *or* Y_1) will be [6] [7]:

$$Z_1 = \frac{K^2}{Z_t} \qquad Y_1 = \frac{J^2}{Y_t} \tag{3.19}$$

$$\begin{bmatrix} A & B \\ C & D \end{bmatrix} = \begin{bmatrix} 0 & jK \\ j/K & 0 \end{bmatrix} \qquad \begin{bmatrix} A & B \\ C & D \end{bmatrix} = \begin{bmatrix} 0 & j/J \\ jJ & 0 \end{bmatrix} \tag{3.20}$$

here K is real and defined as the characteristic impedance of the inverter K-inverter, J-inverter is real and defined as the characteristic admittance of the J-inverter. The admittance and impedance inverters used are characterized by their ABCD matrices (3.20).

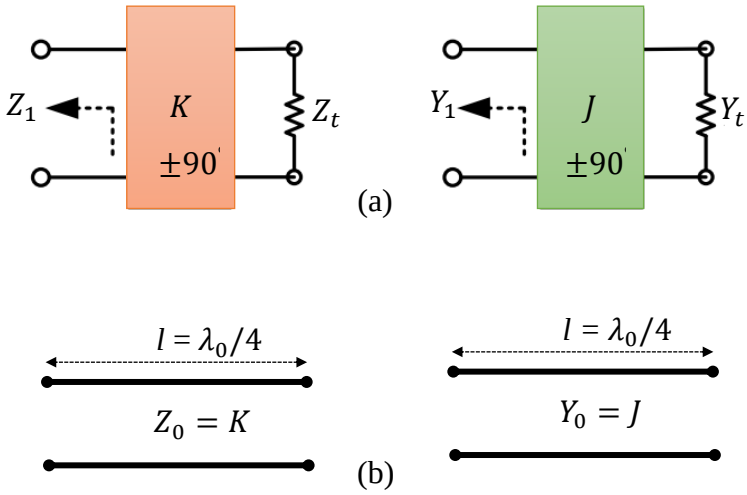

Figure 3.9 Network representation of the single terminated (a) K-inverter and J-inverter, (b) Example of realization of the inverters by quarter-wavelength distributed lines.

One of the simplest alternatives of the inverter is the use of a quarter wavelength of characteristic impedance K or J for an admittance inverter (Figure 3.9(b)). Quarter wavelengths can transform a series connected element to shunt, and vice versa.

The impedance and frequency transformation used to obtain the bandpass filter from the lowpass prototype results in a filter network containing parallel and serial resonators [7]. However, to simplify the filter topology and make it practically feasible, it is practically advantageous to use one of the two types of resonators, either in series or parallel. The transformation from one type of resonator to another is obtained by using the previously proposed circuit called an impedance or admittance inverter. The impedance inverter can be used for the design of bandpass filters with series resonators only. Similarly, the admittance inverter is used for the design of bandpass filters using only parallel resonators. Figure 3.10 shows the use of impedance and admittance inverters to convert series resonators to parallel and vice versa.

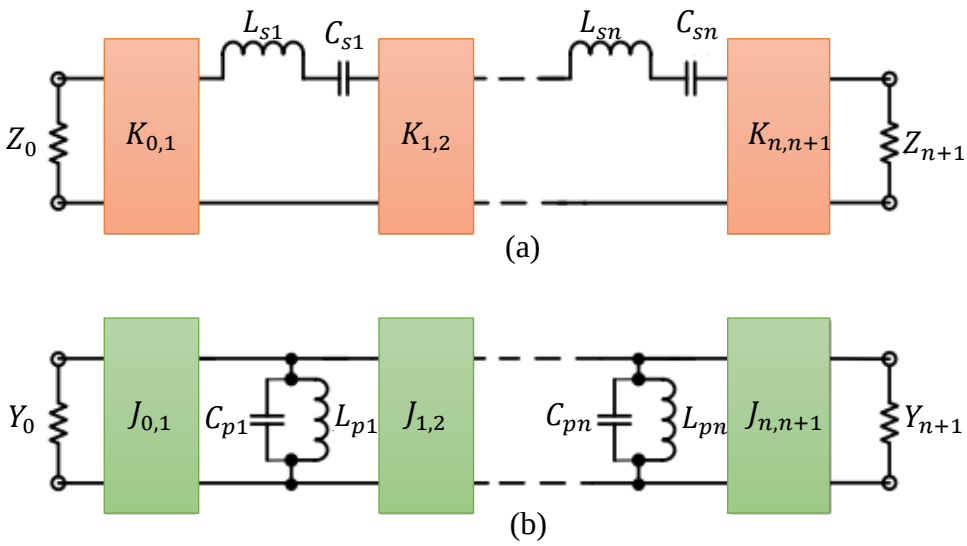

Figure 3.10 Bandpass filters with: (a) impedance inverter, and (b) admittance inverter.

The representation of an nth order filter (in Figure 3.10(b)) consists of *n* resonators (LC) parallel and coupled to each other by n+1 inverters. The admittance Y_i can be expressed by:

$$Y_i = \frac{1}{jL_i\omega} + jC_i\omega = jB_i(\omega) \tag{3.21}$$

where B_i is the susceptance.

The parameter of admittance slope b_i (slope parameter) is expressed as follows:

$$b_i = \left.\frac{dB_i(\omega)}{d\omega}\right|_{\omega=\omega_0} \tag{3.22}$$

3.2.5 Richards transformation

In order to convert lumped elements (L, C) into equivalent transmission lines, Richards transformation is used [6] [7]. It makes a direct analogy between lumped and distributed elements around a resonance frequency f_0. A transmission line can be assimilated into a resonant circuit according to its length and load (open or short circuit). Table 3.1 presents a summary of equivalent results from the Richards transformation.

Table 3.1 Transmission lines equivalent circuit in lumped element.

	$l = \frac{\lambda_0}{8}$	$l = \frac{\lambda_0}{4}$	$l = \frac{\lambda_0}{2}$
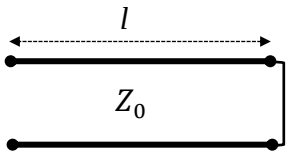	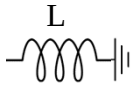	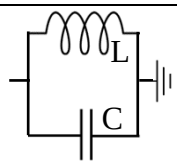	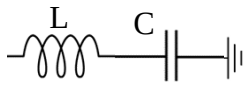
short circuit	$L = \frac{Z_0}{\omega_0}$	$L\omega_0 = \frac{1}{C\omega_0} = \frac{\pi Z_0}{2}$	$L\omega_0 = \frac{1}{C\omega_0} = \frac{2Z_0}{\pi}$
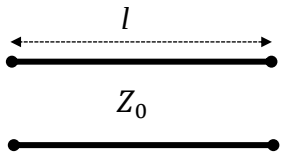		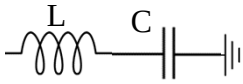	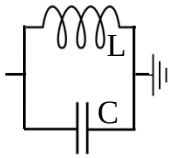
Open circuit	$C = \frac{1}{Z_0\omega_0}$	$L\omega_0 = \frac{1}{C\omega_0} = \frac{4Z_0}{\pi}$	$L\omega_0 = \frac{1}{C\omega_0} = \frac{\pi Z_0}{4}$

3.2.6 Stub-type microstrip bandpass filters

Ultra-Wide Band (UWB) technology has great potential in the development of various modern transmission systems. UWB microstrip filters can be constructed from distributed elements. Such a type of bandpass filter is the quarter-wavelength shunt short-circuited stubs. It consists of a cascade shunt short-circuited stubs of electrical length $l = \lambda_0/4$, which is the equivalent circuit of transmission line (TL) in short circuit configuration (see Table 3.1), separated by $\lambda_0/4$ inverters (equivalent TL is presented in (Figure 3.9(b)), so-called connecting lines (Figure 3.11), where λ_0 is the wavelength in the medium propagation at the operating frequency f_0.

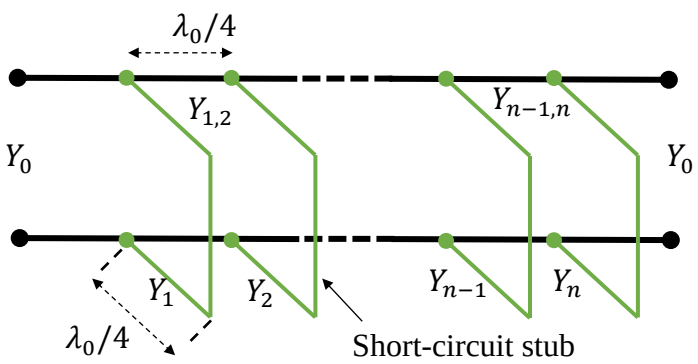

Figure 3.11 General circuit model of quarter-wavelength shunt short-circuited stubs.

The lowpass prototype should be used to determine the g-parameters (section 3.2.2). The filter has *n* shunt stubs for *n*-reactive elements in the prototype. The characteristic admittances of the stubs Y_i and the connecting lines (quarter-wavelength inverters) $Y_{i,i+1}$ are obtained using the well-known formulas [6] [7].

Characteristic admittances of the connecting lines can be found by:

$$Y_{i,i+1}\Big|_{i=1\ to\ n-1} = Y_0\left(\frac{J_{i,i+1}}{Y_0}\right) \tag{3.23}$$

where $J_{i,i+1}$ is the J-inverter given by:

$$\frac{J_{1,2}}{Y_0} = g_0\sqrt{\frac{C_a}{g_2}}$$

$$\frac{J_{n-1,n}}{Y_0} = \sqrt{\frac{C_a g_{n+1}}{g_0 g_{n-1}}}$$

$$\frac{J_{i,i+1}}{Y_0}\Bigg|_{i=2\ to\ n-2} = \frac{g_0 C_a}{\sqrt{g_i g_{i+1}}} \tag{3.24}$$

with $C_a = 2.d.g_1$, and d is a dimensionless constant ($0 < d \leq 1$) that may be assigned to another value to give a convenient admittance level inside the filter [7].

The characteristic admittances of the shunt stubs can be found by:

$$Y_1 = g_0 Y_0 (1-d) g_1 \tan\theta_l + Y_0\left(N_{12} - \frac{J_{1,2}}{Y_0}\right) \tag{3.25}$$

$$Y_i|_{i=2\ to\ n-1} = Y_0\left(N_{i-1,i} + N_{i,i+1} - \frac{J_{i-1,i}}{Y_0} - \frac{J_{i,i+1}}{Y_0}\right) \tag{3.26}$$

$$Y_n = Y_0(g_n g_{n+1} - d g_0 g_1)\tan\theta_l + Y_0\left(N_{n-1,n} - \frac{J_{n-1,n}}{Y_0}\right) \tag{3.27}$$

here $\theta_l = \frac{\pi}{2}\left(1 - \frac{FBW}{2}\right)$, and $N_{i,i+1}\Big|_{i=1\ to\ n-1} = \sqrt{\left(\frac{J_{i,i+1}}{Y_0}\right)^2 + \left(\frac{g_0 C_a \tan\theta_l}{2}\right)^2}$.

Figure 3.12 shows the configuration of the bandpass filter constructed with half-wavelength open-circuited stubs connected by $\lambda_0/4$ inverters (connecting lines). Using $\lambda_0/2$ stubs is advantageous to create transmission zeros at $\omega_0/2$ and $3\omega_0/2$, thus, this filter has an improved frequency selectivity. This is done by replacing the quarter-wavelength short-circuited stubs (presented in Figure 3.11) by half-wavelength open-circuited ones that use two quarter-wavelength stubs, the resultant filter will have similar passband characteristics but quite different stopband characteristics. This type of filters will have additional bandpass in the vicinity of $\omega_0 = 0$ and $\omega = 2\omega_0$, and at other corresponding periodic frequencies [7].

The stepped impedance half-wavelength open-circuited stubs, which are composed of $\lambda_0/4$ inner line and $\lambda_0/4$ outer open stub are found using the characteristic admittance of the transmission line [7]:

$$Y_i' = \frac{Y_i(a\tan^2\theta_l - 1)}{(a+1)\tan^2\theta_l} \tag{3.28}$$

$$Y_i'' = a\,Y_i' \tag{3.29}$$

where $a = \cot^2\theta_l\left(\frac{\pi\omega_\infty}{2\omega_0}\right)$, and $\omega_\infty < \omega_1$ is the frequency at which the shunt open-circuited stub presents a short circuit to the main transmission line and causes a transmission zero or attenuation pole [7].

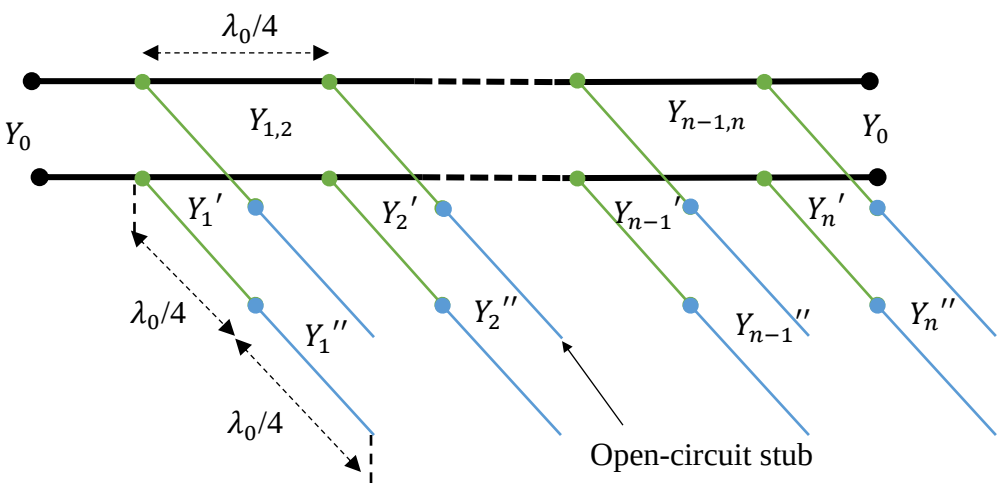

Figure 3.12 General circuit model of half-wavelength shunt open-circuited stubs connected by quarter-wavelength inverters.

3.2.7 Generalized coupling matrix

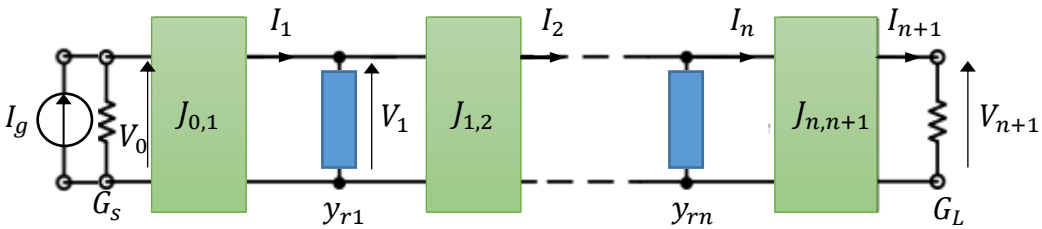

Figure 3.13 Network of bandpass filters of order n with admittance inverter.

In Figure 3.13, the lumped resonator (LC elements) of a bandpass filter (Figure 3.10) is replaced by transmission lines, using the half-wavelength open-circuited stubs (presented in section 3.2.6).

The overall admittance y_{ri} which contains the outer and inner admittances (see Figure 3.12) can be obtained from the following:

The impedance of the outer open stubs ($Z_{r1,i}$) of quarter-wavelength line can be calculated by [8]:

$$Z_{r1,i} = -\frac{Z_i''}{jtan\beta l}, \qquad \textit{for } i = 1 \textit{ to } n \tag{3.30}$$

where Z_i'' is the characteristic impedances of the outer open stubs.
From transmission-line theory, the total impedance of the stub can be calculated by [8]:

$$Z_{r2,i} = Z_i' \frac{Z_{r1,i} + jZ_i' tan\beta l}{Z_i' + jZ_{r1,i}\, tan\beta l} \tag{3.31}$$

where Z_i' is the characteristic impedances of the inner lines.

For a quarter-wavelength line ($l = \lambda_0/4$), the overall impedance Z_{ri} at the center frequency can be obtained by dividing the numerator and denominator of (3.31) by $tan\beta l$ and taking the limit as the tangent function argument approaches $\beta l = (2\pi/\lambda_0)(\lambda_0/4) = \pi/2$:

$$Z_{ri} = \lim_{\beta l \to \pi/2} Z_{r2,i} = -\frac{Z_i'^2}{Z_i''} jtan\beta l = \infty \tag{3.32}$$

$$y_{ri} = \frac{1}{Z_{ri}} = 0 \tag{3.33}$$

Then, the overall admittance is given by (3.33) at the central frequency.

A voltage-current relationship for each node in the network shown in Figure 3.13 can be combined into the matrix form which is convenient to manipulate as follows:

$$\begin{bmatrix} I_g \\ 0 \\ \vdots \\ 0 \end{bmatrix} = \begin{bmatrix} G_s & j.J_{0,1} & & \cdots & 0 \\ j.J_{0,1} & y_{r1} & & \ddots & \vdots \\ \vdots & \ddots & \ddots & y_{rn} & j.J_{n,n+1} \\ 0 & \cdots & & j.J_{n,n+1} & G_L \end{bmatrix} . \begin{bmatrix} V_0 \\ V_1 \\ \vdots \\ V_{n+1} \end{bmatrix} \tag{3.34}$$

The network is defined by the following system of equations:

$$[I] = [\mathrm{Y}].[V] \qquad \text{with} \qquad [\mathrm{Y}] = [G] + [y_{ri}] + \mathrm{j}.[J] \tag{3.35}$$

where:

- $[I]$ is the current vector of dimension $(n+2)$ for which $[I] = [I_g, 0,..., 0]^t$,
- $[V]$ is the voltage vector of dimension $(n+2)$ with $[V] = [V_0, V_1 ,..., V_{n+1}]^t$,
- [Y] is the nodal matrix $(n+2, n+2)$. It is always symmetrical with respect to the diagonal,
- $[G]$ is the conductance matrix $(n+2, n+2)$.
- $[y_{ri}]$ is the admittance matrix of resonators $(n+2, n+2)$ with all entries, except the diagonal, set at zero,
- $[J]$ is the admittance inverter matrix $(n+2, n+2)$. It contains values of the mutual coupling between the nodes of the network. If the coupling occurs between sequentially numbered resonator, it is referred to as direct coupling. The entries on the main diagonal, $J_{i,i}$, $J_{i,i+1}$ and $J_{i,i-1}$ are direct couplings, whereas all other couplings between the non-sequentially numbered resonator are known as cross couplings.

$$[J] = \begin{bmatrix} J_{1,1} & J_{1,2} & \cdots & J_{1,n-1} & J_{1,n} \\ J_{2,1} & J_{2,2} & \cdots & J_{2,n-1} & J_{2,n} \\ \vdots & \vdots & \ddots & \vdots & \vdots \\ J_{n-1,1} & J_{n-1,2} & \cdots & J_{n-1,n-1} & J_{n-1,n} \\ J_{n,1} & J_{n,2} & \cdots & J_{n,n-1} & J_{n,n} \end{bmatrix}$$

3.2.8 Cross coupling

One approach to achieve the flat group delay or the variation group delay characteristics is utilizing the cross-coupling between nonadjacent resonators. The cross coupling between nonadjacent resonators is used to generate transmission zeros at a suitable real resonant frequency. A negative cross coupling, on one hand will increase the filter rejection, and on the other hand it will increase the variation in the group delay. However, a positive cross coupling will reduce the filter rejection and flatten the group delay.

To observe the effects of inserting a cross coupling on the nodal matrix, we consider the example of a 6th order filter in which resonator 1 is coupled with resonator 6. The coupling is modeled by an ideal admittance inverter of $J_{1,6}$ characteristic admittance as shown in Figure 3.14. The feed lines of the filter are designed with a characteristic impedance of 50 ohms, the first J-inverters $J_{0,1}$ and last J-inverters $J_{n,n+1}$ can be neglected.

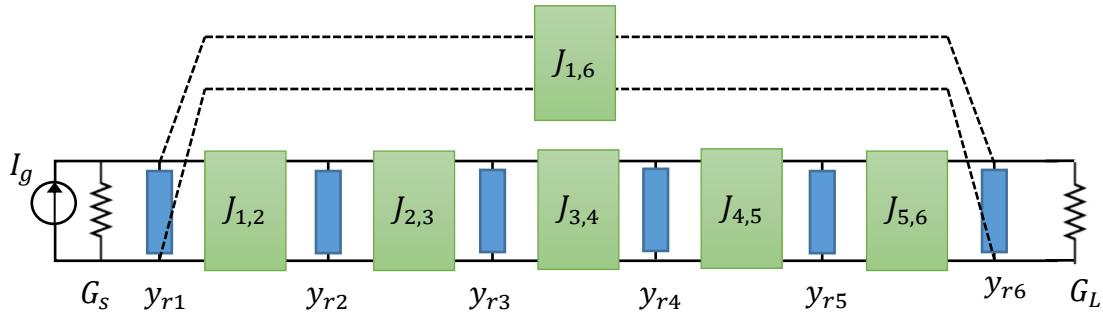

Figure 3.14 Bandpass filters of order 6 with cross coupling 1-6.

We obtain the following nodal matrix from Table 3.2 in which the $J_{1,6}$ coupling appears on a secondary diagonal at the intersection between the row of resonator 1 and the column of resonator 6.

Table 3.2 Nodal matrix of a 6th order filter with a cross coupling resonator between 1 and 6.

		Source	Resonators						Load
[Y]		0	1	2	3	4	5	6	7
Source	0	G_s	j. $J_{0,1}$	0	0	0	0	0	0
Resonators	1	j. $J_{0,1}$	y_{r1}	j. $J_{1,2}$	0	0	0	j. $\boldsymbol{J_{1,6}}$	0
	2	0	j. $J_{1,2}$	y_{r2}	j. $J_{2,3}$	0	0	0	0
	3	0	0	j. $J_{2,3}$	y_{r3}	j. $J_{3,4}$	0	0	0
	4	0	0	0	j. $J_{3,4}$	y_{r4}	j. $J_{4,5}$	0	0
	5	0	0	0	0	j. $J_{4,5}$	y_{r5}	j. $J_{5,6}$	0
	6	0	j. $\boldsymbol{J_{1,6}}$	0	0	0	j. $J_{5,6}$	y_{r6}	0
Load	7	0	0	0	0	0	0	0	G_L

where $G_S = G_L = Y_0$.

3.3 Tunable radio frequency filter

In order to obtain a tunable delay to negate the delays caused by SOA, a full description of the proposed tunable RF filter is presented in this section.

3.3.1 Tunable filter design with ideal transmission lines

In a first step, a description of the proposed filter with ideal transmission lines is implemented on the ADS circuit simulator. We choose the Chebyshev filter, which is characterized by ripples that exist in the passband bandwidth. We have started the design of a symmetrical bandpass filter using the synthesis of Chebyshev lowpass prototype filter mentioned in section 3.2.2, the 6th order filter is suitable for the RF filter design with 0.01 dB ripples in passband bandwidth. The reason behind the choice of 6th order bandpass filter is to have a degree of freedom in cross coupling between non-adjacent resonators, such as 2-5 and 1-6. Table 3.3 illustrates values of the elements obtained by applying all the equations of (3.13).

Table 3.3 Element values of 6th order Chebyshev lowpass prototype with L_{Ar} = 0.01 dB.

g_0	g_1	g_2	g_3	g_4	g_5	g_6	g_7
1	0.7813	1.3600	1.6896	1.5350	1.4978	0.7098	1.1007

The bandpass filter is usually designed using short-circuited stubs. The disadvantage of using shortened stubs is the presence of via holes which need for additional cost-effective process. In the proposed design, we choose the half-wavelength shunt open-circuited stubs as the stub-type microstrip bandpass filter of 6th order (the concept is in section 3.2.6). This eliminates the need for via holes in case of short-circuited stubs. Moreover, a negative cross coupling line is placed between the two non-adjacent resonators 1 and 6 to adapt the two resonant frequencies responsible for the coupling value of $J_{1,6}$ hence to introduce two transmission zeroes at both sides of the passband. Thus, the negative cross coupling 1-6, will introduce variation in the group delay. Then, the group delay ripple within the center part of the passband can be tuned. A chain matrix of ideal J-inverter (3.20) is placed between resonator 1-6, the chosen value for $J_{1,6}$ is −0.002 to obtain a small value of delay ripple.

The proposed initial design of half-wavelength shunt open-circuited stubs bandpass filters of 6th order with cross coupling 1-6 is illustrated in Figure 3.15. This structure has 6 inner lines, 6 open circuited stubs (outer stubs), and 5 connecting lines (inverters). The center frequency of the bandpass filter is designed at 10 GHz. The feed lines of the filter are designed with a characteristic impedance of 50 ohms, which gives Y_0 = 1/50 (siemens). The parameters used in the calculation are summarized in Table 3.4. The characteristic admittance of the inner lines and outer stubs, and the connecting lines are calculated from (3.23) to (3.29), and presented in Table 3.5.

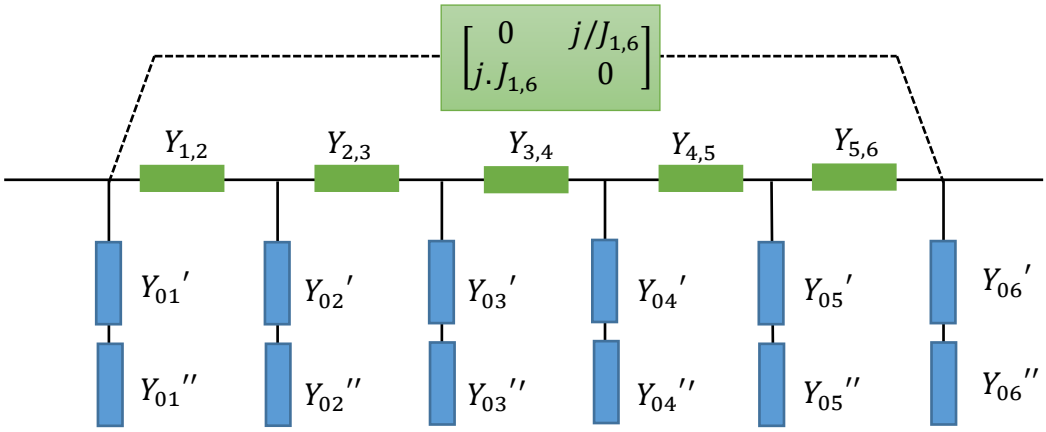

Figure 3.15 Initial design of half-wavelength shunt open-circuited stubs bandpass filters of order 6 with cross coupling 1-6.

Table 3.4 Parameters used in synthesis of half-wavelength shunt open-circuited stubs.

Y_0	FBW	a	d	C_a	θ_l
1/50 $\left(\frac{1}{\Omega}\right)$	0.29	0.5	0.52	0.81	77°

Table 3.5 Design parameters of the synthesized initial design half-wavelength shunt open-circuited stubs order-6 bandpass filter.

Admittance inverters	**Resonators n° 1, 3, 4 and 6**	**Resonators n° 2 and 5**
$Y_{1,2} = Y_{5,6} = 0.015$	$Y_{01}' = Y_{03}' = Y_{04}' = Y_{06}' =$ 0.016	$Y_{02}' = Y_{05}' = 0.015$
$Y_{2,3} = Y_{4,5} = 0.011$ $Y_{3,4} = 0.010$	$Y_{01}'' = Y_{03}'' = Y_{04}'' = Y_{06}'' = 0.008$	$Y_{02}'' = Y_{05}'' = 0.007$
$l = \frac{\lambda_0}{4}$	$l = \frac{\lambda_0}{4}$	$l = \frac{\lambda_0}{4}$

After having determined all the analytical expressions necessary for the synthesis (in section 3.2.6 and 3.2.7), we can now calculate the coefficients of our nodal matrix (Table 3.2). From (3.33) the overall admittance y_{ri} is 0. Factoring (3.23) into (3.35), the nodal matrix of 6th order filter with cross coupling resonator between 1 and 6 is given as follow:

		Source	Resonators						Load
[Y]		0	1	2	3	4	5	6	7
Source	0	G_S	0	0	0	0	0	0	0
Resonators	1	0	0	j.0.75	0	0	0	−j.0.002	0
	2	0	j.0.75	0	j.0.55	0	0	0	0
	3	0	0	j.0.55	0	j.0.50	0	0	0
	4	0	0	0	j.0.50	0	j.0.55	0	0
	5	0	0	0	0	j.0.55	0	j.0.75	0
	6	0	−j.0.002	0	0	0	j.0.75	0	0
Load	7	0	0	0	0	0	0	0	G_L

Two transmission zeroes are introduced to the bandpass filter response at both sides at the two edges of its passband at 8 and 12 GHz as shown in Figure 3.16, by inserting a capacitive cross coupling between resonators 1-6. The cross-coupling line (placed between resonators 1-6) is used to adjust the two resonant frequencies responsible for the coupling value of $J_{1,6}$. The insertion loss S_{21} and return loss S_{11} are 0.4 and 14 dB, respectively. Figure 3.17 shows a ripple in the group delay at the center frequency in the range of 9.5 to 10.5 GHz.

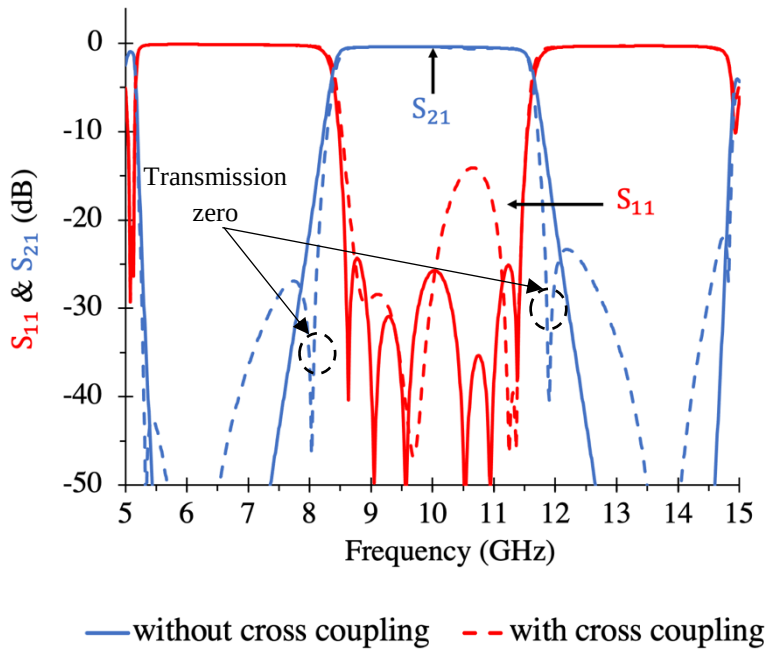

Figure 3.16 S-parameters for the simulated initial circuit obtained with half-wavelength shunt open-circuited stubs order-6 bandpass filter. Solid line without cross coupling 1-6, dashed line with cross coupling.

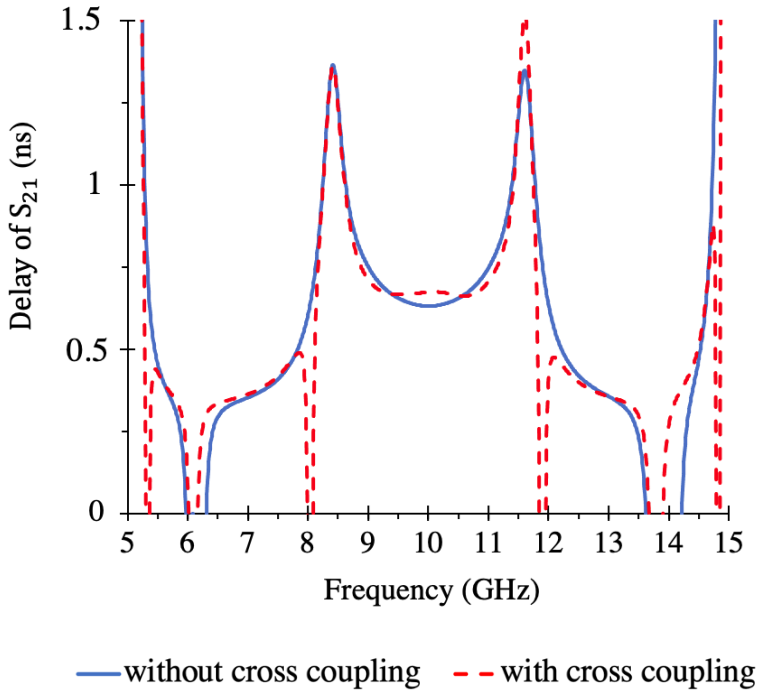

Figure 3.17 Delays of S_{21} for the simulated initial circuit obtained with half-wavelength shunt open-circuited stubs order-6 bandpass filter. Solid line without cross coupling 1-6 and dashed line with cross coupling.

Nevertheless, the proposed initial structure (Figure 3.15) is constrained around the value of cross coupling $J_{1,6}$. This is due to the inability to find the required equivalent capacitance of $J_{1,6}$ (C = 0.031pF). The smallest widely available capacitance that can be found has a value 0.1pF.

Generally, the maximum electric field occurs for:

- Short circuited stub for a quarter-wavelength long present at its other extremity.
- Open circuited stub for a quarter-wavelength long or half-wavelength long at its extremity.

For a half-wavelength stub terminated at its free end by an open circuit the largest electric field is concentrated at the ends of two extremity of the stub. In the middle of the stub at $\lambda_0/4$ there is an electric short circuit (zero electric field), as in the case of the end of quarter-wavelength stub. It is therefore clear, for the half-wave stub, the capacitor must be placed near the zero electric field if we want to use significant capacitance value.

In the previous proposed initial design, the capacitor (C) is placed at the maximum of electric field (Figure 3.15). To overcome the capacitance constraint and limitation, we proposed a modified design where C is therefore placed near the minimum of electric field, located in the

middle of the stub at $\lambda_0/4$, which is located between the inner line and outer stub, as shown in Figure 3.18. This allows us to increase the capacitance value of C.

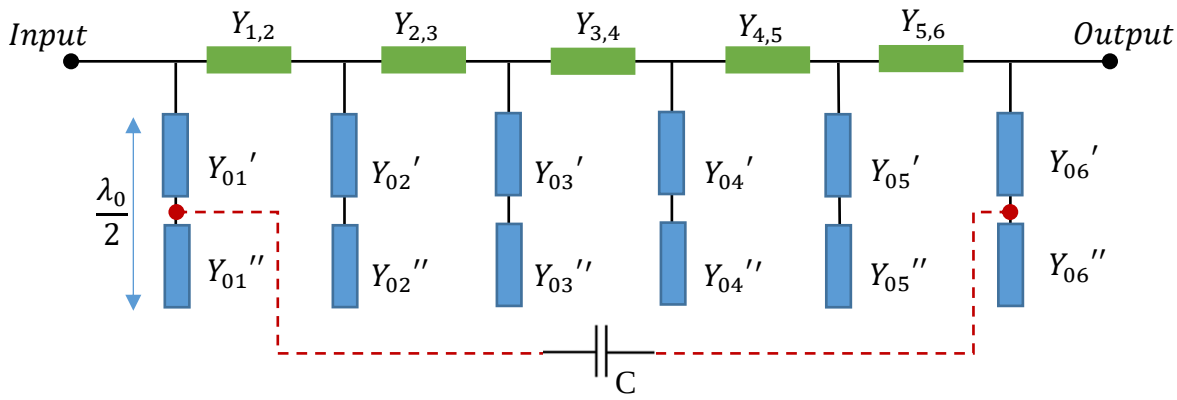

Figure 3.18 Modified bandpass filters of order 6 with cross coupling 1-6.

3.3.2 Synthesis of the tunable RF filter with distributed lines

Instead of using a long transmission line for the cross coupling 1-6 presented in the modified design, we optimize the design presented in Figure 3.18 by RF folded filter design (RF-FF) as shown in Figure 3.19. Besides, we consider the fringe effect, compensation for the open-end of the open-circuited stubs. The open-end effect in the microstrip is modeled in the frequency domain as an extension to the length of the microstrip stub. By applying the microstrip design equations described in theory parts (3.6) and (3.7), the widths and guided quarter-wavelengths associated with the characteristic admittances can be calculated. The microstrip lines are modeled using the MLIN component (via ADS), including conductor loss, dielectric loss and dispersion. The design has been simulated on a conventional RO4003 substrate ε_r = 3.55, h = 0.813 mm, tan δ = 0.0027, and T = 17 μm. Once the physical dimensions have been obtained, the next design step is the electrical simulation and circuit tuning. The tuning consists of retouching the lengths of the lines to adjust the electrical response of the filter. In order to adjust the electrical response in microstrip lines of the 6th order filter, it is necessary to slightly adjust the lengths of the stubs, the optimized lengths are presented in Table 3.6.

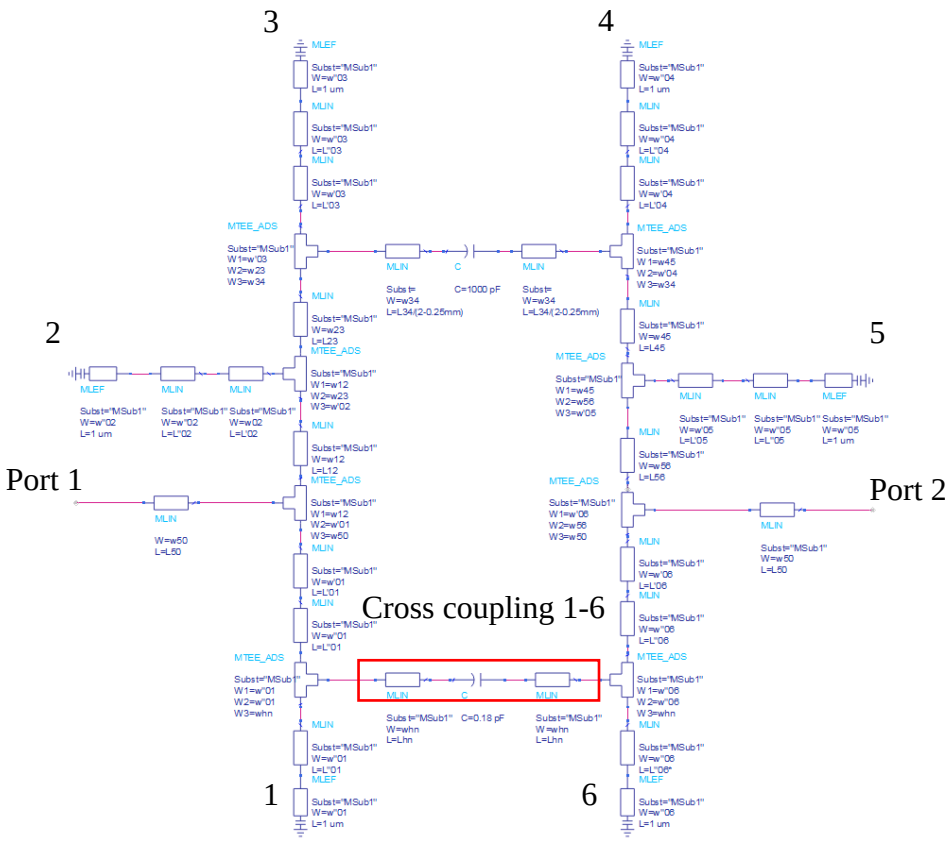

Figure 3.19 Schematic of RF-FF with cross coupling between the stub 1 and 6.

Table 3.6 Dimensions of microstrip lines for RF-FF.

Admittance inverters	***Resonators n°1, 3, 4 and 6***	***Resonators n°2 and 5***
$w_{1,2} = w_{5,6} = 1.163\ mm$ $w_{2,3} = w_{4.5} = 0.529\ mm$ $w_{3,4} = 0.452\ mm$	$w_{01}' = w_{03}' = w_{04}' = w_{06}' = 1.301\ mm$ $w_{01}'' = w_{03}'' = w_{04}'' = w_{06}'' = 0.244\ mm$	$w_{02}' = w_{05}' = 1.032\ mm$ $w_{02}'' = w_{05}'' = 0.156\ mm$
$L_{1,2} = L_{5,6} = 4.52\ mm$ $L_{2,3} = L_{4,5} = 4.65\ mm$ $L_{3,4} = 4.68\ mm$	$L_{01}' = L_{03}' = L_{04}' = L_{06}' = 4.5\ mm$ $L_{01}'' = L_{03}'' = L_{04}'' = L_{06}'' = 4.7\ mm$	$L_{02}' = L_{05}' = 4.54\ mm$ $L_{02}'' = L_{05}'' = 4.80\ mm$

Other transmission lines
Input/output (50 ohms line): $w_{50} = 1.821\ mm$ and $L_{50} = 20\ mm$
Cross coupling connecting line: $w_{hn} = 1.5\ mm$ and $L_{hn} = 2.35\ mm$

Optimization

Admittance inverters	***Resonators n°1, 3, 4 and 6***	***Resonators n°2 and 5***
$L_{1,2} = L_{5,6} = 4.83\ mm$ $L_{2,3} = L_{4,5} = 4.87\ mm$ $L_{3,4} = 4.78\ mm$	$L_{01}' = L_{06}' = 3.85\ mm$ $L_{03}' = L_{04}' = 3.76\ mm$	$L_{02}' = L_{05}' = 5.10\ mm$
	$L_{01}'' = L_{06}'' = 5.44\ mm$ $L_{03}'' = L_{04}'' = 5.25\ mm$	$L_{02}'' = L_{05}'' = 4.82\ mm$

L: line length. w:line width.

Figure 3.20 shows the simulated frequency response of the RF-FF, and Figure 3.21 shows the simulated group delay response of the filter, with and without coupling between the stubs of resonators 1 and 6 across wideband frequency ranging from 5 to 15 GHz. Here, C = 0.18 pF. For the case of cross coupling (in dotted lines), the two transmission zeros are located at 8.33 and 12.53 GHz. The insertion loss S_{21} and return loss S_{11} with coupling are 0.45 and 12.08 dB, respectively.

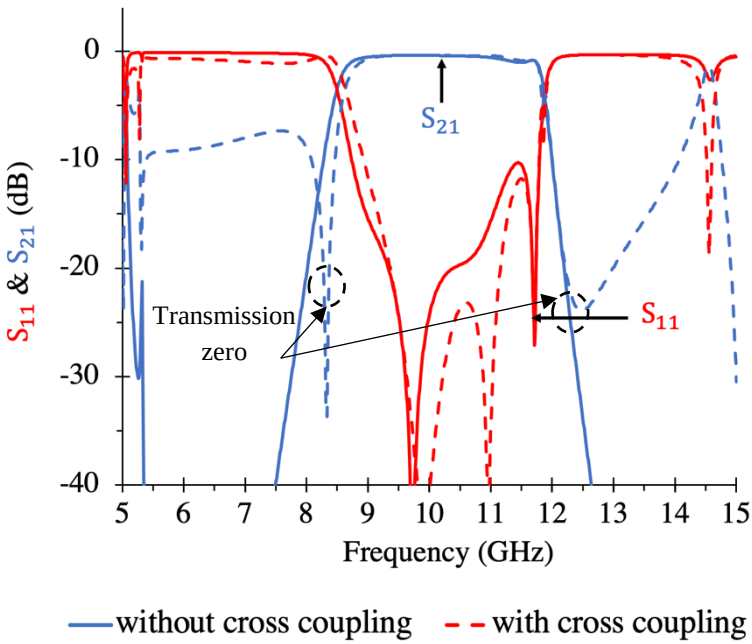

Figure 3.20 Circuit simulation results of S-parameters of RF-FF. Solid line without cross coupling, dotted line with cross coupling.

A ripple appears in the group delay at the center frequency with 1 GHz of frequency band using C = 0.18 pF, this verifies that the new placement of C located at the minimum of electric field is a feasible solution.

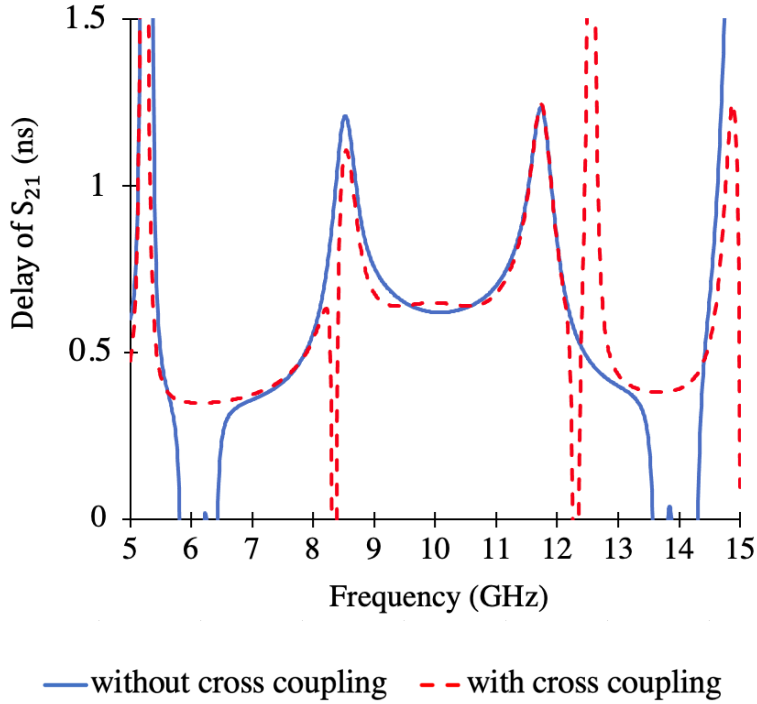

Figure 3.21 Delays of S_{21} for circuit simulation results of RF-FF. Solid line without cross coupling, dotted line with cross coupling.

3.3.3 Basic model of varactor diodes

A varactor diode is assimilated into a variable capacitance, depending on the bias voltage applied in a reverse bias. Indeed, reverse biasing the diode, enlarges the depletion zone, which leads to a decrease in capacitance as a function of the applied voltage and vice versa. Varactor diodes present good performance qualified by low switching time, low bias voltage and relatively low capacitance values (a few pF). An equivalent circuit of the reverse-biased diode is given in Figure 3.22 where C_j is the variable capacitance, C_p parasitic is the parallel parasitic capacitance, Ls is the parasitic inductance, and R_s is the parasitic resistance of the diode.

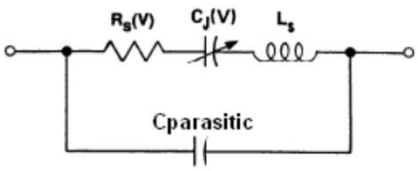

Figure 3.22 Flip tuning varactor equivalent circuit [9].

Figure 3.23 shows the ADS implementation of MA46H120 varactor from M/A-COM [9] [10], where $C_j = C = 0.1394$ pF and $R_s = 0.88\ \Omega$. We have exploited the S-parameters of the diode for various polarization values. Our simulation Figure 3.24 shows that the used varactor diode has capacitances ranging from 0.16 pF to 0.82 pF for a control voltage varying from 1 to 20 Volts, respectively. From this figure, we can extract the value of the voltage variation used in our simulation and the values of the corresponding capacitances.

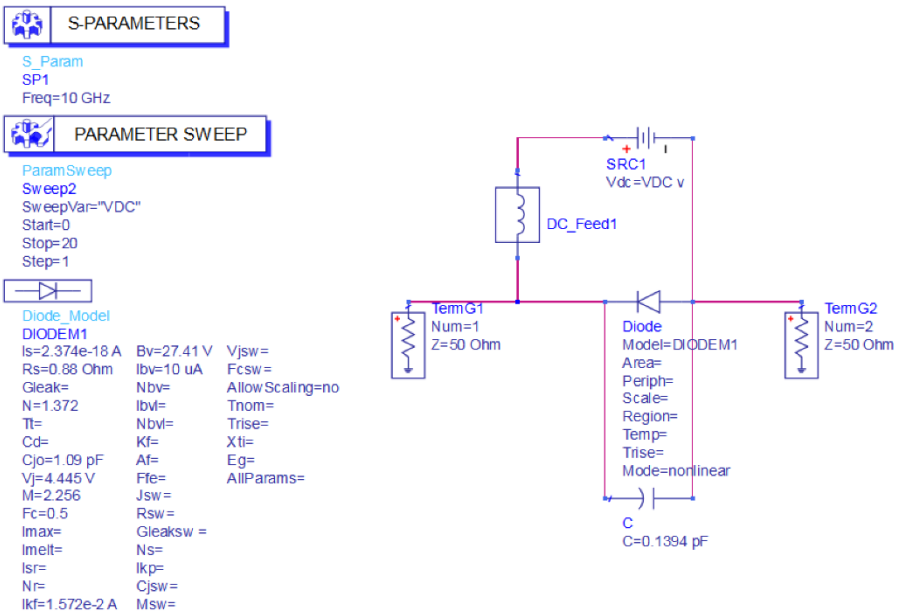

Figure 3.23 MA46H120 varactor model in ADS.

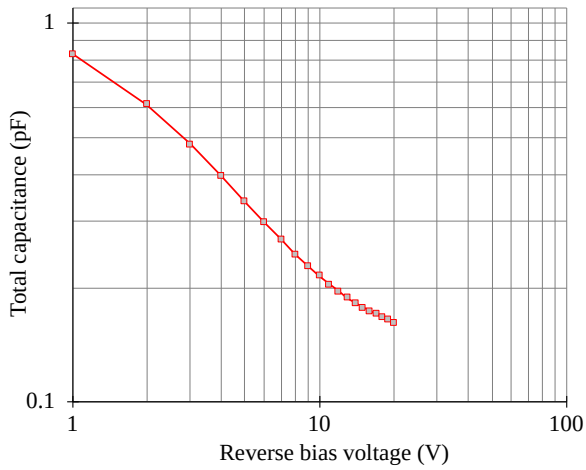

Figure 3.24 Varactor capacitance variation versus bias voltage.

3.3.4 Layout and EM simulation

The second part of the design procedure is to perform circuit layout and electromagnetic simulation. The EM-simulations of RF filters (RF-FF and RF-CF) were simulated using ADS Momentum.

3.3.4.1 Folded design

Figure 3.25 displays the top view of the folded design layout and contains the DC block C_b and the varactor C_v. In order to reduce the parasitic couplings between port 1-2 and the stubs 2 and 5, we increase the space gap between them, by inclining port 1 and port 2 by 5°. The capacitor between stubs 1 and 6 is replaced by a MA46H120 varactor which has a capacitance tuning range from 0.16 pF to 0.82 pF and a parasitic resistor R_s of value 0.88 Ω. The ADS simulation (section 3.3.3) of this varactor is used as a guide to find their required biasing voltages based on the needed capacitances (Figure 3.24). The EM-simulations in amplitude and group delay of the filter with coupling between the stub's resonators 1 and 6, are presented in Figure 3.26.

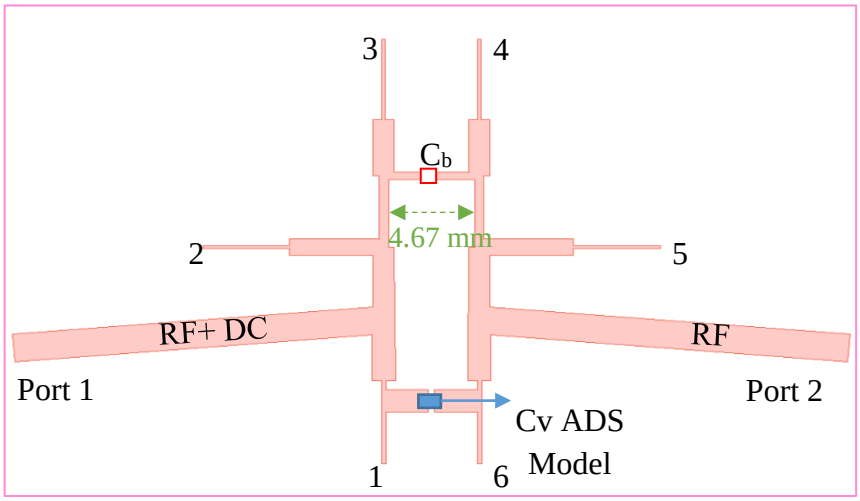

Figure 3.25 Layout of RF folded filter (RF-FF), where C_b is the DC blocking capacitors and C_V is the MA46H120 varactors.

The transmission zeros on either side of the bandwidth are obtained at 7.87 and 12.3 GHz. At frequencies between 8 GHz and 12 GHz, the insertion loss S_{21} and return loss S_{11} are 0.7 and 12.1 dB, respectively. It can be noticed that the EM-simulated responses are close in terms of insertion loss is less than 1 dB and return loss is more than 10 dB to the circuit-simulated (Figure 3.20). However, some differences are present for transmission zeros.

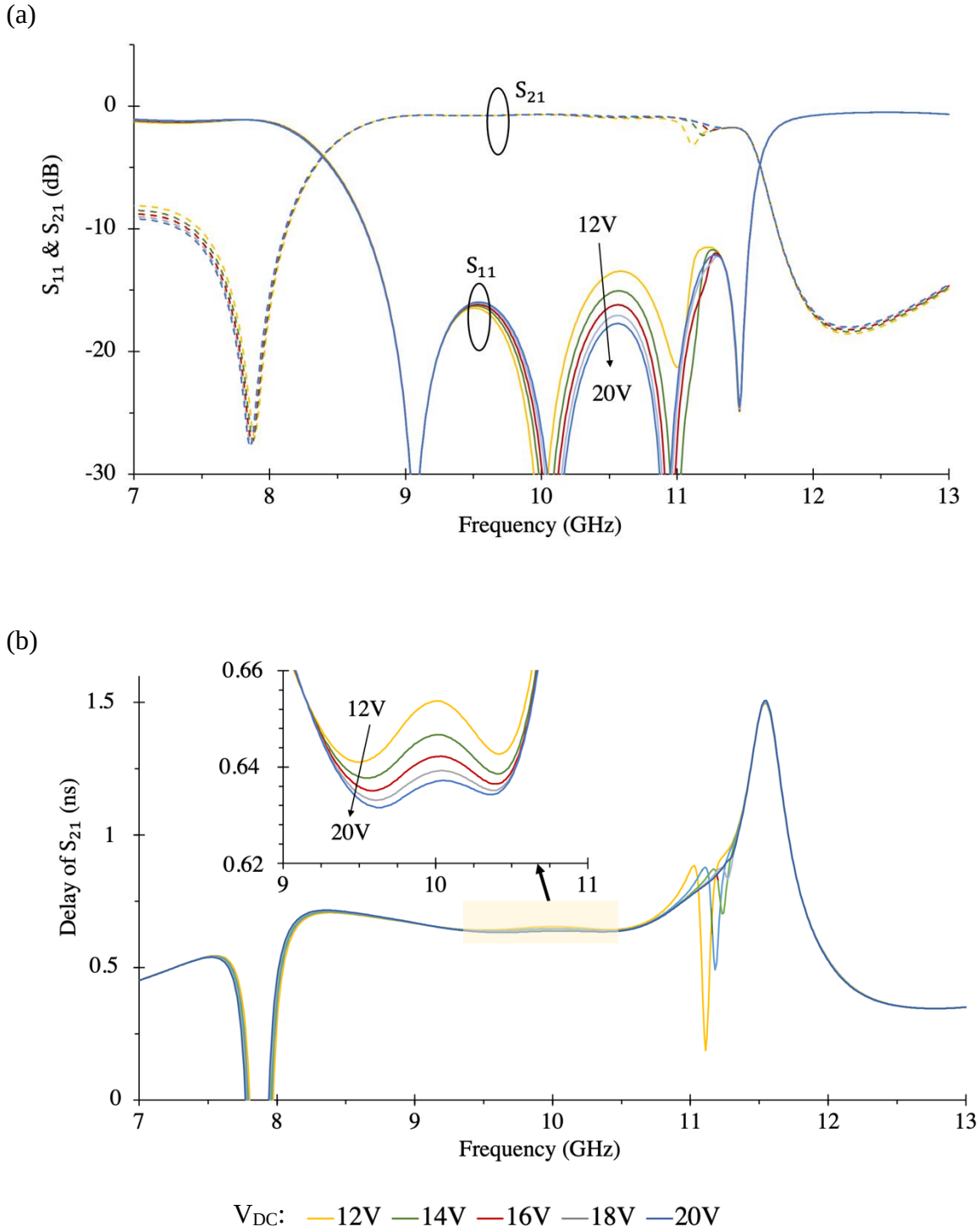

Figure 3.26 Electromagnetic simulation (Momentum) of RF-FF (a) S-parameters, (b) delay of S_{21}.

A ripple in the group delay appears at the center frequency in a range of 1 GHz (9.5 ~10.5 GHz), it can be tuned by varying the V_{DC}. Table 3.7 shows the delay ripple of the folded design for a control voltage varying from 12 to 20 Volts.

Table 3.7 Delay ripple of RF-FF for various voltages.

Voltages	*Delay ripple (9.5-10 GHz)*	*Delay ripple (10-10.5 GHz)*
12 V	11.43 ps	10.39 ps
14 V	8.21 ps	7.49 ps
16 V	6.53 ps	5.32 ps
18 V	5.60 ps	3.76 ps
20 V	5.07 ps	2.65 ps

3.3.4.2 Curved design

In order to improve the results, we increase the spacing between the symmetric connecting lines and to avoid the parasitic couplings, we replace the lines $L_{1,2}, L_{2,3}, L_{4,5}, L_{5,6}, L_{01}'$ *and* L_{06}' of the RF folded filter circuit by curved lines. The dimensions of each curve are listed in Table 3.8. The layout of the curved design is shown in Figure 3.27, and contains the DC block and the varactor.

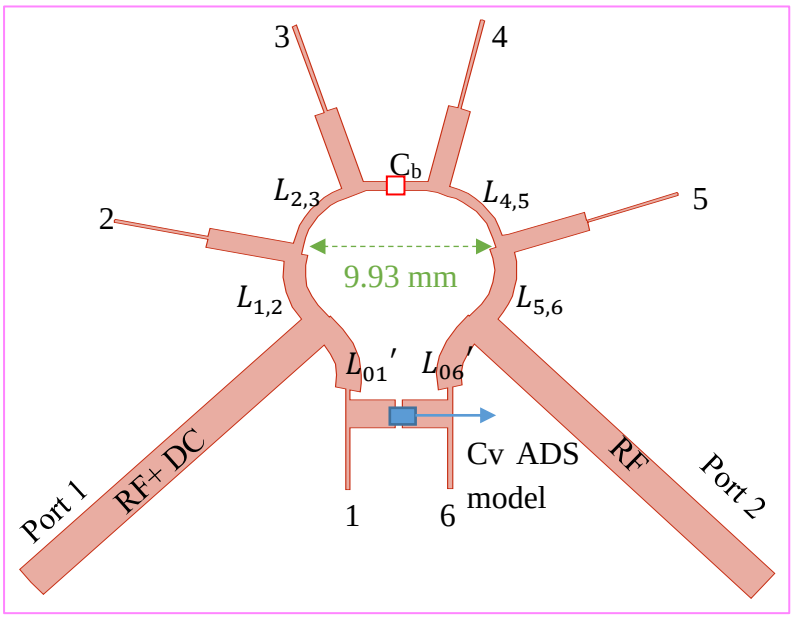

Figure 3.27 Layout of RF curved filter (RF-CF).

The spacing between two opposite connecting lines for folded design is 4.67 mm (Figure 3.25), while for RF curved filter (RF-CF) is about 9.93 mm.

(a)

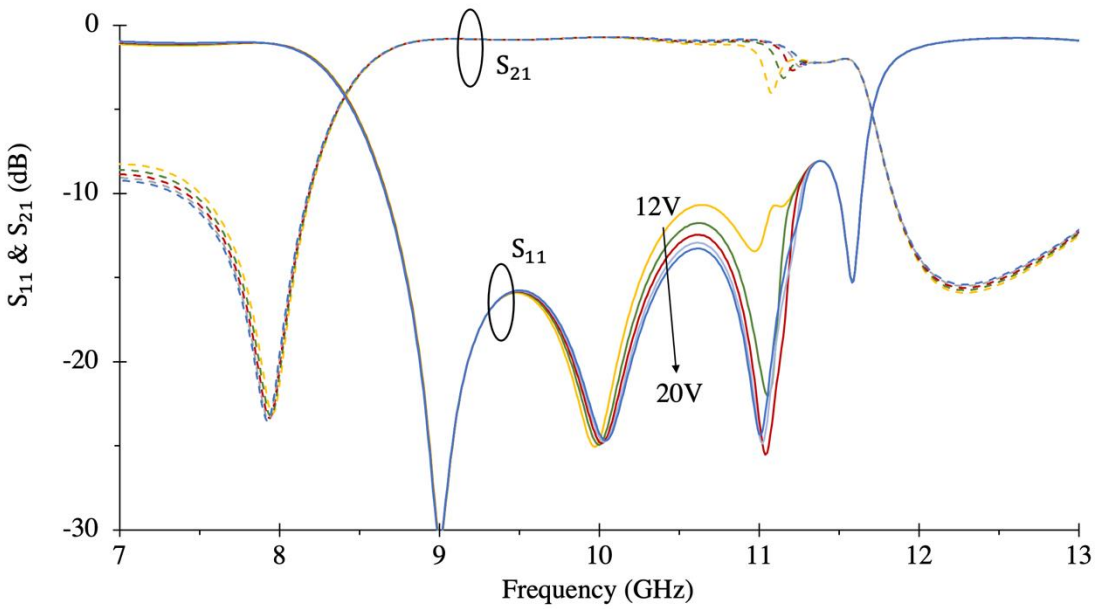

(b)

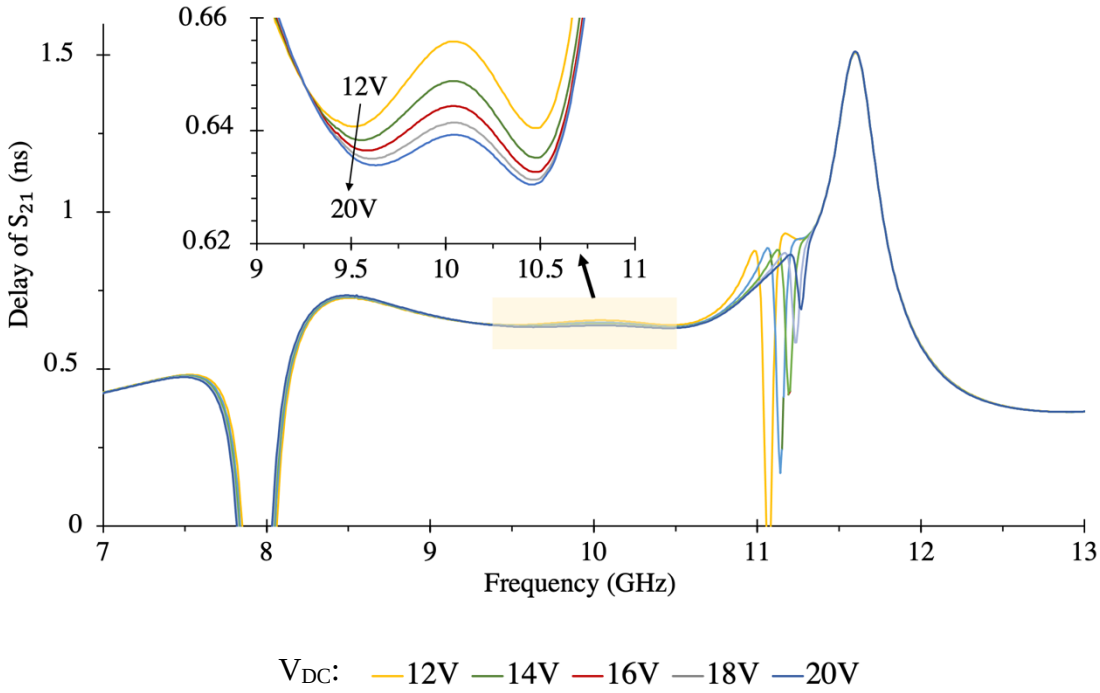

Figure 3.28 Electromagnetic simulation (Momentum) of RF-CF (a) S-parameters, (b) Delay of S_{21}.

EM-simulations in amplitude and group delay of RF-CF with coupling between the stubs of resonators 1 and 6, are depicted in Figure 3.28. The insertion loss S_{21} and return loss S_{11} are 0.7 dB and 11.5 dB, respectively. The first transmission zero is located at 7.92 GHz, and the second one is located at 12.3 GHz. By comparing RF-FF and RF-CC, both have an insertion loss is less than 1 dB, and a return loss is more than 10 dB. However, the first transmission zero is located at a slightly different by 0.05 GHz, but the second transmission zero occurs practically exactly at the frequency (12.3 GHz).

A ripple in the group delay appears at the center frequency in a range of 1 GHz (9.5 ~10.5 GHz). Table 3.9 shows the delay ripples of the folded design for a control voltage varying respectively from 12 to 20 Volts. The obtained delay ripple of RF-CF is greater than the one obtained by RF-FF (see Table 3.7 and Table 3.9).

Table 3.8 Curved lines.

Lines	***Angle***
$L_{1,2}$ *and* $L_{5,6}$	53°
$L_{2,3}$ *and* $L_{4,5}$	60°
L_{01}' *and* L_{06}'	55°

Table 3.9 Delay ripple of RF-CF for various voltages.

Voltages	***Delay ripple (9.5-10 GHz)***	***Delay ripple (10-10.5 GHz)***
12 V	15.61 ps	12.69 ps
14 V	10.59 ps	11.48 ps
16 V	7.78 ps	9.51 ps
18 V	5.82 ps	8.05 ps
20 V	4.55 ps	7.39 ps

3.4 Tunable radio frequency phase shifter

As seen in the beginning of this chapter, to achieve TTD, a RF-phase shifter is needed after the RF-filter in order to provide a tunable phase offset ϕ_{offset}. In a phase shifter, different configurations may have the same slope of phase shift, hence the phase difference between two different configurations can be constant over a given frequency range. In true time delay

(TTD), instead, different configurations have different slopes, thus, phase difference between two different configurations is not constant over frequency. What is constant in this case is the group delay difference between various configurations, which is defined in (1.12).

To obtain an offset on the phase response, a linear phase shift is required over the bandwidth of operation. The most promising technique employs analog phase shifters, which are built with varactor diodes and offer continuous phase shift by controlling the voltage of the varactor. Many analog passive phase shifters have been reported in the literature, such as reflection type phase shifters (RTPS) [11], RTPS based on coupled-lines [12], and loaded transmission lines phase shifters [13].

In order to obtain an offset on the output phase response, we present here a topology based on transmission lines and varactor diodes. This technology meets the low cost, simple voltage control, easy implementation requirements, furthermore, it allows a continuous tunable phase shift. The basic building blocks for the proposed RF-PS shown in Figure 3.29 consist of two parallel networks. First, the upper network composed of one varactor diode (C_{v1}). Second, the lower network which consists of a loaded lines phase shifter containing two cascading identical microstrip transmission lines (TL) and a shunt varactor diode (C_{v2}). To provide a continuously tunable phase offset, two varactor diodes are used as variable capacitors. The varactor provides an electronically adjustable phase shift through changing the diodes bias voltages over the X-band without increasing the phase shifter size. The optimized placement of varactors (C_{v1} and C_{v2}) is set as all-pass network topology, as in [14] [15].

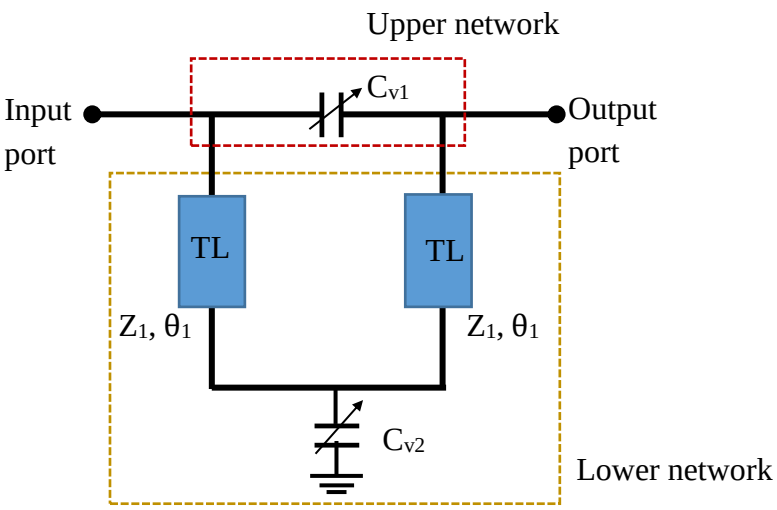

Figure 3.29 Schematic of the proposed tunable RF-PS.

3.4.1 Analysis of the proposed structure

The proposed RF-PS can be divided into two circuits, upper and lower, as seen in Figure 3.29. The lower circuit is constituted of three cascading networks containing two lossless transmission lines (TL) with a shunt varactor (C_{v2}). In this case, it is favorable to have transmission parameters that can be multiplied one to another. ABCD matrices can be used to achieve this function; it is often used for the analysis of cascaded structures, an ABCD matrix for the lower circuit is given below:

$$\begin{bmatrix} A_l & B_l \\ C_l & D_l \end{bmatrix} = \begin{bmatrix} A_{TL} & B_{TL} \\ C_{TL} & D_{TL} \end{bmatrix} \times \begin{bmatrix} 1 & 0 \\ j\omega C_{v2} & 1 \end{bmatrix} \times \begin{bmatrix} A_{TL} & B_{TL} \\ C_{TL} & D_{TL} \end{bmatrix}$$

$$\begin{bmatrix} A_l & B_l \\ C_l & D_l \end{bmatrix} = \begin{bmatrix} cos\theta_1 & jZ_1 sin\theta_1 \\ \frac{jsin\theta_1}{Z_1} & cos\theta_1 \end{bmatrix} \times \begin{bmatrix} 1 & 0 \\ j\omega C_{v2} & 1 \end{bmatrix} \times \begin{bmatrix} cos\theta_1 & jZ_1 sin\theta_1 \\ \frac{jsin\theta_1}{Z_1} & cos\theta_1 \end{bmatrix} \tag{3.36}$$

with:

- $A_l = cos\theta_1\, cos\theta_1 - \frac{Z_1}{Z_1}\, sin\theta_1\, (\omega C_{v2}\, Z_1 cos\theta_1 + sin\theta_1)$
  $= cos2\theta_1 - \frac{Z_1 \omega Cv_2}{2}\, sin2\theta_1$.

- $B_l = j[Z_1 sin\theta_1 cos\theta_1 + Z_1 sin\theta_1 (cos\theta_1 - \omega C_2 Z_1 sin\theta_1)]$
  $= j[Z_1 sin2\theta_1 - {Z_1}^2 \omega C_{v2} sin^2\theta_1]$.

- $C_l = \frac{j}{{Z_1}^2}[Z_1 sin\theta_1 cos\theta_1 + Z_1 cos\theta_1 (\omega C_{v2} Z_1 cos\theta_1 + sin\theta_1)]$
  $= \frac{j}{{Z_1}^2}[Z_1 sin2\theta_1 + {Z_1}^2 \omega C_2 cos^2\theta_1] = j\,[\frac{sin2\theta_1}{Z_1} + \omega C_{v2} cos^2\theta_1\,]$.

- $D_l = \cos2\theta_1 - \frac{Z_1 \omega C_{v2}}{2}\, \sin2\theta_1$.

where Z_1 and θ_1 are the characterictic impedance and electrical length of the lower circuit transmission lines, respectively. The electrical length of the transmission line is directly proportional to its operating frequency of a transmission line.

$$\theta_f = \theta_{f_0} \frac{f}{f_0} \tag{3.37}$$

where θ_{f_0} is the electrical length defined at the operating frequency f_0.

The ABCD matrix of the upper circuit which is comprised of C_{v1} in series is given below:

$$\begin{bmatrix} A_u & B_u \\ C_u & D_u \end{bmatrix} = \begin{bmatrix} 1 & \frac{1}{j\omega C_{v1}} \\ 0 & 1 \end{bmatrix} \tag{3.38}$$

The upper and lower circuits are two-port networks connected in parallel. In this case, it is preferable to have transmission parameters that can be summed up by computing the Y-matrix. The transformation from $[A_u]$ to $[Y_u]$ matrix of upper circuit and $[A_l]$ to $[Y_l]$ of lower circuit can be expressed as:

$$[Yu] = \begin{bmatrix} \frac{D_u}{B_u} & \frac{B_u C_u - A_u D_u}{B_u} \\ -\frac{1}{B_u} & \frac{A_u}{B_u} \end{bmatrix} = \begin{bmatrix} j\omega C_1 & -j\omega C_1 \\ -j\omega C_1 & j\omega C_1 \end{bmatrix} \tag{3.39}$$

$$[Yl] = \begin{bmatrix} \frac{D_l}{B_l} & \frac{B_l C_l - A_l D_l}{B_l} \\ -\frac{1}{B_l} & \frac{A_l}{B_l} \end{bmatrix} \tag{3.40}$$

For two-port networks where y-parameters are connected in parallel, the equivalent two-port y-parameters of the overall structure depicted in Figure 3.29 is then calculated by $[Y] = [Yl] + [Yu]$, and is found to be:

$$[Y] = \begin{bmatrix} Y_{11} & Y_{12} \\ Y_{21} & Y_{22} \end{bmatrix} = \begin{bmatrix} \frac{D_u}{B_u} + \frac{D_l}{B_l} & \frac{B_u C_u - A_u D_u}{B_u} + \frac{B_l C_l - A_l D_l}{B_l} \\ -\frac{1}{B_u} - \frac{1}{B_l} & \frac{A_l}{B_l} + \frac{A_u}{B_u} \end{bmatrix} \tag{3.41}$$

Once the Y-matrix is obtained, the S-parameters of the design can be obtained using the well-known Y-to-S-parameters transformation as shown below:

$$S_{21} = \frac{-2\, Y_0\, Y_{21}}{(Y_0 + Y_{11})(Y_0 + Y_{22}) - Y_{12} Y_{21}} \tag{3.42}$$

$$S_{11} = \frac{(Y_0 - Y_{11})(Y_0 + Y_{22}) + Y_{12} Y_{21}}{(Y_0 + Y_{11})(Y_0 + Y_{22}) - Y_{12} Y_{21}} \tag{3.43}$$

where Y_0 is the characteristic admittance of the transmission line.
Finally, the phase shift of the complete structure of RF-PS can be expressed as:

$$\phi = arctan(S_{21}) \tag{3.44}$$

3.4.2 RF-PS design and simulation

RF-PS has been designed at a central frequency f_0 of 10 GHz to obtain a linear phase shift with respect to frequencies in the range of 8 to 12 GHz. The schematic diagram of the proposed tunable RF-PS is built on ADS, presented in Figure 3.30. The upper circuit is connected in parallel with the lower circuit that includes two transmission lines (TL) with characteristic impedance Z_1 = 110 ohm and electrical length θ_1 = 75° with a 1000 pF DC block (C_b). Two DC blocks are placed between the first varactor C_{v1} to block the biasing voltage from input and output ports. C_{v1} is fed into the DC via a $\lambda_g/4$ transmission line, where λ_g is the wavelength in the medium propagation at the operating frequency f_0. The circuit has radio frequency chokes (RFC) to isolate the microwave signal from the biasing line via a radial stub and $\lambda_g/4$ transmission line transformers, which transform the short circuit into an open circuit on the signal line.

The varactor diode C_{v1} is connected from one side to the biasing network and from the other side with a short circuit transmission line of a length $\lambda_g/4$, that form a ground plane. The capacitance C_{v2} is set to two times greater than the C_{v1} capacity to accommodate an optimum broadband adaptation. The varactor diode C_{v2} is connected from one side with the TL and from the other with a ground plane. The design parameters of the simulation and the optimized physical lengths and widths of microstrip lines which are calculated from (3.6) and (3.7) are summarized respectively in Table 3.10 and Table 3.11.

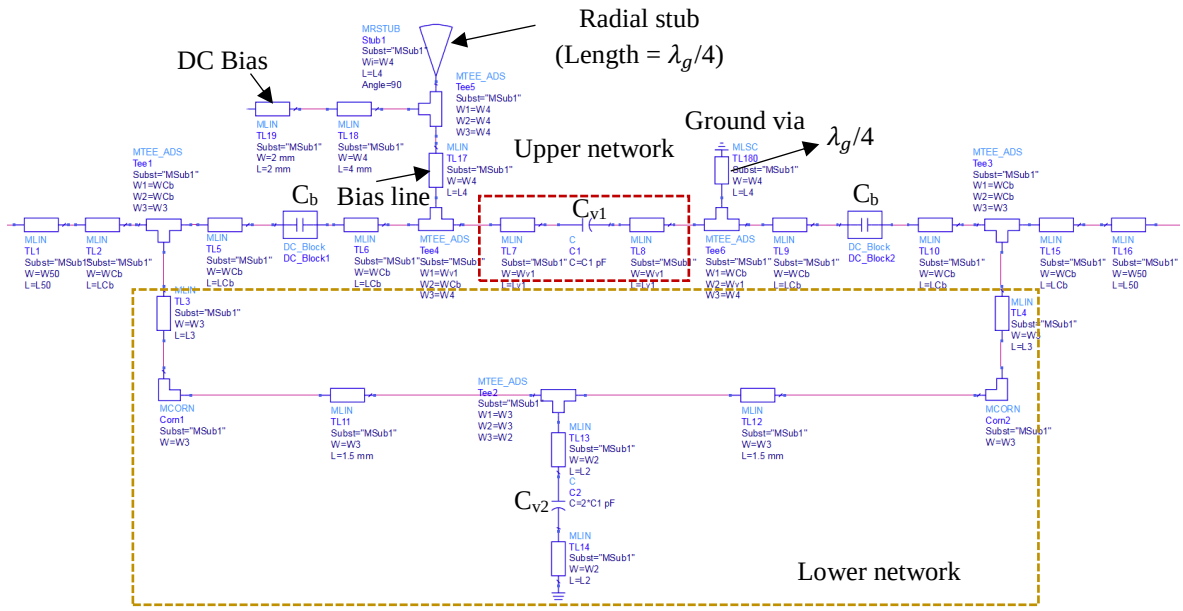

Figure 3.30 Schematic of the proposed tunable RF-PS.

Table 3.10 Design parameters of simulation.

Parameters	***Value***
PCB	RO4003C
Substrate thickness (h)	508 μm
Relative permittivity (ε_r)	3.55
Copper thickness (T)	17 μm
tan δ	0.0027
C_b	1000 pF
C_{v1}	0.15-0.5 pF
C_{v2}	$2\times C_{v1}$

Table 3.11 Design parameters and dimension values for the proposed RF-PS in 8-12 GHz frequency band.

Line width	***Value (mm)***	***Line length***	***Value (mm)***
W_{cb}	0.35	L_{cb}	0.45
W_{v1}	0.35	L_{v1}	0.45
W_2	0.75	L_2	0.75
W_3	0.20	L_3	3.99
W_4	0.15	L_4	4.82
W_{50}	0.11	L_{50}	5

W: line width, L: line length

The layout design creates a physical representation of the circuit that must adhere to the limitations imposed by the manufacturing process such as the minimum line width and distance between lines (gap) and the width of the lines which is about 150 μm. After optimization, the layout of the design is shown in Figure 3.31, and the dimensions of each microstrip line are listed in Table 3.11. The overall tunable RF-PS has a dimension of 16.9×15.02 mm. We simulated the layout design of RF-PS with ADS software (Momentum Simulator), using the substrate RO4003C. C_{v1} is varied from 0.15 to 0.5 pF, and $C_{v1} = 2\times C_{v1}$ (summarized in Table 3.11).

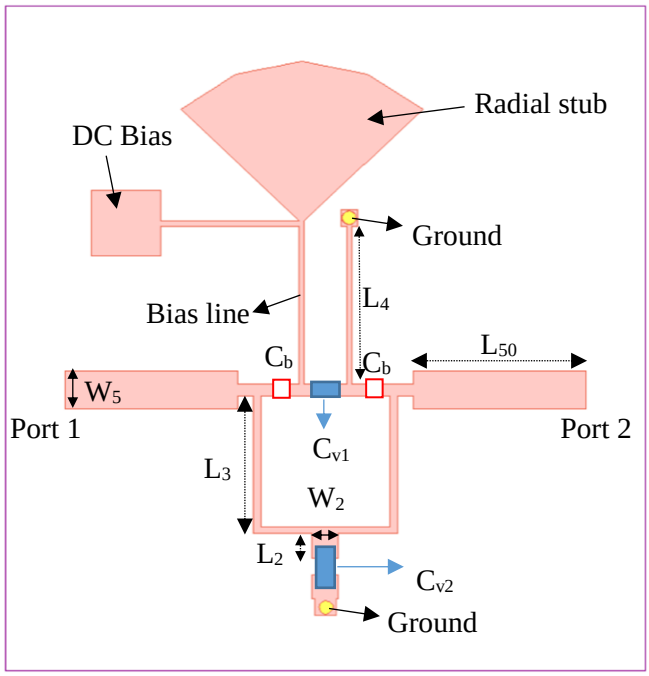

Figure 3.31 Layout of tunable RF-PS.

Table 3.12 Slope and offset of S_{21} phase for different values of capacitors in the frequency range from 9.5 GHz to 10.5 GHz.

C_{v1} (pF)	***Slope***	***Offset***
0.15	−48.8	258.3°
0.18	−47.8	233.4°
0.2	−46.9	222.0°
0.25	−45.7	200.4°
0.3	−45.1	186.5°
0.35	−44.6	177.2°
0.4	−44.3	170.4°
0.45	−44.08	165.9°
0.5	−43.95	161.5°

Figure 3.32(a) that the reflection coefficient S_{11} is lower than −10 dB over the entire frequency range of interest. An insertion loss of 0.8 dB is shown in Figure 3.32(b). The simulated phase of S_{21} versus frequency is presented in Figure 3.33(a). We achieve a phase up to a range

between −220° and −415° at 8 GHz and 12 GHz, for a capacitance of C_{v1} = 0.5 pF. The phase-shift variation range is up to 90°.

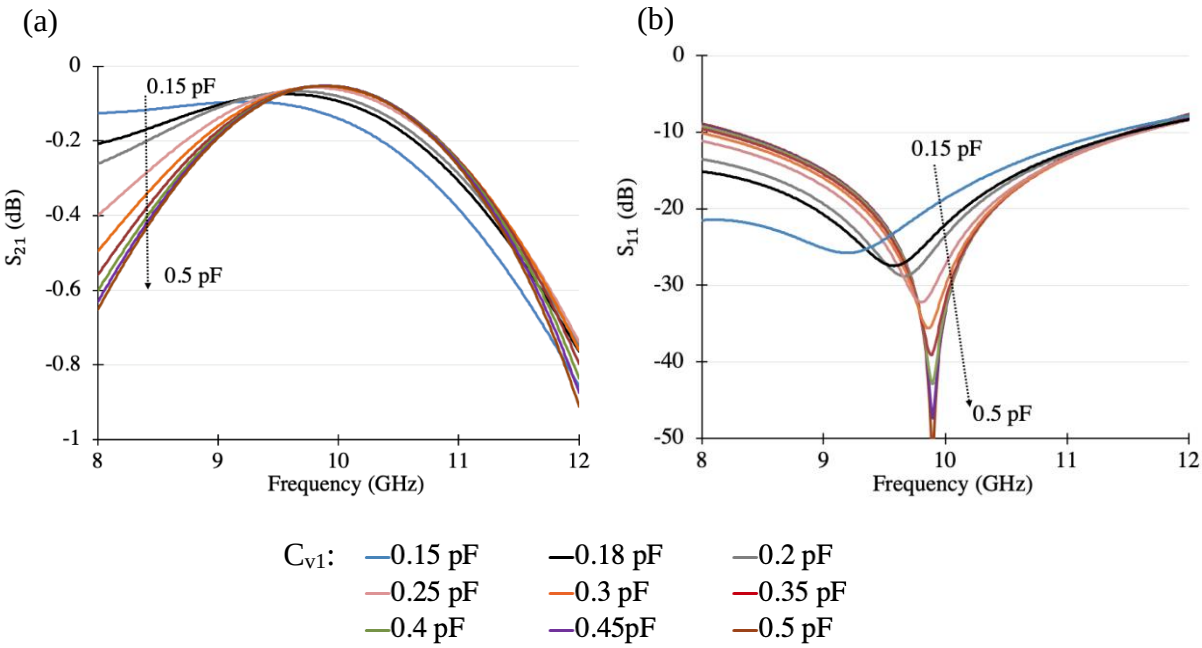

Figure 3.32 Simulated S parameters of the tunable RF-PS for different capacitances values. Amplitude variations of (a) reflection coefficient S_{21}, and (b) Transmission coefficient S_{11}.

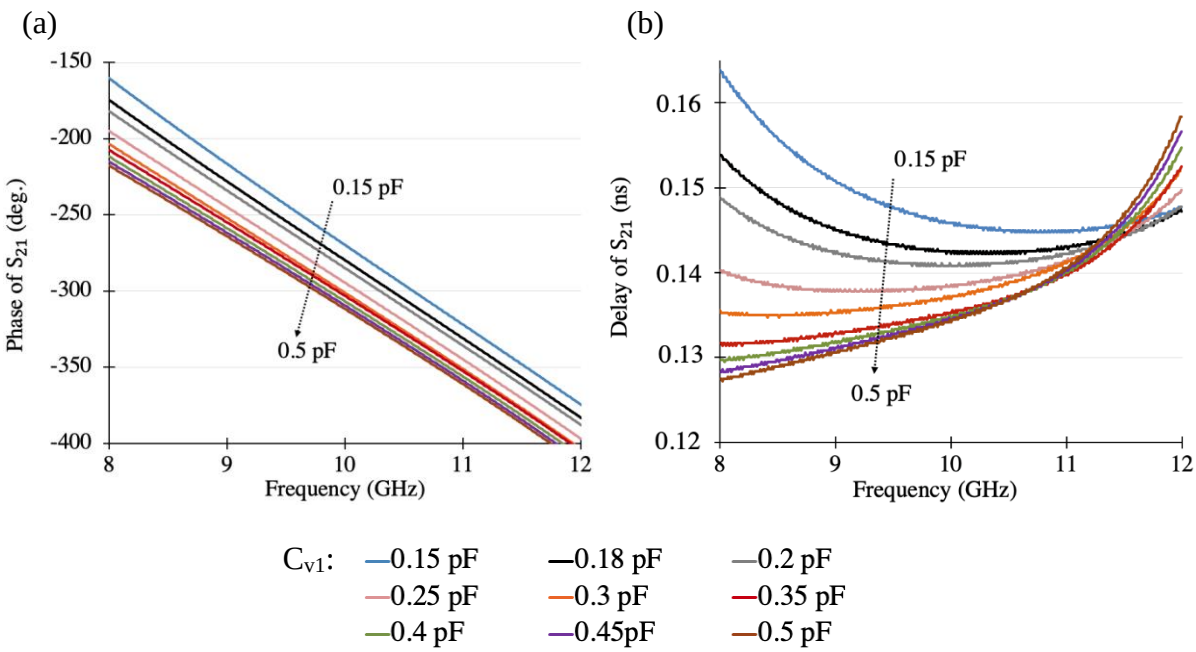

Figure 3.33 Simulated frequency characteristics of the tunable RF-PS for different values of C_{v1}. (a) Phase variations of S_{21}, and (b) delay variation of S_{21}.

Figure 3.33(b) shows the delay line's behavior, which is not constant over all the frequency range, due to the nonlinearity of the phase response.

The regression line of each phase is calculated from Figure 3.33(a) in order to define the slope and the offset. The slope and offset are given in Table 3.12 for different values of capacitors over the frequency range of 9.5 GHz to 10.5 GHz. The maximum phase ~ 258° is obtained at C_{v1} = 0.15 pF. Besides, RF-PS has a tuning phase range of ~ 97° between lowest and highest capacitors values.

In Table 3.13, the performances of this analog RF-PS are compared with other studies based on topologies with varactors and distributed lines. In comparison, the phase shifter presented in this study has good performances and requires only two varactors.

Table 3.13 Varactor-based analog phase shifters.

Principle	***Num. varactors***	***Bandwidth (GHz)***	***Phase control***	***Max. IL (dB)***	***Ref.***
All-pass network	3	12-14	180°	4.7	[14]
All-pass network	3	6-7	180°	1.8	[15]
Schiffman PS (simulation)	6	10-13	168°	1.8	[16]
RTPS (simulation)	4	1.7-2.7	390°	1.5	[17]
Line loaded by varactors (simulation)	16	5-6	360°	5.7	[18]
RF-PS (simulation)	**2**	**8-12**	**97°**	**0.8**	**This work**

Num.: number, IL: insertion loss

3.5 Simulation of hybrid structure

As seen in Chapter 2, SOAs have nonlinear responses. In order to obtain a TTD, first we need to correct the nonlinearities responses of SOAs. In the current study, the nonlinearities of SOA responses can be corrected by combining a second RF stage, which is placed after the first stage (SOA). In this section, we choose the SOA-NL for simulation study since it has a nonlinear response. To correct the nonlinearity response of SOA-NL, RF-FF is used for the

"Hybrid correction structure" stage. RF delay (τ) is constant with respect to RF frequency, which yields a linear phase shift with respect to the RF frequency: $\phi = 2\pi\tau f + \phi_{offset}$, with $\phi_{offset} = 360^{\circ} \times$ k and k an integer number. Next, in order to realize a TTD, a tunable phase shifter is needed in order to adjust the phase offset, this is done in the "TTD hybrid structure" stage, which comprises a RF-FF and RF-PS in second stage.

The simulation of the hybrid structure is composed of two parts, in the first part the correction of SOA-NL response is presented in section 3.5.1 for the gain 0 and 5 dB (10 dB gain is fixed as reference), this is the hybrid correction structure. In the second part the simulation of the whole TTD hybrid structure is presented in section 3.5.2.

We compare, with and without using the hybrid correction, delay responses structure in terms of peak-to-peak variation $\Delta_{delay\ p-p}$, % of improvement of reduction in $\Delta_{delay\ p-p}$, standard deviation σ_{delay} to measure the divergence from the mean value, and the ratio of corrected σ_{delay} with respect to non-corrected ones. The comparisons of RF power are done in terms of variation of peak-to-peak $\Delta_{RFpower\ p-p}$, standard deviation and the ratio of $\sigma_{RFpower}$ with respect to non-corrected ones. All the numerical calculations are done versus frequency bands.

3.5.1 Simulation results of delay correction

Figure 3.34 shows the structure of hybrid correction structure using ADS from Keysight. The first stage "SOA-NL photo-detected" contains the theoretical (calculated) values of the normalized RF power and phase responses using Up-CPO for SOA-NL based on experimental data (section 2.5.3.2), which was obtained from fitting the pump-probe frequency measured responses in section 2.5.3.1.

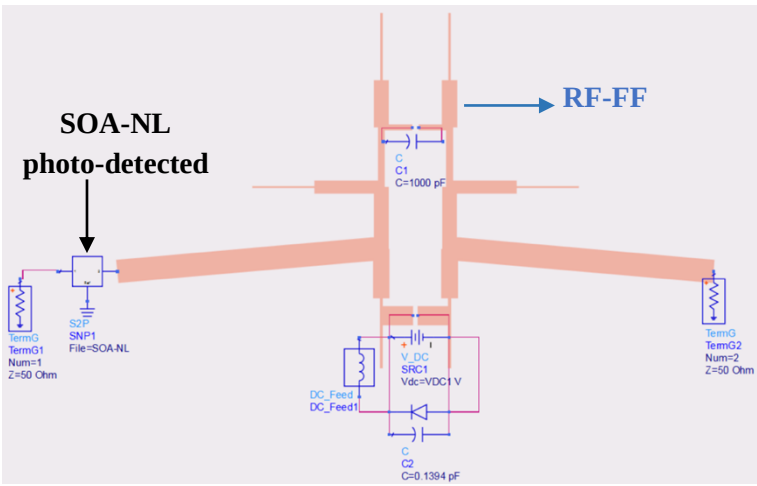

Figure 3.34 Schematic structure of hybrid correction structure in ADS. RF-FF: RF folded filter.

The block of SOA-NL photo-detected contains S_{21} parameters based on experimental data. The second stage contains the RF folded filter (RF-FF), which is done in section 3.3.4.1. Table 3.14 summarizes the delay depths and delay ripples obtained from Table 2.7 and Table 3.7. The delay correction is done by matching, for each delay depth of SOA-NL operating conditions, a corresponding delay ripple. Thus, we select for the SOA-NL gains: 0 dB and 5 dB of the first stage, the corresponding RF-FF V_{DC}: 12 V and 14 V, respectively.

Table 3.14 Delay response of SOA-NL and RF-FF over frequency range 9.5 GHz to 10.5 GHz.

Stage #1: SOA-NL		***Stage #2: RF-FF***		
Gain	***Delay depth***	***V_{DC}***	***Delay ripple (9.5~10 GHz)***	***Delay ripple (10~10.5 GHz)***
0 dB	8.1 ps	12 V	11.43 ps	10.39 ps
5 dB	7.7 ps	14 V	8.21 ps	7.49 ps
		16 V	6.53 ps	5.32 ps
		18 V	5.60 ps	3.76 ps
		20 V	5.07 ps	2.65 ps

We began our study by setting in second stage, V_{DC} of RF-FF to 12 V, for gain 0 dB. In a second separate case, V_{DC} is set to 14 V for a gain of 5 dB. The simulation results of delay correction over 1 GHz of frequency band are presented in Figure 3.35(a) for both cases.

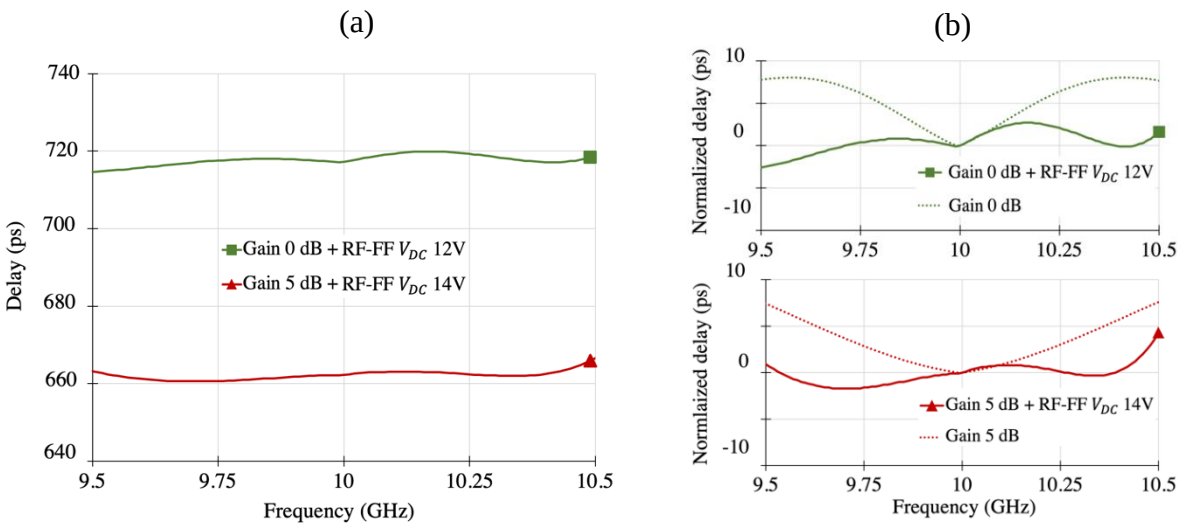

Figure 3.35 Hybrid delay correction (a), Normalized delay of SOA-NL (dotted line) and normalized hybrid delay correction (b).

Figure 3.35(b) shows the normalized delay correction of gain 0 and 5 dB compared to normalized delay response of SOA-NL (presented in section 2.4.3). We notice that the delay responses of gains 0 and 5 dB are enhanced over the total instantaneous bandwidth of 1 GHz, compared to delay of SOA-NL (in dotted line) as shown in Figure 3.35(b).

The comparison in terms of $\Delta_{delay\ p-p}$ and its improvement versus the frequency band, for the cases with and without the hybrid correction structure at gain 0 dB where RF-FF is set to 12 V, are presented in Figure 3.36(a). We can see an improvement in $\Delta_{delay\ p-p}$ in the range of 0.15 GHz to 1 GHz. A maximum improvement of 58.5 % is obtained for frequency bands ranging from 0.5 GHz to 0.75 GHz. The obtained results show that we can achieve delay correction in the range of 0.15 GHz to 1 GHz. This can be related to the fact that for a frequency band ≤ 0.125 GHz, SOA-NL has a low nonlinearity delay response, in other words a minimal depth. RF-FF cannot correct the minimum depth, due to the limit in ripples range of RF-FF.

(a)

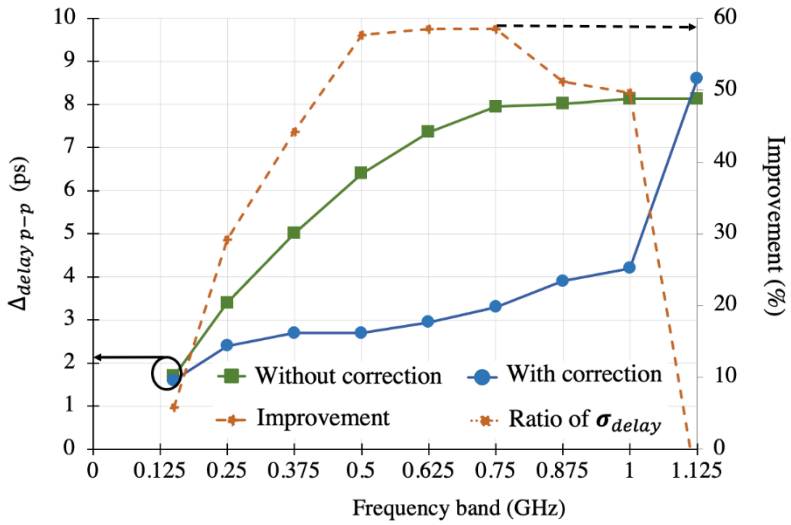

(b)

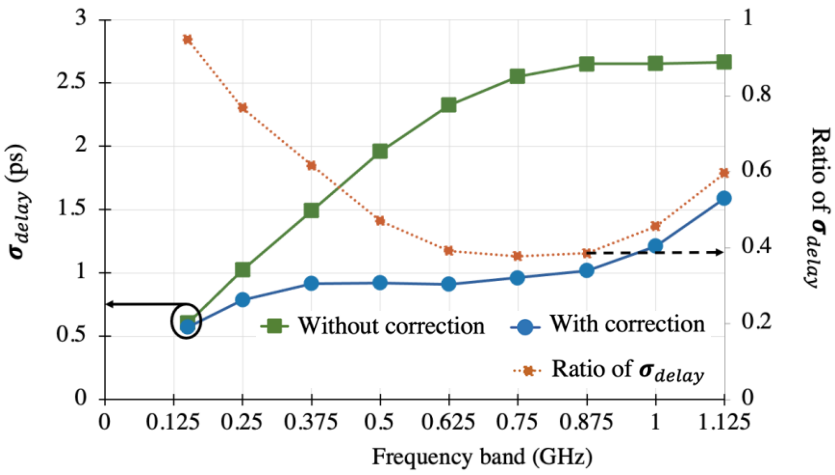

Figure 3.36 Results of gain 0 dB for: $\Delta_{delay\ p-p}$ with and without using the hybrid correction structure and % of improvement (a). σ_{delay} and the ratio of σ_{delay} (b).

Figure 3.36(b) shows the standard deviation σ_{delay} versus frequency band with and without using the delay correction. It also shows the ratio of σ_{delay}, which is defined as $\frac{\sigma_{delay\ with\ correction}}{\sigma_{delay\ without\ correction}}$. An improvement in terms of reduction of standard deviation is registered for gain 0 dB combined with a folded filter (RF-FF) at 14 V, over the entire frequency band. A smaller σ_{delay} indicates that the values tend to be close to the mean. A small ratio of σ_{delay} of about 0.38, is registered in the frequency band range from 0.625 GHz to 0.875 GHz. The use of RF-FF is effective in terms of $\Delta_{delay\ p-p}$ and σ_{delay}.

(a)

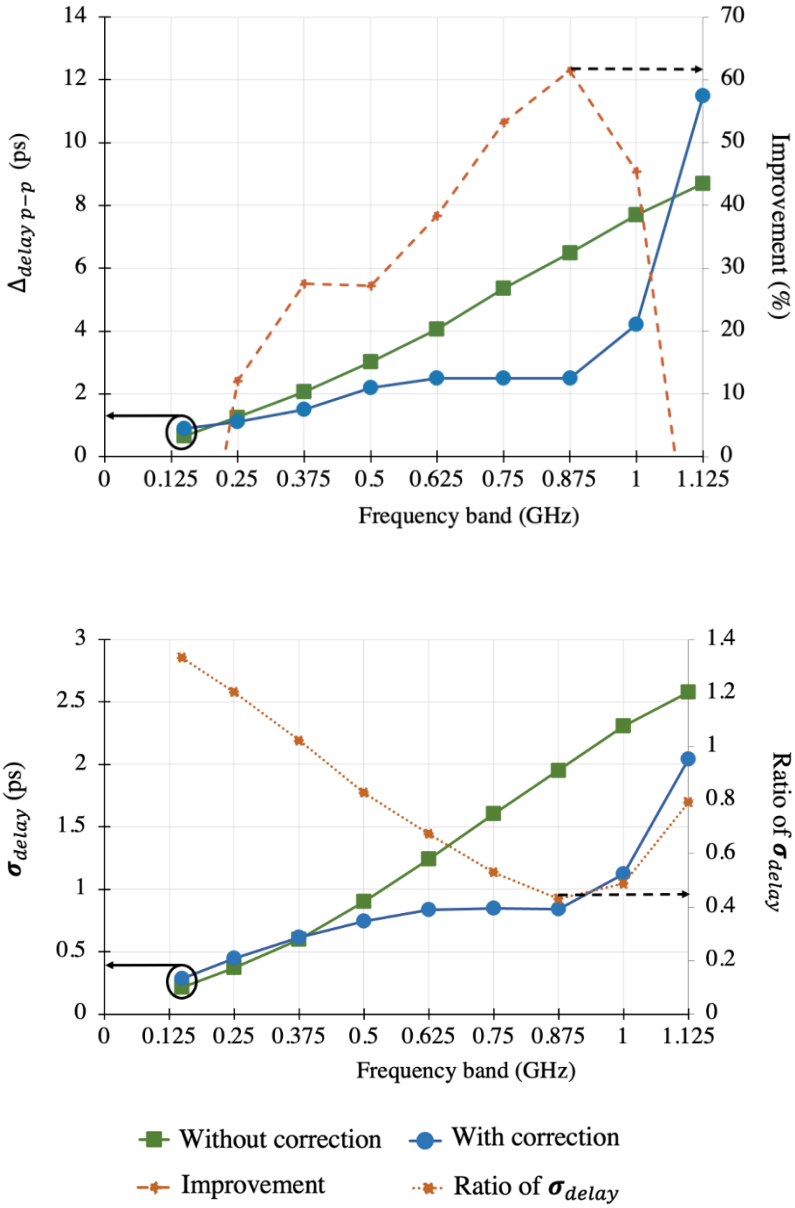

(b)

Figure 3.37 Results of gain 5 dB for: $\Delta_{delay\ p-p}$ with and without using the hybrid correction structure and % of improvement (a). σ_{delay} and the ratio of σ_{delay} (b).

Figure 3.37(a) shows, $\Delta_{delay\ p-p}$ and its improvement versus frequency band, for cases with and without hybrid correction structure at gain 5 dB where RF-FF is set to 14 V. We can see that $\Delta_{delay\ p-p}$ improved in the range from 0.375 GHz to 1 GHz. A maximum enhancement of 61.5 % is obtained for 0.875 GHz frequency band, for frequency bands lower than 0.25 GHz, RF-FF cannot correct at the minimum depth, due to the limit in minimum ripples range of RF-FF.

Additionally, we notice a smaller improvement at the frequency band range of $\Delta_{delay\ p-p}$, compared to the case of gain 0 dB (0.15 GHz to 1GHz). This is due to the fact that, the higher the gain is, the higher the injection current, the less the depth in delay response of SOA (Table 2.7).

Figure 3.37(b) presents the standard deviation of corrected and non-corrected delays, and the delay ratio. It shows that the improvement in σ_{delay} occurs in the frequency band from 0.5 GHz to 1.125 GHz. A low ratio of σ_{delay} around 0.42 is obtained at 0.875 GHz frequency band. The use of RF-FF is effective in terms of both $\Delta_{delay\ p-p}$ and σ_{delay}, in the frequency band ranging from 0.375 GHz to 1 GHz.

Figure 3.38(a) shows, the normalized RF power for the hybrid delay correction for both cases, gain 0 and 5 dB versus frequency. Table 3.15 shows the variation of normalized RF power noted as $\Delta_{RFpower\ p-p}$, with and without delay correction for both gains.

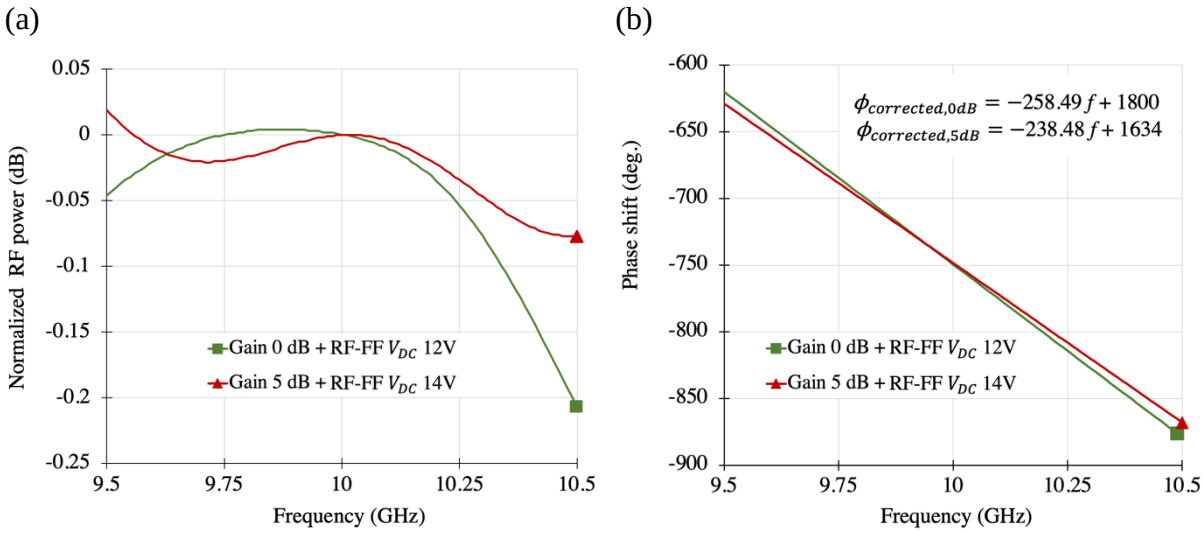

Figure 3.38 Response of the hybrid correction structure: Normalized RF power (a), Phase shift (b).

It shows that, the normalized RF power manifests in a maximum variation of 0.2 dB and 0.08 dB over 1 GHz for "gain 0 dB + RF-FF V_{DC} set to 12 V" and "gain 5 dB + RF-FF V_{DC} set to 14 V", respectively. Compared to using only SOA-NL, the normalized RF power is enhanced over the entire frequency band for "gain 5 dB + RF-FF V_{DC} set to 14 V". We can deduce that RF-FF does not degrade the system in terms of RF power.

Table 3.15 $\Delta_{RF\ power\ p-p}$ (dB) of the normalized RF power comparison between responses of SOA-NL without and with hybrid correction structure versus frequency band.

	0.15 GHz		***0.25 GHz***		***0.5 GHz***		***0.75 GHz***		***1 GHz***	
Gain	N.C	**C.**	N.C	**C.**	N.C	**C.**	N.C	**C.**	N.C	**C.**
0 dB	0.007	**0.005**	0.014	**0.012**	0.05	**0.05**	0.06	**0.12**	0.06	**0.203**
5 dB	0.004	**0.004**	0.009	**0.008**	0.045	**0.034**	0.07	**0.06**	0.115	**0.08**

N.C: No correction (response of SOA-NL only).

C.: Correction using hybrid correction structure (SOA-NL + RF-FF).

Figure 3.38(b) presents the corresponding phase shift of the hybrid correction structure, showing a linear phase shift over the instantaneous bandwidth. The evaluation of the linear relationship between the measured relative phase shift of the hybrid correction structure with respect to the linear regression line of phase shift, $\phi = 2\pi\tau f + \phi_{offset}$, are expressed by the linear phase error "ϵ". The linear regression line of each phase shift is calculated in order to define the delay and the offset. The phase shift regression lines are given by:

$$\phi_{corrected,0dB} = -258.49\, f + 1800, \text{ with } \epsilon = 0.3\times10^{-6}$$

$$\phi_{corrected,5dB} = -238.48\, f + 1634, \text{ with } \epsilon = 0.2\times10^{-6}$$

It shows that a low error around 0.2×10^{-6} in phase linearity is registered for $\phi_{corrected,5dB}$, using "gain 5 dB + RF-FF V_{DC} set to 14 V". Besides, we notice from equations $\phi_{\text{corrected,0dB}}$ and $\phi_{\text{corrected,5dB}}$ that the offsets ϕ_{offset} of the corrected delay responses are different, about 1800 and 1634 degrees, respectively. In other words, the microwave phase shift does not correspond to a true time delay. This reaffirms what we have presented before, which is that in order to obtain a TTD, a second RF filter should be added.

3.5.2 Simulation results of TTD hybrid structure

In this section, we present the simulation of the TTD hybrid structure (see Figure 3.39) by placing RF-PS (presented in section 3.4.2) in series after a RF folded filter, so that the phase offset of the corrected responses can be tuned to achieve a TTD, by varying the capacitance values of RF-PS.

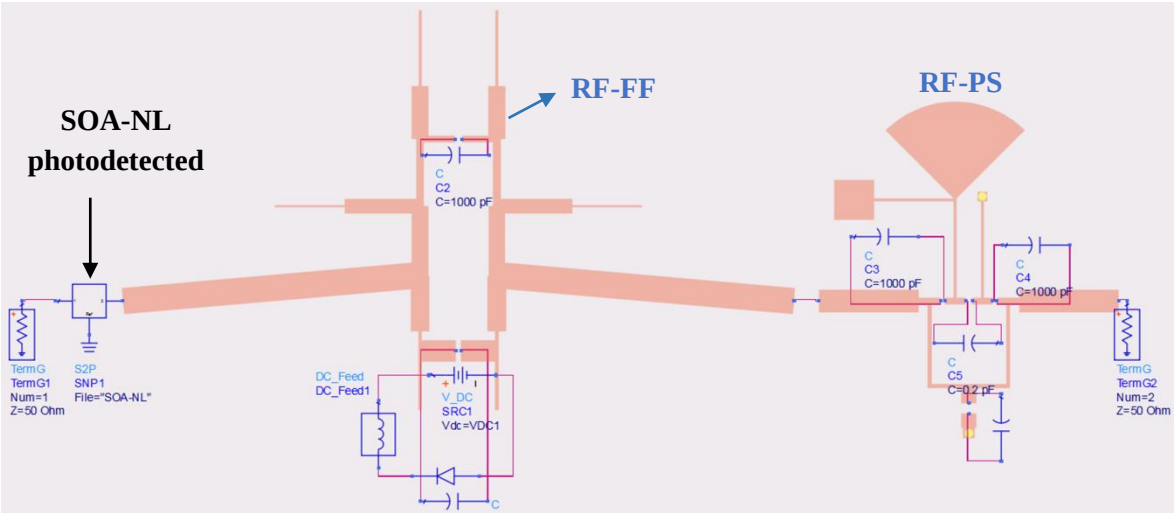

Figure 3.39 Schematic of TTD hybrid structure in ADS, RF-FF: RF folded filter, RF-PS: RF phase shifter.

In order to obtain TTD, a reference phase offset of 1800° needed to be attained, which corresponds to ϕ_{offset} = 360° × k (k = 5). Therefore, an offset of 166° is needs to be added to the offset of the corrected "gain 5 dB + RF-FF V_{DC} 14V" having phase offset of 1634°. From Table 3.12 we select C_{v1} = 0.45 pF, which has an offset of ~166°.

The simulation results of the TTD and normalized RF power of the hybrid structure are shown in Figure 3.40(a) shows the TTD response deviating by 4.6 ps with σ_{delay} of 1.25 ps over 1 GHz of bandwidth. Using the folded filter with a V_{DC} set to 14 V + RF-PS set to 0.45 pF for gain 5 dB yields, rather than 4 ps using delay correction structure, a σ_{delay} of 1.12 ps. This is due to the response of the delay for C_{v1} = 0.45 pF not being constant (see Figure 3.33(b)). Besides, we can notice that TTD response is shifted by 127 ps, compared to the response of delay correction, for "gain 5 dB + RF-FF 14 V + RF-PS 0.45 pF". A tunable TTD range of 67 ps is registered.

Figure 3.40(b) shows that the TTD hybrid normalized RF power exhibited a 0.13 dB variation $\Delta_{RFpower\ p-p}$ for "gain 5 dB + RF-FF 14 V + RF-PS 0.45 pF". Compared to hybrid correction structure, the normalized RF power is degraded by 0.015 dB for "gain 5 dB + RF-FF V_{DC} set

to 14 V + RF-PS 0.45 pF", over 1 GHz. This is due to the response of the delay for C_{v1} = 0.45 pF not being ideally constant (see Figure 3.32(a)). A low standard deviation no more than 0.03 dB is registered for "gain 5 dB + RF-FF V_{DC} set to 14 V + RF-PS 0.45 pF", over 1 GHz.

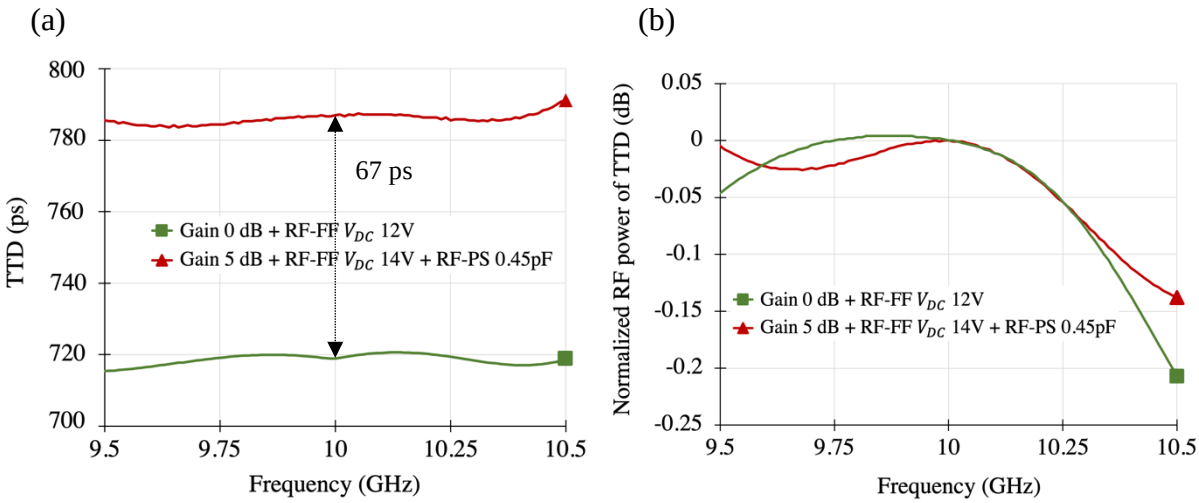

Figure 3.40 (a) TTD hybrid structure response. (b) Normalized RF power response of TTD hybrid structure.

Figure 3.41 presents phase shifts of the TTD hybrid structure, where the responses are linear with respect to frequency over the 1 GHz bandwidth. We calculate the regression line of the TTD hybrid structure phase shift for both gains and the error of phase linearity. As a result, we obtain the same offset:

$$\phi_{\mathrm{TTD,0dB}} = -258.49\, f + 1800, \text{ with } \epsilon = 0.4\times10^{-6}$$

$$\phi_{\mathrm{TTD,5dB}} = -282.56\, f + 1800, \text{ with } \epsilon = 0.5\times10^{-6}$$

This shows that a maximum error in phase linearity around 0.5×10^{-6} is registered for $\phi_{\mathrm{TTD,5dB}}$ over 1 GHz. Besides, we can see that both phase shifts intersect at the ϕ-axis at a phase shift offset ϕ_{offset} of 1800°. The point of intersection with the ϕ-axis occurs at the null frequency, as shown in Figure 3.41(b). Thus, TTD is achieved, it is about 718.1 ps and 784.9 ps, for $\tau_{TTD,0dB}$: "gain 0 dB + RF-FF 12 V" and $\tau_{TTD,5dB}$: "gain 5 dB + RF-FF 14 V + RF-PS 0.45 pF", respectively.

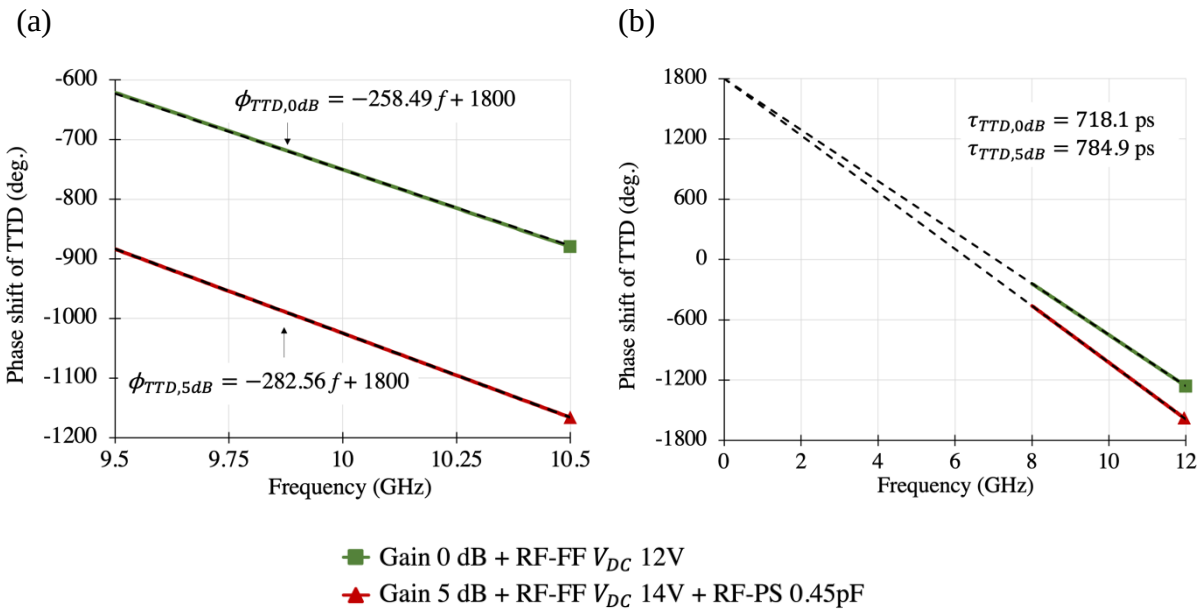

Figure 3.41 Phase shifts of TTD (a). Zoom out of phase shifts of TTD phase shifts (b). Dashed lines are the linear phase shift regression lines of TTD hybrid structure.

3.6 Conclusion

In this chapter, the concept of compact tunable RF phase shifts and tunable RF filter is presented. The concept of compact structure of tunable RF phase shift is validated through simulation. The tunable RF filter is realized by using half-wavelength open circuit stubs with cross coupling between resonators 1 and 6. The use of cross coupling creates additional transmission zeros which alters the filter responses of the group delay. As a result, a ripple appears at center frequency. We showed that the placement of capacitor, located at the minimum of electric field is a feasible solution, and demonstrated the suitability of our synthesis of folded and curved filters through simulation. Tunable delay is achieved by altering the bias voltage of the varactor. We have proposed a new configuration and, to the best of our knowledge, for the first time, the correction of the nonlinear responses of SOA-NL. It consists of a tunable RF phase shift, based on a RF folded filter, which aims to correct the nonlinearity in responses of the first stage. The corrected delays can be electrically controlled by voltage control of variable capacitances of RF filters with respect to the operating point of SOA. TTD hybrid structure is presented and validated through simulation based on experimental data; by combining two stages SOA-NL and the RF stage (RF-FF + RF-PS). TTD ~718.1 ps and 784.9 ps are obtained for SOA-NL, by adding RF-PS to the second stage. Additionally, a TTD tuning range of 67 ps is obtained. In the next chapter, we will experimentally present the hybrid correction structure of SOA-XN. Therefore, we will test the feasibility study of the hybrid correction structure through the association of two stages based on experimental data.

Bibliography of chapter 3

[1] Y. K. Awasthi, H. Singh, M. Sharma, S. Kumari, and A. K. Verma, “Computer-aided design-based circuit model of microstrip line for terahertz interconnects technology,” *J. Eng.*, vol. 2017, no. 9, pp. 512–526, Sep. 2017, doi: 10.1049/joe.2017.0078.

[2] Q. J. Gu, “THz interconnect: the last centimeter communication,” *IEEE Commun. Mag.*, vol. 53, no. 4, pp. 206–215, Apr. 2015, doi: 10.1109/MCOM.2015.7081096.

[3] E. J. Denlinger, “Losses of Microstrip Lines,” *IEEE Trans. Microw. Theory Tech.*, vol. 28, no. 6, pp. 513–522, Jun. 1980, doi: 10.1109/TMTT.1980.1130112.

[4] E. O. Hammerstad, “Equations for Microstrip Circuit Design,” in *1975 5th European Microwave Conference*, Hamburg, Germany, Oct. 1975, pp. 268–272, doi: 10.1109/EUMA.1975.332206.

[5] I. J. Bahl and D. K. Trivedi, "A Designer's Guide to Microstrip Line", Microwaves, May 1977, pp. 174-182.

[6] J. S Hong and M. J. Lancaster, “Microstrip Filters for RF/Microwave Applications”, New York: Wiley, pp. 89-91, Jul. 2001.

[7] L. Young G. Matthaei and E. M. T. Jones, “Microwaves Filters, Impedance-Matching Networks and Coupling Structures”, Boston, Artech House, 1980. 1096p.

[8] D. M. Pozar, “Microwave Engineering”, 3rd Edition, John Wiley & Sons, Inc., New York, 2005.

[9] MA46H120 series, ADS Spice Diode Model, Available at: http://cdn.macom.com.

[10] MA46H120 series, GaAs constant gamma Flip-chip Varactor diode, Available at: http://www.macomtech.com/datasheets/MA46H120.pdf, MA-COM.

[11] J. C. Wu, C. C. Chang, S. F. Chang, and T. Y. Chin, “A 24 GHz full 360° CMOS r eflection-type phase shifter MMIC with low loss-variation,” in *2008 IEEE Radio*

Frequency Integrated Circuits Symposium, Atlanta, GA, USA, Jun. 2008, pp. 365–368, doi: 10.1109/RFIC.2008.4561455

[12] J. J. P. Venter, T. Stander, and P. Ferrari, "X-Band Reflection-Type Phase Shifters Using Coupled-Line Couplers on Single-Layer RF PCB," IEEE Microw. Wirel. Compon. Lett., vol. 28, no. 9, pp. 807–809, Sep. 2018, doi: 10.1109/LMWC.2018.2853562.

[13] S. Y. Zheng, W. S. Chan, and K. F. Man, "Broadband Phase Shifter Using Loaded Transmission Line," *IEEE Microw. Wirel. Compon. Lett.*, vol. 20, no. 9, pp. 498–500, Sep. 2010, doi: 10.1109/LMWC.2010.2050868.

[14] H. Hayashi, T. Nakagawa, and K. Araki, "A miniaturized MMIC analog phase shifter using two quarter-wave-length transmission lines," *IEEE Trans. Microw. Theory Tech.*, vol. 50, no. 1, pp. 150–154, Jan. 2002, doi: 10.1109/22.981259.

[15] K. Khoder, M. Le Roy, and A. Perennec, "An an all-pass topology to design a continuous phase shifter with low insertion loss and constant differential phase shift," in *2014 9th European Microwave Integrated Circuit Conference*, Rome, Italy, Oct. 2014, pp. 612–615, doi: 10.1109/EuMIC.2014.6997931.

[16] R. Wali, L. Osman, T. Razban, and Y. Mahé, "Electronically Reconfigurable Two-Stage Schiffman Phase Shifter for Ku Band Beam Steering Applications," *Int. J. Adv. Comput. Sci. Appl.*, vol. 9, no. 11, 2018, doi: 10.14569/IJACSA.2018.091178.

[17] A. M. Abbosh, "Compact Tunable Reflection Phase Shifters Using Short Section of Coupled Lines," *IEEE Trans. Microw. Theory Tech.*, vol. 60, no. 8, pp. 2465–2472, Aug. 2012, doi: 10.1109/TMTT.2012.2198232.

[18] F. Ellinger, H. Jackel, and W. Bachtold, "Varactor-loaded transmission-line phase shifter at C -band using lumped elements," *IEEE Trans. Microw. Theory Tech.*, vol. 51, no. 4, pp. 1135–1140, Apr. 2003, doi: 10.1109/TMTT.2003.809670.

CHAPTER 4

Hybrid correction structure

4.0 Introduction **165**

4.1 Manufacture and experimental results of the RF filter **166**

4.1.1 Experimental results of RF-FF using VNA bias tee 166
4.1.2 Experimental results of RF-FF using an external bias tee 173

4.2 Characterization of SOA-XN **174**

4.3 Complete hybrid correction structure **179**

4.3.1 Measurement of the hybrid correction structure 179
4.3.2 Simulation of the hybrid correction structure based on experimental data of SOA-XN 182

4.4 Conclusion **193**

Bibliography of chapter 4 ..... **194**

4.0 Introduction

The aim of this chapter is to test the hybrid correction structure based on experimental data. First, we present the measurement results of tunable RF filters; both folded (RF-FF) and curved (RF-CF). In the complete hybrid measurement, we can't use the DC input of the VNA, so we have to use an external bias tee to polarize the varactors in the RF-FF circuit. Therefore, we investigate the effects of using an external bias tee on the response behavior of RF-FF. Then, we introduce the problematic response of Up-CPO measured at low operating frequency, followed by a complete measurement of the hybrid correction structure. We show how the low operating frequency and the external bias tee affect the correction; this is done through measurement of the complete hybrid correction structure. In order to test the feasibility of the hybrid correction structure, we separate the measurement of the two blocks, then we present the simulation of the hybrid correction structure based on experimental data, by coupling the measured data of the first block “SOA-XN” with the measured data of “RF-FF”.

4.1 Manufacture and experimental results of the RF filter

In order to validate the proposed folded and curved designs, the final designs are fabricated and evaluated. The designed filters are implemented on a conventional RO4003 substrate (ε_r = 3.55, h = 0.813 mm, tan δ = 0.0027, T = 17 μm), and fabricated using laser engraving technology. The dimensions with feeding lines of the folded and curved designs are 47×32 and 40×28 mm, respectively. In addition, we used RF standard SMA Southwest connectors (292-04A-6). A photograph of the fabricated filters is provided in Figure 4.1. Measurements were performed using a Vector Network Analyzer (VNA), with a VNA output power of −10 dBm, calibrated with a Short-Open-Load-Thru (SOLT) calibration kit.

(a) (b)

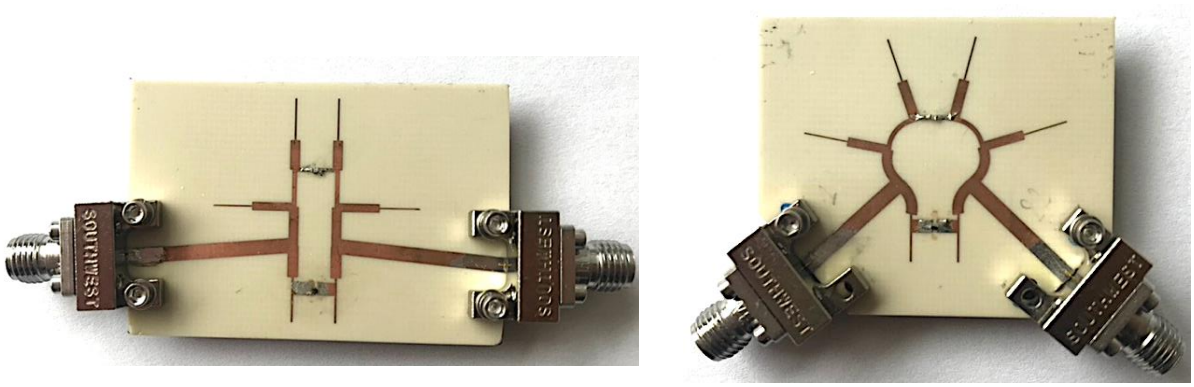

Figure 4.1 photograph of (a) RF-FF, (b) RF-CF.

4.1.1 Experimental results of RF-FF using VNA bias tee

The selected varactor is a MA46H120 with a capacitance tuning voltage ranging from 12 to 20 Volts. During the measurement, an external DC bias is connected directly into the VNA's bias tee. Thanks to the internal bias tee of the VNA, both the RF signal and the DC bias are applied to the RF filter through the VNA port-1. The DC block capacitor (C_b) then blocks DC signal from passing thru port-2 of the VNA. Thus, port-2 acts as a ground plane for the varactor. Figure 4.2 provides a photograph of the experimental setup of the S-parameters measurement of RF filter.

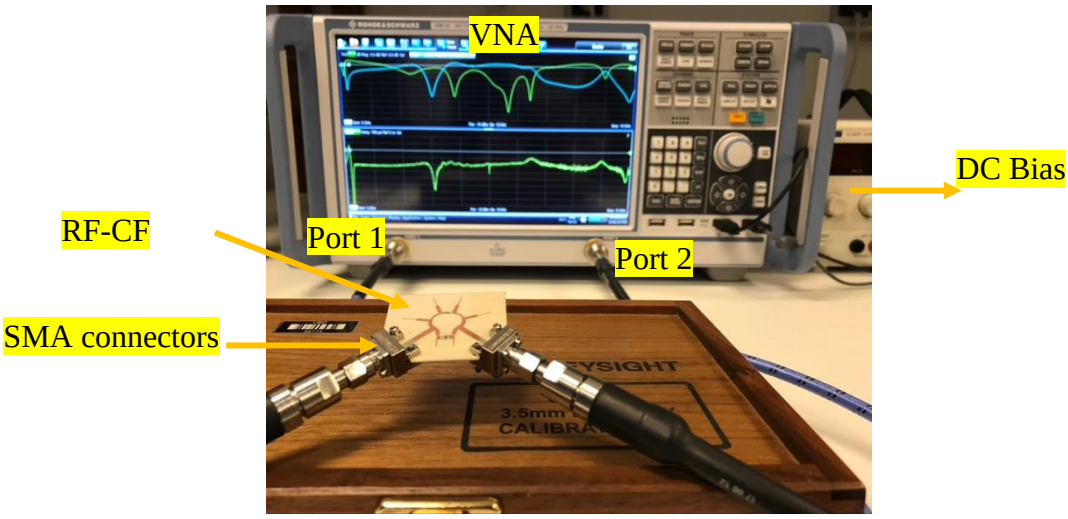

Figure 4.2 Experimental setup of S-parameters measurement of RF curved filter.

The simulated and measured results of the RF folded filter for V_{DC} = 16 Volts are reported in Figure 4.3(a). Both return losses are greater than 12 dB across the wide band range from 8 to 12 GHz. As it can be observed, there is a frequency offset that slightly shifts the measurement insertion and return losses to a lower frequency when compared to the simulated ones; there is also more insertion loss than projected by the EM-simulator. The transmission zeros for the measured design are obtained at 7.74 and 12.14 GHz, compared with the simulated ones of 7.86 and 12.3 GHz. The measured insertion loss is 2.5 dB, compared with the simulated value of 0.8 dB, across the frequency range from 8 GHz to 12 GHz, respectively. The insertion loss is due to losses in the copper, the dielectric substrate, and fabrication tolerances.

Figure 4.3(b) shows the delay response based on measured data of the phase shift. A shift in response to lower frequencies occurs compared with the simulated ones where the delay ripple in the frequency of interest (9 to 11 GHz) is reported at 9.7 GHz, compared to the simulated one at 10 GHz.

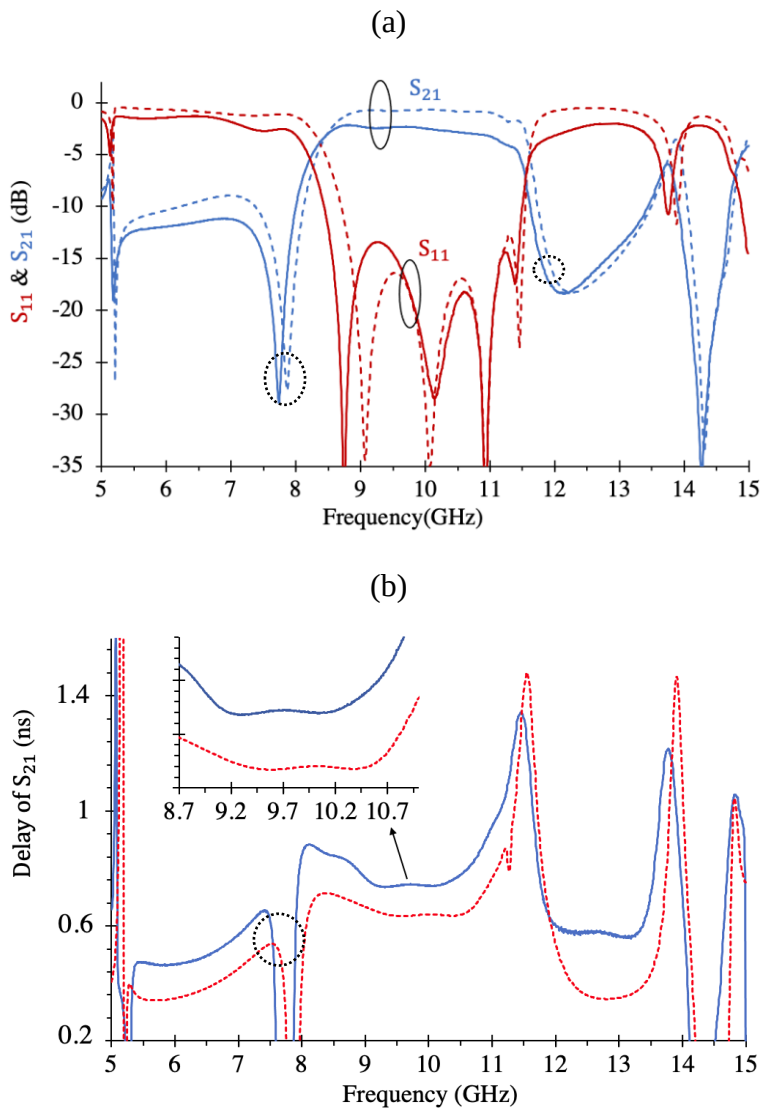

Figure 4.3 S_{11} and S_{21} of RF-FF for V_{DC} =16V (a). Delay of RF-FF for V_{DC} =16V (b). Simulated results (dashed lines) and measured results (solid lines).

We observed that there is a divergence between the simulated and measured performances. This is due to differences between the ideal theoretical varactor model and the real-world performance of the varactors as well as the manufacturing tolerances and real characteristics of the printed circuit board (PCB). To examine the sensitivity of the design to dielectric variations, we simulate the RF folded filter using different dielectric constants. We take $\varepsilon_r = 3.65$ as the best correspondence to real design; this method is so-called retrofit simulation.

Figure 4.4(a) illustrates the S_{11} and S_{21} responses of the retrofit EM-simulation for V_{DC} = 16 V. The EM-simulation of the RF folded filter shows that the transmission zeros of both simulated and measured results are obtained at 7.74 and 12.14 GHz, and the measured and simulated filters have the same bandwidth. However, for measured S_{21} the level is -2.5 dB, which is lower compared to simulated ones. The frequency shift between both sets of data is likely

caused by the discrepancies in the filter's simulated and fabricated substrate relative dielectric constant ε_r. Besides, measured S_{11} is in alignment with simulated results for frequencies larger than 11 GHz. Figure 4.4(b) shows the simulated and calculated delay responses of S_{21} based on measured data.

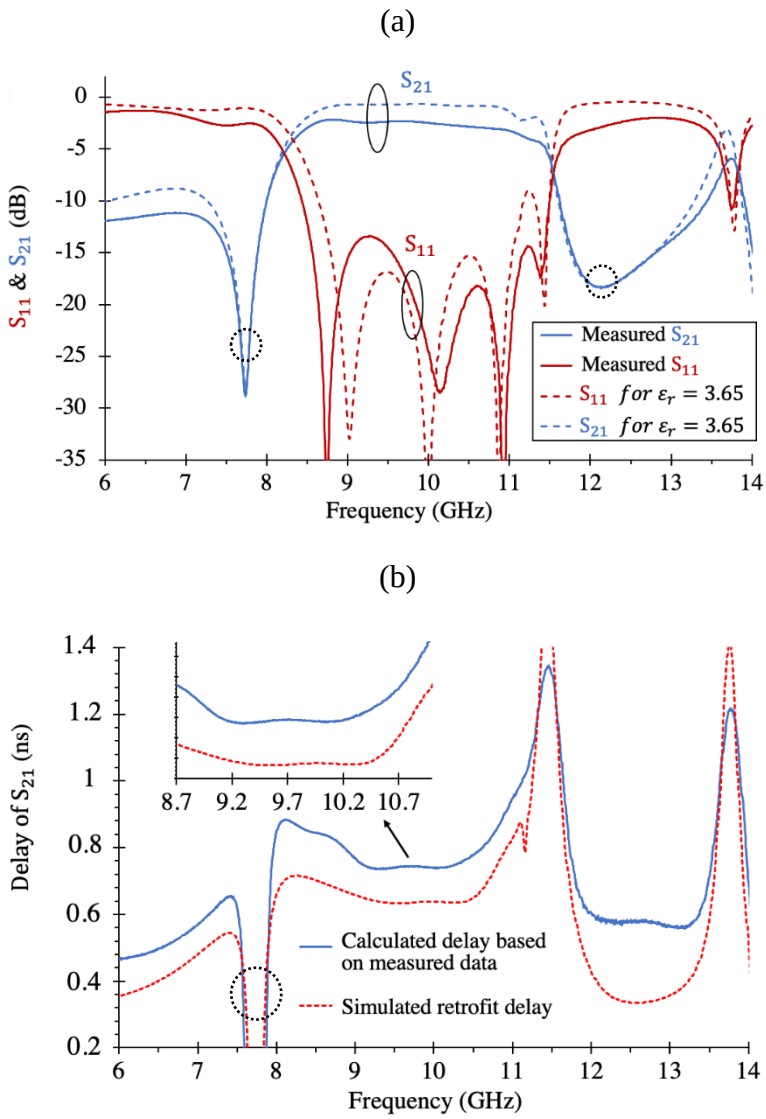

Figure 4.4 Retrofit electromagnetic simulation and measured results of RF-FF for V_{DC} =16V: S_{11} and S_{21} (a). Delay of S_{21} (b). Retrofit simulated results (dashed lines) and measured results (solid lines).

Figure 4.5 shows all the measured results of RF-FF when V_{DC} is varied between 14 and 20 V. The transmission zeros are obtained at 7.74 and 12.14 GHz (Figure 4.5(a)). The insertion and return losses are 2.5 dB and 14 dB across the frequency range from 8 to 12 GHz, respectively.

A ripple in the group delay appears at 9.7 GHz in a range of 0.8 GHz (9.3 ~10.1 GHz). From prior simulation, it was expected that the ripple in the group delay would be located at 10 GHz, experimentally it was shown to appear at 9.7 GHz (Figure 4.5(b)). This is due to the sensitivity of the dielectric constant ε_r of the substrate and the effect of the SMA connectors.

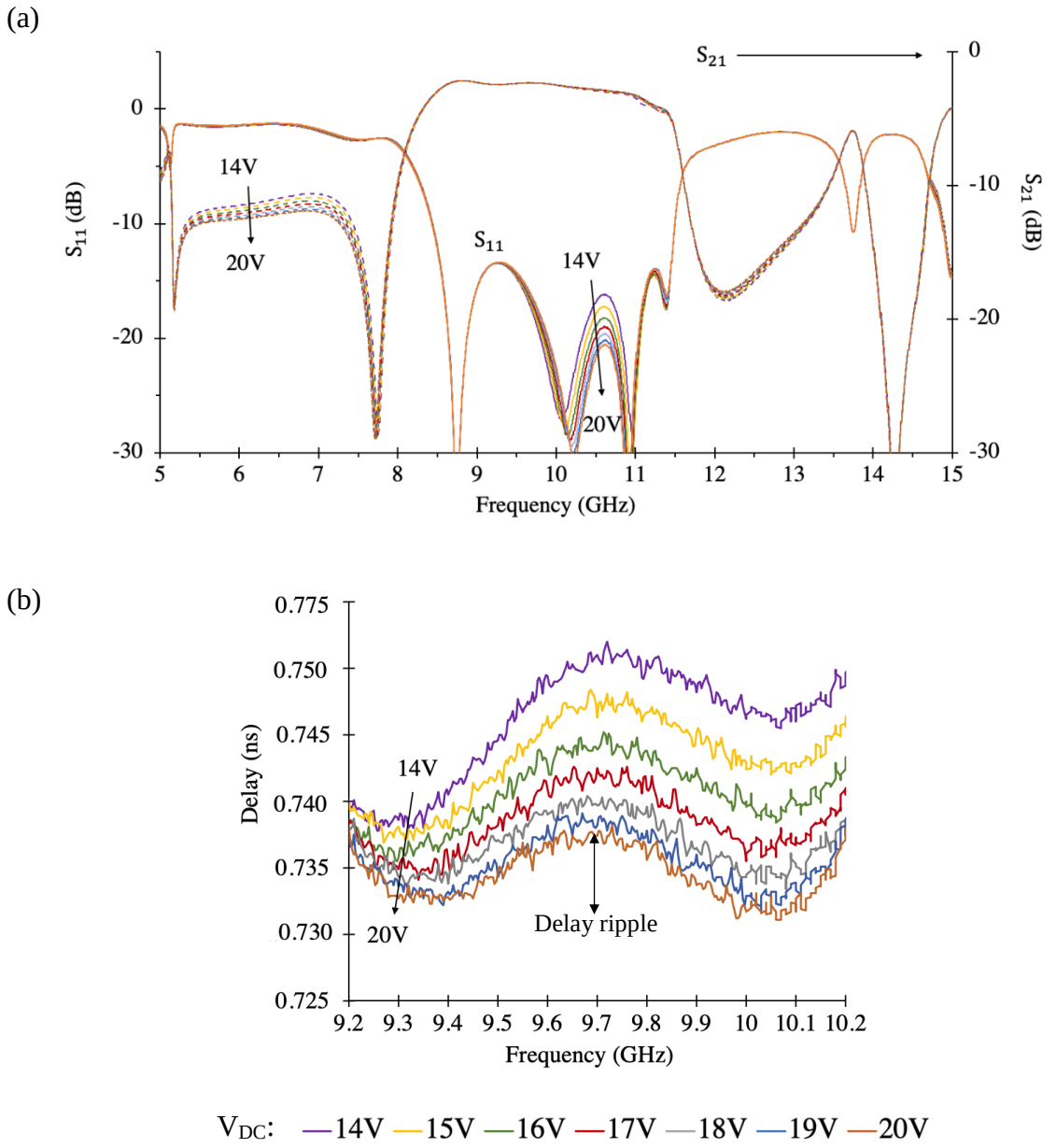

Figure 4.5 Measurement of RF-FF (a) S_{11} and S_{21}, (b) Delay of S_{21} with 5% moving averages.

Table 4.1 shows the tunable delay ripple of the folded design for a control voltage varying from 14 to 20 Volts at 1-Volt increments. For the high tunable voltages 18 V to 20 V, the ripples in delay, are almost symmetric (deviation of $\pm$ 0.2 ps) in the frequency band of 9.2 to 10.2 GHz.

Table 4.1 Delay ripple of measured RF-FF for various voltages.

Voltages	***Delay ripple (9.2~9.7 GHz)***	***Delay ripple (9.7~10.2 GHz)***
14 V	12.6 ps	4.6 ps
15 V	10.7 ps	5.3 ps
16 V	8.7 ps	5.9 ps
17 V	7.4 ps	5.7 ps
18 V	6.0 ps	5.8 ps
19 V	5.9 ps	6.1 ps
20 V	5.2 ps	5.4 ps

Figure 4.6 shows the measured S_{11} and S_{21} for the curved design. An important ripple appears in the overall frequency band, that causes a large ripple in the delay at 9.7 GHz, this was probably induced by residual solder acting as a parasitic capacitance. In turn, this leads to significant ripple increases in the delay at frequency 9.7 GHz as shown in Figure 4.7. Table 4.2 gives the delay ripples of RF-CF for various voltages.

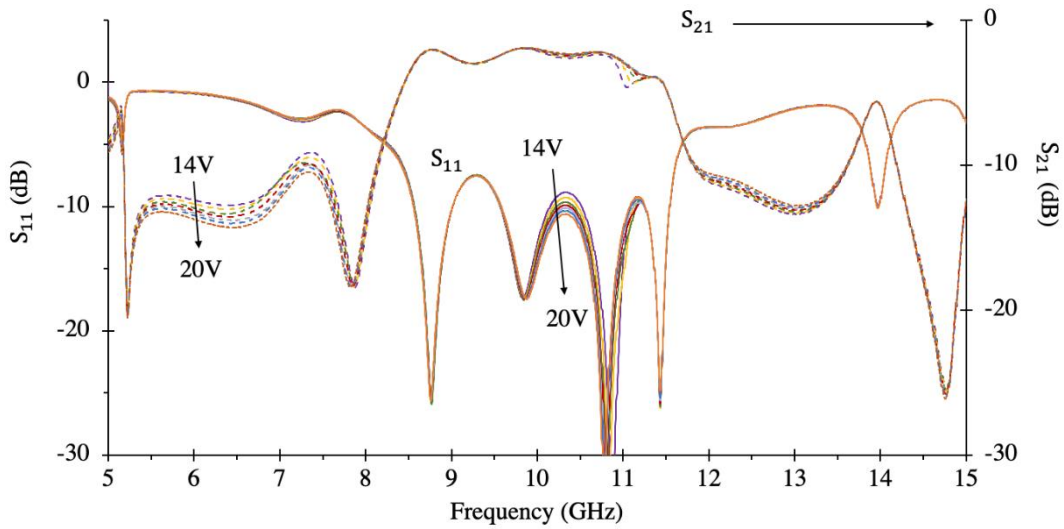

Figure 4.6 Measurement of RF-CF S_{11} and S_{21}.

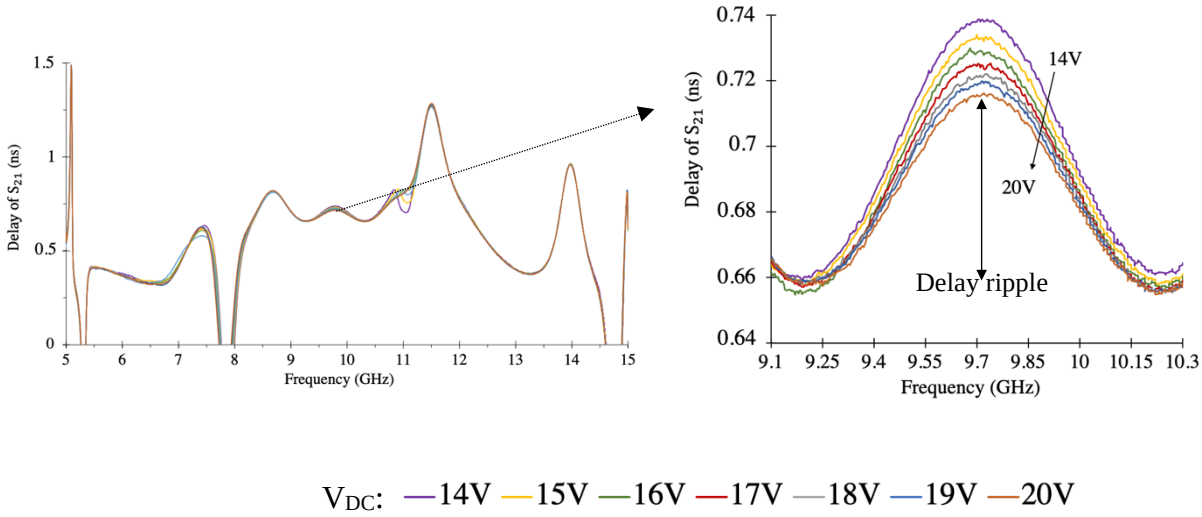

Figure 4.7 RF-CF delay of S_{21} with 5% moving averages.

Table 4.2 shows the tunable delay ripple of the curved filter design for a control voltage varying from 14 to 20 Volts at 1-Volt increments. The minimum delay ripple of 57 ps is obtained at 20 V, and the maximum delay ripple of around 79 ps is obtained at 14 V, in the frequency band of 9.2 to 10.2 GHz.

Table 4.2 Delay ripple of measured RF-CF for various voltages.

Voltages	***Delay ripple (9.2~9.7 GHz)***	***Delay ripple (9.7~10.2 GHz)***
14 V	79 ps	78 ps
15 V	75 ps	76 ps
16 V	70 ps	72 ps
17 V	66 ps	68 ps
18 V	64 ps	67 ps
19 V	60 ps	63 ps
20 V	57 ps	60 ps

As seen in section 2.5.6, the maximum delay depth for gain 5 dB, for SOA-NL and SOA-XN, is shown to be around 8.2 and 13.5 ps, respectively. Besides, the maximum delay ripple of RF-FF is 12.6 ps at V_{DC} = 14V, while for RF-CF the maximum is 79 ps at V_{DC} = 14V. In order to correct the Up-CPO response of SOA-XN, the RF-FF will be used in the hybrid correction structure, since its delay ripple of 12.6 ps is contained within the range of the SOA-XN delay depth.

4.1.2 Experimental results of RF-FF using an external bias tee

In order to proceed with the measurement of the hybrid correction structure, the constraint that we face is that the Anritsu vector network analyzer used for measurements of the hybrid correction structure has no DC port to allow us to directly bias the varactor of the RF folded filter. In this case, an external bias tee is needed. The RF-FF is then characterized with the presence of an external bias tee.

The delay induced by the RF folded filter employing an external bias tee is illustrated in Figure 4.8. We can clearly see that the delays are not symmetric around 9.7 GHz over 1 GHz of frequency band. We can attribute this to the response of the bias tee. We define the ripple, first for 13 V, and 14 V, as the difference between point A and point B (minimum). Then, for 15 V, 16 V, 18 V, and 20 V we define the ripple as the difference between point A and point B' (minimum). Among all voltage values, the ripple is mostly symmetric in the range of 9.7 $\pm$ 0.25 GHz for 13 V, 14 V, and 15 V. The delay ripples are summarized in Table 4.3.

An increase in the delay ripple is observed when using the external bias tee, compared to the case of using the internal bias tee of the VNA. Figure 4.9 shows the delay response of RF-FF at V_{DC} = 20 V using an external bias tee compared to RF-FF using the internal VNA bias tee. We can see that for a frequency band ranging from 9.4 GHz to 9.65 GHz the two responses are identical. An important difference between these two responses starts to appear at frequencies larger than 9.7 GHz, where an undesirable depth occurs at frequencies larger than 9.65 GHz which will be harmful to the correction of the Up-CPO response when we will cascade the SOA by the RF-FF via a photodiode.

The obtained results highlight a bias network must be integrated in the early stage of the design layout of the RF-FF.

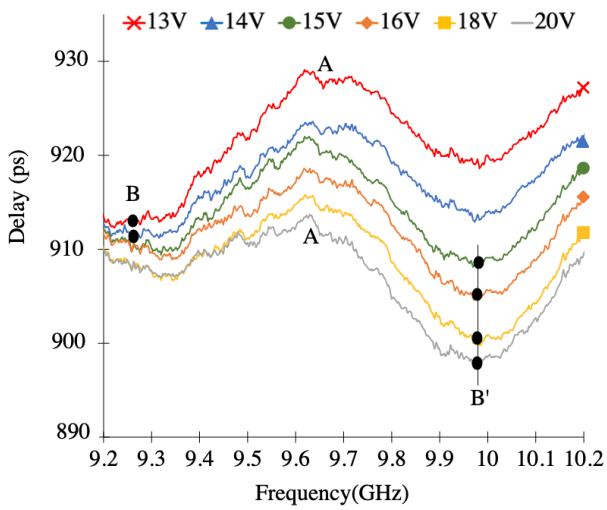

Figure 4.8 Delay of RF-FF employing an external bias tee.

Table 4.3 Delay ripples of RF-FF and external bias tee

Voltage	***Ripple (ps)***
13 V	15.2
14 V	11.4
15 V	12.1
16 V	12.6
18 V	14.1
20 V	14.8

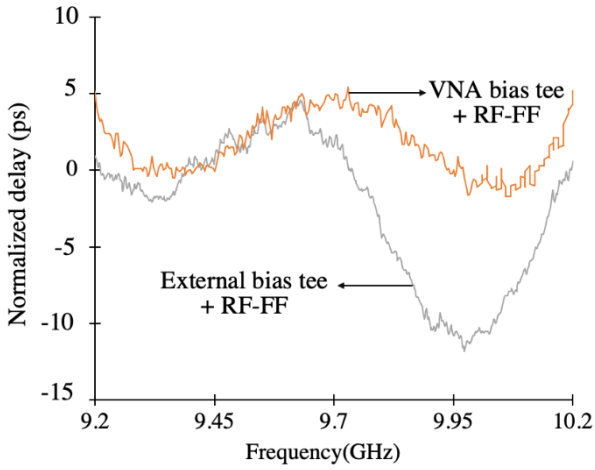

Figure 4.9 Normalized delay of RF-FF employing an external bias tee and VNA bias tee at V_{DC} = 20 V.

Before proceeding to the complete hybrid measurement, the characterization of the SOA-XN needs to be done.

4.2 Characterization of SOA-XN

In this section, we evaluate the Up-CPO response of the SOA-XN for different bias currents at 9.7 GHz. Regarding the response of RF-FF, we choose to correct the Up-CPO response of SOA-XN at the operating frequency of 9.7 GHz instead of 10 GHz, due to the fact that the delay ripple of RF-FF is located at 9.7 GHz, as seen in section 4.1.1.

As the characterization of SOA responses in chapter 2 was performed for only 3 different bias currents, we start first by characterizing the XGM and Up-CPO responses of the SOA-XN at more different bias currents.

For the XGM responses, we first recall the experimental pump-probe setup from section 2.5.3.1 in which an intensity-modulated optical pump of 5 dBm at 1545 nm and a continuous-wave (CW) optical probe of −5 dBm at 1550 nm were simultaneously injected into the SOA. An optical filter with a 1 nm bandwidth was used at the SOA output to measure the converted signal at 1550 nm through XGM. The measurement results of the XGM response are presented in Figure 4.10.

The RF power of the output RF signal is measured relatively to a back-to-back measurement, without the SOA in the optical path. Therefore, the measured RF power is obtained by $20\log(|S_{21,z}|) - 20\log(|S_{21,y}|)$, where z refers to SOAs bias current and y is the back-to-back measurement without SOA.

A low-pass response of the RF power of SOA-XN from 0.1 GHz to 40 GHz is registered for different bias currents (Figure 4.10). The experimental results of relative RF power show that for bias currents higher than 300 mA, the SOA presents a cutoff frequency higher than the operating frequency of 9.7 GHz of the RF-FF. It can reach up to 22.7 GHz (for 450 mA) as depicted in Table 4.4.

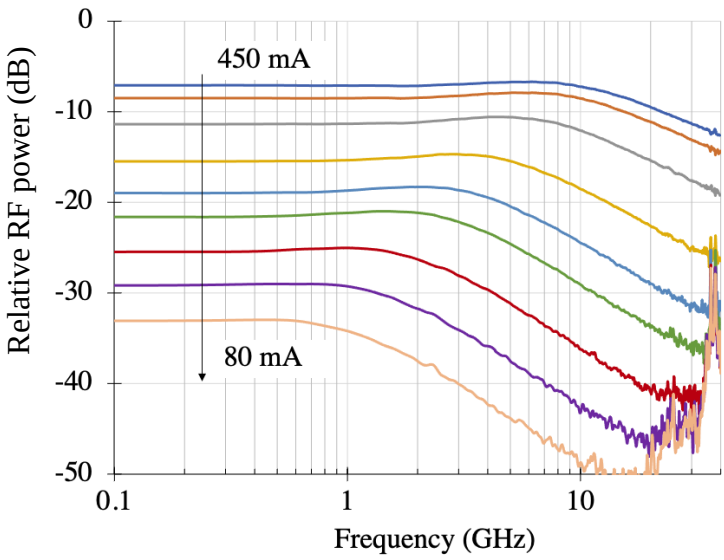

Figure 4.10 Measured relative RF power of SOA-XN with different bias currents.

Table 4.4 Cutoff frequency of SOA-XN.

Bias current	***Gain (dB)***	***f_{-3dB} (GHz)***
450 mA	13.5	22.74
400 mA	11.5	21.58
300 mA	9.5	16.38
200 mA	6.5	9.91
150 mA	6	6.65
125 mA	4.75	5.01
100 mA	4.25	3.25
85 mA	3	2.21
80 mA	2.25	1.52

As the SOA-XN can present a higher bandwidth than f_c = 9.7 GHz and as the theoretical Up-CPO response is independent from the operating frequency f_c (see chapter 2 section 2.5.5), we characterize the Up-CPO at f_c = 9.7 GHz and 30 GHz. Our experimental setup of Up-CPO is presented in Figure 4.11. A first optical signal is modulated at f_c via the Mach-Zehnder modulator MZM1. A second signal is modulated at a low RF frequency f_d < 2 GHz via the Mach-Zehnder modulator MZM2. Both modulated signals propagate through the SOA-XN. The wavelengths of the optical signal are emitted at λ_c = 1550 nm and λ_d = 1545 nm. An EDFA amplifies the modulated input data signal. The optical input powers are adapted by the optical attenuators Att1 and Att2, respectively at −5 and 5 dBm. The optical power of the Up-CPO signal at the output of SOA-XN is filtered by an optical filter (OF) tuned at λ_c with an optical bandwidth of about 1 nm, detected by a photodiode (Pd). After the photodiode (Pd), the RF power and the phase shift of the RF signal $P_{e,out}$ are measured by a VNA at different bias currents for SOA-XN. The VNA generates the signal at the frequency f_{VNA} which is converted by an RF mixer down to f_d, and amplified by an RF amplifier. A photograph of Up-CPO experimental setup using SOA-XN is presented in Figure 4.12.

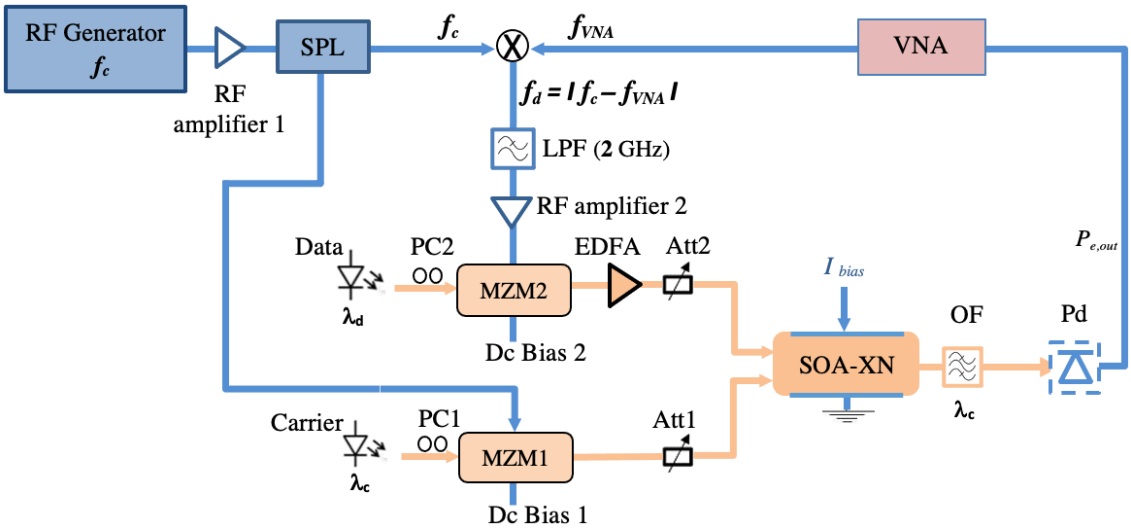

Figure 4.11 Up-CPO experimental set-up using SOA-XN. SPL: RF splitter, LPF: Low Pass Filter, PC: Polarization Controller, Att: Attenuator, Pd: Photodiode, OF: Optical Filter, VNA: Vector network analyzer.

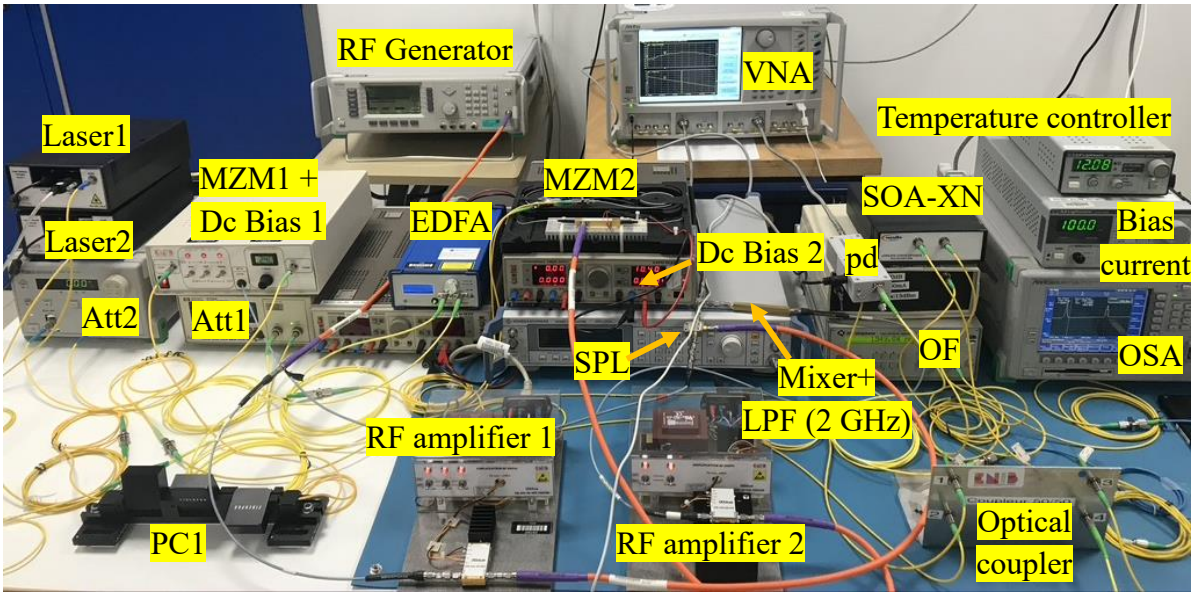

Figure 4.12 Photograph of Up-CPO experimental set-up using SOA-XN. OSA: Optical Spectrum Analyzer.

Before starting the Up-CPO measurement, we need to select a reference in order to measure the phase shift. We take a high bias current I = 450 mA, which has a large bandwidth as a reference, in measurement of RF power and phase shift, the phase being, under these conditions, almost constant as a function of the frequency.

We apply a 5% moving average to the measured phase shift, the delay is then calculated based on experimental data of the phase shift, using the negative derivative of phase shifts versus frequency (1.12). Figure 4.13(a) and (b) present the calculated delay for f_c at 9.7 GHz and 30 GHz, respectively, based on experimental data.

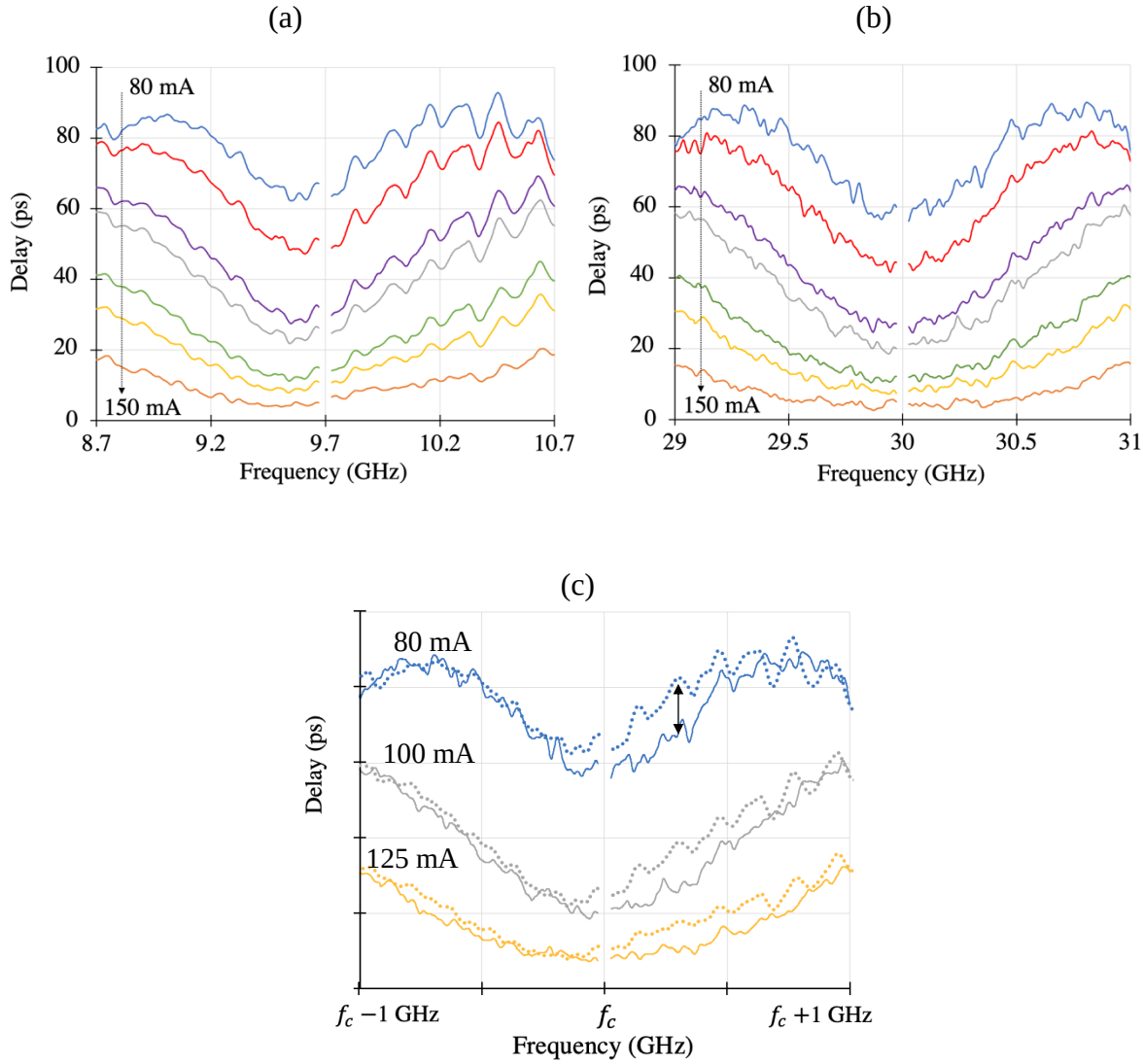

Figure 4.13 Calculated delay response of SOA-XN: at 9.7 GH (a) and at 30 GHz (b). Delay at both 9.7 GHz (solid lines) and 30 GHz (dotted lines) (c).

For f_c = 9.7 GHz, the delay response shows additional ripples and a small asymmetry in the delay response. The ripples and the asymmetry that appear in the experimental results, mostly above f_c, are a result of the operating frequency f_c (9.7 GHz) being smaller than the frequency bandwidth of XGM of about 22 GHz for the reference phase (I = 450 mA). For f_c = 30 GHz, the delay response is more symmetric, and the ripples are less frequent, compared to the case

of f_c= 9.7 GHz (see Figure 4.13(b)). The delay for both operating frequencies is presented in Figure 4.13(c), where we can see a good agreement in delay response for both while the frequency is below f_c. As we go over f_c we start to notice a divergence in delay response between 9.7 GHz (dotted line) and 30 GHz (solid line).

As the Up-CPO response is independent from the operating frequency f_c and to avoid asymmetry and ripples in the Up-CPO response, we will use for the simulation with experimental results the delay of Up-CPO response characterized around f_c = 30 GHz. The higher the frequency is compared to the frequency bandwidth of XGM, the lower the presence of an additional ripples in the measured response. We will later shift the Up-CPO response from 30 GHz to 9.7 GHz.

In order to evaluate the variation of the delay around f_c = 30 GHz, we first calculate the delay through the negative derivative of measured phase shifts versus frequency, and we shift the response to 9.7 GHz by calculation.
As the delay is not constant over the entire frequency range, we define the depth in delay response in the frequency range of 1 GHz (frequency band of interest) as peak-to-peak variation between the maximum value at 10.2 GHz (point B) and the minimum value at 9.7 GHz (point A). The calculation of the depth is done by using a polynomial fit of the calculated delay based on measured data. The calculated delay and polynomial fits of the delay are shown in Figure 4.14. This information will be used when correcting the Up-CPO response by the RF-FF filter.

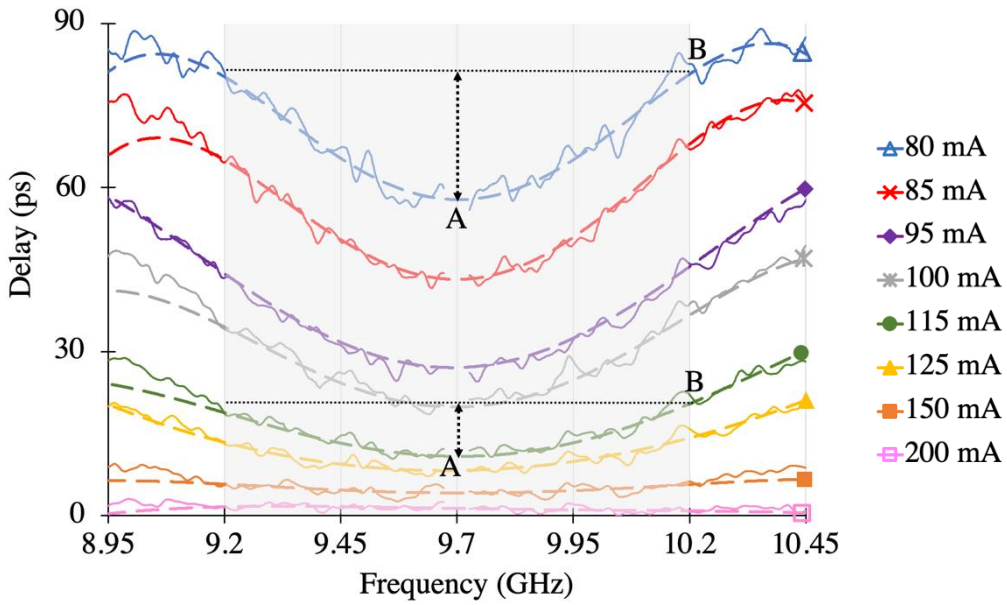

Figure 4.14 Calculated delay from measurement data at 30 GHz, shifted at 9.7 GHz at different bias currents for SOA-XN. Delay polynomial fits (dashed line).

4.3 Complete hybrid correction structure

In the previous section, we have first shown the impact of including an external bias tee to the RF-FF on its response. Secondly, we have shown the effects of operating at a low frequency on the SOA-XN response. In section 4.3.1, we experimentally shown the combined effects of both a low operating frequency and the external bias tee in the hybrid correction structure. In order to evaluate the combination of the two stages (SOA-XN and RF-FF), despite the above-mentioned limitations, a solution is proposed in section 4.3.2.

4.3.1 Measurement of the hybrid correction structure

In order to experimentally test the complete hybrid correction structure, a measurement at 9.7 GHz is taken. The design of the RF-FF is limited to one operating frequency, which in our case is fixed at 9.7 GHz, regardless of the additional ripples in response to the Up-CPO at this operation frequency (as seen in section 4.2).

Figure 4.15 shows the experimental setup of the hybrid correction structure including the circuit of RF-FF with an external bias tee. A first optical signal emitted at λ_c = 1550 nm is intensity-modulated at a high radiofrequency f_c = 9.7 GHz via the MZM1. A second signal emitted at λ_d = 1545 nm is intensity-modulated via the MZM2 by a low RF frequency f_d varying from 0.1 to 1 GHz. Both optical signals are propagating into the SOA-XN. The signal of CPO at the frequency f_d is generated by the difference between f_{VNA} and f_c using an RF mixer, amplified by an RF amplifier. An EDFA amplifies the modulated input data signal. The optical injected powers are adjusted by the optical attenuators Att1 and Att2. Inside the SOA, the gain modulation induced by CPO modulates the second signal and an Up-CPO signal is created by XGM at $f_c \pm f_d$. The optical power of the Up-CPO signal at the output of SOA-XN is filtered by an optical filter (OF) tuned at λ_c with an optical bandwidth of about 1 nm, and then detected by a photodiode (Pd). The RF-FF associated to an external bias tee, is then placed after the photodiode (Pd). The experimental controls are the input optical powers and the input bias current to the SOA-XN, the microwave modulation frequencies, and the voltage control of the RF filter. The tunable delay correction can be obtained by tuning the pair “Bias current ~Gain” of SOA-XN and “V_{DC}” of RF-FF.

We fix a high bias current I = 450 mA, which refers to gain 13.5 dB. The relative RF power and the relative phase shift of the RF signal $P_{e,out}$ are then measured by a VNA at different bias currents (different gains of SOA-XN) and different RF-FF V_{DC} with respect to the reference. A photograph of the whole bench of the complete hybrid correction measurement is presented in Figure 4.16.

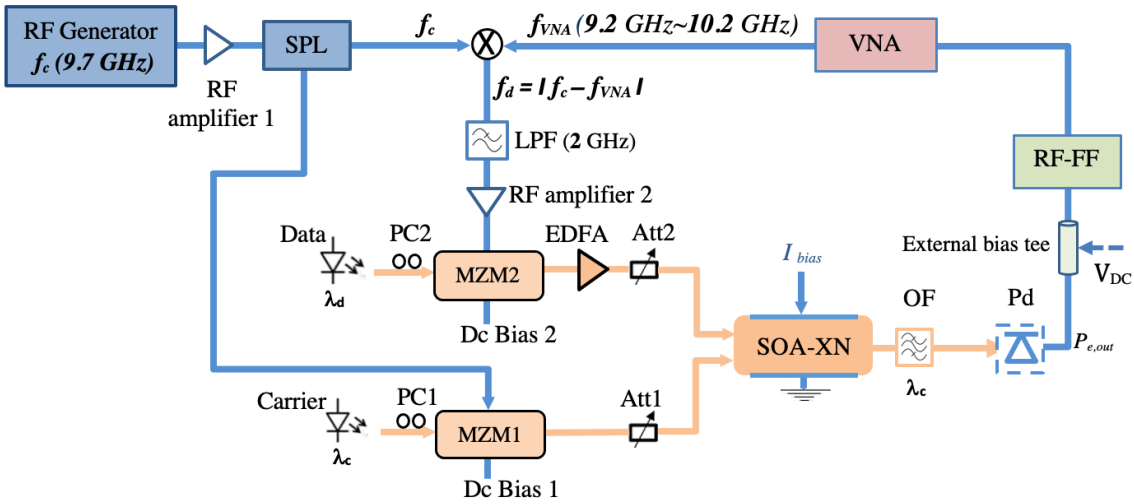

Figure 4.15 Experimental set-up of hybrid correction structure using RF-FF with external bias tee.

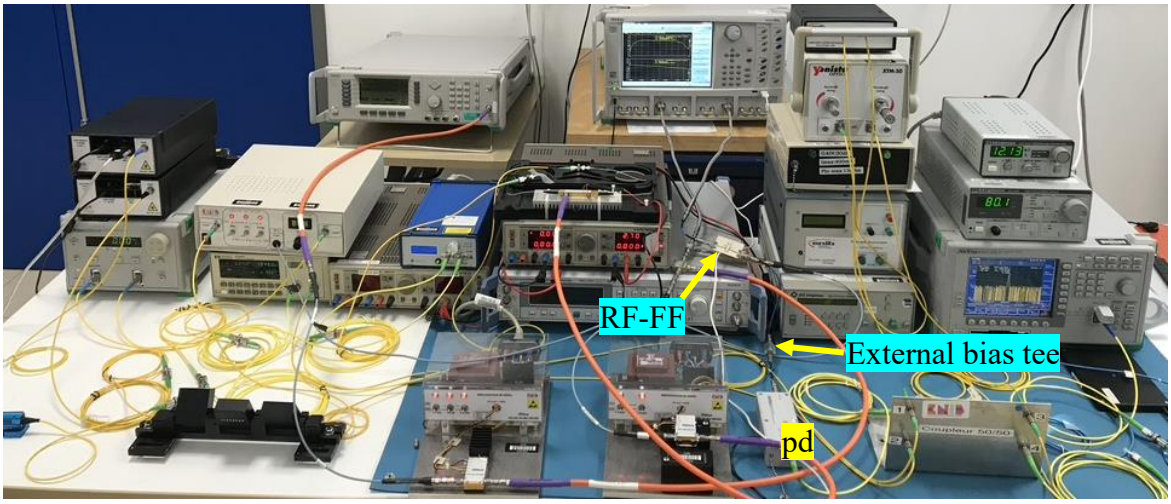

Figure 4.16 photograph experimental set-up of hybrid correction structure using RF-FF with external bias tee.

For each SOA-XN gain, we select a specific V_{DC}. Figure 4.17(a-b) depicts the measured relative RF power and the relative phase shift response of the hybrid correction structure. We notice that there are small ripples occurring over the measured relative RF power response, compared to the mean value (in dotted line). Besides, the level of relative RF power range can vary from −14.5 dB to −23.4 dB (maximum and minimum mean values).

We apply a 10% moving average to the measured relative phase shift response (of Figure 4.17(b)) before calculating the delay correction response noted as “Hybrid delay”. The results

are presented in Figure 4.17(c). We observe that additional ripples occur over the hybrid delay response. This is due to the effects of low operating frequencies on the SOA-XN response as seen in section 4.2. In the complete hybrid measurement, the use of the external bias tee with its imperfections, as seen in section 4.1.2, limits the possibility of the correction of the Up-CPO responses. In fact, the correction of the delay response is partially done for the frequency interval 9.2 - 9.7 GHz, but the response of hybrid delay is asymmetric and shifted towards the low frequencies, which induces a significant shift at frequencies larger than 9.7 GHz, compared to frequencies smaller than 9.7 GHz.

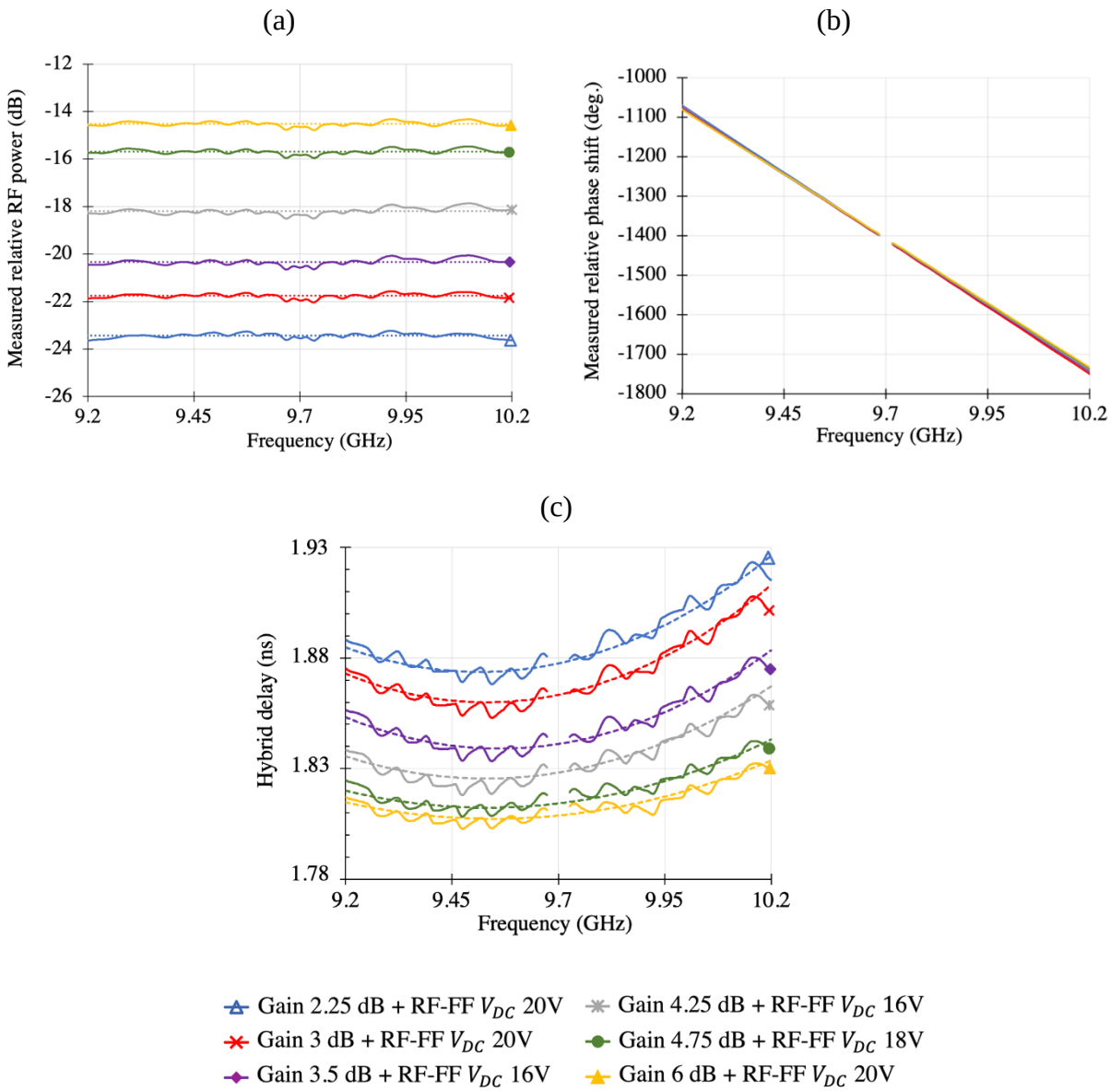

Figure 4.17 Measurement of hybrid correction structure over 1 GHz of: (a) relative RF power (solid lines) and mean values (dotted lines). (b) Relative phase shift. (c) Calculated delay (solid line) and polynomial fit (dashed lines).

In order to verify the functionality of the hybrid correction structure without the artifact from the bias tee and from the low operating frequency, we need to separate the measurements of the SOA-XN and the RF folded filter. A solution of the simulation of hybrid correction structure based on experimental data is proposed in the next section.

4.3.2 Simulation of the hybrid correction structure based on experimental data of SOA-XN

This section presents the simulation of the hybrid correction structure of the SOA-XN coupled with the RF-FF filter, via the ADS simulator, based on the experimental data.

Figure 4.18 below shows the structure of the hybrid delay generation for simulation. The first stage contains RF power and phase shift responses of Up-CPO for SOA-XN, based on experimental data presented in section 4.2. The second stage contains the measurement results of the RF folded filter employing a bias tee internal to the VNA, as presented in section 4.1.1. After obtaining the results of the first and second stages separately, we combine both stages through the ADS simulator.

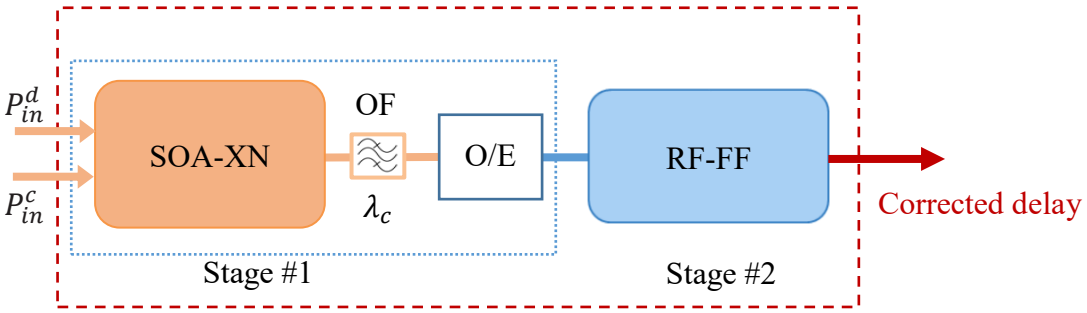

Figure 4.18 Hybrid correction structure of SOA-XN + RF-FF (RF folded filter).

Figure 4.19(a-b) depicts the delay response of Up-CPO using SOA-XN (stage #1), and the delay response of RF-FF (stage #2), over 1 GHz of frequency band (which is the desired correction region from 9.2 to 10.2 GHz). Figure 4.19(c-d) presents the normalized delay responses of stages #1 and #2. We can see from all the precedent figures Figure 4.19(a-d) that in the frequency range 9.3 to 10.1 GHz, RF-FF presents an opposite ripple compared to the delay response of Up-CPO using SOA-XN. So, the combination of the two stages will give an expected optimum correction in this frequency range (9.3 to 10.1 GHz).

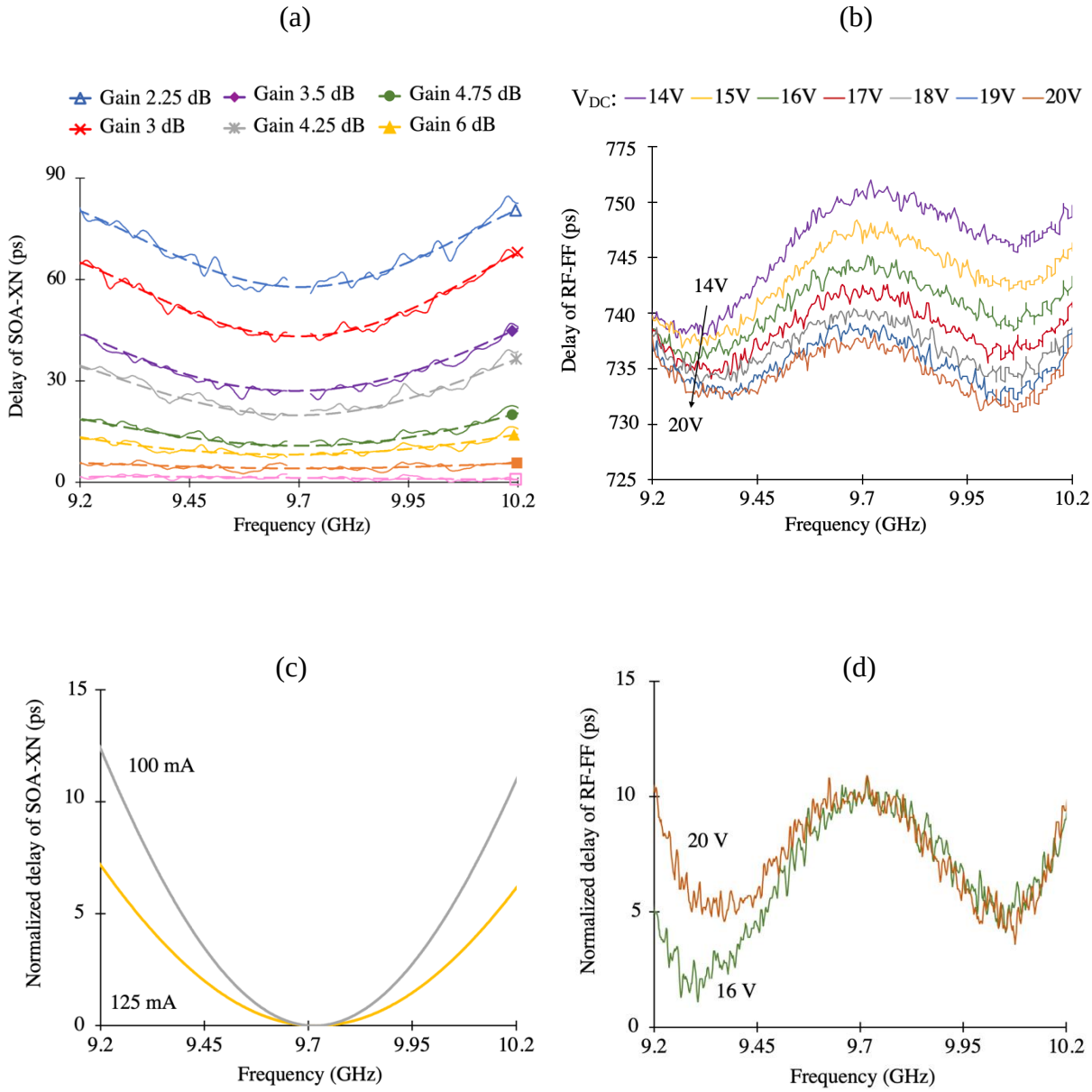

Figure 4.19 Calculated delay response from measured phase shift of: SOA-XN and polynomial fits (dashed line) (a). RF-FF (b). Normalized calculated polynomial delay of SOA-XN (c), and normalized calculated delay of RF-FF (d).

Table 4.5 represents delay depth values of stage #1 with respect to the bias current varying from 80 mA to 450 mA over 1 GHz, and the values of delay ripples of stage #2 (calculated in Table 4.1). We report that the minimum depth is about 0.2 ps and the maximum is 25.1 ps, for 300 mA and 95 mA, respectively. The calculated delay ripples of RF-FF, have a minimum ripple of 5.4 ps at V_{DC} = 20 V, and a maximum of 12.6 ps at V_{DC} = 14 V. When comparing the values of RF-FF delay ripples with the values of delay depths of Up-CPO (Table 4.5), we notice that we cannot correct the delay response for I ≤ 150 mA (which is referred to as a gain higher than 6 dB), since the maximum depth in Up-CPO response of SOA-XN is 2.5 ps, much smaller

than the minimum value of RF-FF ripple of about 5.4 ps at V_{DC} = 20 V (as we can see in Table 4.5).

Table 4.5 Delay response of SOA-XN and RF-FF over frequency range 9.2 GHz to 10.2 GHz.

Stage #1: SOA-XN			***Stage #2: RF-FF***		
Bias current (mA)	***Gain (dB)***	***Delay depth (ps)***	***V_{DC}***	***Delay ripple (9.2~9.7 GHz) (ps)***	***Delay ripple (9.7~10.2 GHz) (ps)***
80	2.25	22.9	14 V	12.6	4.6
85	3	25.1	15 V	10.7	5.3
95	3.5	16.5	16 V	8.7	5.9
100	4.25	15.1	17 V	7.4	5.7
115	4.75	8.9	18 V	6.0	5.8
125	6	6.9	19 V	5.9	6.1
150	6.5	2.5	20 V	5.2	5.4
200	9.5	0.3			
300	11.5	0.2			
450	13.5	0			

The delay correction for each gain is done by selecting for each delay depth of SOA-XN the suitable delay ripple from Table 4.5. To properly chose the correct delay ripple, we select the one closest to the delay depth and having the most symmetric response. Thus, we select for the SOA-XN gains: 3.5 dB, 4.25 dB, 4.75 dB, and 6 dB of the first stage, the corresponding RF-FF V_{DC}: 16 V, 16 V, 18 V, and 20 V, respectively. Gains 2.25 and 3 dB have a delay depth larger than the delay ripple of RF-FF (over 1 GHz). Besides, we notice that these delays have a depth up to 6.8 ps across 0.5 GHz frequency range. Therefore, we select for these two gains the RF-FF V_{DC}: 20 V, which has a complementary and more symmetric response across 0.5 GHz frequency band.

The simulation results of the combination of SOA-XN delay depths correction of each gain using the ripples of the RF folded filter based on experimental data of both stages are presented in Figure 4.20 and Figure 4.21.

Figure 4.20 shows the normalized delay correction response of SOA-XN+RF-FF of each gain, compared to the normalized delay response without using the hybrid correction structure. We

notice that the delay responses for each gain is enhanced over the total instantaneous bandwidth of 1 GHz, compared to the delay of SOA-XN (dashed line).

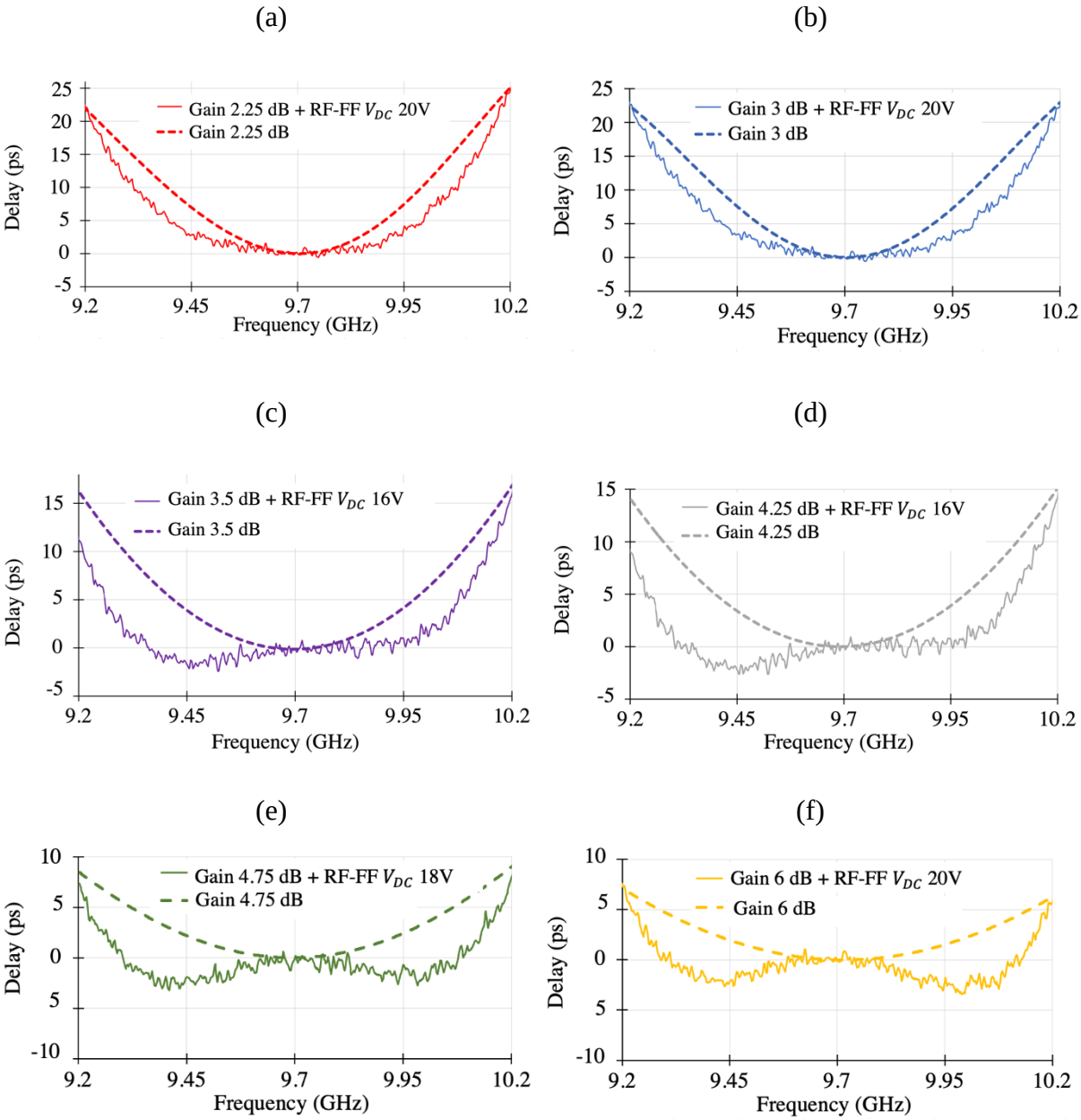

Figure 4.20 Normalized delay response of SOA-XN with (solid line) and without (dashed line) the hybrid correction structure for different gains (a)-(f).

The asymmetric response occurs in Figure 4.20(c)-(d) for frequencies smaller or equal to 9.55 GHz, due to the asymmetric response of the RF-FF for V_{DC} = 17 V to 14 V (Figure 4.5(b)). A numerical comparison of each case (a)-(f) with and without using the hybrid correction structure is presented next.

The delay response of the hybrid correction structure is presented in Figure 4.21. A tunability of ~ 56 ps for the corrected delay is obtained (between minimum and maximum mean values of gain).

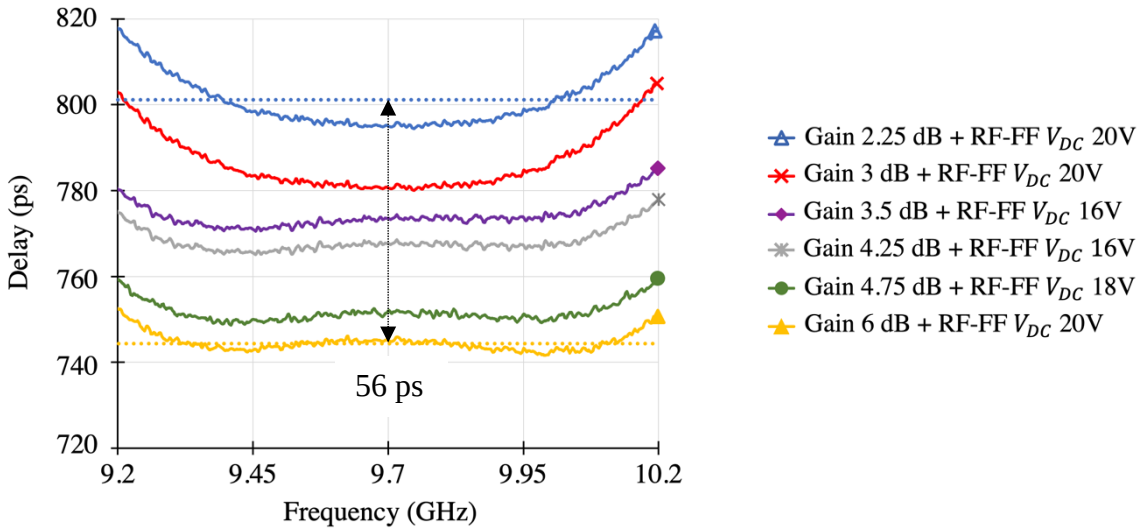

Figure 4.21 Delay response of the hybrid correction structure for different gains. Mean values (dotted line) over 1 GHz.

In the following, we perform multiple numerical comparisons of the delay response with and without using the hybrid correction structure in terms of peak-to-peak variation $\Delta_{delay\,p-p}$, % of improvement in terms of $\Delta_{delay\,p-p}$ reduction, standard deviation σ_{delay} to measure the divergence from the mean value and the ratio of corrected to non-corrected σ_{delay}. We divided the comparisons into three categories of gain SOA-XN:

a- Large delay depths: the first category refers to gains of 2.25 and 3 dB, where the delay depth is maximum. Figure 4.22 illustrates $\Delta_{delay\,p-p}$ of the first category with and without correction, with the percentage of $\Delta_{delay\,p-p}$ improvement. We can see that $\Delta_{delay\,p-p}$ is improved in the frequency band ranging from 0.125 to 0.875 GHz for gains of 2.25 and 3 dB (Figure 4.22(a-b)). A maximum improvement of 80 % is achieved for 0.375 GHz frequency band as seen in Figure 4.22, at the gain 2.25 dB + RF-FF set to V_{DC} = 20 V. This is due to the fact that SOA-XN has a depth equal to the delay ripple (RF-FF set to V_{DC} = 20 V) at a frequency band ≤ 0.5 GHz. At 1 GHz the delay depths at gains 2.25 and 3 dB are larger than 20 ps, but RF-FF cannot correct the depth larger than 12.6 ps, due to limitations in ripple ranges of RF-FF (Table 4.5).

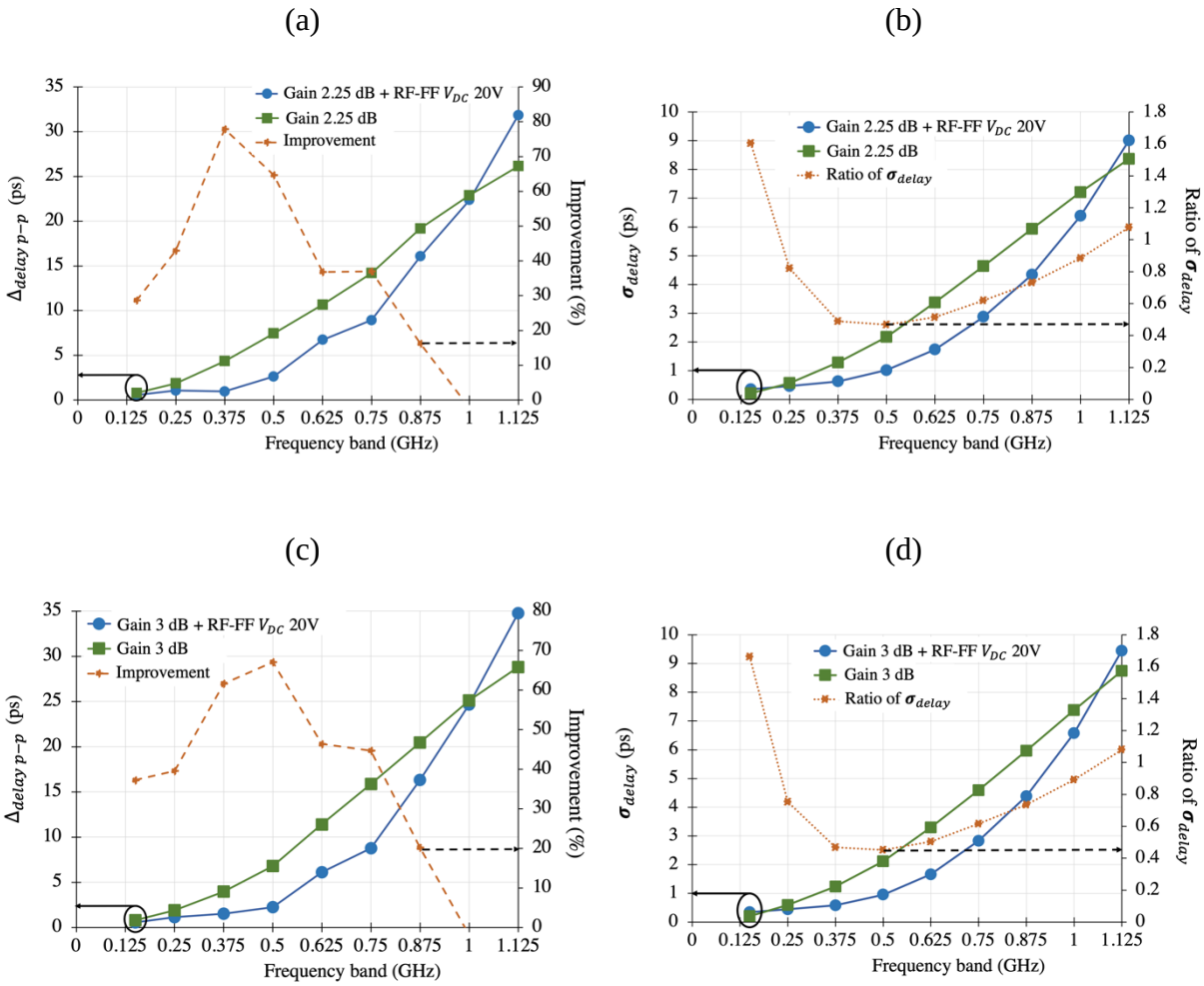

Figure 4.22 Results of first category for: $\Delta_{delay\ p-p}$ and % of improvement (a) and (c). σ_{delay} and the ratio of σ_{delay} (b) and (d).

Besides, an improvement in σ_{delay} is registered from 0.25 to 1 GHz of frequency band at "gain 2.25 dB + RF-FF V_{DC} 20 V" (see Figure 4.22(b)), and from 0.25 to 1 GHz frequency band is registered at "gain 3 dB + RF-FF V_{DC} 20 V" (Figure 4.22(d)). For both gains, a minimum ratio of σ_{delay} ~0.45 is obtained at the frequency band of 0.5 GHz.

b- Medium delay depths: the second category refers to gains of 3.5 and 4.25 dB, which have medium delay depths. Figure 4.23(a) and Figure 4.23(c) present, $\Delta_{delay\ p-p}$ with and without correction, and the percentage of $\Delta_{delay\ p-p}$ improvement for the results of the second category. They show that we can achieve delay corrections in the frequency band range of 0.25 GHz, up to 0.875 GHz. This is due to the response of RF-FF filter set at V_{DC} = 16 V: it has less depth on the extremities; between 9.2 GHz to 9.35 GHz and 10.1 to 10.2 GHz (as seen in Table 4.5). A maximum improvement of almost 65 % is achieved at frequency band of 0.5 GHz at "gain 4.25 dB + RF-FF V_{DC} = 16 V". At "gain 3.5 dB + RF-FF V_{DC} = 16 V", 55 % of $\Delta_{delay\ p-p}$ maximum

improvement is attained at 0.625 GHz frequency band. Besides, an enhancement in σ_{delay} is registered from 0.375 to 1 GHz of frequency band (see Figure 4.23(b) and Figure 4.23(d)). A small ratio of σ_{delay} ~0.49 is obtained for a frequency band of 0.75 GHz.

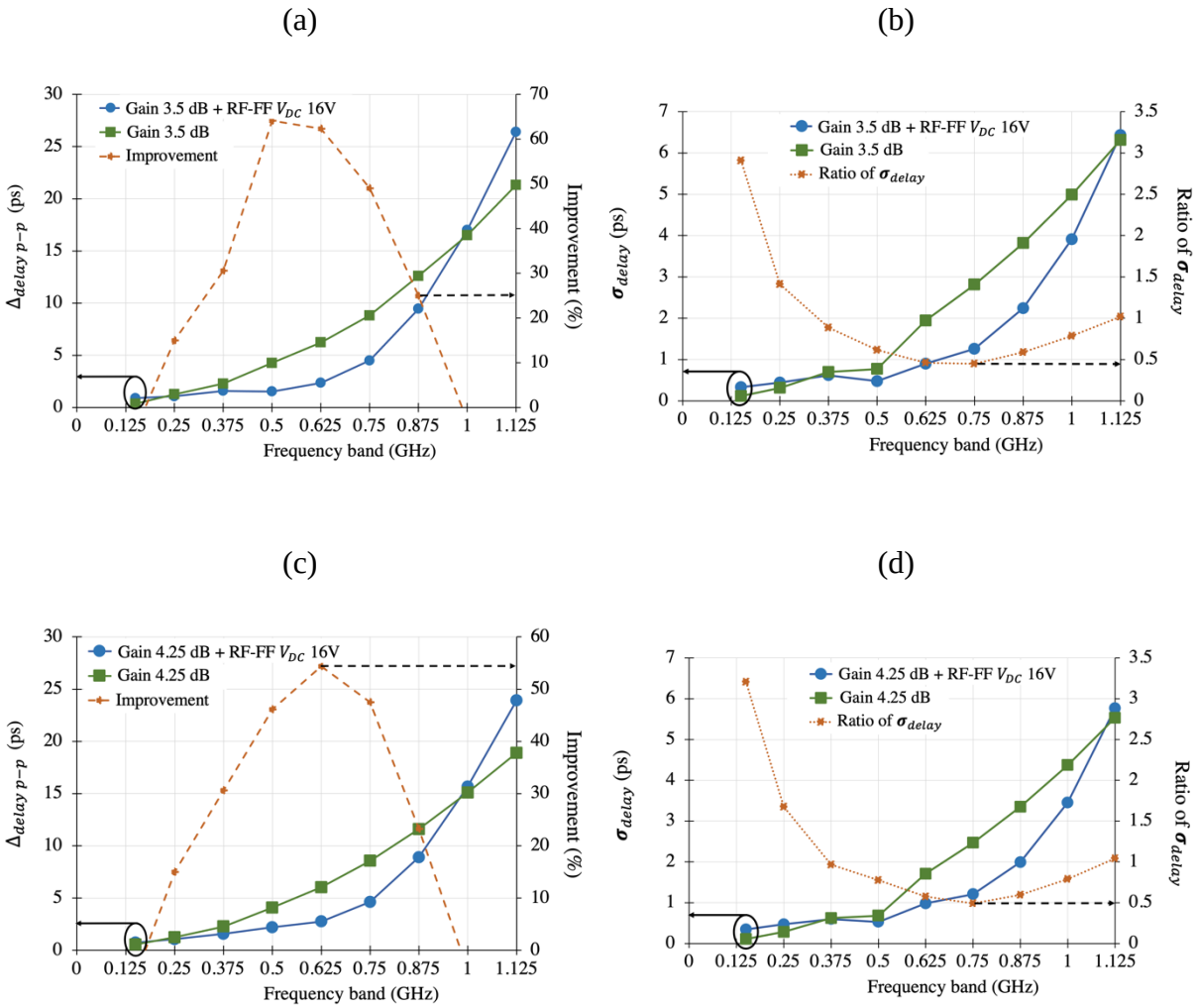

Figure 4.23 Results of second category for: $\Delta_{delay\ p-p}$ and % of improvement (a) and (c). σ_{delay} and the ratio of σ_{delay} (b) and (d).

c- Minimum delay depth: the third category refers to a minimum delay depth registered for gains of 4.75 and 6 dB, over 1 GHz frequency band. Figure 4.24(a) and Figure 4.24(c) show that we can realize a delay correction in the frequency band range between 0.25 and 0.875 GHz. A maximum reduction of ~64% in the variation of delay for gain 4.75 dB is registered using RF-FF V_{DC} set to 18 V, at the frequency band 0.625 GHz (Figure 4.24(a)). These improvements are not only limited to the reduction of the delay variation, but also in the divergence from the mean value σ_{delay}, in the range of 0.625 to 1 GHz (Figure 4.24(b and d)).

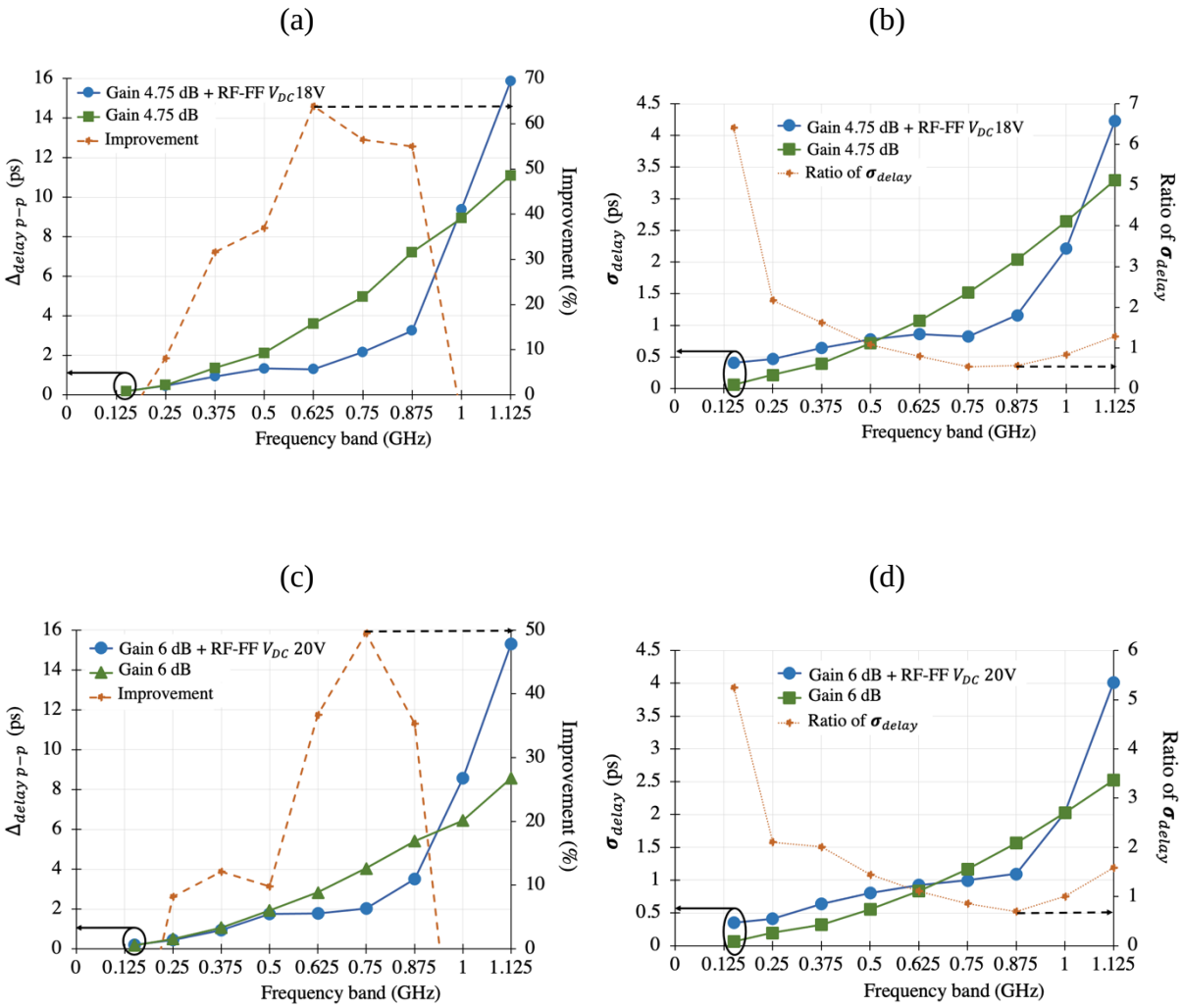

Figure 4.24 Results of third category for: $\Delta_{delay\ p-p}$ and % of improvement (a) and (c). σ_{delay} and the ratio of σ_{delay} (b) and (d).

Figure 4.25 shows the relative RF powers based on experimental data of the hybrid corrected structure (solid lines) and the mean values (dotted lines). Hence, the mean value is calculated from the measured data over the range of 9.2 to 10.2 GHz. It shows that the relative RF power have close response to the mean value.

The whole results are reported in Table 4.6, where we can see that over 1 GHz of frequency band we have a small improvement of no more than 0.29 dB for $\Delta_{RFpower\ p-p}$ using the hybrid correction structure (C), compared to when no correction is employed (N.C).

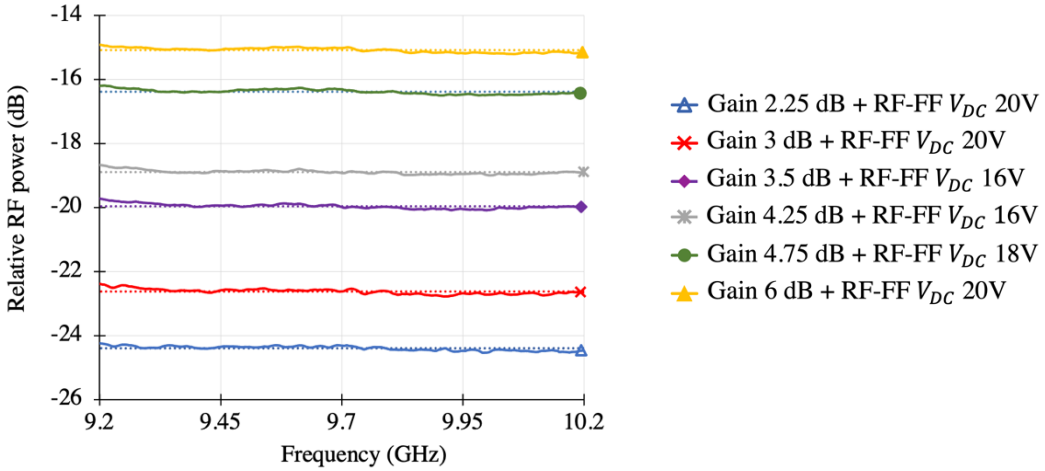

Figure 4.25 Hybrid correction structure response of relative RF power (solid lines) and mean value (dotted lines).

Table 4.6 shows that when using correction, $\Delta_{RFpower\ p-p}$ is always lower than the non-corrected one in overall frequency band of 1 GHz. The common frequency band correction among the three gain categories ranges from 0.25 GHz to 0.875 GHz.

Table 4.6 $\Delta_{RFpower\ p-p}$ (dB) of the normalized RF power comparison between responses of SOA-XN without and with hybrid correction structure versus the frequency band.

	0.15 GHz		***0.25 GHz***		***0.5 GHz***		***0.75 GHz***		***1 GHz***	
Gain	N.C	**C.**	N.C	**C.**	N.C	**C.**	N.C	**C.**	N.C	**C.**
2.25 dB	0.121	**0.076**	0.121	**0.115**	0.121	**0.117**	0.215	**0.135**	0.301	**0.148**
3 dB	0.095	**0.089**	0.111	**0.109**	0.173	**0.137**	0.236	**0.144**	0.429	**0.207**
3.25 dB	0.065	**0.060**	0.151	**0.124**	0.151	**0.116**	0.229	**0.153**	0.449	**0.206**
4.25 dB	0.081	**0.079**	0.098	**0.095**	0.111	**0.093**	0.228	**0.111**	0.446	**0.152**
4.75 dB	0.111	**0.095**	0.146	**0.097**	0.112	**0.108**	0.151	**0.113**	0.383	**0.175**
6 dB	0.098	**0.083**	0.122	**0.120**	0.122	**0.120**	0.171	**0.108**	0.336	**0.171**

N.C: No correction (response of SOA-XN only).

C.: Correction using hybrid correction structure (SOA-XN + RF-FF).

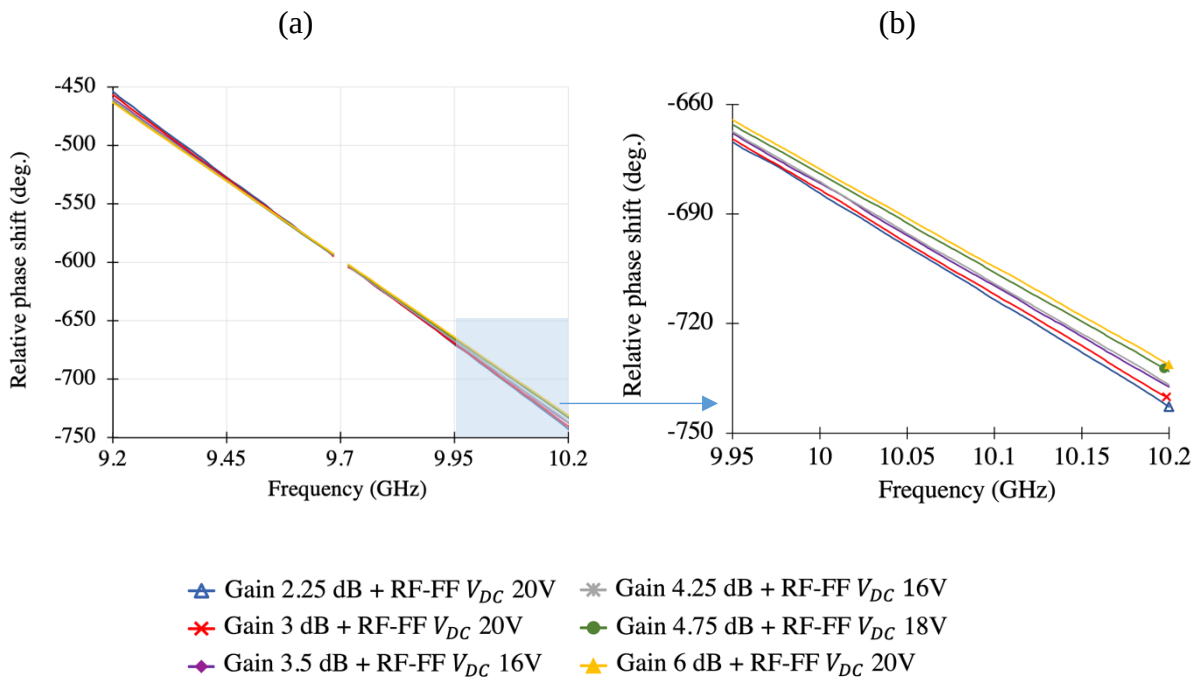

Figure 4.26 Hybrid correction structure response: (a) Relative phase shift over 1 GHz. (b) Relative phase shift across 9.95 to 10.2 GHz.

The corresponding relative RF phase shifts are also depicted in Figure 4.26. The evaluation of the linear relationship between the measured relative phase shift of the hybrid correction structure with respect to the linear regression line of phase shift, $\phi = -2\pi\tau f + \phi_{offset}$, are expressed by the linear phase error "ϵ". The linear phase error is the difference between the relative phase shift of the hybrid correction structure and the linear regression line.

Table 4.7 gives the phase shift regression line equations for each case. It shows that at most 1.88×10^{-5} error in phase linearity occurs for "gain 2.25 dB + RF-FF 20 V" (case 1), while at least 0.16×10^{-5} error in phase linearity registered for "gain 6 dB + RF-FF 20 V" (case 6). Thus, the relative RF phase shifts in Figure 4.26 has a linear phase response over the frequency.

In this section, we have only corrected the Up-CPO response of SOA-XN. We notice that for all configuration cases, the phase offset in Table 4.7 (ϕ_{offset}: 2186.2, 2144.9, 2090.3, 2069.5, 2020.6, and 2000.5) is not the same.

In order to obtain the same offset, in other words a TTD, which refers to a regression graph to the point where the line intersects with the Y-axis, a second RF-PS can be added to the second stage. For cases 2 to 6, RF-PS must have a maximum phase shift of ~160° to attain a reference phase offset of 2160°, which corresponds to ϕ_{offset} = 360° × k. Phase offsets of 15°, 70°, 90°, 140° and 160° can be added to cases 2 to 6, respectively, to obtain this phase reference. As a result, the intersection of the phase shift linear regression line for each configuration case of the tunable device at f = 0 Hz is at ϕ_{offset} = 2160°: a TTD is obtained.

Table 4.7 Linear regression line for phase shift of the hybrid correction structure over 1 GHz of frequency band.

Case	***Hybrid correction structure***	***Linear regression line***	ϵ
1	*Gain 2.25 dB + RF-FF 20 V*	$\phi = -287.07\,f + 2186.2$	1.88×10^{-5}
2	*Gain 3 dB + RF-FF 20 V*	$\phi = -282.97\,f + 2144.9$	1.03×10^{-5}
3	*Gain 3.5 dB + RF-FF 16 V*	$\phi = -277.21\,f + 2090.3$	0.58×10^{-5}
4	*Gain 4.25 dB + RF-FF 16 V*	$\phi = -275.08\,f + 2069.5$	0.74×10^{-5}
5	*Gain 4.75 dB + RF-FF 18 V*	$\phi = -269.95\,f + 2020.6$	0.22×10^{-5}
6	*Gain 6 dB + RF-FF 20 V*	$\phi = -267.82\,f + 2000.5$	0.16×10^{-5}

A comparison between our work and different types of delay lines/TTD - which was presented in chapter 1- is summarized in Table 4.8. The comparison focuses on the delay range, the instantaneous bandwidth and the tunability.

In [1] a tunable delay is varied from 0.5 to 10 ns with an instantaneous bandwidth of 100 MHz, while increasing the Stimulated Brillouin Scattering (SBS) pump power. For TTD, the optical carrier phase shift is adjusted to ensure a constant extrapolated phase offset at the origin of RF frequencies (null frequency). The signal carrier is passed through a separate optical filter implementing an RF phase shift. Through altering the pump power, a tunable TTD of 0.5 to 50 ns is obtained over an instantaneous bandwidth of 10 MHz [2].

In [3] the time delay varies from 2.5 to 24 ns with an instantaneous RF bandwidth of 15 MHz, while the pump power is adjusted from 5.7 to 14.4 dBm. For TTD operation, the optical carrier (OC) phase shift has to be adjusted for each delay by tuning the DC bias of the DPMZM. Therefore, the Separate Carrier Tuning (SCT) delay line can operate as a TTD, providing a tunable TTD up to 24 ns. Using TTD hybrid structure, which is comprised of a SOA-NL cascaded with a RF-FF and a RF-PS (presented in chapter 3), and by tuning for each bias current (SOA-NL gain) the suitable V_{DC} bias of folded filter and RF-PS, a tunable TTD 718.1 to 784.9 is obtained. Approximately 67 ps of tunability range is achieved over 1 GHz of instantaneous bandwidth.

For tunable delays using Up-converted CPO by XGM, a tunable delay from 0 to 380 ps is achieved by adjusting the SOA's current with an instantaneous bandwidth of 320 MHz [4].
For the simulated hybrid correction structure based on measured data, approximately 56 ps of tunability range is achieved over 1 GHz of instantaneous bandwidth by changing the pair of the "bias current" of the SOA and "V_{DC}" of RF-FF.

Table 4.8 Comparison between tunable delay/TTD approaches.

Tunable delay lines/TTD	***Delay range***	***Instantaneous bandwidth***	***Tunability***
[1]	0.5 to 10 ns	100 MHz	-Carrier frequency
[2]	0.5 to 50 ns	10 MHz	-Pump power -Frequency detuning
[3]	2.5 to 24 ns	15 MHz	-Pump power -Dc bias of DPMZM
[4]	0 to 89 ps	320 MHz	-Bias current of SOA -Pump power
TTD hybrid structure simulation (SOA-NL)	718.1 to 784.9 ps	1 GHz	-Bias current of SOA-NL -Dc bias of RF-FF -Dc bias of RF-PS
Simulated hybrid correction structure based on measured data	745 to 801 ps	1 GHz	-Bias current of SOA-XN -Dc bias of RF-FF

4.4 Conclusion

In this chapter, the experimental results of tunable RF filters are presented (RF-FF and RF-CF). We have presented, and experimentally proved the combined effects of both a low operating frequency and an external bias tee addition. For RF-FF, the bias network must be integrated in the early stage of the design. Based on experimental data, we have also demonstrated, to the best of our knowledge, the feasibility of our approach to correct the Up-CPO responses of a SOA. We have also demonstrated that the improvement of reduction in delay variation is achieved by using a simulated hybrid correction structure based on measured data (SOA-XN and RF-FF). The common frequency band correction among the three gain categories is ranging from 0.25 GHz up to 0.875 GHz. We achieved a delay line tunability range of ~56 ps. A tunable delay is achieved by changing the bias voltage of the varactor with respect to gain categories of SOA-XN. A constant phase shift must be added after the RF folded filter, in order to tune the offset that will give an intersection point ϕ_{offset} = 360° × k located at null frequency for all the operating points. Thus, a TTD can be obtained. A comparison between our work and different types of delay lines/TTD has been presented.

Bibliography of chapter 4

[1] S. Chin *et al.*, “Broadband true time delay for microwave signal processing, using slow light based on stimulated Brillouin scattering in optical fibers,” *Opt. Express*, vol. 18, no. 21, p. 22599, Oct. 2010, doi: 10.1364/OE.18.022599.

[2] J. Lloret, J. Sancho, I. Gasulla, S. Sales, and J. Capmany, “True time delays and phase shifters based on slow light technologies for microwave photonics applications,” in *2011 13th International Conference on Transparent Optical Networks*, Stockholm, Sweden, Jun. 2011, pp. 1–4, doi: 10.1109/ICTON.2011.5971119.

[3] W. Li *et al.*, “True-time delay line with separate carrier tuning using dual-parallel MZM and stimulated Brillouin scattering-induced slow light,” *Opt. Express*, vol. 19, no. 13, p. 12312, Jun. 2011, doi: 10.1364/OE.19.012312.

[4] P. Berger, J. Bourderionnet, F. Bretenaker, D. Dolfi, and M. Alouini, “Time delay generation at high frequency using SOA based slow and fast light,” *Opt. Express*, vol. 19, no. 22, p. 21180, Oct. 2011, doi: 10.1364/OE.19.021180.

Conclusion and outlook

This thesis presents theoretically and experimentally the analysis of CPO and Up-CPO SOA responses, the design and the characterization of RF tunable filters and the demonstration of realizing high frequency tunable delay lines and a true time delay via a hybrid structure.

The thesis began with the principle of MWP systems, we investigated the differences between phase shifter and true time delay. We have provided a review of the implementation of phase shifters, based on electrical and optical approaches, as well as an implementation of true time delay based on optical approaches. Electrical approaches operating at high frequency are susceptible to electromagnetic interference, and tend to be bulky and lossy. Indeed, CPO in a semiconductor optical amplifier is the most favorable technique, which suits the requirements in terms of bandwidth to a few GHz, low power, small footprint, and tunability of phase shift/delay based on SOA current or input optical power.

Chapter 2 has investigated at first, CPO effects in SOA devices for microwave photonics phase shifters, theoretically as well as experimentally. The obtained microwave phase shift is determined by the gain dynamics. We experimentally showed, via four SOAs structures, that we can attain a relative phase shift up to 89.3°, close to the theoretical maximum around 1 GHz for an extra nonlinear SOA (SOA-XN) at the cost of an increase in the RF gain penalty. Also, using SOA-XN, we showed theoretically and experimentally that a particular response with a high RF phase shift appears near 180° at low frequencies. In the second part of chapter 2, we showed that we can optically have control of the RF phase shifting in a SOA based on the addition of the XGM response of a CW signal at a SOA output. The phase shift can be independently controlled from the operating conditions of the SOA by varying the external CW power. The impact of the XGM response of the amplified spontaneous emission on the signal relative phase shift has also been studied. A small-signal analysis is developed, and a numerical calculation is used to analyze the controllable RF phase shift. The measurement results for several control signal powers are presented. We have obtained tunable phase shifts in the range from 16° to 45°, for an input optical signal at −15 dBm and an external CW power of 5 dBm.

In the last part of chapter 2, we have theoretically and experimentally analyzed the Up-CPO signal undergoing CPOs and pump-probe configuration in four different SOA structures. We have calculated the amplitude, phase, and delays of Up-CPO signal responses. We demonstrate that modeling SOAs by two sections is sufficient, both for linear and nonlinear SOAs, with a good agreement between theoretical and experimental results. Finally, we evaluate the absolute response delay of the SOAs, and we propose the use of a second stage to correct the nonlinear delay response of SOA-NL and SOA-XN in order to obtain a tunable delay line and a TTD system.

In chapter 3, the concept of compact tunable RF filter and tunable RF phase shifter is presented. We introduce a new approach of "Tunable RF filter" by using half-wavelength open circuit stubs with a cross coupling between resonators 1 and 6, in order to tune the delay response. We showed that the installation of a capacitor, located at the minimum of electric field is a feasible solution, and demonstrated the suitability of our synthesis of folded and curved filters through simulation and implementation. The tunable RF phase shifter (RF-PS) is implemented based on transmission lines and varactor diodes. The simulation results of tunable RF filters and RF phase shifter are presented. Tunable delay is achieved by altering the bias voltage of the varactor.

In the second part of chapter 3, a TTD hybrid structure is proposed and validated through simulation. By combining two stages SOA-NL and the RF stage (RF-FF + RF-PS), a TTD is obtained for SOA-NL. A maximum improvement of 60 % in the reduction of delay depth at Gain 0 dB is registered for frequency bands ranging from 0.5 GHz to 0.75 GHz. The obtained results show that we can achieve delay correction in the frequency band ranging from 0.15 GHz to 1 GHz, at Gain 0 dB and Gain 5 dB. A low error around 0.2×10^{-6} in phase linearity is registered for $\phi_{corrected,5dB}$, using "gain 5 dB + RF-FF V_{DC} 14 V". Finally, by adding RF-PS to the second stage, a TTD is achieved over a 67 ps range from 718.1 ps to 784.9 ps.

In chapter 4, we demonstrated by simulation, based on experimental data, the feasibility of our approach to correct the nonlinear responses of SOA-XN. This is the first time that the RF phase shift technique has been applied to correct the nonlinear response of SOA devices to the best of our knowledge. The improvement of the reduction in delay variation is achieved using a hybrid correction structure based on measured data "SOA-XN and RF-FF". A maximum improvement of 80% is achieved for a frequency band of 0.375 GHz, at "gain 2.25 dB + RF-FF set to V_{DC} = 20 V". The mutual frequency band correction among the three categories of gains is ranging between 0.25 GHz and 0.875 GHz. We obtained a delay line tunability range of ~56 ps for SOA-XN with a hybrid correction structure using a RF folded filter. Additionally, the effects of both a low operating frequency and the bias tee are experimentally investigated.

In experimental setup, an increase in delay ripple is observed when using a bias tee for linking the optical and the RF stages, compared to the case without one, which prevented to estimate

the tunable delay improvement. In future work, a bias network must be integrated in the design layout of the RF tunable filter.

In our TTD hybrid structure, the RF second stage “RF-FF and RF-PS” was placed after the photonic stage “Up-CPO”, which requires a new development of the RF stage when the working frequency is changed. On the contrary, Up-CPO has a full tunability up to some THz. In order to take the advantage of this feature, a possible correction can be done in the early stage by using a pre-distortion RF stage. Consequently, the nonlinearity in SOA response will be corrected at low frequencies by the microwave device before the step of increasing the frequency by the means of the Up-CPO technique which has the advantage to have a device independent of the carrier frequency. On the other hand, the device works at intermediate frequency, rather than at very high frequency, making its design and characterization easier. This development will be performed within the upcoming project READER (Architecture d’un système de REtards Accordables photonique micro-ondes DEporté pour des Réseaux d'antennes allant jusqu’au THz) which is supported by the Brittany Region and the Finistère Departement Council.

Glossary of Acronyms

ADS: Advanced Design System
APD: Avalanche photodiode
ASE: Amplified Spontaneous Emission
Att: Attenuator
BPF: Band Pass Filter
BW: Bandwidth
CPO: Coherent Population Oscillations
CW: Continuous Wave
DC: Direct Current
DCF: Dispersion Compensating Fiber
DF: Dispersion Fiber
DSB-SC: Double Sideband Suppressed Carrier Signal
DSF: Dispersion-Shifted Fiber
DS-SMF: Dispersion Shifted Single-Mode Fiber
DPMZM: dual-Parallel Mach-Zehnder Modulator
EDFA: Erbium Doped Fiber
EM: Electromagnetic
FBG: Fiber Bragg Grating
FWM: Four Wave Mixings
HPF: High Pass Filter
IL: Insertion loss
LNA: Low Noise Amplifier
LO: Local oscillator
LPF: Low Pass Filter
MLIN: Microstrip Line
MEMS: Micro-Electro-Mechanical Systems
MWP: Microwave Photonics
MZM: Mach-Zehnder Modulator
OC: Optical Carrier
O/E: Optical to Electrical
OF: Optical Filter
OSA: Optical Spectrum Analyzer
OSSB: Optical Single Sideband
PC: Polarization Controller
Pd: Photodiode

PS: Phase Shifter
RF: Radio Frequency
RFC: Radio Frequency Chokes
RF-CF: Radio Frequency Curved Filter
RF-FF: Radio Frequency Folded Filter
RF-PS: Radio Frequency Phase Shifter
RTPS: Reflection Type Phase Shifter
SBS: Stimulated Brillouin Scattering
SCT: Separate Carrier Tuning
SGM: Self-Gain Modulation
SMF: Single-Mode Fiber
SOA: Semiconductor Optical Amplifier
SOA-L: Semiconductor Optical Amplifier-Linear
SOA-NL: Semiconductor Optical Amplifier-NonLinear
SOA-XN: Semiconductor Optical Amplifier-Extra NonLinear
SPDT: Single Pole Double Throw Switches
SPM: Self-Phase Modulation
PAAs: Phased Array Antennas
TFBG: Tilted Fiber Bragg Grating
TL: Transmission Line
TLS: Tunable Laser Source
TTD: True Time Delay
Up-CPO: Up-converted Coherent Population Oscillations
UWB: Ultra-Wide Band
VNA: Vector Network Analyser
VOA: Variable Optical Attenuator
XPM: Cross Phase Modulation
XGM: Cross Gain Modulation

List of Figures

Figure 1.1 Illustration of error. *18*

Figure 1.2 illustrated beam squint. *18*

Figure 1.3 Beam steering (a) using a phase shifter, and (b) using a delay line. [2] *19*

Figure 1.4 Beam patterns of 3 microwave frequencies with (a) phase shifter, (b) true-time delay, Blue: 12 GHz. Red: 15 GHz. Black: 18 GHz. [3] *20*

Figure 1.5 Delay/phase shift experienced by RF signal travelling through transmission line. *21*

Figure 1.6 Basic schematic of switched-line phase shifter. *22*

Figure 1.7 Schiffman phase shifter. *23*

Figure 1.8 Loaded-line phase shifter, switch here is to choose between two lines of different length and impedance. *24*

Figure 1.9 Schematic of the RTPS using 90° *hybrid coupler and loaded lines.* *26*

Figure 1.10 Tunable MWP delay line structure by using a length of DF. *27*

Figure 1.11 Spectral distribution of Brillouin gain and loss resonances and the associated optical phase shifts. *28*

Figure 1.12 Experimental configuration of tunable RF phase shift using SBS in optical fibers. *29*

Figure 1.13 Fiber Bragg grating. *31*

Figure 1.14 TFBG based microwave photonic phase shifter, OSSB: optical signal-sideband, Pd: photodetector. *31*

Figure 1.15 Principle of CPO illustrated in a gain medium of two levels (E1 and E2), (a) Ω at low frequency, (b) Ω at high frequency. [36] *32*

Figure 1.16 Schematic diagram of CPO based phase shifter.....32

Figure 1.17 Principle of Up-CPO, OF: Optical filter, Pd: Photodiode.....34

Figure 1.18 TTD beamforming system based on an FBG prism. TLS, Tunable laser source; PC, Polarization controller; Pd, photodetector; MZM, Mach-Zender modulator. [50].....35

Figure 1.19 Principle of TTD (a) covering the full bandwidth and (b) using the separate carrier tuning technique. [53].....36

Figure 1.20 Experimental set-up, DFB-LD; Distributed Feedback Laser Diodes DFB, EOM; electro-optic modulator, DSF; dispersion shifted fiber, PC; polarization controller, EDFA; erbium doped fiber amplifier, VOA; variable optical attenuator, Pd; photodetector.[54].....37

Figure 1.21 Schematic configuration of the TTD system, TLS: tunable laser source; DPMZM: dual-parallel Mach-Zehnder modulator; DSF: dispersion shifted fiber; EDFA1 and EDFA2: erbium-doped fiber amplifier; VOA: variable optical attenuator; PC: polarization controller; Pd: photodetector. [53].....38

Figure 1.22 SSB-SC + OC modulation are realized by counter propagating a DSB-SC + OC signal at a frequency of ν_{RF} and a DSB-SC pump signal at a frequency of ν_P in a length of DSF. [53].....38

Figure 2.1 Schematic of: Spontaneous emission (a), and (b) Stimulated emission.....49

Figure 2.2 Schematic diagram of an SOA.....50

Figure 2.3 Evolution of the SOA gain as a function of bias current of SOA at low input signal power (a), output optical power (b), and wavelength (c).....52

Figure 2.4 Schematic of dividing the cavity of the SOA into M-sections.....55

Figure 2.5 Experimental results of optical gain of the four SOAs as function of: the input optical powers applied at their input at bias current I_{max} (a), the output optical powers (b), the bias currents with input optical power at -20 dBm (c), and wavelength by fixing input optical power at -20 dBm and Imax (d).....58

Figure 2.6 Evolution of $R\alpha$ as function of K for several SOA gains.....63

Figure 2.7 Asymptotic responses of poutx in frequency domain of: (a) amplitude response, and (b) phase response, for the case of positive $R\alpha$.....64

Figure 2.8 Asymptotic responses of poutx in frequency domain of: (a) amplitude response, and (b) phase response, for the case of negative $R\alpha$.....65

Figure 2.9 Experimental setup to measure microwave phase shifts induced by CPO effects in a SOA. PC: Polarization controller.....66

Figure 2.10 Measured RF power as function of the frequency for different optical gains. 67

Figure 2.11 Measured relative phase shift as function of the frequency for different optical gains. 68

Figure 2.12 Measured relative phase shift as function of the frequency over 0.5 GHz for different optical gains, SOA-L (a), SOA-NL1 (c). Measured RF power as function of the frequency for different optical gains over 0.5 GHz, SOA-L (b), SOA-NL1 (d). 70

Figure 2.13 Measured relative phase shift as function of the frequency over 0.5 GHz for different optical gains, SOA-NL (a), and SOA-XN (c). Measured RF power as function of the frequency for different optical gains over 0.5 GHz, SOA-NL (b), SOA-XN (d). 71

Figure 2.14 Measured phase shift as a function of both SOA-XN bias currents and frequency (f_{VNA}) with (a) fixed optical input power (0 dBm). (b) fixed bias current (325 mA). 72

Figure 2.15 Scheme of the operating principle. 73

Figure 2.16 Phasor diagram illustration of the phase in polar form with: (a) $poutsig$, (b) $poutsig + poutASE$, and (c) $poutsig + poutASE + poutCW$. (component signals: solid vectors, resultant: dotted vector). 76

Figure 2.17 (a) Theoretical phase shift and (b) Normalized RF power of p_{out} as function of the frequency for $Pinsig$ = -15 dBm and $PinCW$ = 0 dBm in presence of the ASE. 78

Figure 2.18 (a) Factor K_2. (b) ϕmax of p_{out} as function of $Pinsig$ for several $PinCW$ without ASE. 79

Figure 2.19 Experimental setup to measure the microwave phase shifts induced by CPO effects in a SOA and by adding XGM response of an optical signal. PC: Polarization controller, Att: attenuator, OF: optical filter at λsig, Pd: photodetector, I: Bias current, EDFA: Erbium-doped fiber amplifier. Oc: optical coupler. 80

Figure 2.20 Experimental set-up. 80

Figure 2.21 (a) Measured relative maximum phase shift, and (b) measured RF power of $P_{e,out}$ as a function of frequency. $Pinsig$ is fixed at -15 dBm. 81

Figure 2.22 (a) Measured relative maximum phase shift, and (b) measured RF power of $P_{e,out}$ as a function of frequency for $Pinsig$ = -20 dBm. (c) Measured relative maximum phase shift, and (d) measured RF power of $P_{e,out}$ as a function of frequency for $Pinsig$ = 0 dBm. 82

Figure 2.23 (a) Measured maximum relative phase shift at $fmax$ of $pout$, and (b) RF penalty ρ of $pout$: $poutsig$ only, $poutsig$ with presence of ASE and with injection of several $PinCW$ (-10, -5, 0 and 5 dBm). 83

Figure 2.24 Principle of Up-CPO, OF: Optical filter, Pd: Photodiode. 84

Figure 2.25 Principle of SOA modeling by two calculation sections in presence of an intensity-modulated pump signal $PinPu$ at λPu and a continuous-wave probe signal $PinPr$ at λPr.. 87

Figure 2.26 Gain for sections 1 and 2 for: $PinPr$ = -30 dBm (a), $Pin\ Pr$ = 0 dBm (c). Dynamic carrier lifetime for: $PinPr$ = -30 dBm (b), $PinPr$ = 0 dBm (d). 91

Figure 2.27 Pump-probe setup, OF: Optical filter, Pd: Photodiode.....93

Figure 2.28 Normalized RF power for: SOA-L (a), SOA-NL (b) and SOA-XN (a). Calculated data are in dotted line and measured ones are in solid line.....94

Figure 2.29 Up-CPO normalized phase shift for the three SOAs at gain 0dB (a). Normalized RF power for the three SOAs at gain 0 dB (b).....96

Figure 2.30 Up-CPO normalized phase shift for the three SOAs: at gain 5 dB (a), at gain 10 dB (c). Normalized RF power for the three SOAs: at gain 5 dB (b), and (d) at gain 10 dB. ..97

Figure 2.31 Experimental setup for Up-CPO measurements induced by slow and fast light effects and XGM in a SOA. PC1 and PC2: Polarization Controller, Pd: Photodetector, EDFA: Erbium-doped fiber amplifier, LPF: RF low-pass filter, SPL: RF Splitter. 98

Figure 2.32 Photograph of Up-CPO experimental set-up using SOA-XN. OC: Optical Coupler, OSA: Optical Spectrum Analyzer.....99

Figure 2.33 Measured and calculated results for a gain of 5 dB with a reference gain of 10 dB: (a) relative RF power for SOA-L, SOA-NL and SOA-XN, (b) relative phase shift for SOA-L, SOA-NL and SOA-XN. Calculated data are in dotted line and measured data are in solid line. 100

Figure 2.34 Measured and calculated results for a gain of 0 dB with a reference gain of 10 dB: (a) relative RF power for SOA-L, SOA-NL and SOA-XN, (b) relative phase shift for SOA-L, SOA-NL and SOA-XN. Calculated data are in dotted line and measured data are in solid line. 101

Figure 2.35 Measured relative phase shift using SOA-XN at different operating frequency: (a) at 10 GHz, and (b) at 30 GHz.....102

Figure 2.36 Calculated delay of SOA-L, SOA-NL and SOA-X for 10 GHz of frequency band at Gain 0 dB (a). Normalized delay of SOA-L, SOA-NL and SOA-XN for 1 GHz of frequency band (b).....103

Figure 2.37 Calculated delay of SOA-L, SOA-NL and SOA-X for 10 GHz of frequency band: at Gain 5 dB (a), and at Gain 10 dB (c). Normalized delay of SOA-L, SOA-NL and SOA-XN for 1 GHz of frequency band at: Gain 5 dB (b), and Gain 10 dB (d).....104

Figure 2.38 $\Delta Delay\ p - p$ *and* $\sigma Delay$ *for SOA-NL and SOA-XN versus frequency band at: Gain 0 (a)-(b), and 5 dB (c)-(d).....105*

Figure 3.1 Characteristics of an ideal TTD over the instantaneous bandwidth ($Bins$*) near the carrier operating frequency (*fc*), (a) amplitude frequency response, (b) phase frequency response, (c) delay frequency response. 113*

Figure 3.2 Illustration of hybrid delay correction.....113

Figure 3.3 TTD hybrid structure. 114

Figure 3.4 Schematic of (a) microstrip line, and (b) field distribution at the cross section of a microstrip line, H: Magnetic field (doted lien), and E: Electric field (solid line).....116

Figure 3.5 Idealized filter responses: (a) Low-pass, (b) High-pass, (c) Bandpass, and (d) notch. 118

Figure 3.6 Chebyshev lowpass response, ωc is the cutoff angular frequency [6]. 119

Figure 3.7 Lumped circuits for lowpass prototype Chebyshev filters with even n: first element is a shunt capacitor, and the last element is a series inductor. 120

Figure 3.8 Lumped circuits for bandpass prototype Chebyshev filters with even n: first element is a shunt capacitor and a shunt inductor, and the last element is an inductor and capacitor in series. 121

Figure 3.9 Network representation of the single terminated (a) K-inverter and J-inverter, (b) Example of realization of the inverters by quarter-wavelength distributed lines.....123

Figure 3.10 Bandpass filters with: (a) impedance inverter, and (b) admittance inverter.....124

Figure 3.11 General circuit model of quarter-wavelength shunt short-circuited stubs.....125

Figure 3.12 General circuit model of half-wavelength shunt open-circuited stubs connected by quarter-wavelength inverters.....127

Figure 3.13 Network of bandpass filters of order n with admittance inverter. 128

Figure 3.14 Bandpass filters of order 6 with cross coupling 1-6. 130

Figure 3.15 Initial design of half-wavelength shunt open-circuited stubs bandpass filters of order 6 with cross coupling 1-6. 132

Figure 3.16 S-parameters for the simulated initial circuit obtained with half-wavelength shunt open-circuited stubs order-6 bandpass filter. Solid line without cross coupling 1-6, dashed line with cross coupling. 133

Figure 3.17 Delays of S_{21} for the simulated initial circuit obtained with half-wavelength shunt open-circuited stubs order-6 bandpass filter. Solid line without cross coupling 1-6 and dashed line with cross coupling. 134

Figure 3.18 Modified bandpass filters of order 6 with cross coupling 1-6. 135

Figure 3.19 Schematic of RF-FF with cross coupling between the stub 1 and 6. 136

Figure 3.20 Circuit simulation results of S-parameters of RF-FF. Solid line without cross coupling, dotted line with cross coupling. 137

Figure 3.21 Delays of S_{21} for circuit simulation results of RF-FF. Solid line without cross coupling, dotted line with cross coupling. 138

Figure 3.22 Flip tuning varactor equivalent circuit [9].....138

Figure 3.23 MA46H120 varactor model in ADS. *139*

Figure 3.24 Varactor capacitance variation versus bias voltage. *139*

Figure 3.25 Layout of RF folded filter (RF-FF), where C_b is the DC blocking capacitors and C_V is the MA46H120 varactors. *140*

Figure 3.26 Electromagnetic simulation (Momentum) of RF-FF (a) S-parameters, (b) delay of S_{21}. *141*

Figure 3.27 Layout of RF curved filter (RF-CF). *142*

Figure 3.28 Electromagnetic simulation (Momentum) of RF-CF (a) S-parameters, (b) Delay of S_{21}. *143*

Figure 3.29 Schematic of the proposed tunable RF-PS. *145*

Figure 3.30 Schematic of the proposed tunable RF-PS. *148*

Figure 3.31 Layout of tunable RF-PS. *150*

Figure 3.32 Simulated S parameters of the tunable RF-PS for different capacitances values. Amplitude variations of (a) reflection coefficient S_{21}, and (b) Transmission coefficient S_{11}. *151*

Figure 3.33 Simulated frequency characteristics of the tunable RF-PS for different values of C_{v1}. (a) Phase variations of S_{21}, and (b) delay variation of S_{21}. *151*

Figure 3.34 Schematic structure of hybrid correction structure in ADS. RF-FF: RF folded filter. *153*

Figure 3.35 Hybrid delay correction (a), Normalized delay of SOA-NL (dotted line) and normalized hybrid delay correction (b). *154*

Figure 3.36 Results of gain 0 dB for: $\Delta delay\ p-p$ with and without using the hybrid correction structure and % of improvement (a). $\sigma Delay$ and the ratio of $\sigma Delay$ (b). *155*

Figure 3.37 Results of gain 5 dB for: $\Delta delay\ p-p$ with and without using the hybrid correction structure and % of improvement (a). $\sigma Delay$ and the ratio of $\sigma Delay$ (b). *156*

Figure 3.38 Response of the hybrid correction structure: Normalized RF power (a), Phase shift (b). *157*

Figure 3.39 Schematic of TTD hybrid structure in ADS, RF-FF: RF folded filter, RF-PS: RF phase shifter. *159*

Figure 3.40 (a) TTD hybrid structure response. (b) Normalized RF power response of TTD hybrid structure. *160*

Figure 3.41 Phase shifts of TTD (a). Zoom out of phase shifts of TTD phase shifts (b). Dashed lines are the linear phase shift regression lines of TTD hybrid structure. *161*

Figure 4.1 photograph of (a) RF-FF, (b) RF-CF. 166

Figure 4.2 Experimental setup of S-parameters measurement of RF curved filter. 167

Figure 4.3 S_{11} and S_{21} of RF-FF for V_{DC} =16V (a). Delay of RF-FF for V_{DC} =16V (b). Simulated results (dashed lines) and measured results (solid lines). 168

Figure 4.4 Retrofit electromagnetic simulation and measured results of RF-FF for V_{DC} =16V: S_{11} and S_{21} (a). Delay of S_{21} (b). Retrofit simulated results (dashed lines) and measured results (solid lines). 169

Figure 4.5 Measurement of RF-FF (a) S_{11} and S_{21}, (b) Delay of S_{21} with 5% moving averages. 170

Figure 4.6 Measurement of RF-CF S_{11} and S_{21}. 171

Figure 4.7 RF-CF delay of S_{21} with 5% moving averages. 172

Figure 4.8 Delay of RF-FF employing an external bias tee. 173

Figure 4.9 Normalized delay of RF-FF employing an external bias tee and VNA bias tee at V_{DC} = 20 V. 174

Figure 4.10 Measured relative RF power of SOA-XN with different bias currents. 175

Figure 4.11 Up-CPO experimental set-up using SOA-XN. SPL: RF splitter, LPF: Low Pass Filter, PC: Polarization Controller, Att: Attenuator, Pd: Photodiode, OF: Optical Filter, VNA: Vector network analyzer. 176

Figure 4.12 Photograph of Up-CPO experimental set-up using SOA-XN. OSA: Optical Spectrum Analyzer. 176

Figure 4.13 Calculated delay response of SOA-XN: at 9.7 GH (a) and at 30 GHz (b). Delay at both 9.7 GHz (solid lines) and 30 GHz (dotted lines) (c). 177

Figure 4.14 Calculated delay from measurement data at 30 GHz, shifted at 9.7 GHz at different bias currents for SOA-XN. Delay polynomial fits (dashed line). 178

Figure 4.15 Experimental set-up of hybrid correction structure using RF-FF with external bias tee. 180

Figure 4.16 photograph experimental set-up of hybrid correction structure using RF-FF with external bias tee. 180

Figure 4.17 Measurement of hybrid correction structure over 1 GHz of: (a) relative RF power (solid lines) and mean values (dotted lines). (b) Relative phase shift. (c) Calculated delay (solid line) and polynomial fit (dashed lines). 181

Figure 4.18 Hybrid correction structure of SOA-XN + RF-FF (RF folded filter). 182

Figure 4.19 Calculated delay response from measured phase shift of: SOA-XN and polynomial fits (dashed line) (a). RF-FF (b). Normalized calculated polynomial delay of SOA-XN (c), and normalized calculated delay of RF-FF (d). *183*

Figure 4.20 Normalized delay response of SOA-XN with (solid line) and without (dashed line) the hybrid correction structure for different gains (a)-(f). *185*

Figure 4.21 Delay response of the hybrid correction structure for different gains. Mean values (dotted line) over 1 GHz. *186*

Figure 4.22 Results of first category for: $\Delta delay\ p - p$ *and % of improvement (a) and (c).* $\sigma delay$ *and the ratio of* $\sigma delay$ *(b) and (d).* *187*

Figure 4.23 Results of second category for: $\Delta delay\ p - p$ *and % of improvement (a) and (c).* $\sigma delay$ *and the ratio of* $\sigma delay$ *(b) and (d).* *188*

Figure 4.24 Results of third category for: $\Delta delay\ p - p$ *and % of improvement (a) and (c).* $\sigma delay$ *and the ratio of* $\sigma delay$ *(b) and (d).* *189*

Figure 4.25 Hybrid correction structure response of relative RF power (solid lines) and mean value (dotted lines). *190*

Figure 4.26 Hybrid correction structure response: (a) Relative phase shift over 1 GHz. (b) Relative phase shift across 9.95 to 10.2 GHz. *191*

List of Tables

Table 1.1 Amplitude and phase response in frequency domain for phase shift and TTD. 17

Table 1.2 Typical qualitative performance of integrated phase shifter approaches. 26

Table 1.3 Summary of fiber optic delay line [35]. 39

Table 1.4 Summary of true time delay. 39

Table 2.1 Static characteristics of four commercial SOAs at wavelength 1550 nm. 59

Table 2.2 Maximum relative phase shifts, RF penalty and CPO bandwidth for the 4 SOAs at the gain 10 dB. 69

Table 2.3 Cutoff frequency of SOA-L (GHz) 94

Table 2.4 Cut-off frequency of SOA-NL (GHz) 94

Table 2.5 Cut-off frequency of SOA-XN (GHz) 94

Table 2.6 Phase offset for different bias current, at fc = 10 and 30 GHz. 103

Table 2.7 Delay variation over a frequency band of 1 GHz 105

Table 3.1 Transmission lines equivalent circuit in lumped element. 125

Table 3.2 Nodal matrix of a 6th order filter with a cross coupling resonator between 1 and 6. 130

Table 3.3 Element values of 6th order Chebyshev lowpass prototype with L_{Ar} = 0.01 dB.....131

Table 3.4 Parameters used in synthesis of half-wavelength shunt open-circuited stubs. 132

Table 3.5 Design parameters of the synthesized initial design half-wavelength shunt open-circuited stubs order-6 bandpass filter. 132

Table 3.6 Dimensions of microstrip lines for RF-FF. 136

Table 3.7 Delay ripple of RF-FF for various voltages. *142*

Table 3.8 Curved lines. *144*

Table 3.9 Delay ripple of RF-CF for various voltages. *144*

Table 3.10 Design parameters of simulation. *149*

Table 3.11 Design parameters and dimension values for the proposed RF-PS in 8-12 GHz frequency band. *149*

Table 3.12 Slope and offset of S_{21} phase for different values of capacitors in the frequency range from 9.5 GHz to 10.5 GHz. *150*

Table 3.13 Varactor-based analog phase shifters. *152*

Table 3.14 $\Delta RF\ \mathrm{power}\ p-p$ *(dB) of the normalized RF power comparison between responses of SOA-NL without and with hybrid correction structure versus frequency band.* *158*

Table 4.1 Delay ripple of measured RF-FF for various voltages. *171*

Table 4.2 Delay ripple of measured RF-CF for various voltages. *172*

Table 4.3 Delay ripples of RF-FF and external bias tee *173*

Table 4.4 Cutoff frequency of SOA-XN. *175*

Table 4.5 Delay response of SOA-XN and RF-FF over frequency range 9.2 GHz to 10.2 GHz. *184*

Table 4.6 $\Delta RF\mathrm{power}\ p-p$ *(dB) of the normalized RF power comparison between responses of SOA-XN without and with hybrid correction structure versus the frequency band.* *190*

Table 4.7 Linear regression line for phase shift of the hybrid correction structure over 1 GHz of frequency band. *192*

Table 4.8 Comparison between tunable delay/TTD approaches. *193*

Publications

Articles:

1. **N. Hamdash**, A. Sharaiha, T. Rampone, D. Le Berre, N. Martin, C. Quendo, "Small-Signal Analysis in two calculation sections and Experimental Validation of Up-Converted Coherent Population Oscillations in Semiconductor Optical Amplifiers," *IEEE Photonics Journal,* vol. 13, no. 4, pp. 1-10, Aug. 2021, Art no. 5500110, doi: 10.1109/JPHOT.2021.3090209.

2. **N. Hamdash**, A. Sharaiha, T. Rampone, C. Quendo, N. Martin, D. Le Berre, "Optically Controlled RF Phase Shifts in SOAs by Adding the XGM Response of an Optical Signal," *IEEE Photonics Technology Letters,* 2019, vol. 31, no 13, p. 1060-1063.

International conferences:

1. **N. Hamdash**, A. Sharaiha, T. Rampone, P. Morel, D. Le Berre, N. Martin, C. Quendo, "Experimental and Small-signal Analysis of Microwave Photonic Phase Shifter based on Slow and Fast Light using Linear and Nonlinear Semiconductor Optical Amplifiers," *IEEE International Topical Meeting on Microwave Photonics*, Toulouse, France, October 2018.

2. **N. Hamdash**, D. kastristsis, T. Rampone, A. Sharaiha, Z. Kyriakos, D. Le Berre, N. Martin, C. Quendo, "Optical functions for microwave signal processing using SOA and SOA-MZI," *XXI Simpósio de Aplicações Operacionais em Áreas de Defesa (XXI SIGE),* São José dos Campos, 2019, 24, Sep 2019.

National Conferences:

1. **N. Hamdash**, A. Sharaiha, T. Rampone, C. Quendo, N. Martin, D. Le Berre, "Architecture hybride optique-hyper fréquence pour la réalisation d'un retard vrai accordable," *Journée du Club Optique et Microondes*, JCOM 2019, Brest, 2019, <hal-02469855> 07, Jun 2019.

2. B. Chouya, **N. Hamdash**, A. Sharaiha, T. Rampone, D. Le Berre, N. Martin, C. Quendo, "Filtrage tout-optique d'une bande latérale avec un SOA-MZI pour l'amélioration d'un déphasage RF obtenu par CPO," *Journée du Club Optique et Microondes*, JCOM 2019, Brest, 2019, < hal-02469865> 07, Jun 2019.

3. **N. Hamdash**, A. Sharaiha, T. Rampone, P. Morel, D. Le Berre, N. Martin, C. Quendo, "Comportement de déphasage RF par l'effet de la lumière lente et rapide dans un SOA non-linéaire," *Journée du Club Optique et Microondes*, JCOM 2018, Toulouse, July 2018.

4. **N. Hamdash**, T. Rampone, A. Sharaiha, D. Le Berre, N. Martin, C. Quendo, “Contrôle optique du déphasage micro-onde généré par l’effet de la lumière lente et rapide dans un amplificateur optique à semi-conducteurs,” *Journée du Club Optique-Microondes,* JCOM 2018, Toulouse, 2018, <hal-02135614> 02, Jul 2018.

Appendix

A.1 Parameter values of the model implemented under ADS

Table A1: Parameter values of the model implemented under ADS

Parameters	***Value***	***Unite***	***Definition***
$\boldsymbol{L}$	750×10^{-6}	m	Length of the active area of SOA
$\boldsymbol{w}$	2.4×10^{-6}	m	Width of the active area of SOA
$\boldsymbol{d}$	95×10^{-9}	m	Thickness of the active area of SOA
$\boldsymbol{a_0}$	5×10^{-20}	m^2	Differential gain
$\boldsymbol{\lambda_0}$	$1\,580\times10^{-9}$	m	Wavelength at peak gain for N_0
$\boldsymbol{N_0}$	6.5×10^{23}	m^{-3}	Carrier density at transparency
$\boldsymbol{\alpha_0}$	2973	m^{-1}	Losses in the active zone at $N_0$and λ_0
$\boldsymbol{\Gamma_0}$	0.234		Reference confinement factor at N_0 and λ_0
$\boldsymbol{A}$	2×10^{9}	s^{-1}	Non-radiative recombination coefficient
$\boldsymbol{B}$	8.64×10^{-19}	$m^3\ s^{-1}$	Spontaneous recombination coefficient
$\boldsymbol{C}$	3.61×10^{-40}	$m^6\ s^{-1}$	Auger recombination coefficient

A.2 SOA-L datasheet

INPHENIX

Semiconductor Optical Amplifier Device (Gain-type)

IPSAD1301/1304 & IPSAD1501/1504 (1310nm/1550nm)

Features

- Wide Optical Bandwidth
- High Saturation Output Power
- Low Polarization Sensitivity
- Low Gain Ripple
- MQW or Bulk Structure
- 40G+ Ready

Applications

- Booster Amplifier (B-type)
- In-line Amplifier (L-type)
- Loss Compensation for Optical Cross-connect

IPSAD1301/1304 SOA Gain Type Device Specifications

Parameter	Symbol	IPSAD1301 In-Line Type			IPSAD1304 Booster Type			Unit
		Min.	Typ.	Max	Min.	Typ.	Max	
Drive Current	I_F		250			250		mA
Peak Wavelength	λ_p	1280		1340	1280		1340	nm
3 dB Optical Bandwidth	$\Delta\lambda_{3dB}$	45			55			nm
Small Signal Gain @ λ_p	G_{max}	18	22		13	16		dB
Gain Ripple with Respect to λ	ΔG		0.5	1.0		0.5	1.0	dB
Saturation Output Power	P_{sat}		10		10			dBm
Polarization Dependent Gain	PDG		0.5	1.0		0.5	1.0	dB
Noise Figure	NF		7	7.5		7	7.5	dB

IPSAD1501/1504 SOA Gain Device Specifications

Parameter	Symbol	IPSAD1501 In-Line Type			IPSAD1504 Booster Type			Unit
		Min.	Typ.	Max	Min.	Typ.	Max	
Drive Current	I_F		350			350		mA
Peak Wavelength	λ_p	1510		1590	1510		1590	nm
3 dB Optical Bandwidth	$\Delta\lambda_{3dB}$	45			55			nm
Small Signal Gain @ λ_p	G_{max}	18	20		12	15		dB
Gain Ripple with Respect to λ	ΔG		0.5	1.0		0.5	1.0	dB
Saturation Output Power	P_{sat}		10			10		dBm
Polarization Dependent Gain	PDG		0.5	1.0		0.5	1.0	dB
Noise Figure	NF			9.0			9.0	dB

A.3 40G-2R-ORP datasheet

PRELIMINARY DATASHEET | 40G-2R2-ORP

CIP Technologies

Twin 40G/s 2R Optical Regenerator

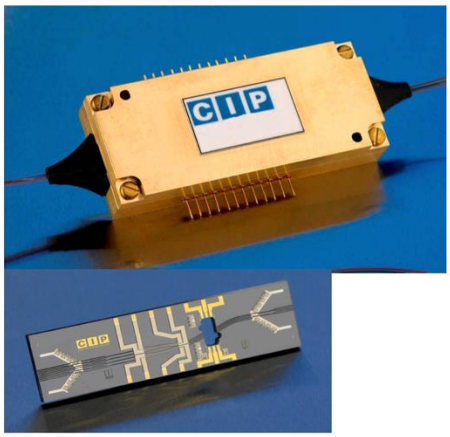

Features

- 40Gb/s operation
- Low switching energies (<100fJ per pulse per SOA)
- Low insertion loss (<5dB fibre to fibre)
- High output power (>0dBm)
- C Band operation (1530-1565nm)
- Single stage 2R regeneration for 2 independent data channels
- Dual stage regeneration for a single data channel

Applications

- Transmission impairment mitigation
- Wavelength conversion
- Cascaded two stage 2R regeneration with or without wavelength conversion
- Optical logic element

Description

CIP Technologies twin optical regenerator provides the capability for 2R regeneration (Re-shaping and Re-amplifying) of degraded data at rates of up to 40Gb/s and is bit rate and protocol transparent. The package houses two 40Gb/s regenerators in the same footprint as that previously required for a single regenerator device (40G-2R-ORP) and can regenerate two independent channels simultaneously. In addition, the two regenerators can be looped back to provide cascaded two stage regeneration and allow the output wavelength to be the same as the input wavelength.

The device can support applications in long-haul, metro and access networks. In addition, the device performs a variety of optical logic functions and can be used in optical processing applications.

The optical module is a hybrid integrated device consisting of two planar silica Mach-Zehnder interferometers with a quad array of non-linear SOAs in the interferometer arms. Independent thermo-optic phase shifters are incorporated to allow precise phase control of the interferometers. The module includes Peltier and thermistor for temperature control, electrical pins for SOA bias currents and phase shifters, 8 way fibre ribbon input (8x FC/APC connectors), and 4 way fibre ribbon output (4x FC/APC connectors). The package dimensions are 90mm x 31mm x 14mm.

Parameter	Rating	Unit
SOA bias current (per SOA)	400	mA
Average switching data power	+13	dBm
Average CW wavelength power	+13	dBm
Peltier Current	2.5	A
Operating Temperature	30	°C

A.4 SOA-NL-OEC-1550 datasheet

PRELIMINARY DATASHEET | SOA-NL-OEC-1550

CIP
Centre for Integrated Photonics

SOA-NL-OEC-1550 - 1.55µm Non-Linear Semiconductor Optical Amplifier (SOA)

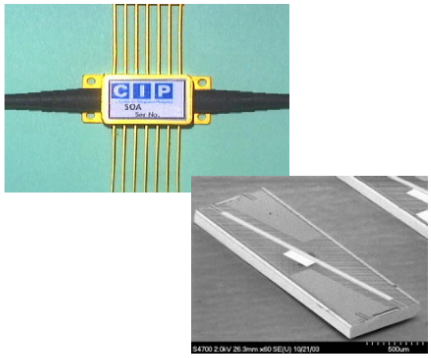

Features

- 1.55µm operation
- High gain (30dB)
- InP Buried Heterostructure design
- TEC cooled
- Suitable for non-linear and switching applications
- Available as packaged device or chip-on-carrier
- APC connectors provided

Description

The Non-linear SOA is a high confinement factor device optimised for high gain and fast optical recovery and hence fast switching speeds. It utilises CIPs proprietary InP buried heterostructure design and is available in either a 14-pin butterfly package with a thermistor, thermo-electric cooler and single mode fibre pigtails or as a custom chip-on-carrier product.

The product is appropriate in wavelength converter or four wave mixing applications and is used in CIPs wavelength converter device. Custom specification variants may be defined as appropriate for other non-linear applications. Arrays of non-linear SOAs are also available either packaged or as chip-on-carrier.

Optical and electrical characteristics All specifications are at 20°C and 1535-1560nm unless stated otherwise.

Item	Test condition	Min.	Typ.	Max.	Unit
Gain	200-300mA	25		34	dB
Polarisation Dependent Gain (PDG)	200mA	0.5		3	dB
Noise Figure (NF)	200mA	8		11	dB
Saturated Output Power (SOP)	200mA	6		8	dBm
ASE Ripple	200mA, at gain peak		1		dB
Gain Peak	200mA	1550		1570	nm
Gain Recovery Time	300mA, P_I >0dBm, 10-90% rise time			80	ps

www.ciphotonics.com .....researching solutions
CIP, Adastral Park, Martlesham Heath, Ipswich, IP5 3RE, UK Tel: +44 (0) 1473 663210 info@ciphotonics.com rev B

A.5 SOA-XN-OEC-1550 datasheet

PRELIMINARY DATASHEET | SOA-XN-OEC-1550

CIP Technologies

SOA-XN-OEC-1550 - 1.55µm Non-Linear Semiconductor Optical Amplifier (SOA)

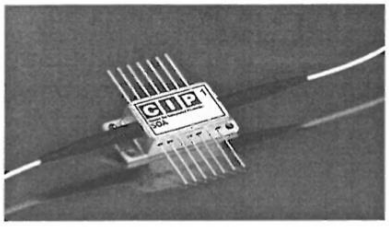

Features

- 1.55µm operation
- High gain
- Low saturation output power
- Very fast gain recovery times
- Low saturated PDG
- InP Buried Heterostructure design
- TEC cooled
- Available as packaged device
- APC connectors provided

Application Examples

- All optical processing
- Wavelength conversion
- Cross-phase modulation
- Cross-gain modulation
- Four-wave mixing

Description

The ultra non-linear SOA-XN is a high confinement factor device optimised for high gain and very fast gain recovery providing very fast optical switching speeds. It utilises CIP's proprietary InP buried heterostructure design and is available in either a 14-pin butterfly package with a thermistor, thermo-electric cooler and single mode fibre pig-tails

The product is appropriate in wavelength converter or four wave mixing applications and can also be used in CIP's hybrid integrated regenerator/wavelength converter products. Custom specification variants may be defined as appropriate for other non-linear applications. Arrays of non-linear SOAs are also available either packaged or as chip-on-carrier.

Optical and electrical specifications

All measurements are at chip temperature of 20°C & 1535-1560nm unless stated otherwise.

Item	Test condition	Min.	Typ.	Max.	Unit
Small signal Gain	I = 500mA		25		dB
Polarisation Dependent Saturated Gain (PDG)	I = 500mA, P_{in}>0dBm		1		dB
Saturated Output Power (SOP)	I = 500mA		12		dBm
Saturated Gain Recovery Time (1/e)	I = 500mA, P_{in}>0dBm, 1555nm		10		ps

DOCTORAT BRETAGNE LOIRE / MATHSTIC

UBO Université de Bretagne Occidentale

Titre : Génération de retards accordables hyperfréquences par des techniques optique-hyperfrequences pour des réseaux d'antennes.

Mots clés : Photonique hyperfréquence, Filtres hyperfréquence, Optoélectronique, Déphaseur, Photonique, Retards accordables vrais, SOA (amplificateurs optiques à semi-conducteurs).

Résumé : La génération de retards accordables vrais (TTD) pour des signaux hyperfréquence par association de technologies hyperfréquence et photonique (MWP) est fondamentale pour les systèmes embarqués, les communications par satellite et les radars. De plus, une structure hybride utilisant les technologies MWP augmente les capacités et les libertés de conception des fonctions à réaliser, tout en bénéficiant d'une forte immunité aux interférences électromagnétiques et des faibles pertes des fibres. Une des approches photoniques les plus prometteuses est l'oscillation de population cohérente (CPO) et la CPO avec montée en fréquence (Up-CPO) dans un amplificateur optique à semi-conducteurs (SOA).

Dans cette thèse, nous analysons, théoriquement par une analyse petit signal puis expérimentalement, les réponses en fréquences CPO et Up-CPO pour quatre structures de SOA différentes. Nous proposons aussi une nouvelle architecture, combinant deux étages, basée sur une approche photonique pour le premier étage utilisant une technique Up-CPO. Le deuxième étage consiste en un déphaseur RF accordable et un filtre RF accordable, qui corrige à la fois les réponses de non-linéarité du premier étage et ajoute un décalage de phase nécessaire pour obtenir un TTD. En utilisant une approche hyperfréquence-photonique combinant Up-CPO dans un SOA avec un filtre accordable RF à une fréquence de fonctionnement de 9,7 GHz, nous démontrons par des simulations utilisant les résultats expérimentaux la possibilité de réaliser un TTD accordable à haute fréquence d'environ 56 ps avec une amélioration maximale de 80% pour une bande de fréquences de 0,375 GHz.

Title : High Frequency Tunable Delay by Microwave-Photonics Techniques for Antenna Networks.

Keywords : Microwave photonics, Microwave filters, Optoelectronics, Phase shifter, Photonics, True time delay, SOAs (Semiconductor Optical Amplifiers).

Abstract : Tunable true-time delay (TTD) at a microwave frequency by association of microwave and photonic (MWP) technologies is extremely valuable for embedded systems, satellite communications and radars. Moreover, a hybrid structure using MWP technology increases the capabilities and design freedoms of functions to be realized while benefiting from a high immunity to electromagnetic interference and low losses of optical fibers. Two of the most promising photonic approaches to provide a tunable microwave phase shift are the Coherent Population Oscillation (CPO) and the Up-converted CPO in a semiconductor optical amplifier (SOA).

In this PhD thesis, we analyze theoretically by small signal analysis and experimentally CPO and Up-CPO RF responses for four different SOA structures. We then proposed a new architecture combining two stages based on a photonics approach for the first stage using an Up-converted CPO technique. The second stage consists of a tunable RF phase shifter and a tunable RF filter, which corrects the non-linearity responses of the first stage and adds a phase offset needed to obtain a TTD.

By using a microwave-photonics approach combining Up-converted CPO in a SOA with an RF tunable filter at an operating frequency of 9.7 GHz, we demonstrate by simulations using the experimental results the possibility of realizing high frequency tunable TTD of about 56 ps with a maximum improvement of 80% for a 0.375 GHz frequency band.